EXCITED STATES IN SPATIALLY-CONFINED [3X3] GRID-TYPE COMPLEXES

STEVEN SMITH

EXCITED STATES IN SPATIALLY-CONFINED [3X3] GRID-TYPE COMPLEXES

by

© Steven Smith, B. Sc. (Honours)

A thesis submitted to the

School of Graduate Studies

in partial fulfillment of the

requirements for the degree of

Master of Science

The Department of Chemistry

Faculty of Science

Memorial University of Newfoundland

August 2011

St. John's Newfoundland and Labrador

ABSTRACT

The field of nanoscience is predicated on the study of organized assemblies on the nanoscale. Through an understanding of the unique properties of highly-ordered molecular assemblies at confined dimensions, the development of new devices can be realized. However, the challenge in the construction of a new device involves an understanding of the properties expressed by each of the components in the combined collective.

Previously synthesized grid-type complexes incorporate both metal ions and π-ligands into a highly-organized spatially-confined nanoscale system. The composition of the grid-type structure can vary from an array of [2x2] metal ions with 4 ligands to [5x5] metal ions with 10 ligands. These nanostructures may be partitioned into substructures which involve a grid-like core of metal ions and a π-stacked ligand framework encompassing the core. An understanding of the electronic properties of these nanostructures involves an understanding of the electronic properties of each of these substructures, and the collective electronic properties expressed through interaction of the core with the ligands. The studies presented in this thesis focuses on the photophysical properties of three self-assembled [3x3] grid-type systems which are composed of $Zn(II)_9$, $Mn(II)_9$, and $Mn(III)_4Mn(II)_5$ metal ions and 6 hydrazone-based (2POAP) ligands.

Comprehensive studies on $[Zn(II)_9(2POAP\text{-}2H)_6](NO_3)_6$ are presented which classify the excited states for the ligand framework in the grid-type complexes studied. The ligands in the [3x3] grid-type complex portray both discrete and emergent charge transfer behaviour which is greatly influenced by spatial-confinement. The ligand excited

states are shown to exhibit intramolecular charge transfer specific to each ligand as well as interligand charge transfer between ligands.

Following a discussion on the ligand states, the excited states for the metal core in $[Mn(II)_9(2POAP\text{-}2H)_6](ClO_4)_6$ and $[Mn(III)_4Mn(II)_5(2POAP\text{-}2H)_6](ClO_4)_{10}$ are presented. Furthermore, the excited states resulting from the interaction of the metal core with the ligand framework are classified. These states are shown to exhibit a range of charge transfer behaviour which includes metal-to-metal charge transfer, ligand-to-metal charge transfer, and metal-to-ligand charge transfer. Moreover, it is shown that the excited states in these open-shell metal complexes retain their characteristic ligand states which are offset by the interaction of the metal with the ligand.

The light-harvesting properties of $[Zn(II)_9(2POAP\text{-}2H)_6](NO_3)_6$ were investigated through titrations with anthracene-9-carboxylic acid. These studies were undertaken to examine the potential application of grid-type complexes as light-harvesting units. The interaction of these molecules results in a supramolecular hydrogen-bonded adduct in which electronic excitation energy transfer is heavily involved in the excited state relaxation process. This excitation energy transfer is shown to occur from the anthracene derivative to a ligand charge transfer state over relatively short (~8 Å) and long distances of up to 50 Å through the Förster mechanism.

To my family and friends

ACKNOWLEDGEMENTS

First of all, I wish to thank my supervisor, Dr. David W. Thompson (Dr. Dave), for his encouragement and support during the course of my study. Dr Dave's supervision has been a great experience and I really appreciated his hands-off approach. I can't imagine a better mentor in which to develop my skills as a researcher and scientist.

I would like to thank the faculty and staff, specifically my supervisory committee, Dr. Peter Pickup and Dr. Yuming Zhao, for their guidance and suggestions during the course of this work.

Over the course of my program, the members of the Photophysics group (Brent, Prateek, Alex, Mohammad, Sam, El-Dali, and Li) have contributed immensely to my personal and professional development at Memorial and I wish to thank them for that experience. I would also like to express my gratitude to Dr. Peter Pickup and the rest of the Pickup group for giving me excellent feedback during our joint group efforts.

The work presented in this project would not have been possible without the synthetic expertise of Dr. Laurence K. Thompson and his group who donated such great grid complexes for me to study. I wish to thank Laurie and his group for giving me the opportunity to classify the excited state properties in these unique grid systems.

I love to learn. Learning is a big part of who I am. It is probably the greatest privilege and experience one could ever have. I would like to thank any previous educators who have taught me over the years. More specifically, I would like to convey my gratitude to my supervisor for introducing me to Photophysics and Photochemistry, Dr. Laurence K. Thompson for introducing me to Supramolecular Chemistry and

Magnetism, and Dr. Ray Poirier for introducing me to Quantum Mechanics and Computational Chemistry.

I would like to convey my thanks and appreciation to my family and friends, especially Meaghan Malone for her unrelenting support and encouragement during the course of my graduate studies. You are far more than anything anyone should ever have. Thank You!

Funding is gratefully acknowledged from NSERC, CFI, IRIF, SGS, and Memorial University.

Steven R. Smith, B. Sc. (Honours.)

Memorial University

August 2011

TABLE OF CONTENTS

LIST OF TABLES

LIST OF FIGURES

LIST OF SCHEMES

LIST OF ABBREVIATIONS AND SYMBOLS (by appearance)

CHAPTER 1

1D	One Dimensional
2D	Two Dimensional
DNA	Deoxyribonucleic acid
NMR	Nuclear Magnetic Resonance
POAP	N'-(pyridin-2-ylcarbonyl)pyridine-2-carbohydrazonamide

CHAPTER 2

$\Delta\nu_{1/2}$	Band width at half maximum
ν	frequency
υ	Ground state vibrational quantum number
υ'	Excited state vibrational quantum number
$\hbar\omega$	Quantum spacing between vibrational levels in the ground state
$\hbar\omega'$	Quantum spacing between vibrational levels in the excited state
χ	Nuclear Wavefunction
Ψ	Total wavefunction
ψ	Electronic wavefunction
DDG	Digital Delay Gate
E	Electrical component of electromagnetic radiation
E_b	Exciton binding energy
E_x	Exciton energy

e^-	Electron
E_0	Energy difference between the ground and excited state zero vibrational levels
F	Force
f_e	Prohibition factor for electronic configurations
f_{es}	Spin-Orbit prohibition factor
f_{ev}	Vibronic prohibition factor
f_s	Prohibition factor for spin configurations
f_v	Prohibition factor for nuclear configurations
H	Magnetic component of electromagnetic radiation
H	Hamiltonian
h	Planck constant
h^+	Electron hole
HP	Hewlett-Packard
I	Intensity
NIR	Near-Infrared
nm	nanometer
PMT	Photomultiplier Tube
PTI	Photon Technology International
s	Second
S	Spin wavefunction
S^v	Huang-Rhys factor
UV	Ultraviolet

Vis	Visible

CHAPTER 3

Φ	Molecular Orbital
DFT	Density Functional Theory
DMSO	Dimethyl Sulfoxide
HOMO	Highest Occupied Molecular Orbital
LUMO	Lowest Unoccupied Molecular Orbital
M	Molar
MeCN	Acetonitrile
PCM	Polarized Continuum Model
ppm	Parts per million
TD	Time-Dependent
tpy	Terpyridine

CHAPTER 4

ΔG	Free Energy Change
$\Delta G^{\ddagger}$	Free Energy of Activation
ΔG_{00}	Free Energy difference between the ground and excited state zero vibrational levels
$\lambda_{o \text{ or } s}$	Solvent or Outer-Sphere Reorganization Energy
$\lambda_{i \text{ or } vib}$	Vibrational or Inner-Sphere Reorganization Energy
λ_t	Total Reorganization Energy
κ	Transmission factor

ν_N	Nuclear Vibrational Frequency
A	Acceptor
ADP	Adenosine Diphosphate
ATP	Adenosine Triphosphate
BChl	Bacteriochlorophyll
BPh	Bacteriopheophytin
Car	Carotenoid
CT	Charge Transfer
D	Donor
et	Electron Transfer
f	Fluorescence
f_i	Force Constant
FCWD	Franck-Condon Weighted Density of States
ic	Internal Conversion
isc	Intersystem Crossing
k	Rate Constant
P	Photosynthetic Special Pair
Q	Quinone
S	Singlet
T	Triplet
TMDO	Tetramethylbenzodioxole
TW	terawatt
V or H_{ab}	Electron Coupling Matrix Element

X	Reduced Coordinate

CHAPTER 5

3D	Three Dimensional
$\vec{\mu}$	Transition Dipole Moment
Å	Angstroms
COSY	Correlated Spectroscopy
E_{op}	Optical Transition Energy
ET	Electron Transfer
f	Oscillator Strength
fl	Fluid
fr	Frozen
G	Gaussian
ILCT	Interligand Charge Transfer
J	NMR Coupling Constant
TFA	Trifluoroacetic acid

CHAPTER 6

JT	Jahn-Teller
LMCT	Ligand-to-Metal Charge Transfer
$\vec{M}$	Transition Dipole
μ	Micro
MLCT	Metal-to-Ligand Charge Transfer
$Mn(II)_9$ grid	$[Mn(II)_9(2POAP\text{-}2H)_6]^{6+}$

$Mn(III)_4Mn(II)_5$ grid $[Mn(III)_4Mn(II)_5(2POAP\text{-}2H)_6]^{10+}$

CHAPTER 7

F(Calc)	Franck-Condon Vibrational Overlap Factor
fs	Femtosecond
J_{DA}	Spectral Overlap Integral
K	Exchange Integral
LH	Light Harvesting
ps	Picosecond
RC	Reaction Center
R_{DA} (or r_{DA})	Distance between donor and acceptor

CHAPTER 8

$AnCO_2(H)$	Anthracene-9-Carboxylic Acid (or 9-Anthroic Acid)
K_d	Dynamic Quenching Constant
K_s	Static Quenching Constant
L	Litre
Q	Quencher
R_Q	Quenching Sphere Radius
V_Q	Quenching Sphere Volume
$Zn(II)_9$ grid	$[Zn(II)_9(2POAP\text{-}2H)_6]^{6+}$

Chapter 1:

"THE GRID-TYPE COMPLEX – SYNTHETIC STRATEGIES AND PROPERTIES OF GRID-TYPE NANOMATERIALS"

Abstract: The research described in this thesis is predicated on classifying and exploring the excited state properties of square [nxn] polymetallic grid-type complexes. The structure of such complexes may be classified in terms of two sub-structures: the multi-metallic core and the organized ligand framework. However, before describing the excited state and dynamic properties associated with each of these sub-structures, a review of the synthetic methodology, the variety of molecules available, and the current properties known for square [nxn] polytopic grid-type complexes is presented in this chapter. In addition, the scope of this thesis is presented as it relates to the discovery of new and unexplored ligand properties inherent to the grid-type complex.

1.1. Introduction

Any type of device may be defined as an assembly of property specific components which cooperate to form an entity with a specific function.[1] At present, device construction follows a top-down approach where device components are crafted at the macroscopic level and then assembled. Due to the interconnection of society and technology, the progression of our species is undoubtedly motivated by the construction of smaller and smaller devices. For the construction of such devices, components must be manipulated into smaller and smaller pieces. As suggested by Moore's law[2], device miniaturization is approaching a practical limit due to technological limitations in building such 'mini'-devices. Ideally, to overcome such a limit and maximize miniaturization, one would prefer to assemble a device through Feynman's "bottom-up

approach" where nanoscale objects assemble into nanostructures.[2] The motivation for obtaining such *nanostructures* is a consequence of bridging further device miniaturization with the current size limitation of the top-down approach. As in the macroscopic level where individual device components combine specific acts to form a functional device, it is envisioned that molecular components may combine in a similar fashion to form a functional molecular device. One approach to molecular device design involves atom-by-atom construction, however, atoms are highly reactive and form covalent bonds with neighbouring atoms.[1] An alternative to atom-by-atom construction involves the use of molecules as building units. This alternative is advantageous as molecules are stable units which carry distinct properties that may be manipulated photochemically and electrochemically.[1] Molecules may also assemble and connect with other molecules to create larger units as is the case within nature where biologically important constructs are built through the assembly of individual molecular units.[1]

At the heart of many biological processes lies an elaborate superstructure consisting of many molecular components bound by a variety of intermolecular interactions such as H-bonding, ionic interactions, and π-π interactions. Such superstructures include DNA, hemoglobin, and various photosynthetic components (Figure 1.1.1). Stemming from nature's approach to the design and assembly of superstructures has been the field of supramolecular chemistry where the construction of a molecular device has been approached through the assembly of highly ordered molecular units into a functional architecture. One of the pioneers of this field – Jehn-Marie Lehn – has described this field as the chemistry of molecular association and the intermolecular bond.[3] For his extensive work in this area, Jehn-Marie Lehn was awarded

the Nobel Prize in Chemistry in 1987 in conjunction with other pioneers of this field, specifically Donald J. Cram and Charles J. Pedersen.

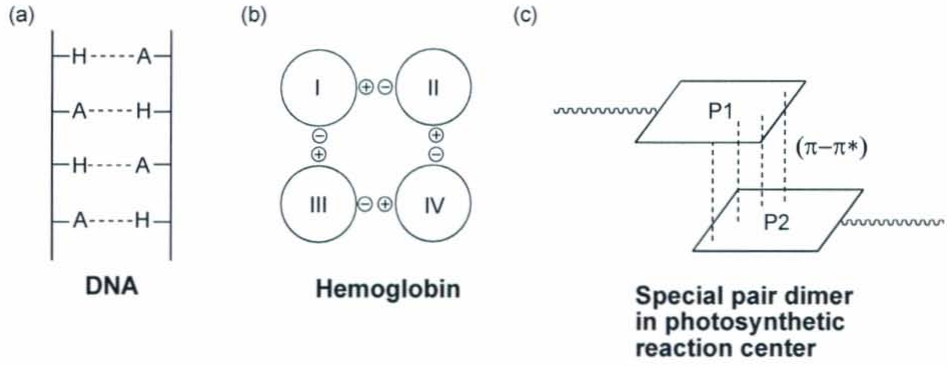

Figure 1.1.1. Examples of superstructures in nature. (a) DNA (left) where single strands are held together by H-bonds; (b) hemoglobin (middle) where subunits are held together by ionic interactions; and (c) the special pair dimer in photosynthetic reaction centers where the porphyrin dimer is held together by π-π^* interactions.

Over the past decade, many attempts towards constructing functional molecular device components have been pursued which include molecular muscle[4], molecular elevators[5], and grid-like metal clusters[6, 7]. Such structures may find applications in areas associated with mechanical motion, shuttling, and memory storage. As synthetic strategies towards such aesthetically pleasing structures become realized in solution, the notion of addressability becomes apparent: how can molecules in solution, which behave independently, be addressed as individual components of a device? Addressability arises as a consequence of the interface of the microscopic world with the macroscopic world where spatial ordering of molecular units must be achieved in some manner to allow coherent formation of molecular components, and ultimately, device functionality.

Obtaining such molecular arrays may be addressed via immobilization of such structures on surfaces or membranes, or through construction of extended supramolecular architectures. The purpose of this chapter is to provide a review on the assembly of ordered arrays from their constituent components. Approaches to the design of metal clusters, grid-type and extended grid-type arrays are discussed, as well as structure-property relationships inherent to these complexes.

1.2. Supramolecular Chemistry

Supramolecular chemistry encompasses the study of the intermolecular noncovalent bond. However, an emerging area of supramolecular chemistry involves the covalent metal-ligand coordination bond and is synonymous with that of highly-organized coordination chemistry. Such an area – metallosupramolecular chemistry – is of growing interest as metal centers possess unique characteristics in that they provide structural specificity (i.e. octahedral, tetrahedral, etc. geometries) and can be highly active redox-centers. One, then, may ask the fundamental question: How do we define supramolecular chemistry? Jean-Marie Lehn has described supramolecular chemistry as "an area taking advantage of the innate nature of the information paradigm within matter where the blueprint for the creation of a complex is contained within its individual components".[8, 9] Through manipulation of *inter-component* interactions, supramolecular chemistry "*explores the storage of information at the molecular level and its retrieval, transfer, and processing... via interactional algorithms operating through molecular recognition events*".[9] Its main purpose is to manipulate spatial and temporal features of matter to

form highly-ordered complex architectures for technological advancement.[9] Although strict definitions of supramolecular chemistry are obscure when one includes coordination bonds as non-covalent (they are nothing but covalent!) and in defining supramolecular chemistry as the new adaptation of the intermolecular interaction, it is without any doubt that supramolecular chemistry is a reflection of a *philosophy to molecular building*. Supramolecular chemistry may then be viewed as an approach to building molecular assemblies; an area bridging traditional synthetic simplicity with architectural complexity (Figure 1.2.1).

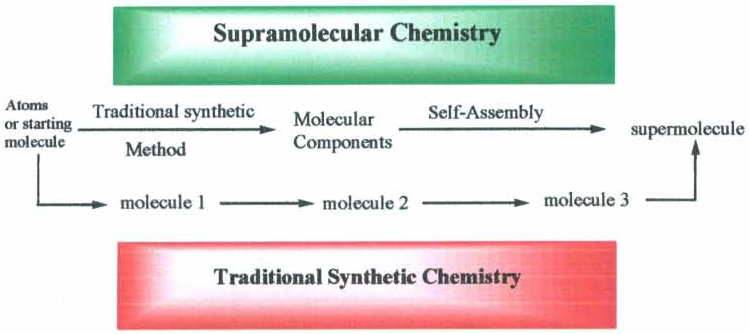

Figure 1.2.1. Connecting traditional synthetic chemistry with "supramolecular chemistry".

The molecule, an assembly of atoms held together via covalent bonds, imparts physical and chemical properties which are related to its structure. Traditional synthetic chemistry has been successful in assembling a variety of molecular entities from as small as ethane to as large as fullerene. However, to assemble higher-ordered structures on par with nature (such as DNA), current synthetic methodologies face substantial limitations such as high cost, low product yields, etc. Therefore, a new challenge facing synthetic

chemists is to develop new methodologies that target the synthesis of nature-scale structures. As such, one might ask: how does nature build such large structures? The approach lies within the building unit of such an entity: the molecule. Nature programs information into the structure of individual molecules (i.e. synthesizes molecules with specific features) which, when assembled, form functional 'supermolecules'. This is the fundamental motivation behind that of supramolecular chemistry (or the "supramolecular philosophy"). Thus, supramolecular assemblies may be viewed as an assembly of molecules which interact to give a higher-ordered structure with structurally related physical and chemical properties (Figure 1.2.2).

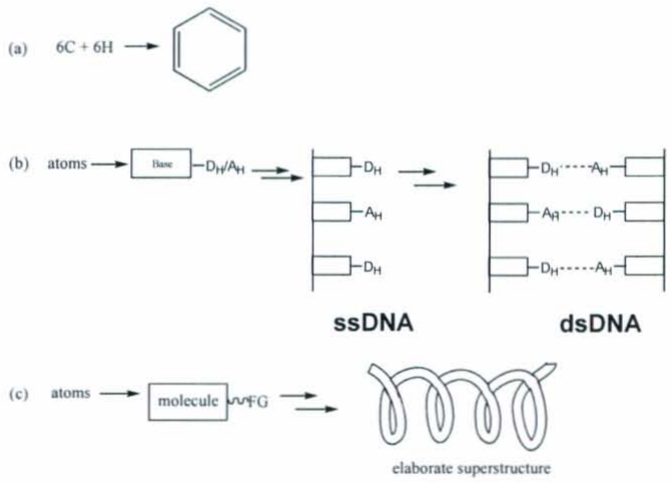

Figure 1.2.2. From atoms to molecules to superstructures. (a) molecules are constructed from atoms. For example, benzene is composed of six carbon and six hydrogen atoms. (b) Nature builds superstructures via the interaction of molecular components with built-in information through its arrangement of atoms. D_H and A_H refer to hydrogen donors and acceptors, respectively. ss- and ds-DNA refer to single-stranded- and double-stranded-DNA. (c) Supramolecular chemistry mimics nature in its approach towards superstructure synthesis.

In reviewing the broad area of supramolecular chemistry, the following themes become apparent: (i) molecular recognition, which relies on the concepts of preorganization and complementarity of host-guest complexes; (ii) the notion of self-assembly and self-organization, which is associated with the spontaneous assembly of components in a pre-programmed fashion to form higher-order architectures; and (iii) the common binding interactions which give rise to highly-organized constructs such as the hydrogen bond, the π-π interaction, and the metal-ligand coordination bond.

1.2.1. Molecular Recognition

Molecular recognition forms the heart of supramolecular chemistry, a well-established concept that dates back to Emil Fischer and his lock and key model in the nineteenth century. It may be viewed as the specific non-covalent association of a substrate (guest) with a receptor (host) to form a host-guest complex. Generally, the host is considered as the molecule exhibiting convergent binding sites within the host-guest complex whereas the guest is considered as the molecule exhibiting divergent binding sites in the complex.[10, 11] These properties may include hydrogen bond donating/accepting abilities, Lewis acidity/basicity, etc. This is best illustrated by Figure 1.2.1.1.

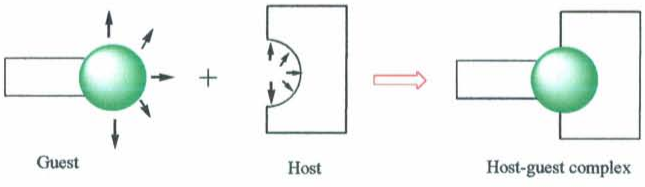

Figure 1.2.1.1. Distinguishing host from guest and the lock and key model for molecular recognition. Outward arrows imply divergence and inward arrows imply convergence.

One very important concept is evident from Emil Fischer's lock and key model for molecular recognition: that of complementarity between the host and guest. For a host and guest to bind, both the host and guest must contain binding sites which are of the correct size, shape, symmetry, and electronic structure to complement the specific association of one with the other. Referring back to the goals of supramolecular chemistry from the perspective of Lehn[9], complementarity may be viewed as a consequence of the spatial features of matter where information is stored in the host and guest molecular (or spatial) structure, and expressed through the binding of the host with the guest. Figure 1.2.1.1 may be used as an illustration of the concept of complementarity where the host binding site contains the correct size, shape, and electronic structure to compliment the divergent binding region of the guest.

When one takes into account the dynamic features of matter such as conformational rearrangement, the notion of preorganization becomes clear within molecular recognition processes. Formation of a host-guest complex may be thought of as consisting of three steps: (i) the host and/or guest may undergo conformational rearrangement in order to arrange their binding sites so that they are complementary to their binding partner; (ii) the host and/or guest solvent cage must also rearrange to accommodate the new host and/or guest structures; and (iii) binding occurs with solvent released from the host and/or guest solvent cage. Reorganization steps (i) and (ii) may require that energy be supplied to the system such that a substantial kinetic barrier to formation of the host-guest complex may exist. The binding step (iii), however, is energetically favourable as a consequence of bond formation. Preorganization, then, may be considered as the pre-positioning of the host and/or guest to form complimentary

binding structures prior to the binding event. The rearrangement must take place prior and not after association as repulsion energies provide a driving force towards dissociation of the complex and an additional barrier to formation of the host-guest complex. This concept is illustrated in Figure 1.2.1.2.[10]

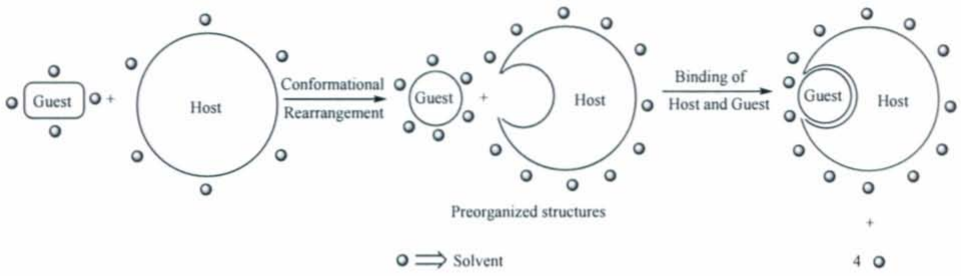

Figure 1.2.1.2. Proposed stages of a host-guest binding process. Conformational rearrangement involving both the host and guest is illustrated here; however, rearrangement of either one of the molecules may occur and is the basis for enzyme catalysis where it is the host which rearranges, binds the guest, and forces the guest to rearrange or react.[10]

As a consequence of the connection between preorganization and the dynamics of matter (*vide supra*), the extension of kinetic and thermodynamic products into the realm of host-guest chemistry are apparent. Preorganization is bound by the rates in which rearrangement occur. If more than one pre-organized construct possesses some degree of complementarity with a rearranged structure of its binding partner, then the rates of interconversion towards each product must be taken into account. Thus, the concepts of kinetic and thermodynamic selectivity are realized as kinetic and thermodynamic complementarity within molecular recognition processes (Figure 1.2.1.3).

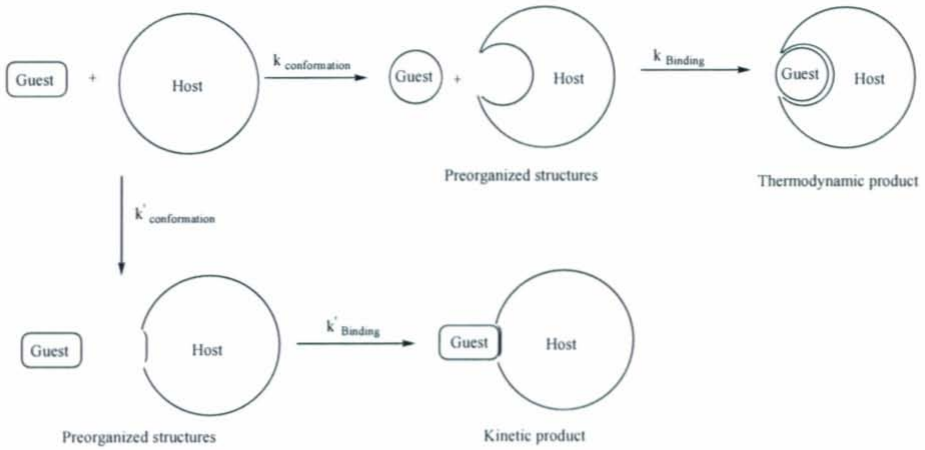

Figure 1.2.1.3. Kinetic and thermodynamic complementarity.[10]

In summary, molecular recognition events are governed by relatively weak interactions; however, the overall effect can be very large. This is due to the accumulation of a large number of these weak interactions. As these interactions are relatively weak, they can be profoundly dependent on solvation effects. As a result, we must take into account solute-solvent and solvent-solvent interactions if we are to further understand natural systems at the molecular level and to develop revolutionary materials for technological advancement.

1.2.2. Self-Assembly and Self-Organization

Ubiquitous in nature, self-assembly is involved in a variety of biologically complex processes such as DNA replication and protein synthesis.[12] The term is associated with the spontaneous assembly of components into a spatially-confined entity.[13] The architecture of such an entity is a consequence of the unique molecular

characteristics of its components. These unique characteristics are "encoded" in terms of the component composition. As such, from a chemical perspective, molecular design directs the assembly of a supermolecular structure. In its simplest form, self-assembly provides the bridge between conventional synthetic methods and higher-ordered structures within chemistry (Figure 1.2.1).

Self-assembly may involve covalent or non-covalent interactions and may be classified as either an organized or disorganized process in the event where higher-ordered structures are formed. Disorganized self-assembly may be taken as the spontaneous assembly of components into an unorganized or randomly-ordered structure. This type of self-assembly is synonymous with that of aggregation - regarded as the collection of entities into a randomly-ordered structure via inter- and/or intra-molecular interactions. Organized self-assembly, however, may be considered as the spontaneous self-assembly of components into an organized structure. Since the structure is organized, some pattern must result as a consequence of the incorporation and integration of individual component interactions with higher-order interactions to give the expressed collective behaviour. The concepts of self-assembly and its distinction as organized and disorganized are illustrated in Figure 1.2.2.1.

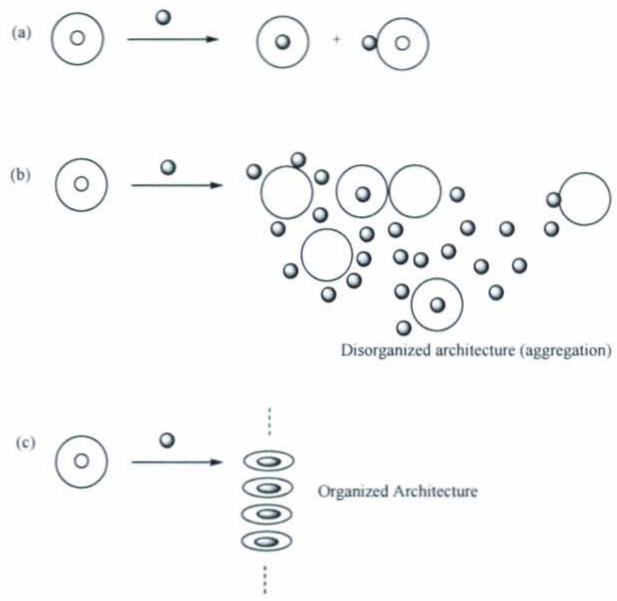

Figure 1.2.2.1. Self-assembly in an organized and disorganized fashion.(a) general self-assembly; (b) aggregation or disorganized self-assembly; (c) organized self-assembly. Self-Organization is used in (c) when only intermolecular interactions are involved in the assembly of the architecture.[10]

Organized intramolecular self-assembly utilizes covalent bonding as a means of organizing the self-assembling entities into a desired structure or pattern. Examples utilizing this type of self-assembly include helicates and grid-like arrays.[6, 7, 13] As organized intramolecular self-assembly utilizes covalent bonding within the self-assembly process, organized intermolecular self-assembly utilizes non-covalent interactions to form supramolecular architectures. This type of self-assembly has been classified by Lehn as *self-organization* which he defines as "*systems capable of spontaneously generating well-defined [or ordered] supramolecular architectures [of higher structural order] from its components under a given set of conditions*".[8, 9, 13] Self-organization is found throughout

nature such as in DNA replication and the formation of membranes.[12] It is believed to be a process that led to the emergence of complex biological matter from inanimate matter.[9]

1.2.3. Common binding interactions in Supramolecular Chemistry

Thus far, concepts such as molecular recognition and self-assembly have been discussed; however, the question still remains: What are the forces that are involved in molecular recognition and the self-assembly process which hold components together? Furthermore, practical molecular devices will undoubtedly require a high-degree of organization in order to function properly. What, then, are the interactions that are involved in molecular recognition and self-assembly which hold components together in an organized spatially-confined manner?

With the exception of the hydrophobic effect, most binding forces originate as a result of some electrostatic interaction. This interaction is viewed as a consequence of the innate nature of attraction and repulsion between like and unlike charges within matter. A manifestation of this principle is given through Coulombs law where the energy of interaction between charges is related to the product of charges (q_1 x q_2) and the inverse product of the distance (r) and screening (ε x ε_o) between those charges (equation 1.2.3.1). Of the electrostatic interactions, two mainly give rise to structurally organized components: H-bonding and π-π interactions.

$$E = \frac{q_1 q_2}{4\pi\varepsilon\varepsilon_0 r} \qquad \textit{eqn. 1.2.3.1}$$

1.2.3.1. Hydrogen Bonding

The hydrogen bond may be regarded as the coulombic attraction between a hydrogen atom attached to an electronegative atom or group to an adjacent atom or molecule. The terms hydrogen bond donor (D_p) and hydrogen bond acceptor (A_p) are commonly used to describe the location of the proton. This type of electrostatic interaction is highly directional in that it operates under specific orientations. It is of paramount importance in DNA where it is a contributing factor for holding DNA single strands together.[12]

1.2.3.2. π-π interactions

π-π interactions are regarded as the interaction between π-systems. π-systems contain regions of negative and positive charge as a consequence of the difference in electronegativities between carbon and hydrogen within the C-H bonding framework. The existence of such regions in conjunction with the aromatic structure gives rise to a quadrupole, leading one to expect that aromatic systems may be involved in a variety of electrostatic interactions. Such an electrostatic model for π-π interactions has been proposed utilizing the attraction between the π-network of one aromatic and the σ-network of another (Figure 1.2.3.2.1).[14] This model adequately predicts the commonly observed geometries of π-stacked systems which include parallel stack, parallel offset, and edge-to-face geometries. Like hydrogen bonding, this type of electrostatic interaction is directional in the sense that the aromatic interaction exhibits an angular dependence (π-systems must be parallel or perpendicular to one another). This type of interaction is also

of relevance within the structure of DNA where π-stacking (or π-σ interactions) between base pairs contributes to the structural integrity of the architecture.

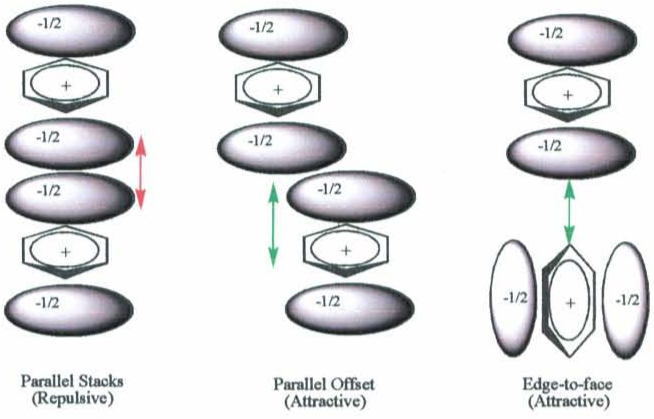

Figure 1.2.3.2.1. π-stacking geometries through an electrostatic model. As the aromatic is neutral, the net charge of the σ-framework is cancelled by the net charge of the π-network. Green arrows refer to a net attraction whereas a red arrow refers to a net repulsion.

1.2.3.3. Preamble to Metallosupramolecular complexes

Other than the directional interactions which involve primarily electrostatic interactions are the inorganic architectures which utilize metal-ligand coordination bonds. Incorporating metals within the architecture of supramolecular complexes is of interest as metals provide a means for holding and orienting components in a given direction (for example in octahedral and tetrahedral geometries, cis- and trans- configurations, etc.). Metals also exhibit or impart a variety of interesting properties within a supermolecule such as redox activity and magnetism. Although the coordinate bond is considered to

exhibit covalent character, a wide range of metal-ligand binding strengths span the scope of non-covalent and covalent interactions.[13] A clear-cut categorization of metal-ligand bonds as covalent or non-covalent proves to be difficult.[13] As such, no distinction between the covalent and non-covalent inorganic architectures has yet been made, although such architectures are commonly referred to as "supramolecular". In essence, metallosupramolecular complexes are synonymous with highly-organized coordination complexes.

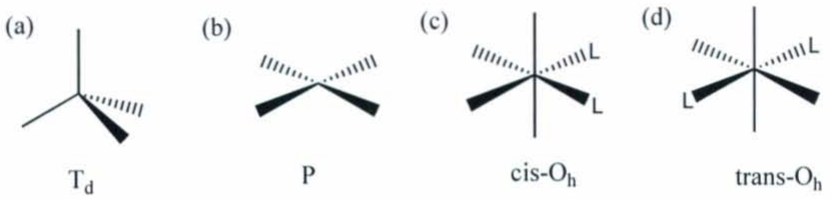

Figure 1.2.3.3.1. Coordinate bond as a directional interaction in building organized superstructures.(a) Tetrahedral; (b) planar; (c) cis-octahedral; and (d) trans-octahedral coordination complexes.

1.3. Metallosupramolecular Chemistry

In explaining bonding in metal-ligand compounds, Werner proposed that metals could bind directly to multiple ligands. His theory required two binding interactions: one electrostatic in nature, where counterions balanced the charge on the metal center; and the other where ligands coordinate directly to the metal center to form a coordination sphere with a defined geometry.[15] Later, Beth and Van Vleck developed crystal field theory which provided a model for predicting coordination sphere geometries that depend on the nature of the metal center (from d^0 to d^{10}) and the resulting crystal field stabilization

energy. This dependence was a result of the electrostatic field provided by ligand electron pairs which effectively split the metal d orbitals such that the degree of splitting is dependent on the degree of electron-electron repulsion between the d orbital and ligand electrons. As a consequence, metal d orbitals which are directed towards the surrounding ligand electron pairs are raised in energy and d orbitals which are directed away from the ligand electron pairs are lowered in energy relative to the average field (or spherical field) where the d orbitals maintain degeneracy within the coordination sphere.[15] This is illustrated in Figure 1.3.1. for an octahedral complex. Since the goal of the supramolecular philosophy is to produce well-defined architectures from multiple components, the choice of metal center in conjunction with the proper design of ligands will lead to distinct supermolecules with the metal center serving as a directing component for ligands and as a chemically-active unit (depending on the choice of the metal center). This area of supramolecular chemistry is known as metallosupramolecular chemistry – a reformulated version of highly-organized coordination chemistry.

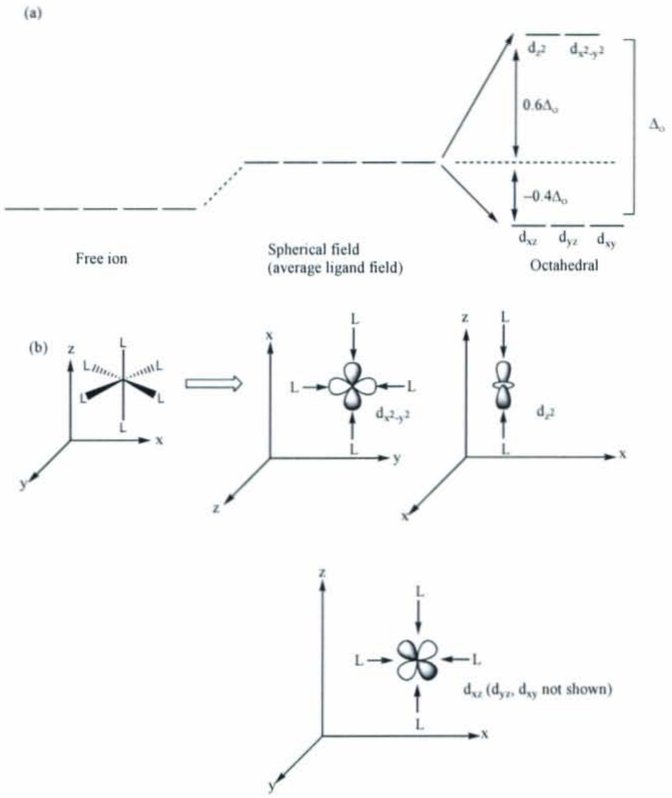

Figure 1.3.1. Crystal field splitting in an octahedral complex. (a) Energy level diagram; (b) orbital representation of splitting.

The first demonstration of a self-assembled metallosupramolecular construct was reported by Lehn *et al* in 1987[16] through the formation of a helical-like complex using a metal ion which specifically coordinates with a suitably instructed or designed ligand (in this case, Cu^I which preferentially forms a tetrahedral coordination geometry). In the presence of the metal ion (Cu^I), the formation of the double-stranded helicate is a

consequence of a specific coordination reading (i.e. tetrahedral reading) of the coordination pockets built within the ligand structure.

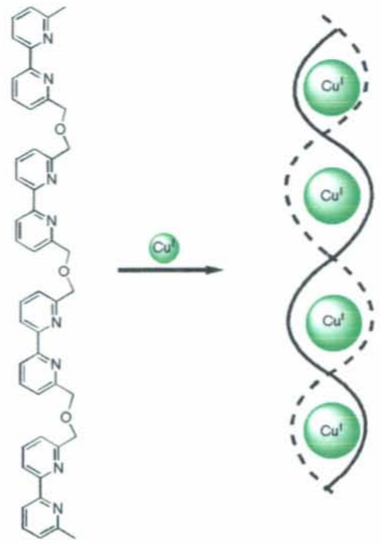

Figure 1.3.2. Self-assembly of a metallosupramolecular helicate.

Metallosupramolecular chemistry (or highly-organized coordination chemistry) may be regarded as a highly-active area of research in supramolecular chemistry in which organic ligands are integrated with metal centers towards the formation of multicomponent architectures with an expressed collective property associated with the combination of the metal ion and the organic ligand.[6, 13] A variety of metallosupramolecular structures have been synthesized which may be exploited in forming functional nanodevices. Such properties include spin crossover, magnetism, and redox activity.[6, 17-19] In this section, metallosupramolecular (or coordination) clusters, grid-type arrays, and extended grid-type arrays will be presented.

1.3.1. Coordination Clusters

Metalloclusters find widespread use in nature such as in iron-sulfur clusters which are involved in electron transfer processes, and the MnO_4 cluster within photosynthesis which ultimately assists in the oxidation of water. The mimicry of such polynuclear metal clusters is a major focal point in coordination chemistry with hopes that such clusters will lead to novel properties. Many previously synthesized clusters have, for example, displayed single molecular magnetic behaviour such as Mn_{12} acetate cluster which displays low temperature magnetic quantum tunnelling.[20, 21] The synthesis of such structures has primarily involved the mixing of both the metal and ligand in appropriate equivalents with the synthetic outcome remaining mainly unknown. Many metal cluster-based structures have been produced through varying the ligand structure and reaction conditions. Through this approach, there is no directing force to cluster synthesis and the synthesis of such clusters is limited by the coordination capacity of the ligand. In this context, coordination unsaturation within the metal (or ligand) forces the metal ion (or ligand) to bind to other ligands (or metal ions), hence providing a means to forming bridged metal structures that ultimately lead to cluster growth.

1.3.2. Metallosupramolecular grid-type arrays

Approaches to the synthesis of metalloclusters have primarily relied on the coordination capacity of the metal and ligand whereby the presence of coordination unsaturation between the metal and ligand ultimately leads to cluster growth. As such, there is a high level of unpredictability in the formation of cluster structures. In essence,

the size and geometry of the cluster within this approach depends on the coordination behaviour of the ligands and on the coordination preference of the metal center.

A more "directed" approach to the synthesis of polynuclear metal clusters has emerged through the synthesis of ligands with unique molecular characteristics. Through this approach, a high level of predictability can be incorporated into the cluster outcome. Such a strategy is based on the encoding of coordination information into the ligand, which when interpreted by the metal concerned, results in a system which builds itself through a self-assembly process.

Through such a ligand directed approach, highly-organized polymetallic entities have been synthesized through the design of ligand coordination pockets which match the allowed coordination geometries of the coordinating metal center. For such entities to form, these pockets must exhibit properties which are complementary to the binding metal, such as the appropriate arrangement and orientation of donor atoms within the pocket, which essentially give rise to a reduction in the metal-ligand bond strain and maximize metal-ligand orbital overlap. This approach has been adopted in creating polymetallic grid-type arrays as is illustrated in Figure 1.3.2.1. Thus, the primary focus of this strategy is associated with ligand design. Through variability of the ligands and the incorporation of substituents, the ultimate size of the complex and its fundamental properties may be tailored.[22]

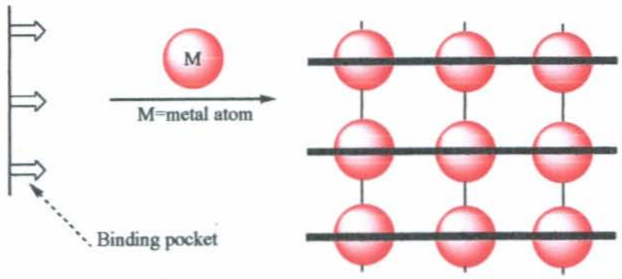

Figure 1.3.2.1. Assembly of a [3x3] grid-like array from a tritopic ligand.

Grid-type arrays ranging from [2x2] to [5x5] have been developed using this ligand-directed strategy which has involved ditopic, tritopic, tetratopic, and higher heterocyclic and hydrazone-based ligands. Furthermore, arrays containing mixed metal cores have also been constructed. Grid-type structures are based on the construction of a square-based core. As squares contain inherent right angles, components must also be at right angles to one another. Due to the nature of the 90° angular orientation of ligands in a tetrahedral and octahedral environment, these geometries are ideal for forming grid-type inorganic complexes. In such geometries, the ligand binding pocket would satisfy about half the coordination requirements of the metal ion leaving vacant binding sites at a 90° twist for other ligands to bind. This amounts to a capping of the metal center in directing the self-assembly of the grid-like architecture.

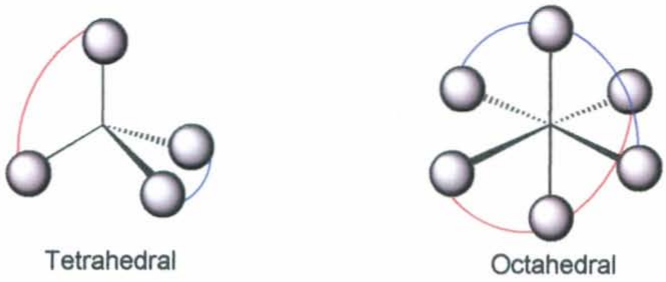

Figure 1.3.2.2. Tetrahedral and octahedral geometries illustrating the right angle orientation of ligand groupings.

In the following sections, select heterocyclic- and hydrazone-based ligands utilized in developing grid-type arrays will be highlighted. Furthermore, the factors which affect the formation of these grid-type and non-grid structures (oligomers) will also be discussed. It is interesting to note that all grid structures produced contain 5-membered chelate rings in the ligand binding pocket. This is a consequence of the structural features of the ligand which have been instructed to form such chelate rings on direct complexation with metal ions to give a linear array of metals in a *syn* conformation.[22]

1.3.2.1. [2x2] Heterocyclic ligand-based grid-like arrays

The first example of a [2x2] grid-like array was based on tetrahedral coordination of Cu^{I} and Ag^{I} and involved a bis(pyridyl)pyridazine type ligand.[23] The structure of the complex consisted of a distorted rhombic metal core with a metal-metal distance of ~3.6 Å.[6, 23]

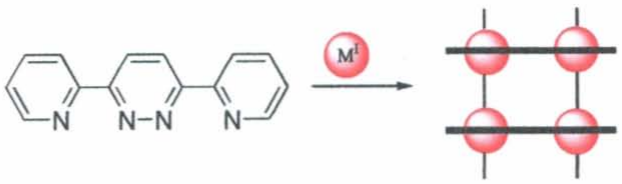

Figure 1.3.2.1.1. Pyridyl based [2x2] grid-like array. M refers to Cu^{I} and Ag^{I}.

Self-assembly of a bis-phenanthroline based ligand with Cu^{I} ions results in a grid-like array where an extra uncoordinated ligand has intercalated between the coordinated bis-phenanthroline ligands.[24] This structure is unusual in the sense that the principle of maximum ligand coordination has been violated (i.e. more ligands are associated with the complex than can be accommodated by the metal center through metal-ligand bonding). The intercalation of extra ligands is a consequence of C-H-N and π-π interactions, which has been supported by NMR and X-Ray structural data.[6, 24]

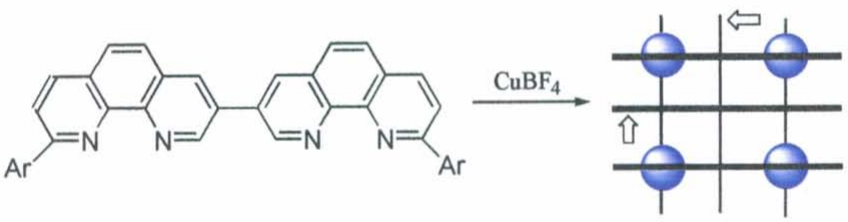

Figure 1.3.2.1.2. Intercalation of ligand within a [2x2] grid-like complex.

Grid arrays containing an octahedral reading of the coordination information stored in a heterocyclic ligand have been constructed and have utilized terpyridine-like coordination with a number of first row transition metals. Such arrays contain metal-

metal distances of ~6.5Å and exhibit a variety of optical and electrochemical properties which may be tuned via ligand substitution.[6, 25]

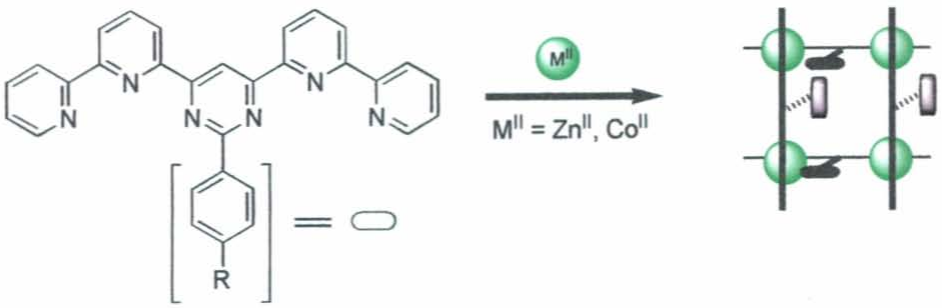

Figure 1.3.2.1.3. Formation of grid array containing an octahedrally coordinated metal center. The R groups represent substituents which serve to tune properties of the grid-like complex such as electrochemical and photophysical properties.

It is interesting to note that in this system, the NMR data indicate that the inner core of the grid gives rise to an inner pocket that is chemically inequivalent to the outer portion of the grid. This is given by the splitting of ortho and meta phenyl protons into inner and outer groups.[25] Furthermore, the rotation of an $-N(Me)_2$ group in the *para* position of the phenyl substituent is suggested by variable temperature NMR data.[25] Emission is observed when the metal center is inactive (Zn^{II}), however, an open metal center such as Co^{II} effectively quenches ligand emission and is believed to be a consequence of a non-emissive highly-distorted metal-centered state.[25]

Thus far, heterocyclic ligands have been used to synthesize grid-type arrays with identical metals constituting the core. However, the selection of metal ions at specific locations within the grid-type array have also been demonstrated and is of vast

importance in addressing metal ions in specific locations within metal arrays. A mixed metal grid has been obtained using heterocyclic based ligands via a sequential synthetic procedure where the mixed metal complex forms as a result of a difference in metal coordinative labilities and coordinative binding strengths.[26] Systems containing two Ru^{II} and two Fe^{II}, two Os^{II} and two Fe^{II}, and one Ru^{II}, one Os^{II} and two Fe^{II} ions in a [2x2] grid-type structure have been generated by this strategy.[26]

Figure 1.3.2.1.4. Sequential synthesis of a mixed [2x2] metal grid-like array.

The synthesis of a mixed metal grid-type complex with two types of metal centers may exist in either of two topoisomeric forms: an anti form where the identical metal ions are in a diagonal arrangement with respect to one another; and a syn form where the identical metal ions are located in parallel arrangement relative to one another. Although it is not possible to predict *a priori* which topoisomer will form on mixing all of the components, the anti isomer can be obtained selectively if a strongly coordinating metal is allowed to bind to a bidentate ligand to form a precursor complex which, when combined with a second lower coordinating metal center, preferentially yields the anti isomer.[26]

1.3.2.2. [3x3] and larger heterocyclic ligand-based grid-like arrays

The synthesis of [3x3] and higher grid-type arrays involves an increase in complexity in the design of the ligand structure. It is this structural information which when read by the metal ion that gives rise to higher-order grid structures. The first designed [3x3] grid-like complex involved an extension of the pyridazine N_2 pocket of the ligand in Figure 1.3.2.2.1. When mixed in the appropriate ratio with nine equivalents of Ag^I ions, nine tetrahedral Ag^I centers resulted with six ligands arranged in two parallel groups above and below the plane of the metal core.[27] The metal core forms a trapezoid structure in response to a slight mismatch between the ligand pocket dimensions and the coordination requirements of the Ag^I center.[7, 27]

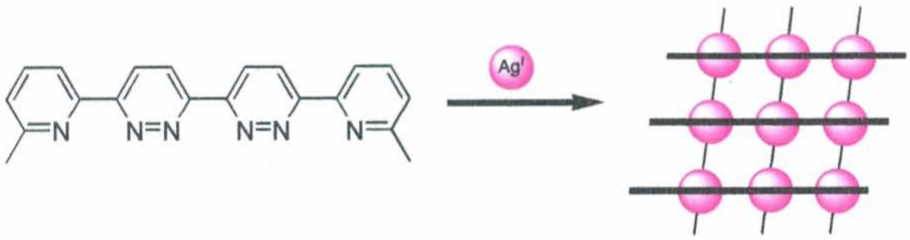

Figure 1.3.2.2.1. Synthesis of first [3x3] grid-like array.

The assembly of octahedrally coordinated metal ions in a [3x3] grid-like fashion using heterocyclic ligands, such as the bis-terpyridine based ligand in Figure 1.3.2.2.1, have been obtained for Pb^{II} and Hg^{II} ions but has proven to be problematic for transition metal ions with incomplete [2x3] grid-like structures as side products.[6, 28] The NMR data for the Zn^{II} [3x3] grid-like array using the bis-terpyridine based ligand previously described exhibits NMR peaks attributed to ligands in chemically inequivalent

environments where the inner ligand and outer ligands give separate proton peaks.[28] It should be noted that for this ligand, a large reorganization energy may result from the bending of the ligand as a consequence of the pinching effect on binding metal ions.[6, 29] However, this pinching is reduced with larger metal ions, such as Pb^{II} and Hg^{II}, so that the ligand is less distorted and the reorganization energy in forming the grid-like array is reduced.[6]

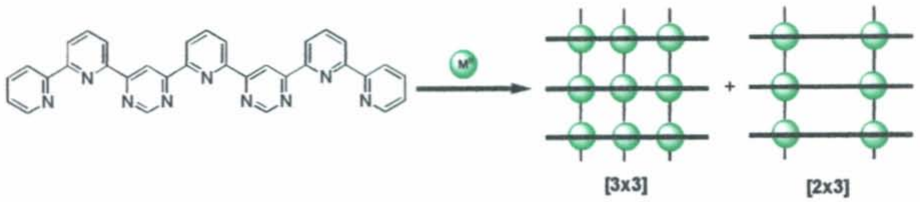

Figure 1.3.2.2.2. Formation of [3x3] grid array from bis-terpyridine based ligand. The [3x3] grid is formed when M is a transition metal whereas the [2x3] grid is a side product when M is a large metal ion such as Pb^{II} and Hg^{II}.

The formation of [4x4] grids using the above bis-terpyridine based ligand has also been observed with large metal centers like Pb^{II}; however, the same restrictions discussed for the [3x3] grid-like structures with transition metals (*vide supra*) still apply.

1.3.2.3. [2x2] hydrazone ligand-based grid-like arrays

Whereas heterocyclic bridging groups separate the coordinated metal over longer distances of ~6 Å and exhibit limited flexibility (i.e. the pinching effect for the bis-terpyridine ligand), hydrazone-based ligands exhibit greater flexibility and lead to shorter metal-metal distances. As a consequence, confinement effects such as magnetic exchange coupling[30] may be more prominent in hydrazone-based grid-like complexes.

Furthermore, the use of oxo-bridged ligands also allows for a more closely packed metal core.

The 1,3-diaminopropan-2-ol based ligand of Figure 1.3.2.3.1 has encoded in its structure two octahedral pockets which when interpreted by transition metals such as Cu^{II} and Mn^{II} results in a [2x2] grid-like array with μ-O bridged metal centers which are separated by ~3.7 Å and exhibit anitferromagnetic coupling.[31, 32] Although the ligand is rotationally flexible, the grid-type complex remains the dominant product and is the dominant coordination outcome.[7]

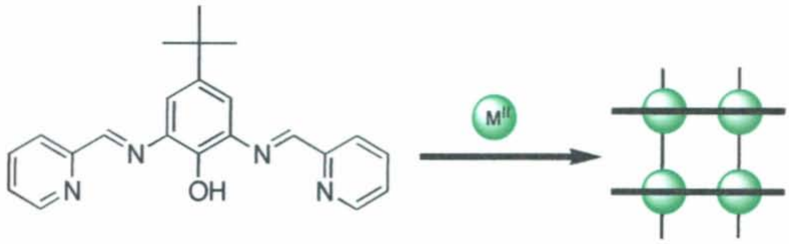

Figure 1.3.2.3.1. μ-O bridged [2x2] grid-like array.

The ditopic hydrazone ligand (POAP – see Figure 1.3.2.3.2) also self-assembles to form μ-O bridged [2x2] systems; however, tautomerization may lead to μ-NN bridged systems.[7, 33] Furthermore, this ligand contains both tridentate and bidentate pockets which may accommodate tetrahedral and octahedral coordination centers. This is best illustrated in Figure 1.3.2.3.3 where both ligand tautomers are present for the [2x2] $Co_2^{II}Co_2^{III}$ grid-type complex.

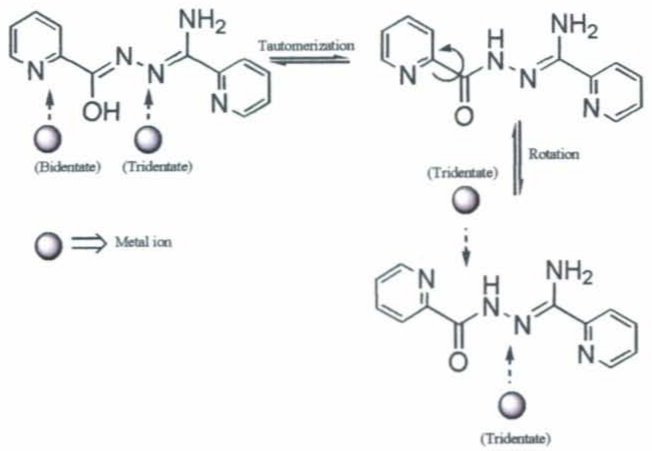

Figure 1.3.2.3.2. Coordination pockets resulting from tautomerization and rotation within the POAP ligand.

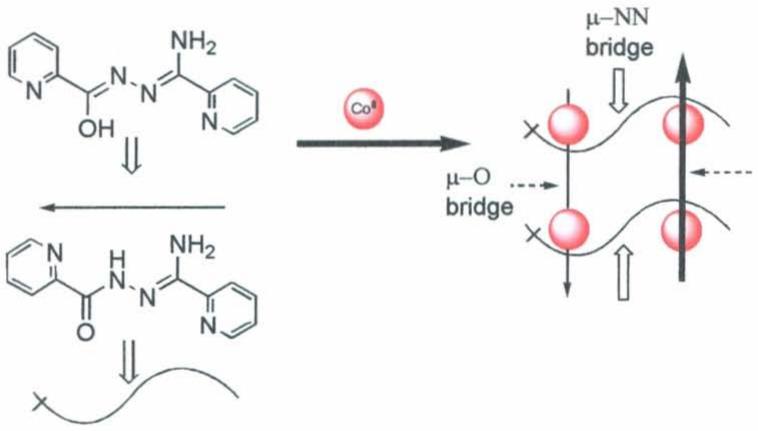

Figure 1.3.2.3.3. Formation of $[Co^{II}_2Co^{III}_2(POAP\text{-}H)_2(POAP\text{-}2H)_2(H_2O)_2]^{4+}$.

Many other [2x2] grid-type structures have been produced using this ligand with transition metals such as Mn^{II}, Cu^{II}, and Zn^{II} with the four ligands arranged in two parallel groups bridged by deprotonated oxygen atoms such as in Figure 1.3.2.3.4.[7] Co-ligands

are required to complete the coordination sphere for the metal ion occupying the bidentate pocket with an octahedral geometry.

Figure 1.3.2.3.4. [2x2] grid-like array resulting from Mn^{II} ions and the POAP ligand. Azide co-ligands are present to complete the coordination complex for the metal centers.

Mixed metal complexes have also been reported using this ligand where a precursor complex is treated with a second metal ion to form the mixed metal array, as is the case when an $[Fe^{III}(POAP\text{-}H)(NO_3)(H_2O)_2]^{2+}$ complex is treated with Ni^{II} ions.[22] This ferrimagnetic complex exhibited an S=3 ground state and an antiferromagnetically coupled core.[34]

Ligands with acidic protons have also been developed with properties which are dependent on the protonation state. The bis-hydrazone based ligand in Figure 1.3.2.3.5 readily form [2x2] grid-like arrays with Co^{II}, Mn^{II}, and Zn^{II} which contain pH dependent optical properties.[35] For example, the absorption profiles of these complexes have bands which appear and disappear as the pH is varied. Furthermore, emission from the Zn^{II} structure is also pH dependent and is thought to originate from a sandwich-like π-π interacting state as a consequence of the phenyl substituents intercalated between the two ligands.[6]

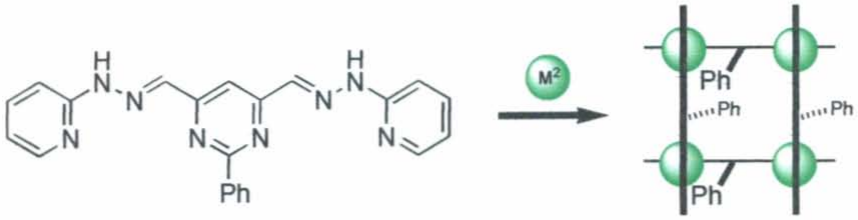

Figure 1.3.2.3.5. Assembly of [2x2] grid displaying pH dependent optical properties. –Y-N-Z- refers to –CH=N-NH-.

1.3.2.4. [3x3] and higher hydrazone ligand-based grid-like arrays

Tritopic hydrazone-based ligands contain three pockets which may coordinate with three metal ions to give a linear metal array. Typically, metal centers in grid-like arrays are present in octahedral and tetrahedral coordination environments (*vide supra*), thus, three other ligands may bind to the linearly arrayed metal centers in a 90° fashion. The most commonly observed structure is a [3x3] grid-like array which has been readily observed for many transition metal ions.

The extension of the POAP ligand (*vide supra*) to form ligands with tridentate pockets and two oxygen bridging atoms (such as 2POAP – see below) has successfully resulted in [3x3] grid-like arrays with Mn^{II}, Cu^{II}, and Zn^{II} as well as mixed metal [3x3] grid-type structures.[6, 7, 22] Metal-metal distances of ~4 Å have been observed whereas ligand-ligand distances are slightly shorter (~3.5 Å).

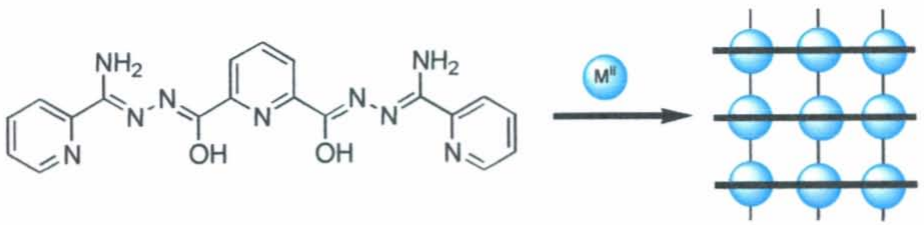

Figure 1.3.2.4.1. Formation of [3x3] grid array using 2POAP ligand. Note some of the main features.

The close proximity of the metal centers through μ-O bridges leads to anitferromagnetic coupling in most cases except for those grids involving Cu^{II} which exhibit ferromagnetic exchange between metal centers.

For the [3x3] grid-type architectures, the symmetric nature associated with the arrangement of metal ions and ligands creates coordination groupings at the corner, middle, and sides of the grid structure. As a result, the construction of heterometallic grid structures may be envisioned through metal substitution on a homometallic [3x3] grid-type complex. Such an approach appears plausible as the most labile sites in terms of metal substitution occur at the corners where only two μ-O atoms bridge metal centers, followed by three μ-O atoms for the side positions and four μ-O atoms for the center position. Furthermore, coordination preferences (i.e. crystal field stabilization energies) and ionic radii may also give rise to preferential occupancy within the [3x3] metal core. As an example, the mixing of a 2POAP derivative with both Mn^{II} and Zn^{II} ions yields a mixed metal grid-like complex where the Zn^{II} ions preferentially bind to the side pockets of the grid as a consequence of a larger charge/radius ratio exhibited by Zn (Figure 1.3.2.4.2).[7] One would then assume that based on this argument, a Zn^{II} ion should

constitute the middle of the grid core as more μ-O bridges result; however, the presence of Mn^{II} at the center is thought to be a result of kinetic factors associated with the substitution reaction.[7]

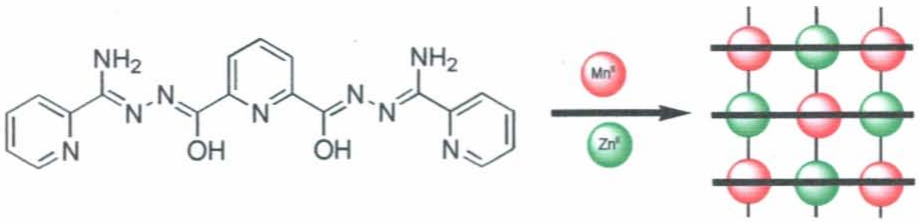

Figure 1.3.2.4.2. Formation of mixed metal grid-type complex as a result of differences in the charge/radius ratio.

Similarly, reaction of a complete Mn^{II}_9 [3x3] grid with Cu^{II} ions yields a mixed metal grid with Cu^{II} constituting the corner positions. Further vigorous conditions then resulted in substitution of all coordinated Mn^{II} ions for Cu^{II} except for the middle ion of the core.[7]

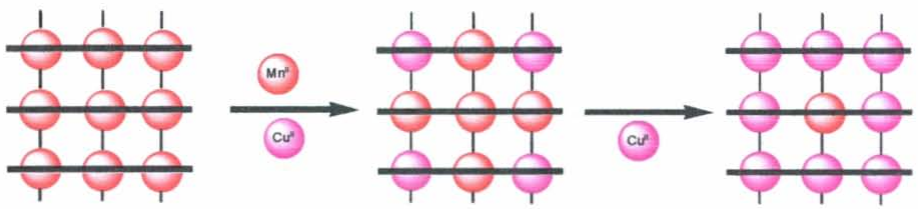

Figure 1.3.2.4.3. Formation of mixed metal grid via metal substitution.

Higher order hydrazone-based grid-like arrays have been developed through increasing the number of coordination pockets within the ligands, as illustrated for the ligands in the following figure.

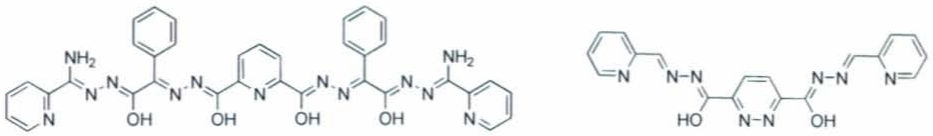

Figure 1.3.2.4.4. Formation of higher order grid-like arrays such as those [4x4] and [5x5] based. X=CH and R=H.

1.3.2.5. Factors which affect grid formation

Many factors must be considered in forming inorganic grid-like structures. These include not only ligand phenomena such as the nature of the donor atoms and their proximity in coordination pockets (for example, the ligand in Figure 1.3.2.2.2 also exhibits a pinching effect), but also the role of the metal ion, the effects of counterions or anions, reaction conditions, and the overall thermodynamics involved in creating such structures.[6, 7, 22, 36] Reorganization energies associated with ligand coordination pocket pre-organization may impart an energetic barrier to grid-type formation; however, formation of such structures may be thought to be driven primarily by the entropy change associated with the self-assembly process, apart from any stabilization imparted by the grid-like structure itself. For example, in the [3x3] grid-type case, 52 particles are liberated as shown below.[22]

$$6LH_2 + 9\,[M(II)(H_2O)_6]^{2+} \rightarrow [M(II)_9(L^{2-})_6]^{6+} + 12H^+ + 54H_2O \qquad \textit{eqn. 1.3.2.5.1.}$$

In considering the role of the metal ion in grid-like structures, one must take into account the crystal field stabilization energy (CFSE) of the associated metal ion. As

CFSE follows the order $Zn^{II} < Cu^{II} < Ni^{II}$, the coordination of such ions will depend on the gain in CFSE and on the conformational flexibility of the ligand to allow access to the stabilized metal geometry. Compared to the heterocyclic-based ligands used in grid formation, hydrazone-based ligands are seen as advantageous as they contain greater structural flexibility as well as selection in donor atoms for the coordinating metal ions (N vs. O). Thus, in hydrazone-based coordination pockets, metal ions are able to choose donor atoms and freely adopt their preferred coordination geometry on the basis of a balance of crystal stabilization effects. Hence, in addition to entropic factors and kinetic barriers, gains in crystal field stabilization energies also affect grid formation as illustrated for a Ni complex where nitrogen donor atoms maximize the CFSE for the Ni^{II} ion, leading to non-grid type structures.[7]

Counterions also have an effect on the synthetic outcome if they act as templates such as for formation of the Ni-based grid below where a larger counter ion results in the formation of a pentagon-like structure.[37, 38]

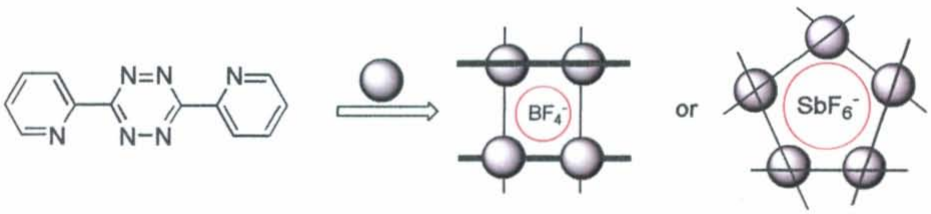

Figure 1.3.2.5.1. Counterion effect on grid-type formation.

1.3.3. Extended grid-type arrays

The extension of grid-like arrays to form 2D structural motifs may provide long range cooperativity between individual units, thus resulting in bulk behavioural

properties. Such bulk properties are of fundamental importance in the building of functional nanodevices. Strategies towards such motifs have primarily involved an extension of the strategies utilized in forming the individual grid-like structures such as the nature of the hydrogen bond and the π-π interaction. The approach may be considered as a "grid-of-grids" and provides a means for addressing individual metal arrays. [39]

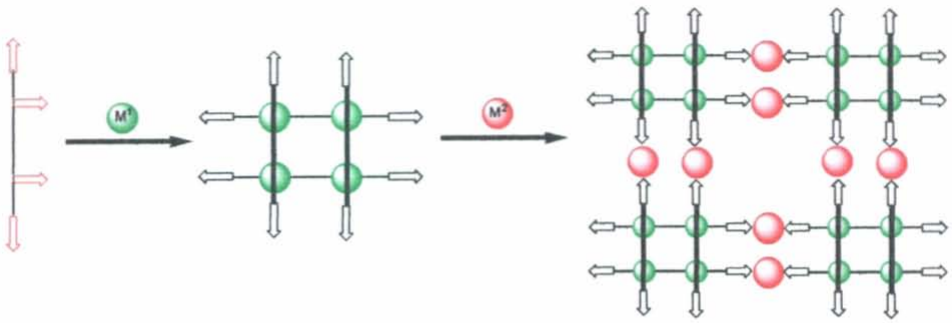

Figure 1.3.3.1. "grid-of-grids" approach to extended grid-like arrays.

The design of ligands bearing particular functional groups allowing for specific inter-grid interactions is the primary focus of this strategy. For example, grid complexes bearing hydrogen bond donating and accepting groups at specific locations along the ligand structure have provided a route towards hierarchical extended arrays.

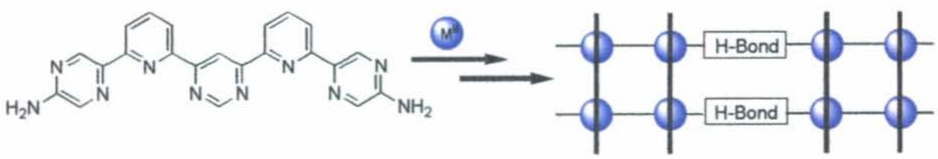

Figure 1.3.3.2. Strategy towards hydrogen bonded grid-of-grids network.

Other examples include the extension of π interactions between grids with enhanced aromatic character. This enhancement is a consequence of designing ligands with extended aromatic end groups. This gave face-to-face and edge-to-face π interactions between grids which resulted in grids in close contact to one another (~3.5 Å).[22]

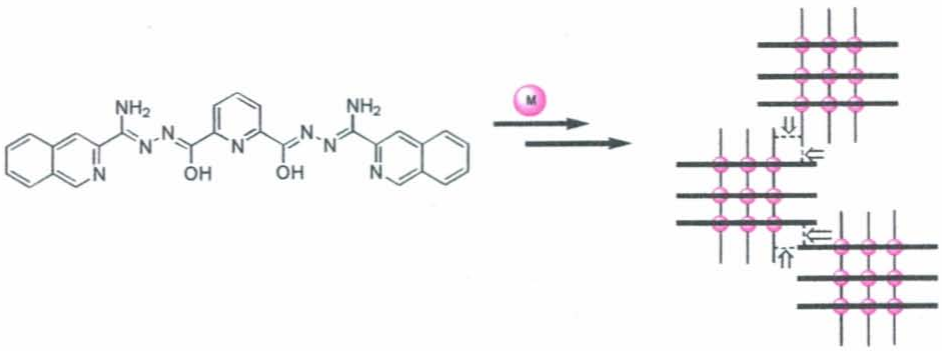

Figure 1.3.3.3. Extended grid-like arrays originating from inter-grid π interactions.

1.4. Electrochemical, magnetic, spin and optical properties of the [nxn] core

The challenge facing the future of modern technology is associated with the building of devices which overcome the limits of the top-down approach. As such, we turn to nanotechnology and molecular manufacturing whereby advanced materials are synthesized with specific properties and functions at the molecular level to serve as components in a molecular device. These properties are determined by the overall form and shape of the material, and the precise location and distribution of atoms in the material. Furthermore, the overall properties and function of the molecular device will be

determined by these same attributes as they relate to the distribution, form, shape, location, and specific properties of the individual components within the device.

Compact grid-type multicenter metal complexes are seen as attractive candidates for device components on the molecular scale. This class of supermolecules have access to a variety of multi-stable states and have been shown to be addressable in terms of arrangements into 2D extended arrays. Grid-like arrays have exhibited accessible and reversible oxidation and spin states, and may possess intervalence charge transfer character. Such properties may find application as components in molecular electronics and information devices.

1.4.1. Electrochemical properties

Thus far, two grid-type systems have exhibited rich electrochemical behaviour: one involving a Co^{II}_4 grid which has been shown to reversibly store (i.e. is reduced) up to twelve electrons[40]; and the other a Mn^{II}_9 grid which has been shown to reversibly release (i.e. is oxidized) up to eight electrons. For the Co^{II}_4 complex, the metal center was found to be inactive in the reduction processes.[40] However, the metal atoms were active in the Mn^{II}_9 complex giving rise to multi-stable metal oxidation states.[41]

1.4.2. Magnetic Properties

Magnetic interactions have at their origins an electrical component whereby the movement of electrical charge gives rise to a magnetic field.[42] As such, atoms and molecules exhibit magnetic phenomena depending on the availability of an electrically charged unit. In the case of a diamagnetic molecule, all electrons are spin-paired with no

unpaired electrons (or free electrically charged units) available to allow for a magnetic interaction. In the case of a paramagnetic molecule, however, unpaired electrons are available to allow for a magnetic interaction under the condition that the spin-spin interaction is more pronounced than the random reorientation of spins as a consequence of the Boltzmann distribution of states. As such, paramagnetic molecules exhibit magnetic behaviour at critical temperatures owing to the enthalpically favoured alignment of spins over the entropically favoured random orientation of spins. Given the relationship between free energy, enthalpy and entropy, entropy dominates at high temperature providing spin disorder whereas enthalpy dominates at low temperature providing spin order.

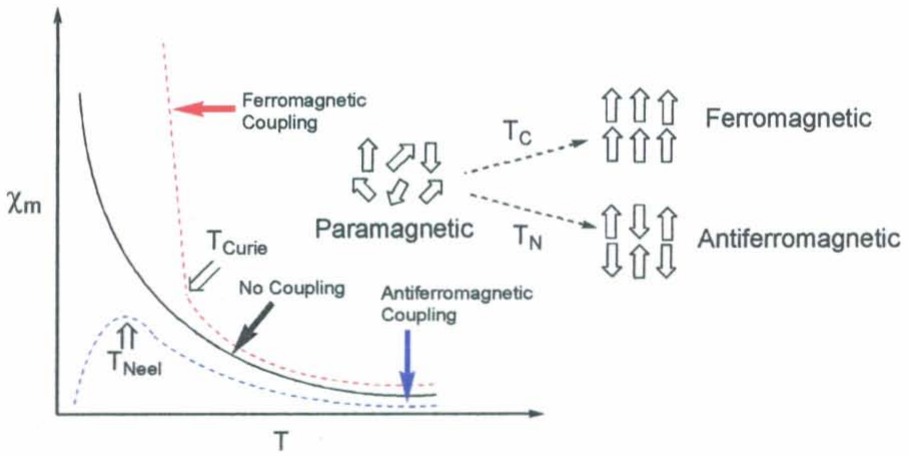

Figure 1.4.2.1. Critical temperatures associated with antiferromagnetic (Neel temperature) and ferromagnetic coupling (Curie temperature).

Unpaired electrons within a paramagnetic center which interact with unpaired electrons contained in a different paramagnetic center in an anti-parallel manner whereby the net spins associated with this interaction cancel to give no net magnetic moment results in antiferromagnetic exchange whereby the unpaired electrons exhibit antiferromagnetic coupling. Likewise, unpaired electrons within a paramagnetic center which interact with other unpaired electrons contained in another paramagnetic center in a parallel fashion to give a net magnetic moment results in ferromagnetic exchange whereby the unpaired electrons exhibit ferromagnetic coupling. For the grid-type complexes presented in this chapter, most complexes demonstrate antiferromagnetic coupling of metal ions within the compact metal core. Many Cu grid-type complexes also exhibit ferromagnetic coupling. Magnetic exchange effects associated with grid-type complexes have already been presented in the previous sections.

1.4.3. Spin state properties

Spin transitions between low spin and high spin states is an attractive process which may be utilized in molecular switching phenomena. Such transitions have been observed in Fe^{II}_4 grid-like systems where the metal spin states could be switched from diamagnetic to paramagnetic via thermal and optical triggers.[19] Ligand effects were also observed where substituents which attenuated the ligand field provided spin transition states.

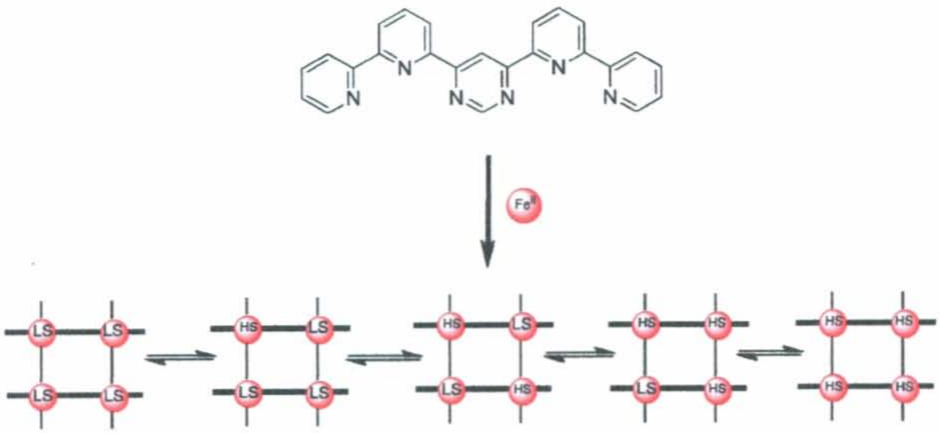

Figure 1.4.3.1. Spin transition in a Fe^{II}_4 grid-type complex where temperature and light may be used to induce the transition.[6, 19]

1.4.4. Optical state properties

Electronic communication in the form of intervalence metal-metal charge-transfer between Mn^{II} and Mn^{III} centers within the grid-like core of a mixed-valent $Mn^{III}_4Mn^{II}_5$ grid-type complex has previously been explored.[41] Analysis of such a transition provides an estimate of the inter-metal electronic coupling element (H_{ab}) and the free energy barrier to electron transfer which were ~1240 cm^{-1} and ~3410 cm^{-1}, respectively.[41] Moreover, the optical states of this mixed-valent grid-type complex also demonstrate π-π^* transitions originating from the coordinated ligands, and a ligand-to-metal charge-transfer presumably from the μ-O to the Mn^{III} center.[41]

1.5. Conclusions

Strategies towards the preparation and development of nanomaterials with unique properties have led to rapid growth in molecular manufacturing and nanotechnology. These strategies are primarily based on a concept where entities are driven together via pre-programming of individual components of the material. This concept is known as self-assembly and has led to a revolution in the approach to the formation of a variety of inorganic nanosystems such as helicates, molecular squares, and extended polygons.

The use of transition metals in forming well-defined ordered structures is advantageous due to the relative strength of the metal-ligand bond (relative to a hydrogen bond), the existence of a variety of multi-stable states such as oxidation and spin states, the directionality within the coordination sphere, and the existence of geometrical states which depend on d orbital electron occupancy.

The capacity of self-assembly to make well-defined nanostructures has been demonstrated through the construction of grid-like metal ion architectures. These metal architectures are viewed as attractive candidates as device components as a consequence of the confinement of a variety of transition metals into a grid-like arrangement. Such structures have been shown to exhibit multi-stable states which are accessible via electrochemical, thermal, and optical means. The synthesis is based on a principle of ligand design which makes use of metal ion coordination preferences within a ligand coordination pocket. Furthermore, these structures have been shown to form extended grid-like arrays. Overall, the existence of chemically active functional groups on the ligands of these structures coupled with an understanding of the properties portrayed by

the ligands in these structures may lead to the utilization of grid-type complexes as components in new technologies and devices.

1.6. Scope of this thesis and origin of the grid samples

For all studies presented in this thesis, the grid samples used have been kindly donated by Professor Laurence K. Thompson (Memorial University). The synthesis of these complexes has been summarized in the previous sections of this chapter. The purity of these samples was assumed to be high as indicated by UV-Vis-NIR absorption and fluorescence data in conjunction with 1D and 2D NMR data.

Overall, the objective of this thesis is twofold. The first objective is to build on the optical spectroscopy of [3x3] grid-type complexes. The second objective is associated with the organized ligand framework. As the properties associated with the organized metal core in [3x3] grid-type complexes have been discussed in terms of magnetic, electrochemical, and optical studies what are the properties of the ligands in theses complexes? i.e. *What properties are projected through the organized ligand framework?* The second objective of this thesis is to classify the optical states of the ligands in [3x3] grid-type complexes which are imparted by ligand organization.

For Chapter 2, an overview of the photophysical theory and the experimental photophysical techniques relevant to this thesis are presented. In this chapter, the physical representation of an "excited state" is illustrated in terms of a higher-lying potential energy surface and the experimental techniques associated with observing transitions between potential energy surfaces are discussed.

In Chapter 3, the photophysical properties of 2POAP, the ligand incorporated into the [3x3] grid-type complexes studied, are described in terms of UV-Vis absorption, fluorescence spectroscopy, and computational studies using TD-DFT methods. Moreover, the effects of coordinating Zn^{II} ions to this ligand (*en route* to the grid-type complex) are presented through computational and experimental means.

To understand excited state charge transfer, an understanding of electron transfer theory is needed. This theory is described in Chapter 4 for a two-state system which includes the formalisms proposed by Mulliken, Marcus, Hush, and Taube. Electronic coupling will be discussed as it relates to the classification of electron transfer systems which will be used to describe the excited states of the [3x3] grid-type complexes described in Chapters 5 and 6.

For Chapter 5, the optical states of a [3x3] $Zn(II)_9$ grid complex are formulated through pH, solvent, and temperature-dependent studies and used to elucidate the optical states of [3x3] $Mn(II)_9$ and $Mn(III)_4Mn(II)_5$ grid complexes in Chapter 6. The fact that the Zn(II) analogue effectively describes the optical states of the organized ligand framework allows for extrapolation of the metal core properties.

Excitation energy transfer theory is described in Chapter 7 and used in Chapter 8 to describe experiments directed towards demonstrating methodologies for assembling grid-type complexes with appropriately derivatised components. In Chapter 8, titration of a grid-type complex with anthracene-9-carboxylic acid suggests the formation of a supramolecular adduct. This interaction will demonstrate that excitation energy transfer is playing a significant role in the excited state relaxation within these assemblies.

In chapter 9, general conclusions are made with respect to the scope of the research described in the previous chapters of this thesis.

References

[1] V. Balzani, A. Credi, B. Ferrer, S. Silvi, and M. Venturi, *Top. Curr. Chem.* **2005**, *262*, 1.

[2] R. Feynman, in *Engineering ans Science, Vol. XXIII*, **1960**.

[3] J.-M. Lehn, *Nobel Prize Lecture* **1987**.

[4] M. Jimenez-Molero, C. Dietrich-Buchecker and J. Sauvage, *Angew. Chem. Int. Ed.* **2000**, *39*, 3284.

[5] J. Badjic, V. Balzani, A. Credi, S. Silva and J. Stoddart, *Science* **2004**, *303*, 1845.

[6] M. Ruben, J. Rojo, F. Romero-Salguero, L. Uppadine and J.-M. Lehn, *Angew. Chem. Int. Ed.* **2004**, *43*, 3644.

[7] L. Dawe, K. Shuvaev and L. K. Thompson, *Chem. Soc. Rev.* **2009**, *38*, 2334.

[8] J.-M. Lehn, *Proceedings of the National Academy of Sciences of the United States of America* **2002**, *99*, 4763.

[9] J.-M. Lehn, *Science* **2002**, *295*, 2400.

[10] J. W. Steed and J. L. Atwood, *Supramolecular Chemistry*, Wiley, **2000**.

[11] D. J. Cram, *Science* **1988**, *240*, 760.

[12] D. Voet, J. G. Voet and C. W. Pratt, *Fundamentals of Biochemistry*, Rev. ed., Wiley, **2002**.

[13] J.-M. Lehn, *Supramolecular Chemistry: Concepts and Perspectives*, VCH, New York, **1995**.

[14] C. A. Hunter and J. K. Saunders, *J. Am. Chem. Soc.* **1990**, *112*, 5525.

[15] G. Miessler and D. Tarr, *Inorganic Chemistry*, 3 ed., Pearson Prentice Hall, New Jersey, **2004**.

[16] J.-M. Lehn, A. Rigault, J. Siegel, J. Harrowfield, B. Chevrier and D. Moras, *Proc. Natl. Acad. Sci.* **1987**, *84*, 2565.

[17] L. Zhao, C. Matthews, L. K. Thompson and S. L. Heath, *Royal Society of Chemistry, Chem. Commun.* **2000**, 265.

[18] L. K. Thompson, L. Zhao, Z. Xu, D. O. Miller and W. M. Reiff, *Inorganic Chemistry* **2002**, *42*, 128.

[19] M. Ruben, E. Breuning, J.-M. Lehn, V. Ksenofontov, F. Renz, P. Gütlich and G. B. M. Vaughan, *Chemistry - A European Journal* **2003**, *9*, 4422.

[20] T. Lis, *Acta. Cryst. B* **1980**, *36*, 2042.

[21] R. Sessoli, D. Gatteschi, A. Caneschi and M. Novak, *Nature* **1993**, *365*, 141.

[22] L. N. Dawe, T. S. M. Abedin and L. K. Thompson, *Dalton Transactions* **2008**, 1661.

[23] M.-T. Youinou, N. Rahmouni, J. Fischer and J. A. Osborn, *Angewandte Chemie International Edition in English* **1992**, *31*, 733.

[24] S. Toyota, C. R. Woods, M. Benaglia, R. Haldimann, K. Wärnmark, K. Hardcastle and J. S. Siegel, *Angewandte Chemie International Edition* **2001**, *40*, 751.

[25] J. Rojo, F. J. Romero-Salguero, J.-M. Lehn, G. Baum and D. Fenske, *European Journal of Inorganic Chemistry* **1999**, *1999*, 1421.

[26] D. M. Bassani, J.-M. Lehn, K. Fromm and D. Fenske, *Angewandte Chemie International Edition* **1998**, *37*, 2364.

[27] P. N. W. Baxter, J.-M. Lehn, J. Fischer and M.-T. Youinou, *Angewandte Chemie International Edition in English* **1994**, *33*, 2284.

[28] E. Breuning, G. S. Hanan, F. J. Romero-Salguero, A. M. Garcia, P. N. W. Baxter, J.-M. Lehn, E. Wegelius, K. Rissanen, H. Nierengarten and A. v. Dorsselaer, *Chemistry - A European Journal* **2002**, *8*, 3458.

[29] G. S. Hanan, C. R. Arana, J.-M. Lehn, G. Baum and D. Fenske, *Chemistry - A European Journal* **1996**, *2*, 1292.

[30] O. Kahn, *Molecular Magnetism*, VCH, New York, **1993**.

[31] J. Rojo, J.-M. Lehn, G. Baum, D. Fenske, O. Waldmann and P. Müller, *European Journal of Inorganic Chemistry* **1999**, *1999*, 517.

[32] A. Gelasco, A. Askenas and V. L. Pecoraro, *Inorganic Chemistry* **1996**, *35*, 1419.

[33] L. N. Dawe and L. K. Thompson, *Dalton Transactions* **2008**, 3610.

[34] S. R. Parsons, L. K. Thompson, S. K. Dey, C. Wilson and J. A. K. Howard, *Inorganic Chemistry* **2006**, *45*, 8832.

[35] M. Ruben, J.-M. Lehn and G. Vaughan, *Chemical Communications* 2003, 1338.

[36] K. V. Shuvaev, T. S. M. Abedin, C. A. McClary, L. N. Dawe, J. L. Collins and L. K. Thompson, *Dalton Transactions* **2009**, 2926.

[37] C. S. Campos-Fernández, R. Clérac and K. R. Dunbar, *Angewandte Chemie International Edition* **1999**, *38*, 3477.

[38] C. S. Campos-Fernandez, R. Clerac, J. M. Koomen, D. H. Russell and K. R. Dunbar, *Journal of the American Chemical Society* **2001**, *123*, 773.

[39] E. Breuning, U. Ziener, J.-M. Lehn, E. Wegelius and K. Rissanen, *European Journal of Inorganic Chemistry* **2001**, *2001*, 1515.

[40] M. Ruben, E. Breuning, J.-P. Gisselbrecht and J.-M. Lehn, *Angewandte Chemie* **2000**, *39*, 4139.

[41] V. A. Milway, S. M. T. Abedin, V. Niel, T. L. Kelly, L. N. Dawe, S. K. Dey, D. W. Thompson, D. O. Miller, M. S. Alam, P. Muller and L. K. Thompson, *Dalton Transactions* **2006**, 2835.

[42] P. Fishbane, S. Gasiorowicz and S. Thornton, *Physics for scientists and engineers, Vol. II*, Prentice Hall, New Jersey, **2005**.

Chapter 2:

"PHOTOPHYSICS AND EXPERIMENTAL PHOTOPHYSICAL TECHNIQUES"

Abstract: When one describes the excited state properties of grid-type complexes, one must have a grasp of the theory for describing and representing an excited state, and knowledge of the experimental techniques associated with measuring their unique characteristics. As such, the intent of this chapter is to provide an overview of the theory for describing and accessing an excited state, and a summary of the experimental photophysical techniques used in this thesis for classifying the excited state characteristics of the square [3x3] polytopic grid-type complex. Initially, the theoretical model describing the interaction of light and matter are presented followed by a quantum mechanical description of an excited state. The experimental photophysical techniques associated with absorption, emission, fluorescence lifetime, temperature dependent fluorescence, and transient spectroscopy are then discussed. In addition, an emission spectral fitting procedure will be presented for extracting a variety of quantum mechanical constants for excited states.

2.1. Interaction of Light and Matter

Light is considered to exhibit both wave- and particle-like characteristics in that it consists of an oscillating electric field which contains photons. Ultimately, these particles (i.e. the photons) allow for exchange of energy between the oscillating electric field of light and the oscillating electric field of a molecule. This exchange of energy may be modelled as an interaction involving the oscillating electric field of light and the oscillating electrons that are confined by the nuclear framework in matter.[1] In essence, the interaction of light and matter may be considered as the interaction of two oscillating dipole systems, one contained in light and the other resulting from electron motion in a chemical system.

When coupled to one another, the oscillating electric fields in light and matter may be viewed to behave as coupled donor-acceptor potential energy systems which participate in a common resonance at a uniquely specified frequency (ν).[1] If the electrons contained in a molecule possess an oscillating frequency which corresponds to a photon's oscillating frequency, then a *resonance effect* can occur between the electrons of a molecule and the photons of light whereby a significant dipole-dipole interaction allows for an exchange of energy between the two particles.[1] Given that light is considered to be an oscillating electric field, and that oscillating electric fields lead to magnetic fields, light therefore contains both an electrical and magnetic component, and is hence considered as an electromagnetic field (Figure 2.1.1). However, in considering the force exerted on an electron (**F**) through both the electrical (**E**) and magnetic (**H**) components of electromagnetic radiation (equation 2.1.1), the magnetic force is commonly neglected as it is dependent on the speed of an orbiting electron relative to the speed of light (i.e. $\nu_{max} \sim 10^{15}$ nm/s and $c \sim 3 \times 10^{17}$ nm/s).[1] As such, the electric force exerted by a light wave on an oscillating electron is much greater than the operating magnetic force.

$$\boldsymbol{F} = e\boldsymbol{E} + \frac{e\nu\boldsymbol{H}}{c} \approx e\boldsymbol{E} \qquad \textit{eqn. 2.1.1.}$$

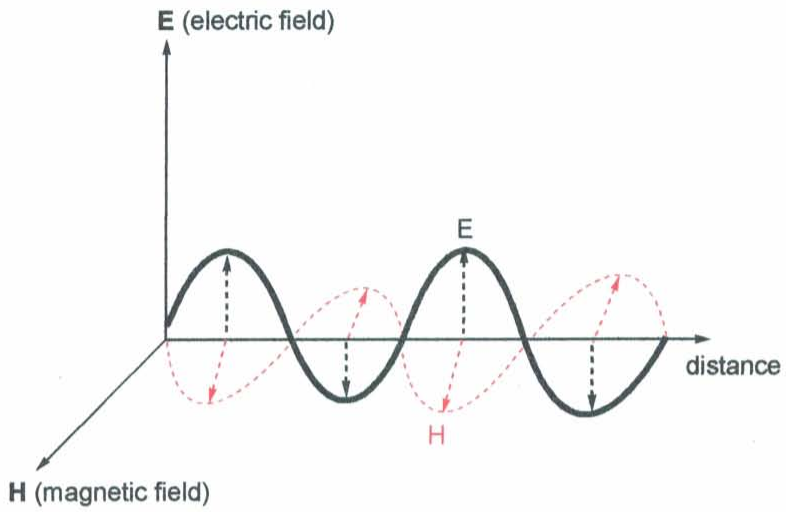

Figure 2.1.1. An electromagnetic wave consisting of an electric field (**E**) in the plane of the page and a magnetic field (**H**) perpendicular to the plane of the page.

For the resonance effect presented above, the effect becomes efficient when there exists a frequency (ν) common to both the photon ($E = h\nu$) of the electromagnetic field and the electronic transition for the molecule ($\Delta E = h\nu$).[1] When this condition is met, transfer of energy from the electromagnetic field to the molecule may occur (*absorption* of a photon by the molecule) thereby resulting in a reduction of the energy of the field and the oscillating electric field component. Likewise, when this condition is met, transfer of energy from the molecule to the electromagnetic field may occur (*emission* of a photon by the molecule), resulting in an increase in the energy of the field and the oscillating electric field component. Thus, the absorption of energy from an electromagnetic field corresponds to the removal of a photon from the field by the molecule to form an excited electronic state. Likewise, emission of energy from a molecule corresponds to the

addition of a photon to the electromagnetic field to reform the ground state (or resting state) of the molecular system. It is in the ground state that electrons are considered to be at rest, oscillating at some resting frequency. However, when in an excited electronic state, electrons contained in a molecule are considered to be in a heightened oscillating state along the molecular framework.

In order to further analyze the resonance condition required for transitions between ground and excited states (i.e. for absorption or emission of a photon) in equation 2.1.2(b), an understanding of the following are essential: the Born-Oppenheimer approximation, the Franck-Condon principle, and the quantum mechanical representation for forming such states.

$$\Delta E_i = h\nu_i \qquad \textit{eqn. 2.1.2(a)}$$

$$\nu_i = \frac{(E_{ES} - E_{GS})}{h} \qquad \textit{eqn. 2.1.2(b)}$$

2.1.1. Molecular Wavefunctions and the Born-Oppenheimer Approximation

Quantum mechanics provides the basis for understanding structure, energetics, and dynamics of a system by computing expected properties through operations on a wavefunction.[2] According to the principles of quantum mechanics, this wavefunction (Ψ) contains all of the information required to define a physical system, and desired information may be extracted through an appropriate operation on that function.[2] Thus, if this function is precisely defined, then one may compute any observable property of interest provided that the form of the mathematical operator (i.e. the forces acting on the system) is exactly known. In essence, quantum mechanics involves solving the

Schrödinger equation (equation 2.1.1.1) for a property of interest whereby Ψ contains both the electronic coordinates (r) and nuclear coordinates (R), and H contains the operators (or forces) acting on the wavefunction (system).

$H\Psi(\mathrm{r},\mathrm{R}) = E\Psi(\mathrm{r},\mathrm{R})$ [time-independent formalism] *eqn. 2.1.1.1(a)*

$i\hbar\frac{\partial}{\partial t}\mathrm{H}\Psi(\mathrm{r},\mathrm{R},\mathrm{t}) = \mathrm{E}\Psi(\mathrm{r},\mathrm{R},\mathrm{t})$ [time-dependent formalism] *eqn. 2.1.1.1(b)*

According to the principles of quantum mechanics, the only possible values of a measurement for a molecular system (i.e. a single molecule) must be eigenvalues of the eigenfunction Ψ.[2] However in reality, there exist many molecules for which a single measurement is obtained. As such, a large number of experiments are actually conducted in a laboratory measurement, and this value therefore represents an average value of each of the molecules present. This average property value (P_{ave}) is given by equation 2.1.1.2.

$$P_{ave} = \int \Psi H \Psi = < \Psi | H | \Psi > \qquad \textit{eqn. 2.1.1.2.}$$

In solving the Schrödinger equation, many approximations are made to simplify the integral in eqn. 2.1.1.2. One very important approximation is that of the Born-Oppenheimer approximation (equation 2.1.1.3). In this approximation, it is assumed that both electronic [ψ(r)] and nuclear motions [χ(R)] are uncoupled from one another (equation 2.1.1.3). This approximation is justified since the motion of electrons in orbits about the nucleus are generally much more rapid than nuclear vibrational motions. This approximate solution can further be simplified using the orbital approximation (equation

2.1.1.3) which separates each electron of the system in terms of its orbital [$\psi_o(r)$] and spin [S(r)] components.

$$\Psi(r,R) \sim \psi(r)\chi(R) = [\psi_o(r)S(r)]\chi(R) \qquad \textit{eqn. 2.1.1.3.}$$

Substitution of this simplified version of the wavefunction into equation 2.1.1.2 provides the basis for the following transition requirements in which electronic transitions must be: (i) orbitally allowed ($<\psi_o(r)|H|\psi_o(r)>$), (ii) spin allowed ($<S(r)|H|S(r)>$), and (iii) vibrationally allowed ($\chi(R)|H|\chi(R)>$). It is the vibrational component $<\chi(R)|H|\chi(R)>$ which provides the basis for the Franck-Condon principle.

$$\begin{aligned} P_{ave} &= <\Psi|H|\Psi> \\ &= <\psi_o(r)S(r)\chi(R)|H|\psi_o(r)S(r)\chi(R)> \\ &= <\psi_o(r)|H|\psi_o(r)><S(r)|H|S(r)><\chi(R)|H|\chi(R)> \end{aligned} \qquad \textit{eqn. 2.1.1.4.}$$

2.1.2. The Franck-Condon Principle and Franck-Condon Factors

According to the Fermi Golden Rule (equation 2.1.2.1), for a transition from an initial state Ψ_1 to a final state Ψ_2 , the rate constant (k_{12}) for this transition may be calculated from the square of the average property value of equation 2.1.1.4, if the wavefunctions for both states are known and the operator (H_{12}) corresponding to the transition is defined.[1] For the case corresponding to the interaction of electrons in molecules with that of a photon, the operator $H_{h\upsilon}$ effectively distorts the wavefunction Ψ_1 such that the wavefunctions Ψ_1 and Ψ_2 successfully mix. The transition from Ψ_1 to Ψ_2 is

then considered to be dependent on the density of states or channels capable of mixing Ψ_1 with Ψ_2 (ρ) during the time scale of the interaction and the degree of overlap between these states (equation 2.1.2.1).

$$k_{12} = \rho < \Psi_1 | H_{hv} | \Psi_2 >^2 \qquad \textit{eqn. 2.1.2.1.}$$

The Fermi Golden Rule provides the basis for transitions between states that are triggered by interactions that are weak relative to the energy separating the states (i.e. weakly interacting states).[1] The incorporation of the matrix element ($<\Psi_1|H_{hv}|\Psi_2>$) into the expression for the rate constant allows for the formulation of selection rules for transitions between weakly interacting states whereby if this matrix element is zero, then the transition probability is zero and the transition is forbidden. Such rules are provided in equation 2.1.2.2 where f_e, f_v, and f_s are the prohibition factors due to changes in electronic, nuclear, and spin configurations. The rate constant incorporating these factors are equated relative to the maximum possible rate constant (k^0_{max}) for the transition.

$$\begin{aligned} k_{12} = \rho < \Psi_1 | H_{hv} | \Psi_2 >^2 &= \rho [E_{12} < \Psi_1 | \Psi_2 >]^2 \\ &= [\rho E_{12}^2] < \psi_1 | \psi_2 >^2 < \chi_1 | \chi_2 >^2 < S_1 | S_2 >^2 \\ &= k^0_{max} [f_e \; x \; f_v \; x \; f_S] \qquad \textit{eqn. 2.1.2.2.} \end{aligned}$$

For a transition involving the same spin, equation 2.1.2.2 states that the rate constant for a transition between Ψ_1 and Ψ_2 is limited by the time it takes for the

electronic wavefunctions (Ψ_1 and Ψ_2) to mix or the time it takes for the nuclear wavefunctions (χ_1 and χ_2) to mix. In the cases where the electronic and nuclear wavefunctions or the electronic and spin wavefunctions are coupled, the rate constant for transitions involving these coupled systems is also limited by the time it takes for the coupled wavefunctions for Ψ_1 and Ψ_2 to mix. An expression similar to equation 2.1.2.2 may be formulated for such systems whereby the prohibition factors corresponding to a vibronic (f_{ev}) and spin-orbit factor (f_{es}) replace their corresponding electronic, nuclear, and spin components in equation 2.1.2.2.

The most important facet of equation 2.1.2.2 is that not only must the orbital and spin configurations of a transition overlap, but the vibrational wavefunctions associated with the initial and final state must also overlap (i.e. $< \chi_1 | \chi_2 > \neq 0$). This provides the basis for the *Franck-Condon principle* and the *Franck-Condon Factor*; this is a measure of the overlap of the vibrational wavefunctions of the initial and final states (equation 2.1.2.3).[1]

$$f_v = < \chi_1 | \chi_2 >^2 \qquad \textit{eqn. 2.1.2.3.}$$

The rates of transitions between electronic states can either be limited by the rate at which the nuclear geometry adjusts to the electronic configuration of the final state or by the rate at which the electronic structure can adjust to the nuclear structure of the final state.[1] Through the Born-Oppenheimer approximation (i.e. that electronic and nuclear motions are decoupled), and noting that electronic motion is much more faster than nuclear motion (i.e. fs time scale for electronic motion versus ps time scale for nuclear motions), the transition rate between electronic states is considered to be limited by the

propensity of the system to adjust to the nuclear geometry of the final state following the electronic redistribution associated with the transition from Ψ_1 to Ψ_2. In essence, the Franck-Condon principle states that the most probable electronic transition between states occurs when the vibrational wavefunction of the initial state resembles the vibrational wavefunction of the final state (i.e. when f_v = 1). This means that at the instant of a transition between Ψ_1 and Ψ_2, the nuclear geometry remains frozen while the electronic structure of the initial state is redistributed to form the electronic configuration of the final state.[1] After this redistribution processes has ended, the nuclei experience the force projected by the new electronic configuration and begin to adjust their positions to compensate. This is illustrated in Figure 2.1.2.1 where v=0 → v′=2 transition (v refers to the ground state vibrational quantum number and v′ refers to the excited state vibrational quantum number) is more probable than the v=0 → v′=0 transition due to a greater overlap of the vibrational wavefunctions of these states.

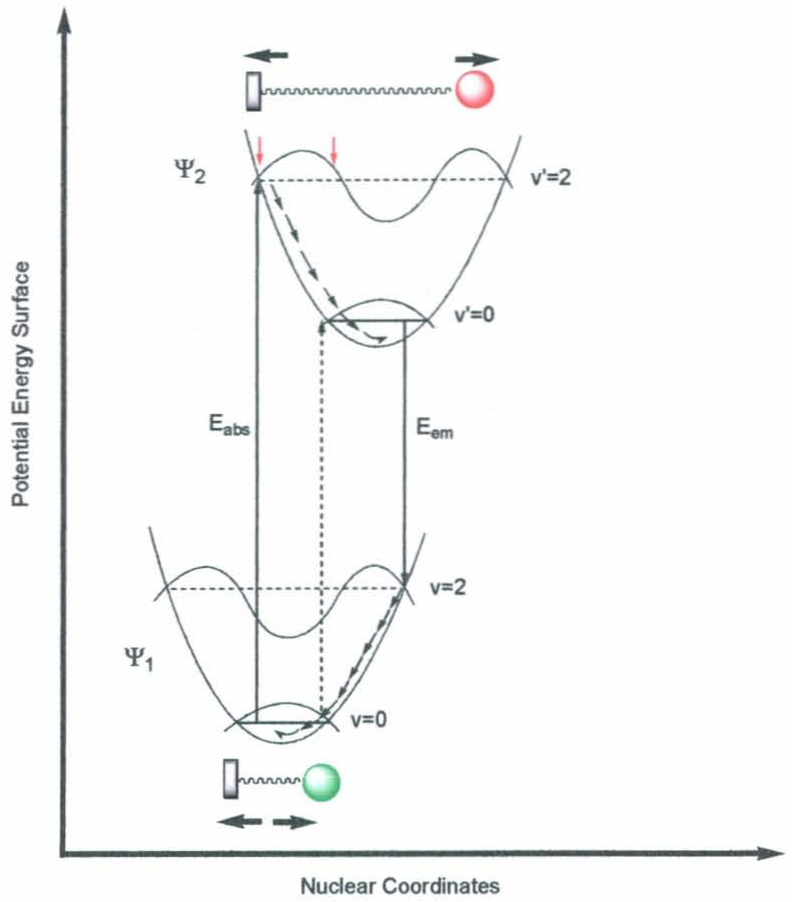

Figure 2.1.2.1. Representation of the Franck-Condon interpretation for the transition between electronic states. The red arrows represent the region of greatest overlap of the vibrational wavefunctions.

In summary, the Franck-Condon principle states that the most probable electronic transitions between states are those which possess similar nuclear configuration and vibrational momentum at the instant of an electronic transition, i.e. the initial and final vibrational wavefunctions which most resemble each other at the instant of an electronic

transition will be the most probable.[1] The degree to which each of these states resembles each other is dictated by the Franck-Condon factor (the integral in equation 2.1.2.3). The larger the Franck-Condon factor, the larger the net constructive overlap between the vibrational wavefunctions, and the more probable the electronic transition.

2.1.3. Visualizing transitions between electronic states

Thus far, the interaction of light and matter has been presented from a strictly physical perspective, along with the assistance of quantum mechanics to describe transitions between electronic states mathematically. However, how should the *chemist* visualize the interaction of light and matter? In the discussion above, the transition from Ψ_1 to Ψ_2 occurs via the distortion of the Ψ_1 state through its interaction with light to yield the Ψ_2 state. In essence, this transition may be modelled in terms of an "equilibrium" between Ψ_1, photons, and Ψ_2. This equilibrium is illustrated in equation 2.1.3.1 where the forward process would involve the absorption of a photon and the reverse process would involve emission of a photon. υ_i is the frequency associated with the transition and is defined by equation 2.1.2b.

$$\Psi_1 + h\upsilon_i \rightleftharpoons \Psi_2 \qquad \textit{eqn. 2.1.3.1.}$$

Mechanistically, one may visualize this transition to involve three species: (i) the initial state Ψ_1; (ii) the mixed wavefunction or Franck-Condon state; and (iii) the final state Ψ_2. This mechanism is given below where λ represents the mixing coefficient for Ψ_2 which can have values from 0 to 1. This parameter is related to the orbital, vibrational, and spin overlap integrals presented previously.

$$\underset{\text{Initial state}}{\Psi_1} + h\upsilon_i \rightarrow \underset{\text{Mixed state}}{[\Psi_1 \pm \lambda\Psi_2]} \rightarrow \underset{\text{Final state}}{\Psi_2} \qquad \textit{eqn. 2.1.3.2.}$$

In modelling the interaction of light and matter in this regard, one may ask: *what does the mixed wavefunction look like?* Essentially, the mixed wavefunctional state $[\Psi_1 \pm \lambda\Psi_2]$ represents a superposition of waves associated with the wavefunctions of Ψ_1 and Ψ_2. Thus, this state will have inherent features which are a combination of the initial and final states. According to the Schrödinger equation, a wavefunction exists in either a positive or negative phase. The time-dependent formalism dictates that these phases are constantly interconverting. Light serves to disrupt this interconversion by dephasing the wavefunction to produce a node with the nuclear configuration of the initial state. This dephased wavefunction may be viewed as the mixed wavefunction or Franck-Condon state discussed previously. The nuclear configuration then relaxes to the configuration of the final state. This is illustrated in Figure 2.1.3.1 and Figure 2.1.3.2. This mechanism may provide insight into the associated resonance condition for electronic transitions in that the appropriate frequency must be met in order to dephase the wavefunction to access the superimposed state. This mixed or superimposed state may be thought of as a conduit connecting the initial and final electronic states and is illustrated in Figure 2.1.3.2 by the solid region.

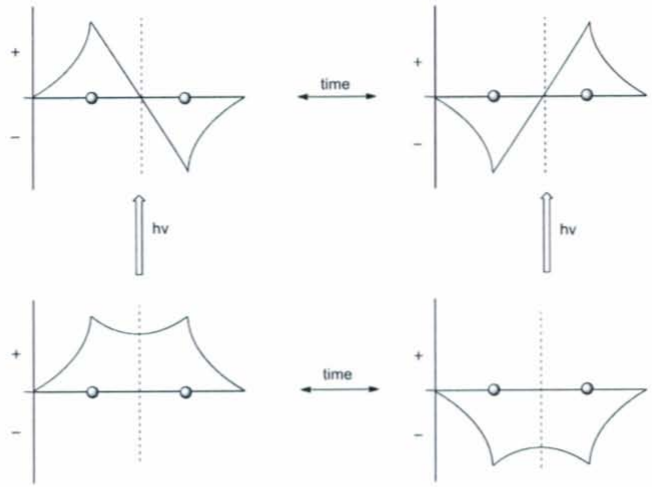

Figure 2.1.3.1. Visualization of the transition between electronic states.

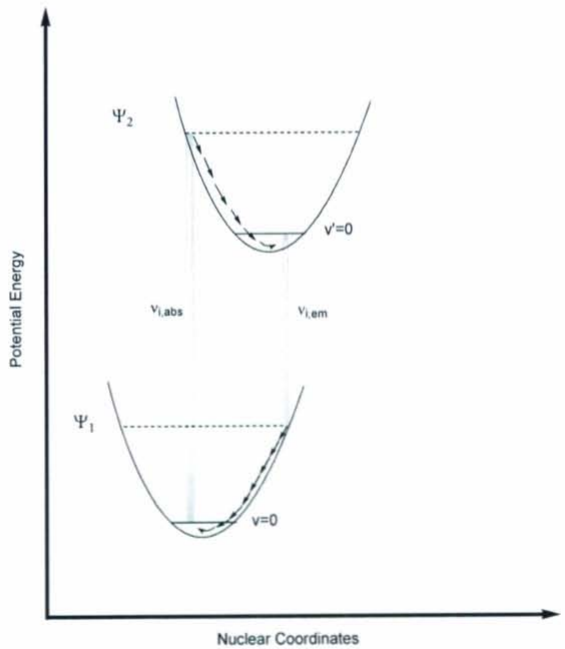

Figure 2.1.3.2. Potential energy surface representation of the transition between electronic states.

2.2. Excited Electronic States in Compact Molecular Systems

Nanoscale systems provide a means to integrate desirable component features into forming new materials of technological interest. Through the assembly of various molecular building blocks, nanometer-sized systems ultimately allow one to explore the relationship between structure and the electronic properties of compact molecular systems.[3] Given the degree of interactions between subunits within nanoscale systems, and that the wavefunctions for such compact systems readily interact, *how does one describe the electronic excited states of these systems?* A model for describing the excited states of such systems has been formulated in terms of describing the excited state as an *exciton*. In essence, the exciton is a representation of an excited state in a significantly compact molecular system such as a nanosystem.

An excited electronic state may be classified in terms of a redistribution of the electron density of the ground state through means of electronic excitation. In terms of an exciton, an exciton is an excited electronic state in which the subunits of the system significantly interact. In such a model, the electronic effect of the subunits is taken into consideration such that the wavefunctions of these subunits mix which serves to move electron density away from individual subunits and partition this density amongst the subunits.[3] Such excitations may be thought of as consisting of an interacting electron [e^-] and a fictitious "electron hole" quasi-particle [h^+], as shown in Figure 2.2.1. Such an interaction leads to the concept of an exciton binding energy (E_b), the coulombic interaction between that of the electron and electron hole.

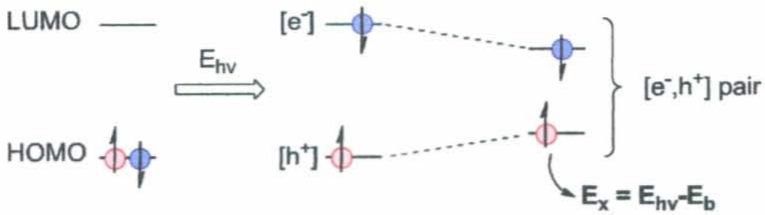

Figure 2.2.1. Exciton model for excited states. The energy of the exciton (E_x) is equated from the excitation energy (E_{exc}) and the exciton binding energy (E_x).

2.3. Instruments in Photophysics

In this section, an overview of the instruments used in this thesis for absorption, emission, flash photolysis, fluorescence lifetime measurements, and temperature dependent fluorescence will be discussed. As well, the theory associated with emission spectral fitting will be presented.

2.3.1. UV-Vis Spectrophotometer

The UV-Vis spectra shown in this thesis were recorded using an Agilent 8453 spectrophotometer. The optical system utilized in this spectrophotometer is illustrated in Figure 2.3.1.1. The radiation source consists of a combination of a deuterium lamp for the UV wavelength range and a tungsten lamp for the Vis wavelength region. A special rear-access lamp design allows for both light sources to be optically combined and focused onto a source lens. This source lens serves to combine both light sources and focus a single beam of light onto the sample. After passing through a source lens, the light beam passes through a shutter/stray light filter then through the sample to a second source lens and slit which serves to focus the light beam onto a concave holographic grating. By

means of this grating, light is dispersed onto a diode array consisting of 1024 photodiodes resulting in an electrical signal which is then interpreted and recorded on an interfaced HP computer.

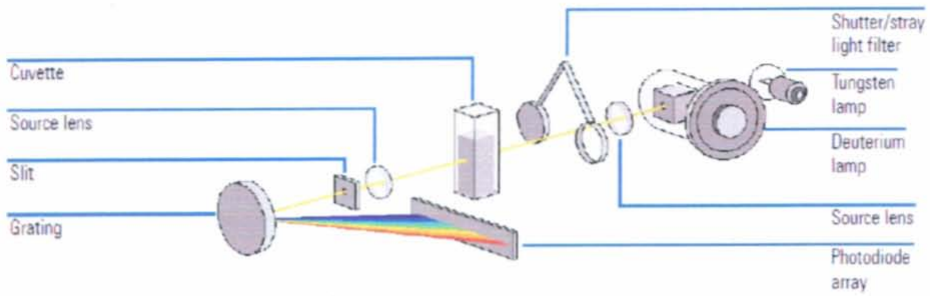

Figure 2.3.1.1. Optical overview of an Agilent 8453 UV-Vis spectrophotometer. Adapted from reference [4].

2.3.2. Fluorescence Steady-State Spectrofluorometer

The emission spectra shown in this thesis were measured on a Photon Technology International (PTI) Quantamaster 40 spectrofluorometer, the operation of which is illustrated in Figure 2.3.2.1. This fluorometer is equipped with a continuous xenon arc lamp as the radiation source through which the excitation wavelength can be set to a value in the 250 nm - 800 nm range. After passing through a slit, the excitation beam is focused onto a sample through an appropriately aligned network of mirrors. Radiation emitted by the sample after excitation is collected at 90° to the excitation beam and detected by a PTI model 810 photomultiplier detection system in photon counting mode which has a detection range of 250 nm – 900 nm. The schematic in Figure 2.3.2.1

includes a pulsed N_2 laser for lifetime measurements which will be discussed in the following section.

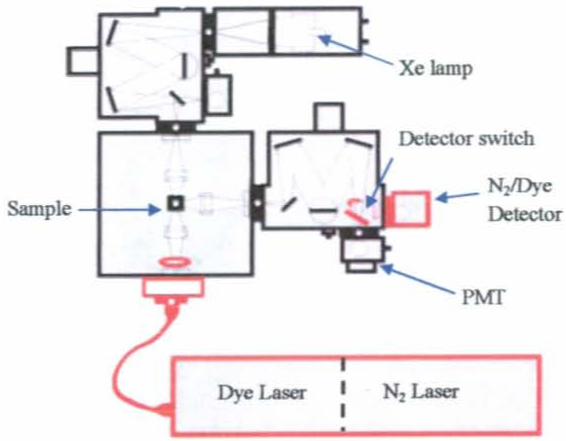

Figure 2.3.2.1. Schematic overview of a PTI spectrofluorometer equipped with a pulsed N_2 laser/dye laser for lifetime measurements. Adapted from reference [5].

2.3.3. Fluorescence Steady-State Lifetime

Fluorescence lifetimes were measured using a LaserStrobe system by a stroboscopic technique based on a PTI nitrogen/dye laser, a schematic of which is shown in Figure 2.3.2.1 and Figure 2.3.3.1. The stroboscopic technique is illustrated in Figure 2.3.3.2. In the LaserStrobe system, a computer generates an output signal with a repetition rate of 20 Hz set by the user that triggers a UV pulse at 337 nm from the N_2 laser. This pulse is then transferred to a dye optical system (the dye laser) which produces a pulse from an appropriately selected dye. After an optical delay, the pulse from the dye laser is fed by a single fibre optic cable to a sample compartment. The sample is then illuminated,

resulting in fluorescence which exhibits a unique exponential decay intensity. Meanwhile, the N_2 laser pulse is detected by a photodiode in the dye laser which initiates a digital delay gate generator (DDG). This DDG delays the pulse by a precisely timed interval which is under computer control and the value of this pulse delay is set in the acquisition software. This delayed pulse then triggers a circuit to send a high voltage pulse to the photomultiplier tube (PMT) detector, resulting in a detection window whereby only photons which fall onto the PMT during the timescale of this high voltage pulse will be detected. The photocurrent which results from photons colliding with the PMT is then detected by an electrometer which is then transferred to a computer. The entire fluorescence decay pattern is detected by varying the time position of the measurement window from well before the excitation pulse to well after the total decay.

Figure 2.3.3.1. Optical system of a pulsed N_2/dye laser for determining fluorescence lifetimes.

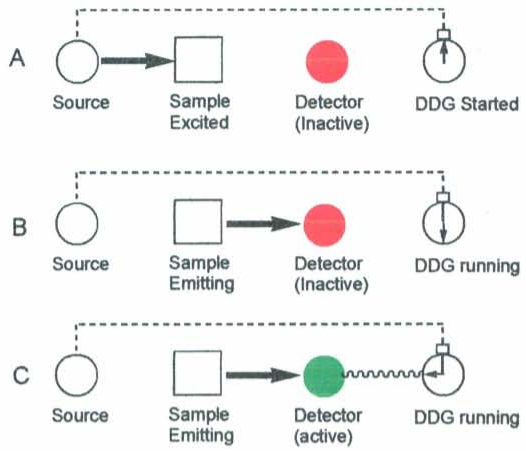

Figure 2.3.3.2. Overview of the stroboscopic technique. A. The laser pulse. B. The sample is excited. C. The detector is initiated for a defined period of time.

2.3.4. Temperature Dependent Fluorescence

Temperature dependent fluorescence data were measured using the PTI spectrofluorometer discussed in section 2.3.2 equipped with an OptistatDN-V liquid nitrogen optical cryostat supplied by Oxford instruments.[6] A schematic overview of this cryostat is given in Figure 2.3.4.1. This cryostat consists of an inner sample chamber and an outer chamber, and optically transparent windows located on each side of the cryostat which allow access to the sample for absorption and emission measurements. A liquid nitrogen reservoir is located above the sample chamber and supplies liquid nitrogen to a heat exchanger through a capillary tube. The flow of liquid nitrogen is controlled by a gas flow control in the exhaust line. The temperature of the sample chamber is controlled by varying the flow of liquid nitrogen and varying the voltage supplied to a thermocouple connected to the heat exchanger via a temperature controller. Under normal operation, the

outer chamber is pumped to vacuum using a Turbo pump supplied by Oxford instruments to remove oxygen which liquefies under liquid nitrogen temperature (77 K).

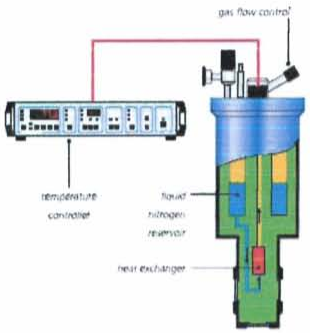

Figure 2.3.4.1. Schematic overview of the optical cryostat used in measuring temperature dependent fluorescence profiles. Adapted from reference [6].

2.3.5. Laser Flash Photolysis

The laser flash photolysis technique is a method for analyzing transient species such as those which are present in excited state relaxation processes. It may be classified as a pump-probe technique whereby laser excitation serves to excite a sample and a lamp probes the resulting relaxation states of the excited species. The basic concept behind this technique is illustrated in Figure 2.3.5.1.

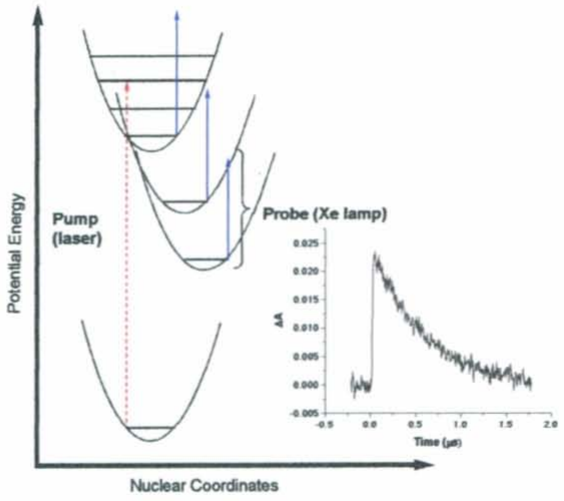

Figure 2.3.5.1. Basic concept for detecting intermediates through laser flash photolysis. The inset represents a sample signal.

There are many system setups used for this technique. For the data presented in this thesis, an LKS.60 system supplied by Applied Photophysics was used. This system has a modular design consisting of a pulsed laser, a pulsed Xe arc lamp, a sample housing unit with adjustable optical mounts and programmable shutters, a grating monochromator, and a photomultiplier tube as a detector. In this setup, the output from a model Brilliant Nd:YAG pulsed laser from Quantel fitted with 2nd and 3rd harmonic generators is directed onto a sample at a right angle to a pulsed Xe arc lamp as the analyzing source. This pulsed source is used to reduce noise effects associated with light scatter and lasts for a few milliseconds by a capacitor discharge. The 2nd and 3rd harmonic generators associated with the laser setup are used to form 355 nm light from the 1064 nm fundamental wavelength of the laser. The lifetime of the 355 nm laser pulse resulting from the harmonic generators is 5 ns. The Xe arc lamp pulse is initiated before the laser is

triggered and shutters associated with the sample housing unit are timed such that the laser output is synchronized to a plateau region of the lamp pulse when analyzing the sample. After the Xe arc lamp is initiated and the lamp shutter associated with the sample housing unit is opened, the analyzing light passes through an adjustable aperture at the entrance of the sample holder, light then passes through the sample and exits through another adjustable aperture to enter a grating monochromator. This monochromator is fitted with a holographic diffraction grating so that stray light is minimized and has an operational range of 250 nm – 1000 nm. The detection wavelength for this monochromator is controlled by a stepping motor drive which is controlled by the user. After the analyzing light has passed through the monochromator at a selected wavelength, the beam is then detected by a photomultiplier tube which detects a photocurrent and sends the data to a HP 54820A digitising oscilloscope which describes the voltage signal using 500 data points. The signal is then converted to an absorbance value, analyzed using appropriate software supplied with the instrument, and stored on an external computer interfaced with the oscilloscope. An overview of the instruments used in the flash photolysis technique is illustrated in Figure 2.3.5.2.

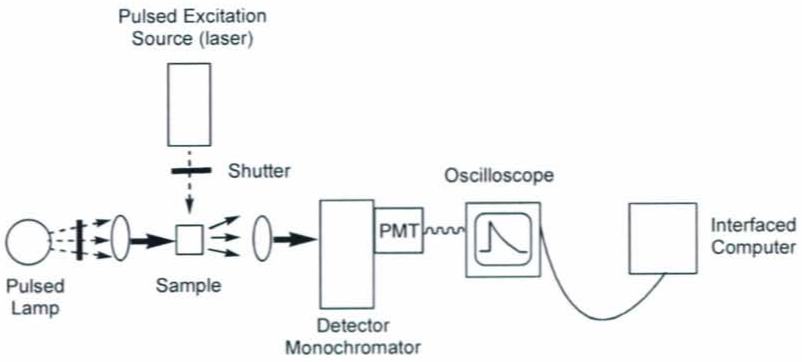

Figure 2.3.5.2. Schematic overview of the instruments used in flash photolysis.

2.4. Emission Spectral Fitting

Emission spectral profiles may be calculated using a Franck-Condon line shape analysis in which an emission band may be fit to a number of N Gaussian functions as defined by equation 2.4.1.[7-9]

$$I(\mathrm{E}) = \sum_{\upsilon=0}^{\upsilon=\mathrm{N}} \left\{ \left(\frac{E_0 - \upsilon\hbar\omega}{E_0} \right)^3 \cdot \left(\frac{S^{\upsilon}}{\upsilon!} \right) \cdot \exp\left[-4\ln 2 \left(\frac{\mathrm{E} - E_0 + \upsilon\hbar\omega}{\Delta\bar{\nu}_{1/2}} \right) \right] \right\} \qquad \textit{eqn. 2.4.1.}$$

The equation defined in eqn. 2.4.1 is only valid when one high-frequency vibration dominates the vibrational progressions associated with the emissive transition.[7-9] In this equation, I(E) is the emission intensity at energy E, υ is the vibrational quantum number of the ground state acceptor vibration, $\hbar\omega$ is the quantum spacing between vibrational levels in the ground state and is assumed to be the quantum spacing of vibrational levels in the excited state through the average mode approximation, $\Delta\bar{\nu}_{1/2}$ is the full width at half maximum of each vibrational component, E_0 is the energy difference between the

ground and excited state vibrational levels, and S^{υ} is the Huang-Rhys factor which reflects the electron-vibrational coupling and is related to the distortion between the ground and excited state potential energy surfaces.

In the fitting procedure, $\hbar\omega$ is fixed and equation 2.4.1 is allowed to converge until a minimum is found in the squared sum of the residuals. E_0, S and $\Delta\bar{\nu}_{1/2}$ are then extracted from the converged equation. Figure 2.4.1 provides an overview for the fitting technique in the case where 5 gaussian-type functions are used to fit the emission spectral profile. Emission data were fit using software previously developed by Juan Pablo Claude. Details can be found elsewhere.[10, 11]

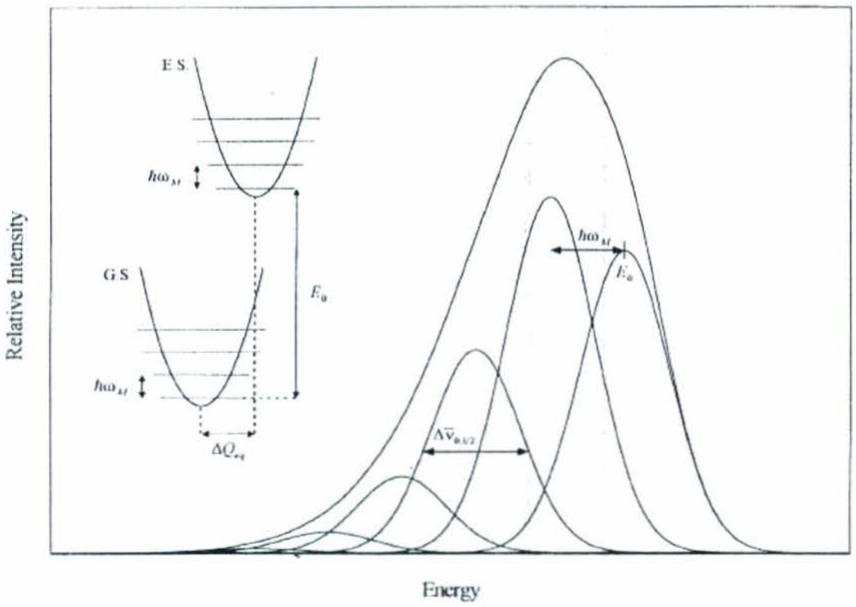

Figure 2.4.1. Emission spectral fitting procedure for spectral profiles with 5 gaussian-type functions. Reprinted with permission from [9]. Copyright 1994 American Chemical Society.

2.5. Conclusion

In this chapter, the interaction of light and matter has been presented and related to electronic transitions within a molecule. A quantum mechanical description of the interaction of light and matter leads to the premise of selection rules for electronic transitions whereby transitions must not only be spin and orbitally allowed, but also vibrationally allowed. It is this vibrationally allowed nature of electronic transitions which leads to the Franck-Condon principle; that is, the principle which states that the most probable electronic transitions are those which possess similar nuclear vibrational configuration and momentum at the instant of an electronic transition.

In visualizing a transition from Ψ_1 to Ψ_2 using light, one may model the interaction as an equilibrium in which the forward rate may be considered synonymous with absorption and the reverse rate may be considered synonymous with emission. The intermediary state may then be viewed as a mixed wavefunctional state. This mixed wavefunctional state may be referred to as the Franck-Condon state. It is this Franck-Condon state which may be considered as a conduit connecting the initial and final state.

In detecting light-induced transitions between an initial and final state, many experimental techniques are available. Such techniques include UV-Vis-NIR absorption, emission (fluorescence and phosphorescence), and laser flash photolysis. Other specialized methods for analyzing excited states include fluorescence lifetime and temperature dependent techniques, and emission spectral fitting. These experimental techniques and methods have been discussed in this chapter. This discussion therefore provides the basis for the experimental data presented in the proceeding chapters of this thesis.

2.6. References

[1] N. J. Turro, V. Ramamurthy and J. C. Scaiano, *Principles in Molecular Photochemistry: An introduction*, University Science Books, **2009**.

[2] C. Cramer, *Essentials of Computational Chemistry: Theories and Models*, 2 ed., Wiley, 2002.

[3] G. D. Scholes, *ACS Nano* **2008**, *2*, 523.

[4] Agilent 8453 UV-Vis Spectroscopy System Service Manual, Agilent Technologies, **2000**.

[5] Quantamaster Information Guide, Photon Technology International **2010**.

[6] OptistatDN-V Liquid Nitrogen Cryostat, Oxford Instruments, **2008**.

[7] G. H. Allen, R. P. White, D. P. Rillema and T. J. Meyer, *Journal of the American Chemical Society* **1984**, *106*, 2613.

[8] J. V. Caspar and T. J. Meyer, *Journal of the American Chemical Society* **1983**, *105*, 5583.

[9] Z. Murtaza, D. K. Graff, A. P. Zipp, L. A. Worl, W. E. Jones, Jr., W. D. Bates and T. J. Meyer, *The Journal of Physical Chemistry* **1994**, *98*, 10504.

[10] J. P. Claude, Ph.D thesis, University of Caroline at Chapel Hill **1995**.

[11] D. W. Thompson, C. N. Fleming, B. D. Myron and T. J. Meyer, *The Journal of Physical Chemistry B* **2007**, *111*, 6930.

Chapter 3:

"EXCITED STATES AND COORDINATION EFFECTS OF 2POAP"

Abstract: The tritopic 2,6-picolinic-dihydrazone ligand 2POAP has provided a route towards many [3x3] grid-like arrays. However, of these grid-type complexes, the properties associated with the ligand framework have yet to be discussed. Before presenting such properties, an understanding of the features inherent to the ligand must first be presented before discussing the ligand when fixed in the grid-type complex. In the proceeding sections of this chapter, structural and spectroscopic properties will be presented for 2POAP. As well, initial experiments which illustrate the effects associated with metal ion coordination to form non-grid structures will be discussed.

3.1. Introduction

Synthetic attempts towards the construction of grid-like metal clusters have primarily relied on the encoding of coordination information into a polytopic ligand, which when interpreted by a specific metal ion of interest, results in a system which displays a unique nanoscale arrangement of metal ions and ligands. Such clusters have been considered as inorganic supramolecular architectures[1, 2] and are associated with the area known as metallosupramolecular chemistry[1, 2], primarily relying on metal centers as directing units towards highly-organized nanoscale systems.

Through such a ligand directed approach, self-assembled polymetallic entities with well-defined nuclearities have been synthesized through the design of ligands with coordination pockets which are optimized to the coordination geometries of the coordinating metal of interest. These pockets exhibit properties which are complementary to the binding metal, such as the appropriate arrangement and orientation of donor atoms within the pocket, which essentially provides a reduction in the metal-ligand bond strain

and maximizes metal-ligand orbital overlap. This approach has been adopted in creating polymetallic grid-like arrays as is shown in the figure below and discussed previously in Chapter 1.

Figure 3.1.1. Synthetic approach towards polymetallic grid-type arrays.

The first step in understanding the properties associated with the ligand in the grid-like structure involves an understanding of the properties of the discrete uncoordinated ligand. As such, in the following sections of this chapter, ground and excited state data will be presented on the tritopic 2,6-picolinic-dihydrazone ligand 2POAP in order to characterize the electronic and structural properties of 2POAP prior to coordination. Following a discussion on the uncoordinated ligand, studies are presented which involve metal ion coordination to form non-grid type complexes. These studies become important when elucidating the properties of the [3x3] grid-type complex involving the 2POAP ligand in Chapters 5 and 6.

3.2. Synthesis and Characterization

The synthesis of 2POAP has been previously reported.[3] It involves the reaction of 2,6-pyridine-dihydrazide with the methyl ester of iminopicolinic acid with a yield of

85%. The synthesis of 2POAP is summarized in Scheme 3.2.1 below. For all studies presented in this chapter, 2POAP samples have been kindly donated by Dr. Laurence K Thompson (Memorial University).

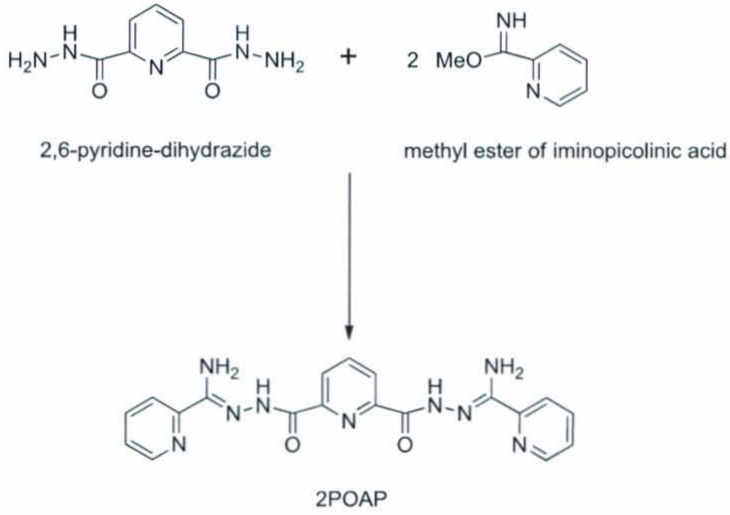

Scheme 3.2.1. Synthesis of 2POAP

3.3. Results and Discussion

3.3.1. 1D and 2D NMR

^{1}H-NMR data on the 2POAP ligand, along with the appropriate peak assignments are given in Figure 3.3.1.1, Figure 3.3.1.2, and Figure 3.3.1.3. 1D NMR data for this ligand has been reported previously.[4] 2D NMR data have not been previously reported. NMR data were collected to access sample purity and to determine structural relationships.

All proton peaks in Figure 3.3.1.1 are located in the aromatic region with the exception of the peak at 11.1 ppm. This suggests that the ligand is composed of primarily

aromatic groups. Notably absent are peaks directly assignable to OH or NH/NH_2 groups which should occur between 1 and 5 ppm. However, the peak at 11.1 ppm may be assigned to either an O-H or N-H as tautomerization may be playing a significant role on this protons electronic environment, as shown in Scheme 3.3.1.1.

Scheme 3.3.1.1. 2POAP tautomerization.

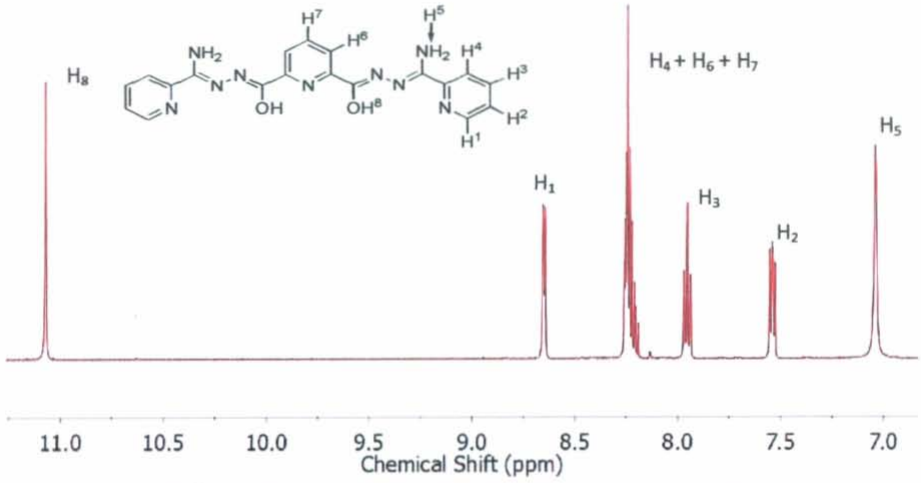

Figure 3.3.1.1. 1D ^{1}H-NMR spectrum for 2POAP in d_3-acetonitrile at 298 K.

In order to correctly assign the proton peaks presented in Figure 3.3.1.1, 2D NMR data were collected and are presented in Figure 3.3.1.2 and Figure 3.3.1.3. The overall method employed for peak identification was to first use (^{1}H-^{13}C) COSY data presented in Figure 3.3.1.2 to determine which peaks originate from C-H bonds. After C-H peaks

were identified, (^{1}H-^{1}H) COSY data presented in Figure 3.3.1.3 were used to determine which protons were adjacent to one another. For a description of these correlated NMR spectroscopic (COSY) techniques, see Friebolin[5].

(^{1}H-^{13}C) COSY data presented in Figure 3.3.1.2 suggest that all peaks are attributable to protons involved in a C-H bonding interaction with the exception of both the H_5 and H_8 peaks. Therefore, both H_5 and H_8 peaks may be assigned to OH or NH/NH_2 groups if the structure of this compound is indeed consistent with that of 2POAP. Since integration of these peaks results in a value of ~4 for H_5 and ~2 for H_8, H_5 is assigned to the NH_2 groups whereas H_8 is assigned to OH or NH groups depending on the specific tautomer present. In addition, the multiplet present at 8.2 ppm exhibits two (^{1}H-^{13}C) COSY peaks which is consistent with the presence of two different C-H bonds.

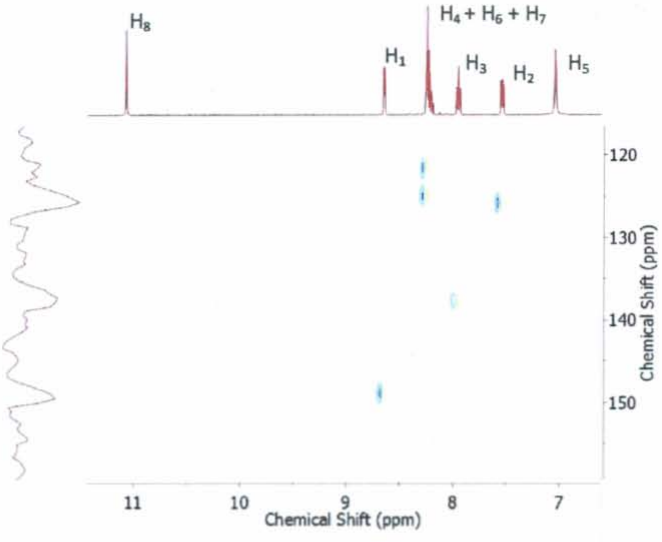

Figure 3.3.1.2. (^{1}H-^{13}C) COSY data for 2POAP in d_3-acetonitrile at 298 K.

(^{1}H-^{1}H) COSY data presented in Figure 3.3.1.3 suggest that both H_5 and H_8 protons are not coupled to any of the peaks present. Therefore, these protons are not adjacent to any of the other protons present in the 2POAP structure. This is consistent with assigning these peaks to NH_2 and OH or NH groups, respectively. What is apparent from the (^{1}H-^{1}H) COSY data is that peak H_1 is coupled to peak H_2, which in turn is coupled to H_3. Moreover, a proton contained in the multiplet assigned as H_4 is coupled to H_3. Since the coupling constant for H_1 is the same as that for H_2 (Table 3.3.1.1), H_1 is coupled to H_2. Therefore, the assignments for the peaks in Figure 3.3.1.1 are justified. A table of NMR parameters are given in Table 3.3.1.1. The remaining H_6 and H_7 protons are assigned to the remaining signals present in the multiplet given that the integral of this peak is 5 which would suggest the presence of 3 additional protons with integral values of 1 for H_7, 2 for H_6, and 2 for H_4. The fact that the (^{1}H-^{13}C) COSY data in Figure 3.3.1.2 indicates that the multiplet at 8.2 ppm is composed of two C-H bonds, and that integration of this peak provides evidence for the presence of three protons suggests that two of these three protons are in the same electronic environment. This is most likely H_6 and H_7 given the structure of the ligand.

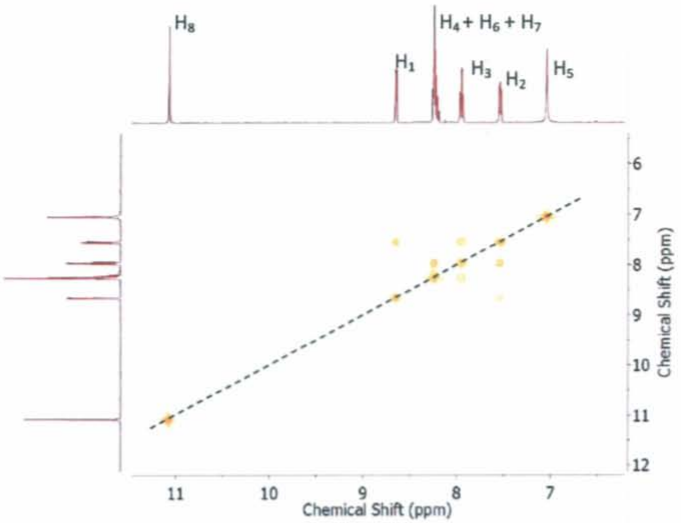

Figure 3.3.1.3. (^{1}H-^{1}H) COSY data for 2POAP in d_3-acetonitrile at 298 K.

Table 3.3.1.1. NMR parameters for 2POAP in d_3-acetonitrile at 298 K

Peak	Chemical Shift (ppm)	Multiplicity	J[b] (Hz)	Integral[d]
H_1	8.6	Doublet	4.5	2
H_2	8.0	Triplet[a]	6.0	2
H_3	7.5	Triplet[a]	4.5	2
$H_4 + H_6 + H_7$	8.2	Multiplet	-	5
H_5	7.0	Singlet	-	3.4[c] (~4)
H_8	11.1	Singlet	-	1.7[c] (~2)

[a] Doublet of doublet signals combined to produce a triplet. [b] Coupling Constant. [c] The integrals are slightly less than expected due to HOD exchange. [d] Integrals relative to peak H_1.

3.3.2. Electronic Spectroscopy

With the ground state structure presented, the ground and excited electronic states for this ligand are now described.

3.3.2.1. UV-Vis Absorption

The UV-Vis absorption spectrum for 2POAP is given in Figure 3.3.2.1.1 with overlaying transitions deconvoluted. Photophysical data are given in Table 3.3.2.1.1. The UV-Vis spectrum was deconvoluted using first and second derivatives. The first and second derivative plots with the proposed locations of transitions are given in Figure 3.3.2.1.2. For a discussion on using first and second derivatives for deconvoluting spectra, see appendix D. The deconvoluted spectrum shows transitions located at 31118 cm^{-1} (321 nm, 25763 $cm^{-1}M^{-1}$), 36587 cm^{-1} (273 nm, 20408 cm^{-1}, M^{-1}), 44468 cm^{-1} (225 nm, 28599 $cm^{-1}M^{-1}$), 46830 cm^{-1} (214 nm, 70923 $cm^{-1}M^{-1}$), and 51423 cm^{-1} (194 nm, 382531 $cm^{-1}M^{-1}$). These transitions are designated as G_a, G_b, G_c, G_d, and G_e, respectively. All proposed transition maxima can be justified with the first derivative as zero and the second derivative as negative except for G_b, G_c, and G_d. G_b and G_d, are justified from the second derivative pattern where at the location for these transitions, the second derivative displays a positive-negative-positive pattern suggestive of a maximum. For G_c, the second derivative is not clear enough to make this determination succinctly. However, not defining a gaussian function at this energy does not result in an adequate fit of the spectrum. Therefore, this suggests that a transition is located at G_c. This transition has been designated with a * in Figure 3.3.2.1.2. All UV-Vis transitions are assumed to be (π-π^*) in nature given that these transitions exhibit large oscillator strengths (f_{osc}) and transition dipoles (μ) which were calculated via equations 3.3.2.1.1 and 3.3.2.1.2, respectively.

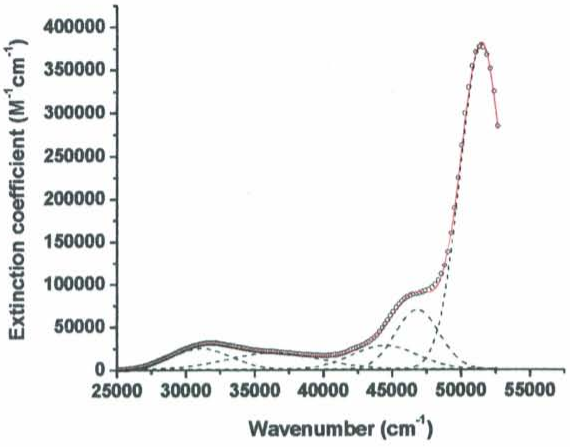

Figure 3.3.2.1.1. Deconvoluted UV-Vis absorption spectrum for 2POAP in acetonitrile. This spectrum was obtained when in DMSO and water.

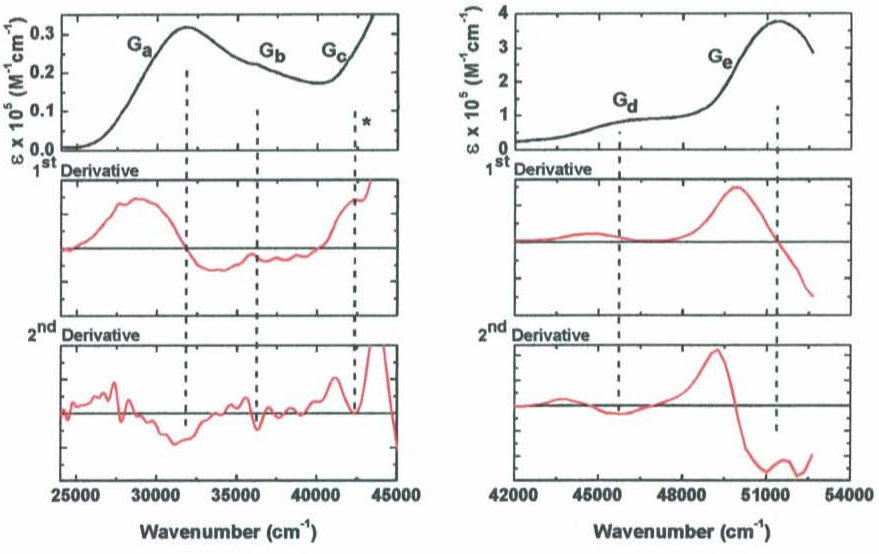

Figure 3.3.2.1.2. Derivative plots for 2POAP in acetonitrile. (a) Data from 24000 cm^{-1} – 45000cm^{-1}; and (b) data from 42000 cm^{-1} – 54000cm^{-1}. The dashed lines correspond to proposed transitions.

Table 3.3.2.1.1. Photophysical parameters for 2POAP in acetonitrile.

	$(\pi\text{-}\pi^*)_1$	$(\pi\text{-}\pi^*)_2$	$(\pi\text{-}\pi^*)_3$	$(\pi\text{-}\pi^*)_4$	$(\pi\text{-}\pi^*)_5$
λ_{abs}, nm	321 (328)[a]	273 (272)[a]	225	214	194
E_{abs}, cm^{-1}	31118 (30477)	36587 (36761)	44468	46830	51423
ε, cm^{-1} M^{-1}	25763	20408	28599	70923	382531
$\Delta\bar{\nu}_{\frac{1}{2}}$, cm^{-1}	5316	8080	5681	3699	3948
f_{osc}	0.59	0.71	0.70	1.14	6.54
μ, eÅ	1.32	1.34	1.21	1.50	3.43

[a] in dimethylsulfoxide (UV-Cutoff at 255 nm).

$$f_{osc} = 4.33 \times 10^{-9} \int \varepsilon(\nu) d\nu \approx 4.33 \times 10^{-9} \left(\varepsilon_{max} \Delta\bar{\nu}_{\frac{1}{2}}\right) \quad \textit{eqn. 3.3.2.1.1.}$$

$$\mu\,(\text{eÅ}) = \left[\frac{f_{osc}}{(1.08\times10^{-5})E_{abs}(cm^{-1})}\right]^{\frac{1}{2}} \quad \textit{eqn 3.3.2.1.2.}$$

3.3.2.2. Emission

Emission data for 2POAP in acetonitrile is given in Figure 3.3.2.2.1. The data indicates that there is no observable emission from 2POAP. The spectrum given is the result of light scattering in the instrument as this emission profile is observed with both solvent and solutions of 2POAP. Emission was also absent in dimethylsulfoxide.

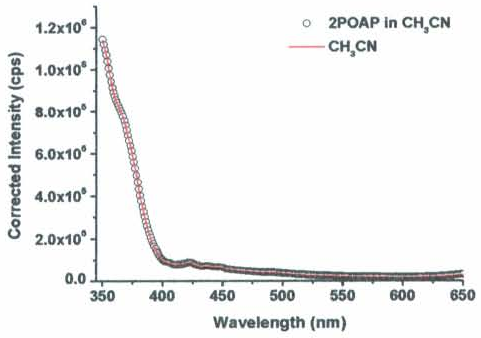

Figure 3.3.2.2.1. Emission spectrum for 2POAP in acetonitrile at λ_{exc} = 321 nm.

The non-emissive nature of the 2POAP ligand is assumed to be due to efficient non-radiative decay associated with structural rearrangements in the excited state. As the ligand is highly flexible, this is not unexpected. One such rearrangement is presumably due to excited state intramolecular proton transfer which is common for many salen-type complexes[6] (Scheme 3.3.2.2.1).

Scheme 3.3.2.2.1. Excited-state proton transfer in salen.

3.3.2.3. Laser Flash Photolysis

Transient experiments with the 2POAP ligand appear to suggest that the ligand is highly unstable under laser excitation. This is demonstrated in Figure 3.3.2.3.1 where after one laser shot, the absorption intensity of the 2POAP solution decreased

substantially. This may suggest that excited state hydride transfer is playing a role given that this type of transfer is common for many aromatic complexes.[7, 8] The products of this laser-induced decomposition have not been characterized.

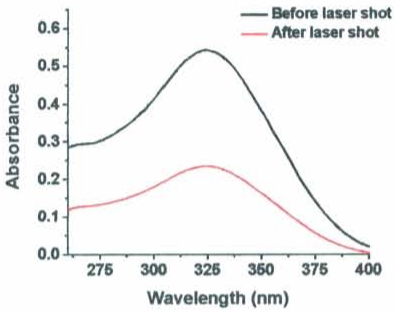

Figure 3.3.2.3.1. UV-Vis spectrum for 2POAP before and after one laser shot at 355 nm excitation in acetonitrile at 298 K.

3.3.2.4. Computational Studies on 2POAP Excited States

Computational data on 2POAP are presented in this section. The purpose of this data is to explore and gain insight into the excited state electronic structure of 2POAP. All calculations were performed using the Gaussian 09 suite of programs.[9] For all density functional theory (DFT) calculations, the B3LYP functional was employed which contains Becke's three parameter hybrid exchange functional[10] with the Lee, Yang, and Parr correlational functional[11]. This hybrid functional has been shown to provide an adequate compromise between computational cost and accuracy with respect to many organic compounds.[12] The Polarizable Continuum model (PCM)[13] was used to include bulk solvent effects to determine the influence of solvent dielectric on the electronic

structure. This method does not account for specific interaction of the solvent and solute. As such, discrepancies between experimental and theoretical data are expected.

Time-dependent density functional theory (TD-DFT) has been shown to be reliable for many aromatic systems.[14, 15] As such, it has been employed here for the calculation of excitation energies. All calculations of excitation energies were obtained using the non-equilibrium solvation approximation for electronic transitions, which is valid for excitations.[13] TD-B3LYP/6-31++G(d,p) calculations were used to calculate excitation energies. Molecular orbitals were plotted using ChemCraft 1.6.

3.3.2.4.1. Excitation Energies

As presented in Scheme 3.3.2.4.1.1, one would assume that the trans isomer is more stable due to less strain associated with the structure when compared to the other comformers. As such, excitation energies were calculated using PCM-TD-B3LYP with the 6-31++G(d,p) basis set for the *trans* and *cis* tautomeric structures and were compared. These energies were then compared to those obtained experimentally to determine which isomer was present in solution. The lowest-lying excitation energies are given in Table 3.3.2.4.1.1. Geometries were initially optimized using PCM-B3LYP/6-31G(d).

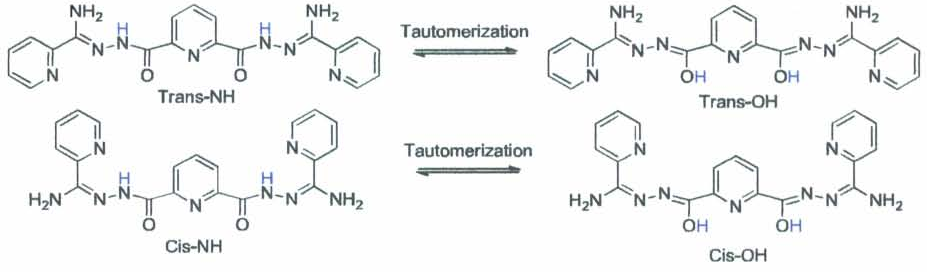

Scheme 3.3.2.4.1.1. Selected isomers for 2POAP.

Table 3.3.2.4.1.1. Lowest-lying excitation energies (eV) for 2POAP. Energies were calculated using PCM-TD-B3LYP with the 6-31++G(d,p) basis set.

	OH	NH	Experimental
	Gas		
Cis	3.53	-	-
Trans	3.37	3.68	
	MeCN (ε = 36)		
Cis	3.50	-	3.84
Trans	3.36	3.88	
	DMSO (ε = 46)		
Cis	3.50	-	3.85
Trans	3.35	3.88	

The data in Table 3.3.2.4.1.1 indicate that the structure of the 2POAP in acetonitrile and dimethylsulfoxide would be the NH-tautomer of the trans-isomer given that the calculated excitation energies for this structure match those that obtained experimentally. As such, the optimized ground state structure for this tautomer is given in Figure 3.3.2.4.1.1. Calculated bond distances and angles are given in Table 3.3.2.4.1.2.

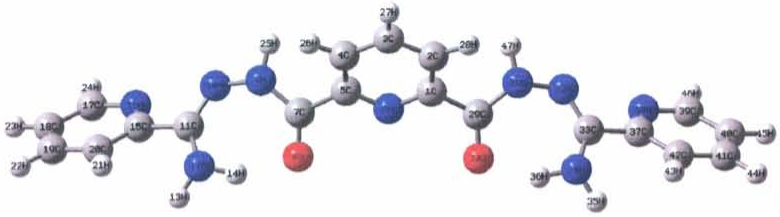

Figure 3.3.2.4.1.1. Optimized structure of 2POAP in solution. Calculation performed using PCM-B3LYP with the 6-31G(d) basis set.

Table 3.3.2.4.1.2. Optimized bond distances and angles for 2POAP in acetonitrile using the polarized continuum model for the solvent and B3LYP with the 6-31G(d) basis set.

Selected bond distances (Å) and angles (°)			
C(1)-C(2)	1.40	C(19)-C(20)	1.39
C(2)-C(3)	1.39	C(20)-H(21)	1.08
N(6)-C(1)	1.34	C(19)-H(22)	1.08
C(2)-H(28)	1.08	C(18)-H(23)	1.08
C(3)-H(27)	1.09	C(17)-H(24)	1.08
C(1)-C(7)	1.52	C(1)-C(2)-C(3)	118
C(7)-O(8)	1.23	C(1)-C(7)-N(9)	113
C(7)-N(9)	1.37	O(8)-C(7)-N(9)	125
N(9)-H(25)	1.01	N(10)-C(11)-N(12)	129
N(9)-N(10)	1.39	N(10)-C(11)-C(15)	115
N(10)-C(11)	1.29	C(11)-N(12)-H(13)	114
C(11)-N(12)	1.38		
N(12)-H(13)	1.01	C(2)-C(1)-C(7)-N(9)	41
C(11)-C(15)	1.50	C(7)-N(9)-N(10)-C(11)	44
C(15)-N(16)	1.34	C(1)-C(7)-N(9)-H(25)	18
N(16)-C(17)	1.33	N(10)-C(11)-C(15)-N(16)	37
C(17)-C(18)	1.40	C(2)-C(1)-C(7)-O(8)	-138
C(18)-C(19)	1.39	N(12)-C(11)-C(15)-C(20)	32

3.3.2.4.2. Electronic Transitions

With an understanding of the structure of 2POAP in the ground state, *how is excitation excitation energy distributed and dissipated in the excited state?* In order to address this question, the time-dependent DFT calculations in Table 3.3.2.4.1.1 for the NH-tautomer were used to obtain a more theoretical description of the redistribution of electron density associated with the excited states for 2POAP. The oscillator strengths, transition energies, and orbital compositions of the six lowest-energy excited states that are predicted from the TD-DFT calculation are listed in Table 3.3.2.4.2.1. The calculated oscillator strengths along with the experimental absorption spectrum are plotted in Figure 3.3.2.4.2.1. The calculation of transition energies are in reasonable agreement with

experiment. Rendering of the molecular orbitals involved in the six calculated excited states using ChemCraft 1.6 are given in Figure 3.3.2.4.2.2. In analyzing these electronic structures, one can have some level of understanding in terms of the redistribution of electron density associated with electronic excitation.

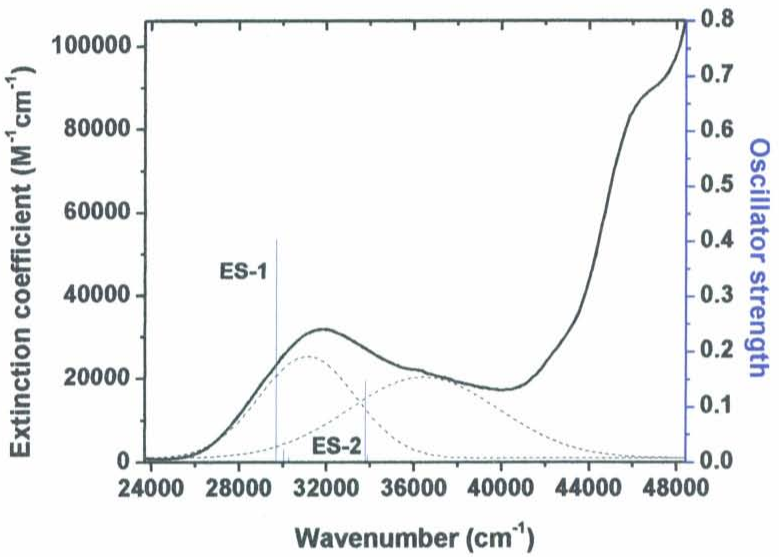

Figure 3.3.2.4.2.1. Lowest energy transitions determined from TD-DFT calculations on 2POAP plotted with the ground state absorption spectrum (solid black). ES-1 and ES-2 are the TD-DFT transitions for excited state 1 and 2 given in Table 3.3.2.4.2.1. Previously deconvoluted transitions are also included (dashed).

Table 3.3.2.4.2.1. Calculated Orbital Composition of the Lowest Spin-Allowed Excited States of 2POAP in Acetonitrile. Calculation performed using PCM-TDB3LYP with 6-31G++(d,p) basis set.

	E (cm^{-1})	f_{calc} [a]	Orbital Transitions (c_i)[b]
Excited State 1	29664	0.4056	104ϕ → 106ϕ (0.59)
			105ϕ → 107ϕ (-0.38)
Excited State 2	30039	0.0242	104ϕ → 107ϕ (-0.26)
			105ϕ → 106ϕ (0.64)
Excited State 3	30250	0.0114	104ϕ → 106ϕ (0.37)
			105ϕ → 107ϕ (0.59)
Excited State 4	30291	0.0010	104ϕ → 107ϕ (0.64)
			105ϕ → 106ϕ (0.27)
Excited State 5	33755	0.1486	100ϕ → 106ϕ (-0.11)
			102ϕ → 106ϕ (0.41)
			103ϕ → 107ϕ (-0.29)
			104ϕ → 109ϕ (0.29)
			105ϕ → 108ϕ (-0.34)
Excited State 6	33878	0.0149	102ϕ → 107ϕ (-0.34)
			103ϕ → 106ϕ (0.39)
			104ϕ → 108ϕ (-0.30)
			105ϕ → 109ϕ (0.29)

[a] Calculated oscillator strength. [b] c_i corresponds to the coefficient for the orbital transition. c_i^2 corresponds to the contribution of each component to the total wavefunction.

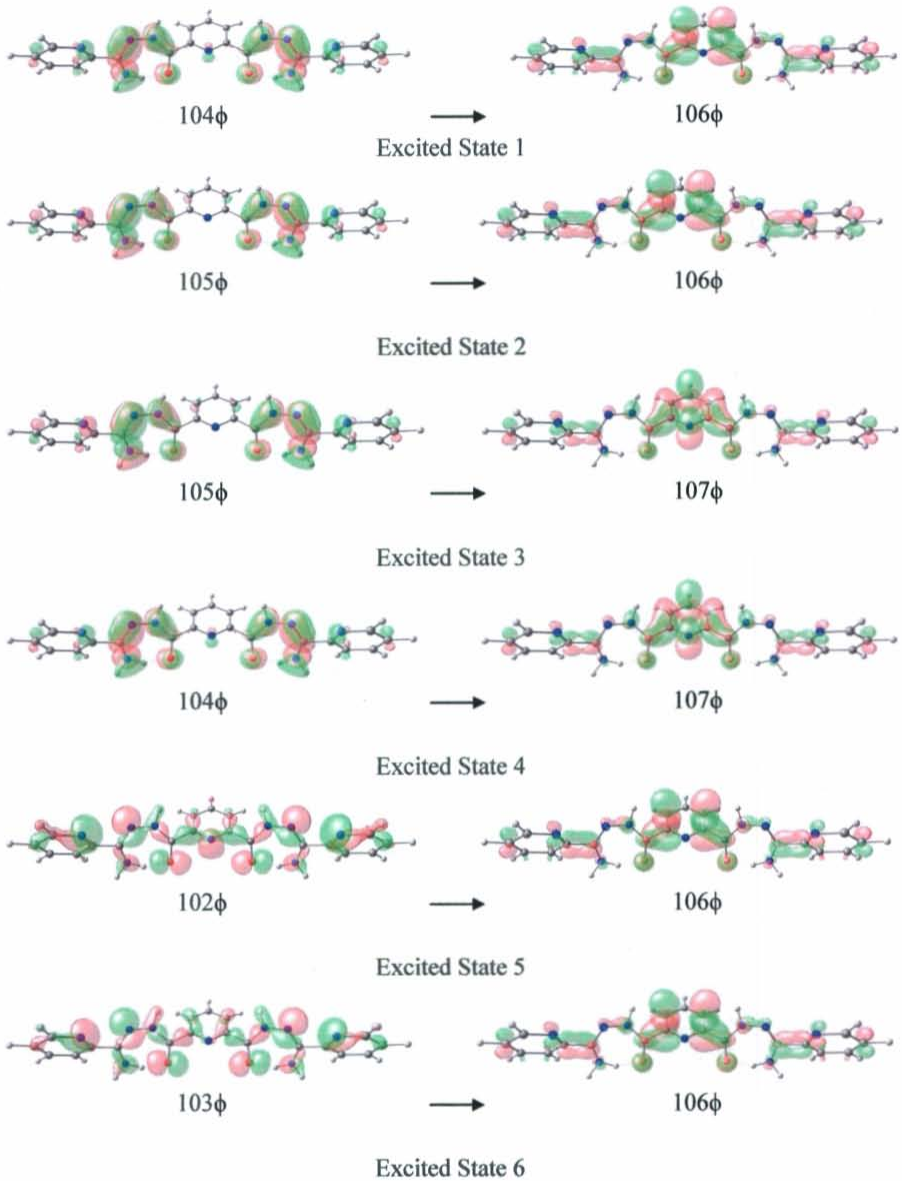

Figure 3.3.2.4.2.2. Drawings of the main orbitals involved in electronic transitions based on TD-DFT calculations. See table 3.3.2.4.2.1 for further details.

Excited states 1 (29664 cm^{-1}), 2 (30039 cm^{-1}), 3 (30250 cm^{-1}), 4 (30291 cm^{-1}), 5 (33755 cm^{-1}), and 6 (33878 cm^{-1}) appear to be (π-π^*) in origin. The lowest-lying excited state (excited state 1) appears to have a contribution from the 105ϕ→107ϕ transition (14%) but is dominated by the 104ϕ→106ϕ component (34%) which exhibits a redistribution of electron density away from the bridge connecting periphery pyridines to the central pyridine unit. In the TD-DFT calculations, only the largest coefficients are included in the output data. As such, the remaining 52% is assumed to be distributed amongst other less dominant orbital transitions.

In the 104ϕ→106ϕ transition, note the redistribution of electron density surrounding the carbonyl carbon: in the orbital 104ϕ, a π bond is present between the carbonyl carbon and a bridge NH group whereas in 106ϕ, the π electron density has been redistributed towards the central pyridine. Given that the bond connecting the carbonyl carbon to the central pyridine does not contain π character in 104ϕ, the bridging group is therefore not in the same plane as the central pyridine. However, since the bond connecting the carbonyl carbon to the central pyridine does contain π character in 106ϕ, the bridging group must become planar with the central pyridine. Therefore, at the instant of electronic excitation, the electronic structure of the bridging group will be in the same plane as the central pyridine whereas its nuclear structure will not. However, as the nuclear structure of this state relaxes, the bridge will become planar with the central ligand. This would suggest that there is a substantial degree of structural rearrangement in the excited state. This would lead to a highly-distorted excited state potential energy surface, and therefore, enhanced non-radiative decay.[16]

3.3.3. Coordination Effects on 2POAP

With a preliminary understanding of the ground and lowest-lying excited states for the 2POAP ligand, this section attempts to build on this knowledge by presenting initial experiments which portray the effects of Zn(II) ion coordination on the ground and excited state properties of 2POAP. Computational data is initially presented and the effects of coordination are proposed from a theoretical perspective. Experimental titration data are then presented which illustrate coordination effects to form non-grid structures involving 2POAP.

3.3.3.1. Computational studies on $[Zn(II)_3(2POAP\text{-}2H)]^{2+}$

A theoretical model representing metal ion coordination to 2POAP is given in Figure 3.3.3.1.1. Bond distances and angles are given in Table 3.3.3.1.1. In this model, Zn^{II} coordination similar to that present in the [3x3] grid-type complex is used as a rubric to illustrate coordination effects. Geometries were optimized using B3LYP/6-31G(d) and excitation energies calculated using TDPCM-B3LYP/6-31+G(d,p). Calculated and experimental excitation energies are given in Figure 3.3.3.1.2 and Table 3.3.3.1.1. The molecular orbitals comprising the majority of the transitions are given in Figure 3.3.3.1.3.

Figure 3.3.3.1.1. Coordination of Zinc(II) to 2POAP to form a section of a grid-type complex.

Table 3.3.3.1.1. Optimized bond distances and angles for $[Zn(II)_3(2POAP\text{-}2H)]$ in acetonitrile using the polarized continuum model for the solvent and B3LYP with the 6-31G(d) basis set.

Selected bond distances (Å) and angles (°)			
C(1)-C(2)	1.40	N(6)-Zn(Center)	1.89
C(2)-C(3)	1.40	O(8)-Zn(Center)	2.00
N(6)-C(1)	1.34	N(16)-Zn(Side)	1.98
C(2)-H(28)	1.08	C(1)-C(2)-C(3)	118
C(3)-H(27)	1.08	C(1)-C(7)-N(9)	120
C(1)-C(7)	1.48	O(8)-C(7)-N(9)	123
C(7)-O(8)	1.41	N(10)-C(11)-N(12)	125
C(7)-N(9)	1.29	N(10)-C(11)-C(15)	123
N(9)-N(10)	1.36	C(11)-N(12)-H(13)	124
N(10)-C(11)	1.32	Zn(Center)-N(6)-C(1)	118
C(11)-N(12)	1.32	Zn(Center)-O(8)-C(7)	108
N(12)-H(13)	1.01	Zn(Side)-O(8)-C(7)	105
C(11)-C(15)	1.51	Zn(Side)-N(10)-C(11)	117
C(15)-N(16)	1.38	Zn(Side)-N(16)-C(15)	109
N(16)-C(17)	1.35	C(2)-C(1)-C(7)-N(9)	0
C(17)-C(18)	1.40	C(7)-N(9)-N(10)-C(11)	180
C(18)-C(19)	1.40	N(10)-C(11)-C(15)-N(16)	-5
C(19)-C(20)	1.40	C(2)-C(1)-C(7)-O(8)	180
C(20)-H(21)	1.08	N(12)-C(11)-C(15)-C(20)	-6
C(19)-H(22)	1.08	Zn(Center)-N(6)-C(1)-C(7)	0
C(18)-H(23)	1.08	Zn(Side)-N(10)-C(11)-C(15)	5
C(17)-H(24)	1.08	Zn(Center)-O(8)-Zn(Side)-N(16)	167
O(8)-Zn(Side)	2.02		
N(10)-Zn(Side)	1.89		

Table 3.3.3.1.2. Excitation energies (eV) for 2POAP and Zinc(II) coordination to 2POAP in acetonitrile. Energies were calculated using TDPCM-B3LYP/6-31+G(d,p) using B3LYP/6-31G(d) optimized geometries.

	Calculated	Experimental
Ligand	3.88	3.84
$Zn_3^{II}(L)$	3.21	3.26 (in grid)

Analysis of the optimized structures in Figure 3.3.3.1.1 and the bond distances in Table 3.3.3.1.1 would suggest that upon coordination, the 2POAP ligand moves from a non-planar structure to a planar structure; as is observed upon Zn(II) coordination to form the [3x3] grid-type complex. Moreover, analysis of the excitation energies in Table 3.3.3.1.2 for these structures would indicate that such coordination to form a planar structure results in a lowering of the excitation energy. This trend is observed experimentally in going from the uncoordinated ligand to the coordinated ligand in the [3x3] grid-type complex.

As was discussed previously for the uncoordinated ligand, how is the excitation distributed and dissipated within this coordination complex? The oscillator strengths, transition energies, and orbital transition compositions of the six lowest-energy excited states that are predicted from TD-DFT calculations are given in Table 3.3.3.1.2. The calculated oscillator strengths and experimental absorption spectrum for the Zn grid (i.e. $[Zn(II)_9(2POAP\text{-}2H)]^{6+}$) are given in Figure 3.3.3.1.2. The calculated transition energies are in reasonable agreement with experiment. Rendering of the molecular orbitals involved in the six calculated excited states using ChemCraft 1.6 are given in Figure 3.3.3.1.3.

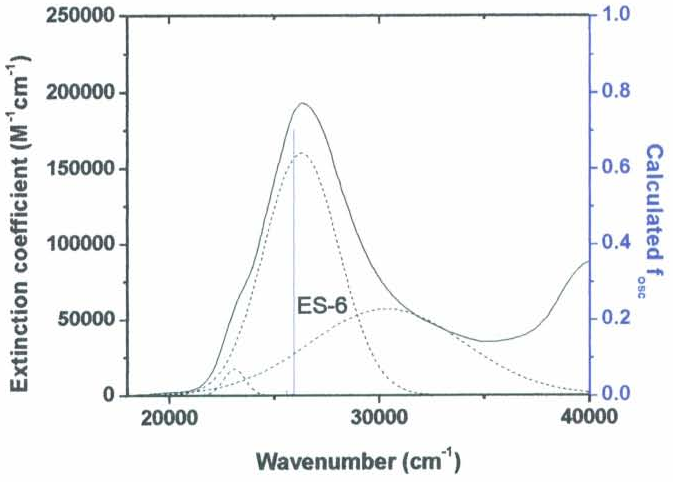

Figure 3.3.3.1.2. Overlay of calculated excitation energies for $[Zn(II)_3(2POAP-2H)]$ with the Zn grid UV-Vis spectrum. ES-6 refers to excited state 6. Deconvoluted gaussians are given as dashed curves (to be discussed in Chapter 5).

Table 3.3.3.1.2. Calculated Orbital Composition of the Lowest Spin-Allowed Excited States of 2POAP in Acetonitrile. Calculation performed using PCM-TDB3LYP with 6-31G+(d) basis set.

	E (cm^{-1})	f_{calc} [a]	Orbital Transitions (c_i) [b]
Excited State 1	15361	0.0000	147ϕ → 148ϕ (0.70)
Excited State 2	19608	0.0020	146ϕ → 148ϕ (0.69)
			147ϕ → 149ϕ (0.14)
Excited State 3	23981	0.0008	146ϕ → 148ϕ (-0.14)
			146ϕ → 152ϕ (-0.13)
			147ϕ → 149ϕ (0.68)
Excited State 4	25575	0.0161	145ϕ → 148ϕ (0.66)
			146ϕ → 149ϕ (0.14)
			147ϕ → 150ϕ (0.11)
			147ϕ → 152ϕ (-0.14)
Excited State 5	25773	0.0002	144ϕ → 148ϕ (0.70)
Excited State 6	25907	0.7058	143ϕ → 148ϕ (-0.25)
			145ϕ → 148ϕ (-0.14)
			147ϕ → 150ϕ (0.63)

[a] Calculated oscillator strength. [b] c_i corresponds to the coefficient for the orbital transition. c_i^2 corresponds to the contribution of each component to the total wavefunction.

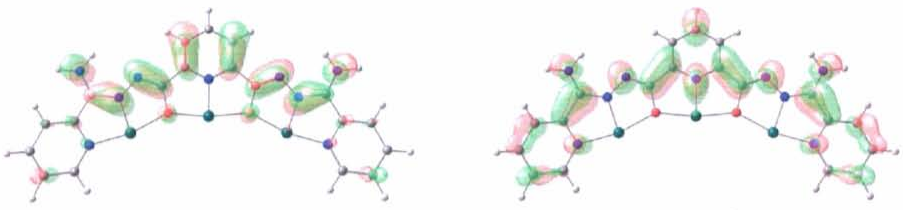

Figure 3.3.3.1.3. Drawings of the main orbitals involved in electronic transitions based on TD-DFT calculations. See table 3.3.4.2 for further details.

Excited states 1 (15361 cm^{-1}), 2 (19608 cm^{-1}), 3 (23981 cm^{-1}), 4 (25575 cm^{-1}), and 5 (25773 cm^{-1}) appear to result from the transition of electron density from the ligand towards the metal core (see appendix A), whereas excited state 6 (25907 cm^{-1}) appears to be (π-π^*) in origin. Excited states 1 to 5 are expected given that in the calculation, Zn(II) is tridentate whereas Zn(II) should have 6 filled coordination sites. Therefore, the analysis of excited states 1 to 5 warrants a cautious interpretation. However, what appears significant is excited state 6. The energy of this excited state is in agreement with the experimental excitation energy obtained for the $[Zn(II)_9(2POAP\text{-}2H)_6]^{6+}$. This state appears to have a contribution from the 143ϕ → 148ϕ and 145ϕ → 148ϕ transitions, but it is dominated by the 147ϕ → 150ϕ component (40 %) which corresponds to a (π-π^*) transition localized on the coordinated 2POAP ligand (Figure 3.3.3.1.3).

3.3.3.2. Non-grid 2POAP Coordination Structures

Experimentally, the effect of Zn(II) coordination to 2POAP is given in Figure 3.3.3.2.1. where a $Zn(NO_3)_2$ solution was added to a solution of 2POAP in acetonitrile.

The data indicate that upon addition of $Zn(NO_3)_2$ to 2POAP, coordination results in growth of a transition centered at ~380 nm. Moreover, coordination results in a lowering of the excitation energies for 2POAP. In addition, overlay of this data with the UV-Vis absorption profile for the Zn grid suggests that the coordination complex formed solely by addition of $Zn(NO_3)_2$ to a concentrated 2POAP solution in acetonitrile does not yield the expected [3x3] grid-type complex (Figure 3.3.3.2.1(b)) as the two absorption profiles differ. Structural characterization has yet to be completed. However, given that 2POAP is the only coordinating ligand present in solution, it is proposed that in order for the metal ion to satisfy its coordination sphere, multiple 2POAP ligands must be coordinated to Zn(II).

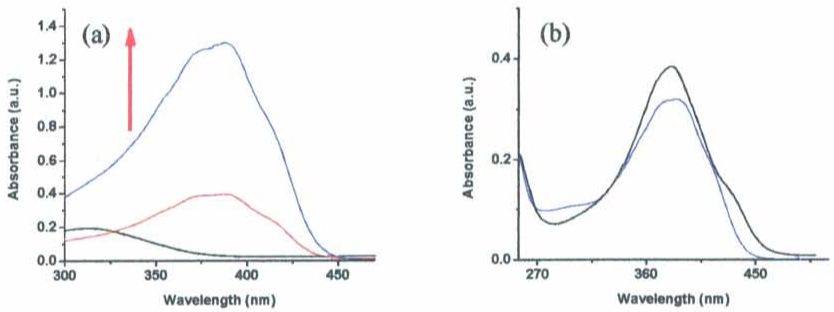

Figure 3.3.3.2.1. Effect of coordination of Zn(II) to 2POAP in acetonitrile. (a) absorption profile of 2POAP upon addition of $Zn(NO_3)_2$ and (b) overlay of absorption spectrum of $[Zn(II)_9(2POAP)_6]^{6+}$ with the absorption spectrum for the 2POAP-$Zn(NO_3)_2$ mixture.

In the above experiment, multiple 2POAP ligands may bind to the metal center in order for the metal ion to satisfy its coordination sphere. Therefore, in an attempt to limit the number of 2POAP ligands which bind to each metal ion, 2,2′,6′2″-terpyridine (tpy)

may be used as a tridentate ligand which should fill the Zn(II) coordination sphere, as illustrated in Scheme 3.3.3.2.1 below. Data for this experiment is presented in Figure 3.3.3.2.2. In this titration, the amount of 2POAP in solution was held constant. An appropriate amount of tpy was added to the 2POAP solution followed by an appropriate amount of $Zn(NO_3)_2$. Throughout the titration, the ratio of tpy:Zn(II) was constant and the ratio of Zn(II):2POAP and tpy:2POAP was varied.

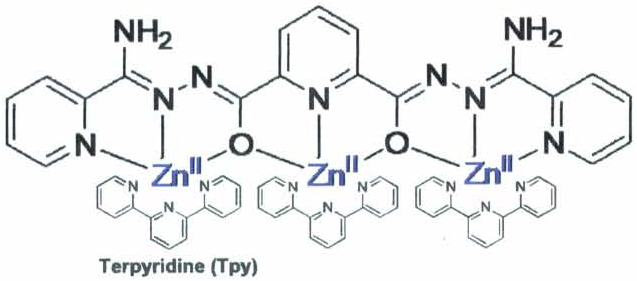

Scheme 3.3.3.2.1. Proposed capping of metal centers coordinated to 2POAP.

Analysis of the data in Figure 3.3.3.2.2 suggests that a mixture of 2POAP and Tpy ligands results in coordination of Zn(II) given the growth in absorption bands when $Zn(NO_3)_2$ is added to this ligand mixture. Moreover, this coordination appears to saturate at approximately a 5:1:5 ratio of Zn(II):2POAP:Tpy (Figure 3.3.3.2.2(b)). As such, the following equation is proposed which reflects the coordination of Zn(II) to 2POAP in this titration. It is assumed that on coordination, 2POAP loses its acidic protons to the solvent.

$$2POAP + 5\ Zn(II) + 5\ tpy \rightarrow [Zn(II)_5(2POAP\text{-}2H)(tpy)_3]^{8+} \qquad \textit{eqn. 3.3.3.2.1.}$$

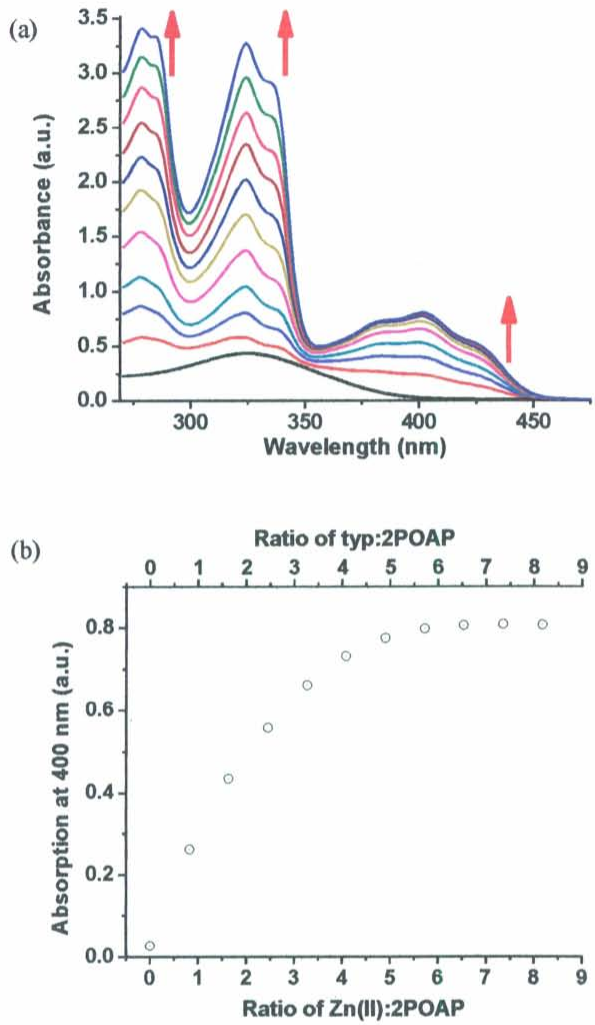

Figure 3.3.3.2.2. (a) UV-Vis absorption data for 10/15, 20/30, 30/45, 40/60, 50/75, 60/90, 70/105, 80/120, 90/135, and 100/150 μL additions of 8.6 mM tpy/8.4 mM $Zn(NO_3)_2$ to 2.5 mL of 26 μM 2POAP. (b) saturation plot for the titration. All solutions were in dimethylsulfoxide.

Given the data in Figure 3.3.3.2.3(a), it appears that growth of the absorption bands at 280 nm and 325 nm in the titration data in Figure 3.3.3.2.2(a) may be attributed to coordination of tpy to Zn(II) ions in solution. Therefore, the new bands centered around 400 nm may be attributed to coordination of Zn(II) to 2POAP. More specifically, given the Zn-2POAP coordination exhibited by the data in Figure 3.3.3.2.1, this coordination is not solely due to coordination to only 2POAP as the UV-Vis absorption profiles differ. Therefore, it is tentatively proposed that the bands present at 400 nm are due to the 2POAP ligand present in $[Zn(II)_5(2POAP\text{-}2H)(tpy)_5]$. This structure is illustrated in Figure 3.3.3.2.4. Structural characterization for this complex has not yet been completed, and therefore, these suggestions should be taken lightly. Moreover, evidence to suggest a non-grid structure such as $[Zn(II)_5(2POAP\text{-}2H)(tpy)_5]$ is provided by the emission data given in Figure 3.3.3.2.3(b) where emission from the Zn(II)-2POAP-tpy mixture differs from that of the $[Zn(II)_9(2POAP\text{-}2H)_6]^{6+}$ complex discussed later in this thesis.

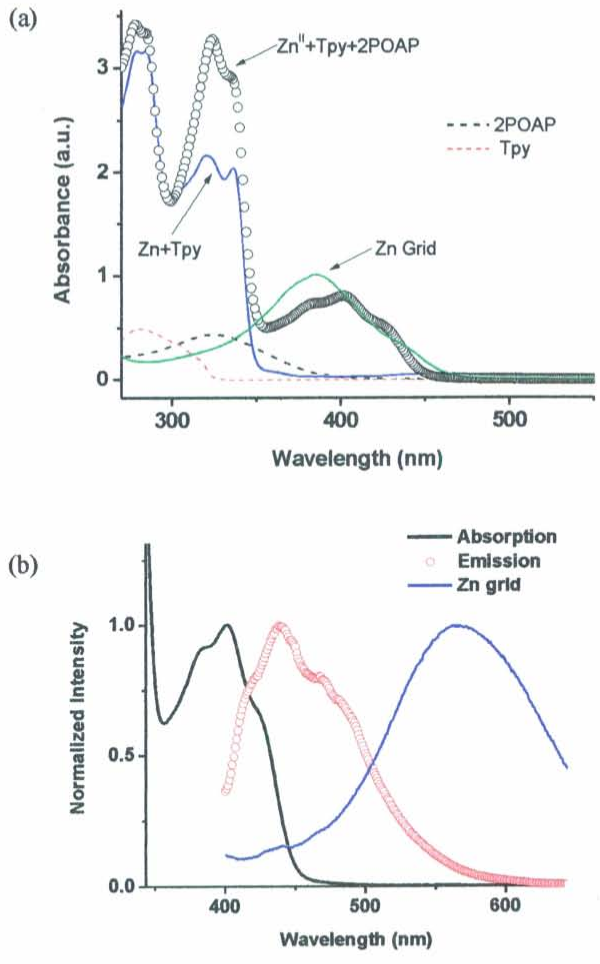

Figure 3.3.3.2.3. (a) overlay of absorption profiles for 2POAP, Tpy, Zn(Tpy), Zn grid, and a Zn-Tpy-2POAP mixture in acetonitrile, and (b) Normalized plot of absorption and emission in the Zn-Tpy-2POAP mixture with Zn grid emission.

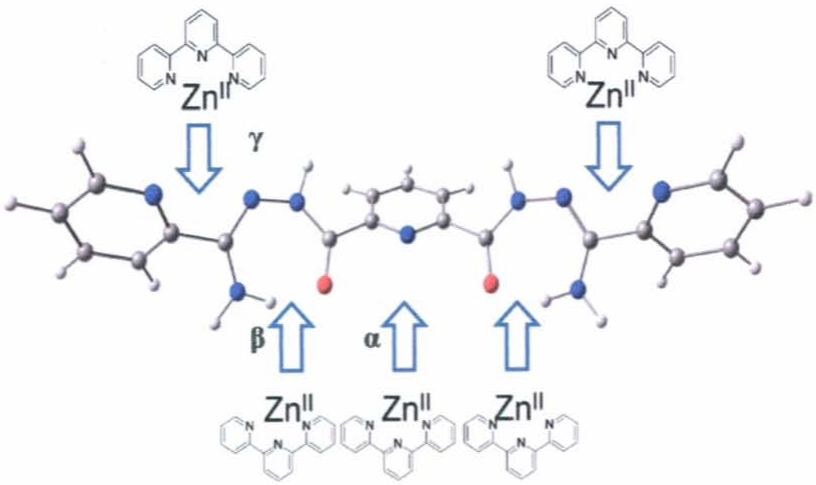

Figure 3.3.3.2.4. Structural representation of $[Zn(II)_5(2POAP)(Tpy)_5]$. α, β, and γ designate Zn(II) coordination types.

As suggested by the proposed structure in Figure 3.3.3.2.4, Zn(II) can be partitioned in terms of three distinct ions: α, β, and γ. In $Zn^{II}(\alpha)$, the coordination sphere encompassing the metal ion is octahedral. However, in $Zn^{II}(\beta)$ and $Zn^{II}(\gamma)$, the coordination sphere is trigonal bipyramidal about the metal center. Since Zn(II) does not exhibit any crystal field stabilization due to its filled d-orbital character, these geometries are possible. However, it is also plausible that both $Zn^{II}(\beta)$ and $Zn^{II}(\gamma)$ are octahedral if the solvent fills a vacant coordination site.

3.4. Conclusion

The function of a device is defined by the properties of its individual components. Highly-organized [3x3] grid-type complexes have previously been shown to exhibit unique properties which may be exploited within the confines of memory storage.

However, an understanding of the components within these complexes, which include metal ions and 2POAP ligands, is a necessity if one wishes to use these complexes in any device-like capacity.

With this necessity in mind, preliminary insights into the electronic properties of the 2POAP ligand have been explored in this chapter. As was illustrated by comparison of computational data to experimental data, the structure of 2POAP in the ground state may be associated with the tautomeric form of the commonly shown hydroxyl version of the ligand. It was also proposed that this ligand's non-emissive nature may be associated with a high-level of structural rearrangement in the excited state since the LUMO for this ligand exhibits π character in an initially non-planar bond.

In addition to the excited state phenomena proposed for the uncoordinated ligand, excitation energy and structural coordination effects were shown to result in planarity and a lowering in the excitation energies for the ligand when coordinated. Moreover, evidence to suggest that metal ion coordination to 2POAP may form non-grid structures was presented and that these structures exhibit many similarities and differences from the discrete ligand in the grid-type complex.

3.5. References

[1] J.-M. Lehn, *Supramolecular Chemistry: Concepts and Perspectives*, VCH, New York, **1995**.

[2] M. Ruben, J. Rojo, F. Romero-Salguero, L. Uppadine and J.-M. Lehn, *Angew. Chem. Int. Ed.* **2004**, *43*, 3644.

[3] L. Zhao, C. Matthews, L. K. Thompson and S. L. Heath, *Royal Society of Chemistry, Chem. Commun.* **2000**, 265.

[4] L. Zhao, M. Sc. thesis, Memorial University **2001**.

[5] H. Friebolin, *Basic One- and Two-Dimenaional NMR Spectroscopy*, 4 ed., Wiley-VCH, **2005**.

[6] T. Kawasaki, T. Kamata, H. Ushijima, M. Kanakubo, S. Murata, F. Mizukami, Y. Fujii and Y. Usui, *Journal of the Chemical Society, Perkin Transactions 2* **1999**, 193.

[7] N. B. Aein and P. Wan, *Journal of Photochemistry and Photobiology A: Chemistry* **2009**, *208*, 42.

[8] D. Mitchell and P. Wan, *Journal of Photochemistry and Photobiology A: Chemistry* **2009**, *205*, 34.

[9] M. J. Frisch, G. W. Trucks, H. B. Schlegel, G. E. Scuseria, M. A. Robb, J. R. Cheeseman, G. Scalmani, V. Barone, B. Mennucci, G. A. Petersson, H. Nakatsuji, M. Caricato, X. Li, H. P. Hratchian, A. F. Izmaylov, J. Bloino, G. Zheng, J. L. Sonnenberg, M. Hada, M. Ehara, K. Toyota, R. Fukuda, J. Hasegawa, M. Ishida, T. Nakajima, Y. Honda, O. Kitao, H. Nakai, T. Vreven, J. A. M. Jr., J. E. Peralta, F. Ogliaro, M. Bearpark, J. J. Heyd, E. Brothers, K. N. Kudin, V. N. Staroverov, R. Kobayashi, J. Normand, K. Raghavachari, A. Rendell, J. C. Burant, S. S. Iyengar, J. Tomasi, M. Cossi, N. Rega, J. M. Millam, M. Klene, J. E. Knox, J. B. Cross, V. Bakken, C. Adamo, J. Jaramillo, R. Gomperts, R. E. Stratmann, O. Yazyev, A. J. Austin, R. Cammi, C. Pomelli, J. W. Ochterski, R. L. Martin, K. Morokuma, V. G. Zakrzewski, G. A. Voth, P. Salvador, J. J. Dannenberg, S. Dapprich, A. D. Daniels, O. Farkas, J. B. Foresman, J. V. Ortiz, J. Cioslowski and D. J. Fox, Revision A.02 ed., Gaussian Inc., Wallingford CT, **2009**.

[10] A. D. Becke, in *Journal of Chemical Physics, Vol. 98*, American Institute of Physics, **1993**, p. 1372.

[11] C. Lee, W. Yang and R. G. Parr, *Physical Review B* **1988**, *37*, 785.

[12] C. Cramer, *Essentials of Computational Chemistry: Theories and Models*, 2 ed., Wiley, **2002**.

[13] J. Tomasi, B. Mennucci and R. Cammi, *Chemical Reviews* **2005**, *105*, 2999.

[14] L. Zhang, G. H. Peslherbe and H. M. Muchall, *Photochemistry and Photobiology* **2006**, *82*, 324.

[15] S. Bhattacharya, *Chemical Physics Letters* **2007**, *446*, 199.

[16] G. F. Strouse, J. R. Schoonover, R. Duesing, S. Boyde, W. E. Jones, Jr. and T. J. Meyer, *Inorganic Chemistry* **1995**, *34*, 473.

Chapter 4:

"ELECTRON TRANSFER THEORY"

Abstract: The excited states associated with the ligand states in [3x3] grid-type complexes will be shown to involve photoinduced charge transfer processes. As such, electron transfer theory will be discussed in this chapter. This chapter cannot be comprehensive in covering all aspects of electron transfer mechanisms and theory. The principles and concepts of electron transfer relevant to the polynuclear grid-type complexes studied in later chapters will be presented. Specifically, the evolution of understanding of electron transfer processes which can be used to assist in the classification of the excited states of the [3x3] grid-type complexes containing Zn_9^{II}, Mn_9^{II}, and $Mn_5^{II}Mn_4^{III}$ metal cores will be discussed. Electron transfer theory will be presented which will include the formalisms proposed by Mulliken, Marcus, and Hush, and the mechanisms proposed by Taube. Potential energy surfaces will be constructed for a two-state system, and an electronic coupling term introduced which will be used as a means to classify electron transfer systems.

4.1.Introduction

For billions of years, plants and photosynthetic bacteria have continuously advanced their ability to harvest solar energy and convert this energy into ATP and other compounds for the organism to survive. The energy to biomass efficiency for this process is ~0.05%; small when one considers the global impact of photosynthesis. However, on a global scale, this limitation is overcome by the vast number of organisms that convert light into redox equivalents which is then used to form biomass. Given that 120 000 TW of energy is supplied to the earth from the sun in a given year, solar energy is therefore a readily abundant energy source in which our current energy consumption (15 TW per year) could easily be achieved simply by covering 0.1% of the earth's surface with a solar

energy conversion system operating at 8% efficiency![1] This natural process, known as *photosynthesis* (equation 4.1 where A is an oxidized electron donor), utilizes a variety of fundamental phenomena whereby light is absorbed by antenna chromophores and funnelled to a reaction center (via excitation energy transfer discussed in Chapter 7) where optical energy is ultimately converted to chemical energy. [2]

$$2n\ CO_2 + 2n\ H_2O + h\upsilon \longrightarrow 2\ [CH_2O]_n + 2n\ O_2 + 2n\ A \qquad \textit{Eqn. 4.1}$$

Photosynthetic organisms are ubiquitous in nature and form the foundation for all higher-order life on this planet. The photosynthetic apparatus is composed of many light-harvesting components and a reaction center where the conversion of photonic energy to chemical energy takes place. The key components of the reaction center include a special pair of bacteriochlorophylls (P), an unpaired bacteriochlorophyll (BChl), a bacteriopheophytin (BPh), and various quinone species (Q). These molecules are held in a fixed geometry which allow for various electron transfer processes to occur at optimal efficiency. Of these electron transfer processes, photoinduced electron transfer may be considered as the most pivotal in terms of the overall progression of photosynthesis.

Photoinduced electron transfer is a process by which an electron is transferred from an electron donor (D) to an electron acceptor (A) through light excitation of one of the components prior to the actual electron transfer event. Through this process, excitation energy is converted into redox energy through the creation of a charge transfer state consisting of a radical cation and radical anion.

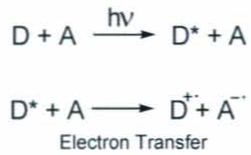

Figure 4.1. Photoinduced electron transfer involving donor excitation.

A charge transfer excited state can undergo further electron transfer (or charge separation) in an appropriately designed molecular assembly prior to relaxation. For example, in the photosynthetic reaction center, the primary charge separation process is a consequence of the specific arrangement and the fundamental nature of a special pair of bacteriochlorophyll molecules, which upon excitation, transfers an electron to an adjacent BChl molecule within ~3 ps.[2] Further electron transfer from the $BChl^{-\cdot}$ to an adjacent BPh occurs in ~1 ps, with direct back electron transfer (or charge recombination) to reform the special pair ground state occurring in ~10 ns.[2] This charge recombination pathway is intercepted via further charge separation with electron transfer from the $BPh^{-\cdot}$ to a quinone (Q_A) occurring in ~200 ps and then to a second quinone (Q_B) in ~200 μs.[2] These electron transfer processes are illustrated in Figure 4.1.2. This quinone then takes up protons to compensate for the charge disparity associated with the transferred electrons, traverses the cell membrane, and releases the protons to create a transmembrane potential. It is this transmembrane potential which leads to the formation of ATP through ATP synthase (Figure 4.1.3).

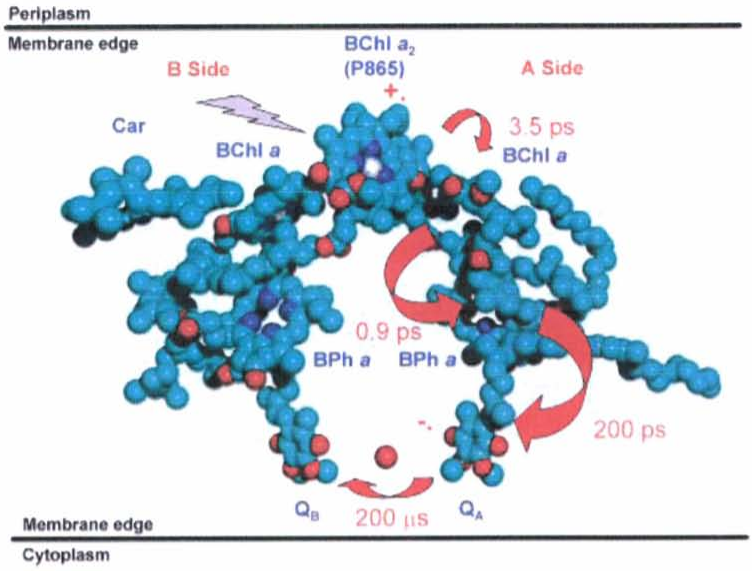

Figure 4.1.2. Charge separation process in purple bacteria. BChl a_2 refers to the special pair. The presence of the carotenoid (Car) represents an environmental difference between the A and B side causing the B side to be deactivated. Reprinted with permission from reference [3]. Copyright 2006 American Chemical Society.

In many organisms, solar energy is converted to chemical energy through the formation of a bond between ADP and phosphate. The electron hole left on the special pair is refilled by the initially transferred electron through an electron transfer cycle involving an array of nearby cytochrome molecules and the quinone which has traversed the cell membrane. However, in other species such as cyanobacteria and plants, this electron hole is used to pump the oxidation state of a nearby Mn_4O cluster. In these species, through a series of oxidation state pumping, the electron hole is ultimately refilled through the oxidation of water (Figure 4.1.3).

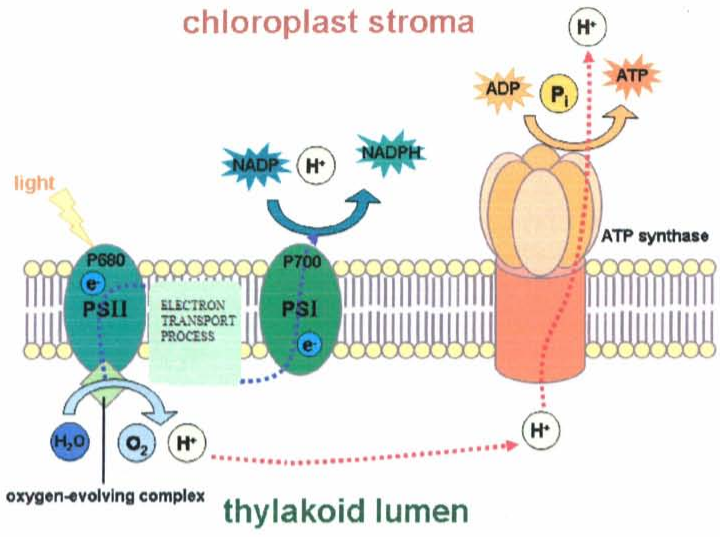

Figure 4.1.3. Representation of photosynthesis in plants. Adapted from reference [4].

In essence, electron transfer processes provide a pivotal means to sustaining life on this planet, as exemplified by photosynthesis. Given societies dependence on fossil fuels, not only is energy derived from the conversion of carbon dioxide and water to form carbohydrates, energy is also derived from the photosynthetic organisms which fixed the fossil fuel in place. Thus, studying electron transfer in well-defined molecular systems, such as the grid-type complex, may lead to key insights into the fundamental processes responsible for solar energy conversion and energy storage on a global scale.

4.2. Electron Transfer

Electron transfer reactions are ubiquitous in chemistry, biochemistry, and a myriad of other processes. Redox reactions result in a change of the electron inventory as an electron is transferred from an electron donor to an electron acceptor. This process

may occur thermally via adiabatic electron transfer or via a non-adiabatic process such as quantum mechanical tunnelling where light is used to drive the electron transfer event. These pathways are illustrated in Figure 4.2.1.

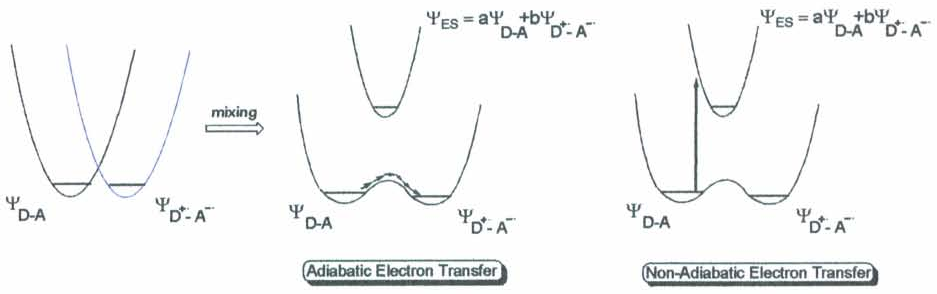

Figure 4.2.1. Adiabatic electron transfer versus non-adiabatic electron transfer.

The formation of a charge separated state is coincident with the formation of a radical cation and radical anion via electron transfer between an electron donor and acceptor. Excited state charge transfer is thus in direct competition with the radiative and non-radiative relaxation processes of the locally excited states of the electron donor and acceptor. As such, as illustrated in the Jablonski diagram below, excited state electron transfer is a non-radiative deactivation pathway of the locally excited state of a donor or acceptor in direct competition with emission, internal conversion, and intersystem crossing (i.e. S→T conversion).

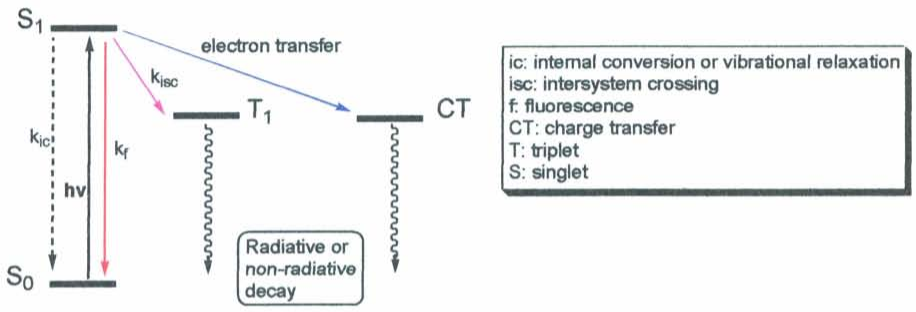

Figure 4.2.1. Jablonski diagram for an excited electron donor or acceptor.

Electron transfer theory may be viewed as combination of Mulliken's charge transfer theory[5], Hush's intervalence theory[6, 7], Marcus's electron transfer theory[8-14], and Taube's inner/outer sphere electron transfer mechanisms[15]. Other notable contributions include Kochi's interior sphere mechanism[16], Sutin's semi-classical treatment,[17] Closs and Miller's[18] experimental verification of the inverted region, and the Robin-Day classifications for electron transfer systems[19]. These theories, mechanisms, and electron transfer classification schemes will be discussed in the following sections. Other notable contributors to electron transfer theory include Jortner and Bixon[20, 21] for non-radiative decay theory. However, this theory will not be discussed here.

4.2.1. Mechanisms of Electron

Taube demonstrated electron transfer processes occurred in terms of two distinctive pathways which differ depending on the transition state through which the process proceeds.[22] These pathways are illustrated in Figure 4.2.1.1. One of these

distinct pathways involves an outer-sphere mechanism where the electronic interaction in the bimolecular [D,A] encounter complex is considered to be weak and the transition state is traversed such that the coordination spheres of both the donor and acceptor remain unchanged. In contrast, the second pathway involves the inner-sphere mechanism where the electron transfer event is mediated by a bridging ligand. It is for this reason that the encounter complex for the inner-sphere mechanism is typically referred to as the bridged-activated complex.

In discussing inner-sphere and outer-sphere electron transfer, the degree of electronic interaction between the donor and acceptor was used to differentiate between the two pathways. Conceptually, it is useful to see how increasing the electronic interaction in the [D,A] encounter complex will move from one mechanism to the other.[16] By progressively increasing the electronic interaction in the [D,A] encounter complex, three distinct cases become apparent. For the weak electronic interaction (or weak electronic coupling) between the donor and acceptor, the "outer-sphere" mechanism dominates. For the relatively moderate electronic coupling between the donor and acceptor, the "inner-sphere" mechanism dominates and includes the formation of the bridged-activated complex. Finally, as introduced by Kochi,[16] a subclass of the inner-sphere mechanism derives from strong electronic coupling between the donor and acceptor and is referred to as the "interior-sphere" mechanism. In this mechanism, the encounter complex is considered to be delocalized forming a delocalized electron-transfer complex whereby the electron-transfer event is solely limited by diffusional encounter of the donor and acceptor. These three electron-transfer mechanisms are illustrated in Figure 4.2.1.1.

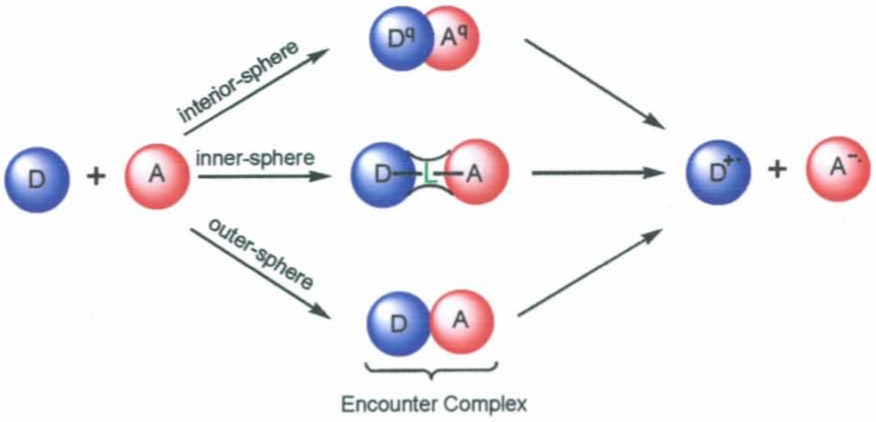

Figure 4.2.1.1. Mechanisms of electron-transfer.

4.2.2. Classical Theory

Overall, a bimolecular electron transfer process may be summarized as follows. Initially the donor and acceptor collide under diffusional control to form a precursor complex. The electron transfer process then occurs to form an activated complex at the transition state. The activated complex is composed of isoenergetic D-A partners where the electron hops. Vibrational and solvent relaxation accompanies the formation of the successor complex which then dissociates to form the bimolecular electron transfer products. This process is summarized in scheme 4.2.2.1.

Scheme 4.2.2.1. Overall process for a bimolecular redox process.

4.2.2.1. Mulliken Charge Transfer and the Encounter Complex

Mulliken[5] envisioned the diffusional encounter of an electron donor (D) with an electron acceptor (A) to form an encounter complex [D,A] which is detectable via the optical charge-transfer transition shown below resulting from a mixing of the HOMO of the donor with the LUMO of the acceptor.

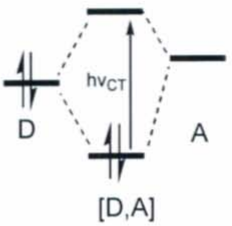

$$D + A \rightleftharpoons [D,A] \overset{h\nu_{CT}}{\rightleftharpoons} [D^{+\cdot},A^{-\cdot}]$$

Scheme 4.2.2.1.1. Illustration of Mulliken charge-transfer.

The first report of the outer-sphere charge transfer complex was that reported by Benesi and Hildebrand[23, 24] in which a benzene donor and a variety of halogen acceptors formed 1:1 charge-transfer complexes.[5] This constituted the experimental basis for the development of Mulliken's charge-transfer theory which is predicated on the ground- and excited-state wavefunctions being expressed as:

$$\Psi_{gs} = a_1\Psi_{[D,A]} + a_2\Psi_{[D^{+\cdot},A^{-\cdot}]} + a_3\Psi_{[D^{\bullet},A]} + a_4\Psi_{[D,A^{\bullet}]} + \ldots \qquad \textit{eqn. 4.2.2.1.1}$$

$$\Psi_{es} = b_1\Psi_{[D,A]} + b_2\Psi_{[D^{+\cdot},A^{-\cdot}]} + b_3\Psi_{[D^{\bullet},A]} + b_4\Psi_{[D,A^{\bullet}]} + \ldots \qquad \textit{eqn. 4.2.2.1.2}$$

Ψ_{gs} and Ψ_{es} are the wavefunctions of the ground and excited states which are composed of the unperturbed state $\Psi_{[D,A]}$, an electron transfer state $\Psi_{[D^{+\cdot},A^{-\cdot}]}$, a locally excited donor

state $\Psi_{[D^{\bullet},A]}$, and a locally excited acceptor state $\Psi_{[D,A^{\bullet}]}$. Terms a_x and b_x correspond to contribution coefficients which define the wavefunctions for the ground and excited states. Thus, the optical colours which were observed are based on the $\Psi_{gs} \rightarrow \Psi_{es}$ transition in which $\Psi_{es} \sim b_2\Psi_{[D^{+\cdot},A^{-\cdot}]}$ and $\Psi_{gs} \sim a_1\Psi_{[D,A]}$ (i.e. $b_2 >> b_1$, b_3, b_4 and $a_1 >> a_2$, a_3, a_4).

A correlation between the energy of the optical charge-transfer transition (the HOMO-LUMO gap) and the oxidation-reduction potentials of the donor and acceptor provides the experimental basis for confirming the charge-transfer character of absorption bands resulting from complexation of a donor with an acceptor. This is illustrated below for a TMDO donor with various aromatic acceptors.

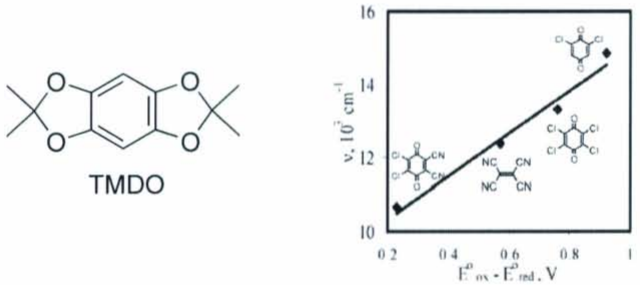

Figure 4.2.2.1.1. Mulliken plot for a TMDO donor with various aromatic acceptors. Reprinted with permission from reference [16]. Copyright 2008 American Chemical Society.

4.2.2.2. Electron self-exchange reactions

Self-exchange processes were one of the first electron transfer reactions studied.[25] These studies illustrated that electron transfer reactions are not solely driven by the free energy change associated with the reaction. In these studies, isotopically

labelled species were used to probe the overall self-exchange reaction. The process is illustrated in Figure 4.2.2.2.1.

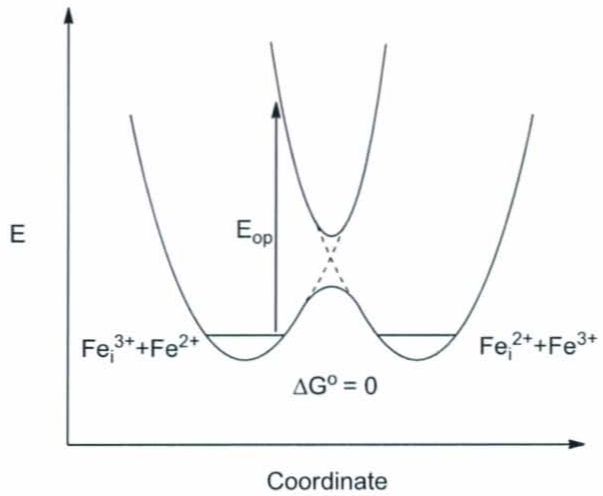

Figure 4.2.2.2.1. Potential energy surface for a self-exchange electron transfer process.

4.2.2.3. Marcus Theory

The field of electron transfer evolved rapidly due to the unique synergy between Marcus` theoretical formalisms and the experimental study of bimolecular redox reactions.[9] The approach taken by Marcus[8-14] employed the harmonic oscillator approximation and assumed that a reaction will only occur if the potential energy surface for the reactants intersects the potential energy surface for the products. This point of intersection was defined as the transition state with the energy at this point being the activation free energy ($\Delta G^{\ddagger}$ or $\Delta G^{\neq}$). Through application of transition state theory to the coupled surfaces, the rate constant for electron transfer was derived to give equation 4.2.2.3.1 below.[8-14] The potential energy surface associated with these coupled parabolas

is given in Figure 4.2.1.3.1 along with associated thermodynamic parameters. It should be noted that Marcus derived the electron transfer equations using statistical mechanics and transition state theory.[8-14] Therefore, at all points along the reaction coordinate, the system is in thermal equilibrium with the surroundings and the transition state is in equilibrium with the reactants.

$$k_{et} = Ae^{\frac{-\Delta G^*}{RT}} = \upsilon_N \kappa e^{\frac{-\Delta G^*}{RT}} \qquad \textit{eqn. 4.2.2.3.1.}$$

In equation 4.2.2.3.1, κ_{el} is the electronic transmission coefficient which represents the probability for electron transfer normalized to the number of times a complex achieves the correct configuration to pass through the transition state; and υ_N is the collisional frequency or vibrational frequency depending on whether the electron transfer is intermolecular or intramolecular.

Mechanistically, the donor and acceptor need to adopt nuclear (λ_{vib}) and solvent (λ_o) configurations such that the redox partners are isoenergtic. The electron then "hops" from the donor to the acceptor. This is required so that energy is conserved during the reaction.

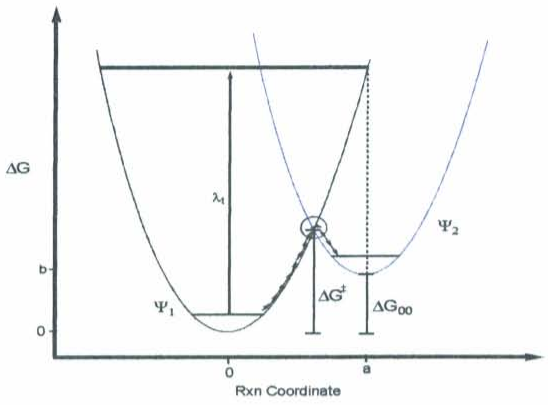

Figure 4.2.2.3.1. Thermodynamic parameters in adiabatic electron transfer.

The derivation of Marcus theory for electron transfer using intersecting parabolas is given in Appendix B. The more famous Marcus expressions for $\Delta G^{\ddagger}$ and k_{et} are shown below.[8-14]

$$\Delta G^{\ddagger} = \frac{(\Delta G_{00} + \lambda_t)^2}{4\lambda_t} \qquad eqn.\ 4.2.2.3.2.$$

$$k_{et} = \nu_N e^{-\frac{(\Delta G_{00} + \lambda_t)^2}{4\lambda_t RT}} \qquad eqn.\ 4.2.2.3.3.$$

Thermodynamically, the more negative the free energy for a process, the more energy is released, therefore the more exothermic and favoured the reaction. Thermodynamic intuition would suggest that the more exothermic a reaction, the greater the magnitude of the rate constant for electron transfer. The relationship between the rate constant for electron transfer and the driving force was predicted by Marcus. The dependence of k_{elt} and ΔG^{o} is illustrated in Figure 4.2.2.3.2 by noticing the change in the location of the transition state and $\Delta G^{\ddagger}$ as the exothermicity of the reaction is increased.

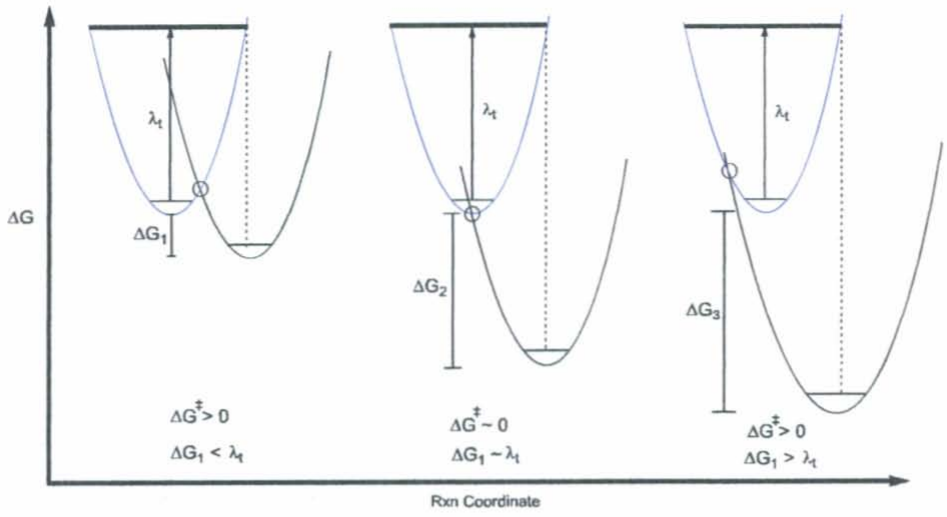

Figure 4.2.2.3.2. Diagram illustrating the effect of increasing the exothermicity of a reaction on the free energy of activation for a process. λ_t is constant.

A more familiar plot illustrating the effect on the rate constant for an increasingly exothermic process is shown in Figure 4.2.2.3.3 which clearly illustrates that at a certain point, the speed of a process decreases as the process becomes more exothermic. In addition, three distinct regions become apparent.

Region 1: The normal region where the rate constant, k_{elt}, increases as the process becomes more exothermic. This is due to the fact that $-\Delta G_{00} < \lambda_t$.

Region 2: The activationless region where the reaction proceeds without an energetic barrier. This is due to $-\Delta G_{00} = \lambda_t$ resulting in $k_{et} = \nu_N \kappa$.

Region 3: The Marcus inverted region where the electron transfer rate constant is attenuated with an increasing ΔG^{o}. This is due to the fact that $-\Delta G_{00} > \lambda_t$.

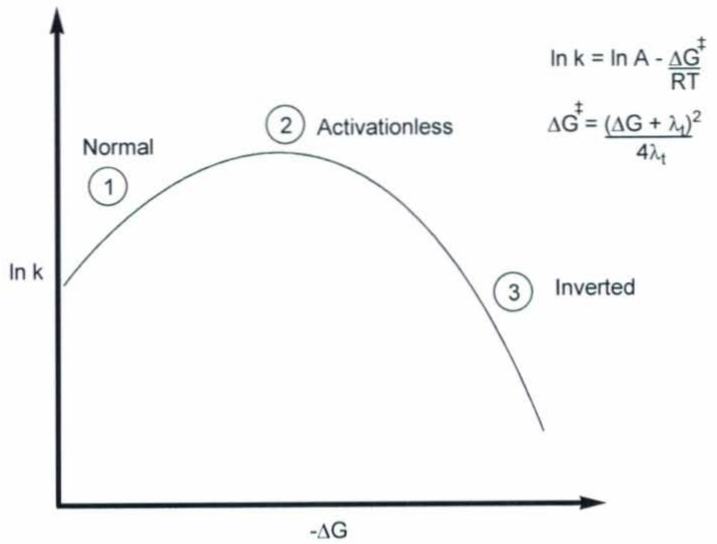

Figure 4.2.2.3.3. The effect of exothermicity on the rate constant for electron transfer.

At the same time Marcus theory was formulated, Hush developed a similar treatment for electron transfer.[6, 7] Although the formalisms of both Hush and Marcus were different, both theories result in the same expression as in equation 4.2.2.3.2 (this expression is commonly referred to as the Marcus-Hush equation). For the Marcus expressions, it was assumed that nuclei (from both the solvent and system) must rearrange before electron transfer occurs. As such, the distribution in electron density was assumed to not be in equilibrium with the nuclear configuration. In contrast, Hush assumed that the distribution of electron density would be in equilibrium with the nuclear coordinates and

that the electron density is partly delocalized between the donor and acceptor in response to the changes in nuclear coordinates. The main difference between each of these theories is that Marcus theory predicts an inverted region whereas the theory presented by Hush does not lead to inverted region behaviour as the electron density is assumed to be delocalized between the donor and acceptor.[6, 7] Marcus theory, however, is the accepted theory for electron transfer as a result of experiments presented by Miller[18, 26-28] which provided evidence for the existence of the inverted region. Combining Marcus and Hush formalisms extends Marcus theory into inner-sphere electron transfer processes.

4.2.2.4. Reorganization Energies

As introduced above, the reorganizational energy λ_t is divided into contributions from oscillations within the molecule (λ_i) and the solvent (λ_s).

$$\lambda_t = \lambda_i + \lambda_s \qquad eqn.\ 4.2.2.4.1.$$

The oscillations from within the molecule may be calculated using the vibrational force constants (f_i) associated with each of the molecular vibrations in both the reactant and product, and the corresponding bond length changes (Δd_o) within the electron donor and acceptor.

$$\lambda_i = \frac{1}{2}\sum f_i\left(\frac{\Delta d_o}{2}\right)^2 \qquad eqn.\ 4.2.2.4.1.$$

$$f_i = \frac{2 f_i^A f_i^B}{(f_i^A + f_i^B)} \qquad eqn.\ 4.2.2.4.2.$$

$$\Delta d_o = |d_i^A - d_i^B| \qquad eqn.\ 4.2.2.4.3.$$

The solvent reorganization energy, however, may be solved using dielectric continuum theory assuming a certain shape for the solvent cavity. The simplest assumption for the solvent cavity is that it is spherical with a donor and acceptor radii of a and b respectively, which lie at a center-to-center distance R at the transition state. By including the optical (ϵ_{op}) and static (ϵ_s) dielectric constants for the solvent, Marcus[9] showed that:

$$\lambda_s = (\Delta e)^2 \left(\frac{1}{2a} + \frac{1}{2b} - \frac{1}{R}\right)\left(\frac{1}{\epsilon_{op}} - \frac{1}{\epsilon_s}\right) \qquad eqn.\ 4.2.2.4.3.$$

Equation 4.2.2.3.3 in conjunction with equation 4.2.2.4.3 predicts that the rate of electron transfer will be dependent on the properties of the solvent and on the distance between the donor and the acceptor.

4.2.3. Semi-classical Theory

In the limit where $\Delta G^o < \lambda_t$ with $H_{DA} << \lambda_t$, the electron transfer may occur via a classical thermal barrier crossing. However, if H_{DA} is small, the electron transition in the activated complex may occur via quantum mechanical tunnelling and thermal activation. The correction required for quantum mechanical tunnelling is given by Γ in equation 4.2.3.1. ν_{nu} is the vibrational frequency and κ_{el} is the transmission coefficient for the event. Note that for tunnelling, the Born-Oppenheimer approximation is no longer valid, as electron and nuclear motion occur on the same timescale. Quantum mechanical tunnelling is illustrated in Figure 4.2.3.1.

$$k_{elt} = \nu_{nu}\kappa_{el}\Gamma e^{-\Delta G^{\ddagger}} \qquad eqn.\ 4.2.3.1.$$

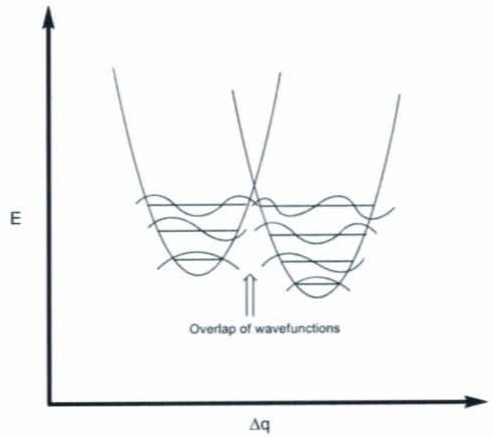

Figure 4.2.3.1. Quantum mechanical tunnelling in electron transfer.

4.2.3.1. The inverted region

Marcus theory predicts an inverse parabolic dependence of the electron transfer rate constant with the free energy change associated with the process. Experimentally, the plot in Figure 4.2.3.1.1 is observed.[18] The observed rate constant for electron transfer is greater than that predicted due to the quantum mechanical tunnelling effect discussed above.

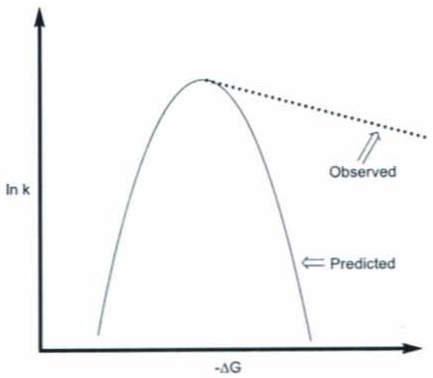

Figure 4.2.3.1.1. Inverted region behaviour.

4.2.4. Quantum Mechanical Theory

The quantum mechanical treatment of electron transfer begins with the Fermi Golden Rule formulation for the probability for a transition between states. In this treatment, the rate constant for electron transfer is expressed as the product of the electronic coupling matrix element V_{DA} (which represents the degree of electronic coupling) and the nuclear coordinates of the system and solvent (i.e. the Franck-Condon Weighted Density of States (FCWD)).

$$k_{et} = \frac{2\pi}{\hbar} V_{DA}^2 (FCWD) \qquad \textit{eqn. 4.2.4.1.}$$

Using this expression, the rate constant for electron transfer may be expressed in terms of the electronic coupling, the total reorganizational energy, and the free energy of reaction assuming the solvent behaves classically as follows:[10, 29]

$$k_{et} = \frac{2\pi}{\hbar} V_{DA}^2 \left(\frac{1}{4\pi\lambda_t RT}\right)^{\frac{1}{2}} e^{-\frac{(\Delta G^o + \lambda_t)^2}{4\lambda_t RT}} \qquad \textit{eqn. 4.2.4.2.}$$

Likewise, the rate constant for electron transfer may be expressed as that given in equation 4.2.4.3 which includes vibrational modes from the solvent. S is the Huang-Rhys factor or electron-vibrational coupling constant defined by equation 4.2.4.6 where S_j is the electron-vibrational coupling constant for the j^{th} vibrational mode. S_j is defined by equation 4.2.4.7 where M_j is the reduced mass and $\Delta Q_{e,j}$ is the change in equilibrium displacement between the ground and excited state potential energy surfaces.

$$k_{et} = \frac{2\pi}{\hbar} V_{DA}^2 \left(\frac{1}{\hbar\omega(|\Delta G^o| - \lambda_o)}\right)^{\frac{1}{2}} e^{-\left[S - \frac{\gamma(|\Delta G^o| - \lambda_o)}{\hbar\omega} + \frac{(\gamma+1)^2 \lambda_o k_B T}{\hbar\omega}\right]} \qquad \textit{eqn. 4.2.4.3.}$$

$$\gamma = \ln\left[\frac{|\Delta G^{o}|-\lambda_{o}}{S\hbar\omega}\right] - 1 \qquad \textit{eqn. 4.2.4.4.}$$

$$\hbar\omega = \frac{\sum_{j} S_{j}\hbar\omega_{j}}{\sum_{j} S_{j}} \qquad \textit{eqn. 4.2.4.5.}$$

$$S = \sum_{j} S_{j} \qquad \textit{eqn. 4.2.4.6.}$$

$$S_{j} = \frac{1}{2}\left(\frac{M_{j}}{\hbar}\right)\left(\Delta Q_{e,j}\right)^{2} \qquad \textit{eqn. 4.2.4.7.}$$

As illustrated in equation 4.2.2.4.3, the rate for electron transfer decreases as the distance between the donor and acceptor increases for a bimolecular electron transfer process. However, how about in covalently-linked donor-acceptor complexes? As illustrated in equations 4.2.4.2 and 4.2.4.3, the rate of electron transfer is explicitly dependent on the electronic coupling matrix element V_{DA}. As the amplitudes of wavefunctions decrease with increasing distance, then the coupling between the donor and acceptor wavefunctions decreases with increasing distance. As such, the electronic coupling between the donor and acceptor may be geometrically modulated as given below by the empirical expression for the distance dependence on the electronic coupling where V_{DA}^{o} is the electronic coupling at the optimal donor-acceptor distance r_o, and r is the distance between the donor and acceptor.[29]

$$V_{DA}^{2} = (V_{DA}^{o})^{2} e^{-\alpha(r-r_{o})} \qquad \textit{eqn. 4.2.4.7.}$$

4.2.5. Electron Transfer and Electronic Coupling

The classical and quantum mechanical theories of electron transfer have been presented in the previous section. Here, we consider the concepts relevant to the potential energy surfaces for the electron donor and acceptor which are characterized as a function of the electronic coupling. Potential energy surfaces are initially derived for a general and unsymmetrical ($\Delta G_{00} \neq 0$) two-state electron transfer system in which there is a net free energy change accompanying electron transfer between an initial state and final state (or a ground and excited state). Using this general expression, potential energy surfaces are defined for a symmetrical ($\Delta G_{00}=0$) system. Through these surfaces, activation energies are defined and the rate constant for electron transfer is reformulated to include electronic coupling. Electron transfer systems are then classified as class I, class II, and class III depending on the strength of the electronic coupling between the donor and acceptor.

4.2.5.1. Potential Energy Surfaces

For a detailed derivation of potential energy surfaces, see appendix C. The energy functions for two adiabatic states (i.e. the ground and excited state) are given below.[30, 31]

$$G_{g.s.} = \frac{1}{2}\left\{(G_{bb} + G_{aa}) - [(G_{bb} - G_{aa})^2 + 4H_{ab}^2]^{\frac{1}{2}}\right\} \qquad \textit{eqn. 4.2.5.1.3.}$$

$$G_{e.s.} = \frac{1}{2}\left\{(G_{bb} + G_{aa}) + [(G_{bb} - G_{aa})^2 + 4H_{ab}^2]^{\frac{1}{2}}\right\} \qquad \textit{eqn. 4.2.5.1.4.}$$

where G_{bb} is the free energy associated with the electron transfer products and G_{aa} is the free energy associated with the encounter complex. H_{ab} is the electron transfer coupling matrix element which arises from mixing reactant and product diabatic states.

In a more workable form, the free energy surfaces for the ground and excited states are equated below where $\lambda = \frac{1}{2} f d^2$ and the reduced coordinate $X = \frac{x}{d}$.[30, 31].

$$G_{g.s} = \frac{1}{2}(\Delta G_{00} + \lambda[2X^2 - 2X + 1]) - \frac{1}{2}\left\{[(\Delta G_{00} + \lambda[2X - 1])^2 + 4H_{ab}^2]^{\frac{1}{2}}\right\} \quad eqn.\ 4.2.5.1.5.$$

$$G_{e.s} = \frac{1}{2}(\Delta G_{00} + \lambda[2X^2 - 2X + 1]) + \frac{1}{2}\left\{[(\Delta G_{00} + \lambda[2X - 1])^2 + 4H_{ab}^2]^{\frac{1}{2}}\right\} \quad eqn.\ 4.2.5.1.6.$$

The equations derived above for the free energies for a two-state system consisting of a ground and excited state can be applied to both unsymmetrical ($\Delta G_{00} \neq 0$) and symmetrical ($\Delta G_{00} = 0$) systems. For a symmetrical system, the free energy surfaces are given below. For simplicity, the remaining discussion will focus on symmetrical systems only.

$$G_{g.s} = \frac{1}{2}(\lambda[2X^2 - 2X + 1]) - \frac{1}{2}\left\{[(\lambda[2X - 1])^2 + 4H_{ab}^2]^{\frac{1}{2}}\right\} \quad eqn.\ 4.2.5.1.7.$$

$$G_{e.s} = \frac{1}{2}(\lambda[2X^2 - 2X + 1]) + \frac{1}{2}\left\{[(\lambda[2X - 1])^2 + 4H_{ab}^2]^{\frac{1}{2}}\right\} \quad eqn.\ 4.2.5.1.8.$$

For a symmetrical system, the point of intersection for each of the diabatic curves occur at X=1/2 (x=a/2). At this reduced coordinate,

$$G_{g.s}(X = \tfrac{1}{2}) = \frac{\lambda}{4} - H_{ab} \quad eqn.\ 4.2.5.1.9.$$

$$G_{e.s}\left(X = \tfrac{1}{2}\right) = \frac{\lambda}{4} + H_{ab} \quad eqn.\ 4.2.5.1.10.$$

As a result of electronic coupling between diabatic states, the splitting at the intersection between curves is $2H_{ab}$. As discussed in the previous section on Marcus theory, the energy at the point of intersection is the activation energy. This energy is

derived below for a symmetrical system with the incorporation of electronic coupling between states. In deriving this equation, the energy minima are corrected for electronic coupling. The rate constant for electron transfer is also given for a symmetrical system when coupling is accounted for. Figure 4.2.5.1.1 illustrates electronically coupled surfaces for a symmetrical system.

$$\Delta G^{\ddagger} = \frac{(\lambda - 2H_{ab})^2}{4\lambda} \qquad \textit{eqn. 4.2.5.1.11.}$$

$$k_{et} = \frac{2\pi}{\hbar} H_{ab}^2 \left(\frac{1}{4\pi\lambda RT}\right)^{\frac{1}{2}} e^{\frac{-(\lambda - 2H_{ab})^2}{4\lambda RT}} \qquad \textit{eqn. 4.2.5.1.12.}$$

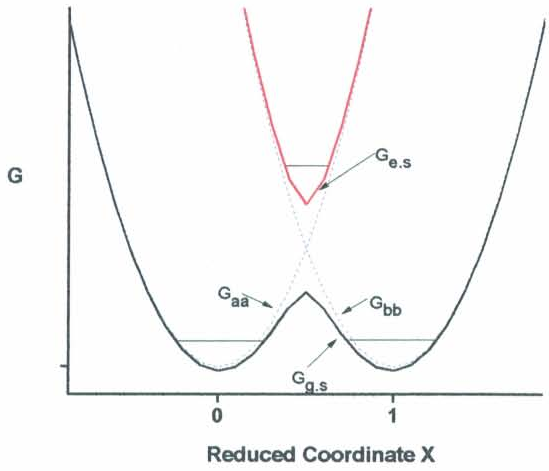

Figure 4.2.5.1.1. Potential energy surface for an electronically coupled symmetrical [D,A] electron transfer system.

A similar expression for the activation energy in an unsymmetrical electron transfer system can be defined as that given below.[17] For simplicity, the expression is given. A detailed derivation is provided elsewhere.[17]

$$\Delta G^{*}_{unsymm} = \frac{\lambda}{4} - H_{ab} + \frac{H^2_{ab}}{(\lambda+\Delta G_{00})} + \frac{\Delta G^2_{00}}{4(\lambda-2H_{ab})} + \frac{\Delta G_{00}}{2} - \frac{H^4_{ab}\Delta G_{00}}{(\lambda+\Delta G_{00})^4} \quad \textit{eqn. 4.2.5.1.13.}$$

Substitution of this equation into the Arrhenius equation with $A=\frac{2\pi}{\hbar} H^2_{ab}(\frac{1}{4\pi\lambda RT})^{\frac{1}{2}}$ yields the rate constant for electron transfer which includes ΔG_{00}, λ, and H_{ab} dependencies.

4.2.5.2. Classification of electron transfer systems

As discussed above, electronic coupling between the diabatic states associated with electron transfer reactants and products results in two adiabatic states in which one adiabatic state is lower in energy than the other. At the point of intersection between diabatic states, electronic coupling results in an energy splitting of $2H_{ab}$. Thus, the greater the coupling between the diabatic states, the greater the energy difference between adiabatic states, and the lower the activation energy for electron transfer. With this trend in mind, three classes of electron transfer systems may be distinguished depending on the magnitude of the electronic coupling between the donor and acceptor: these are class I, class II, and class III.[17, 30, 31] These classes have been described for mixed-valence complexes; however, the general methodology behind defining each class remains the same, irrespective of the type of chemical system.

In class I systems, H_{ab}~0 and the potential energy surface representing the electron transfer process resembles those of the diabatic states (i.e. the properties of class I systems resembles those of the separate states).[17, 30, 31] In class II systems, however, $0<2H_{ab}<\lambda$.[17, 30, 31] In these systems, new and unique properties are expressed which are in addition to the properties of the separate diabatic states. As a result of the degree of electronic coupling in class II systems, they are considered as valence-trapped or charge-

localized systems and are adequately described by a double-well potential energy surface or adiabatic state.[17, 30, 31] For class III systems, $2H_{ab}>\lambda$, and the interaction between the donor and acceptor diabatic states has become so significant that the ground state exhibits a single potential energy minimum.[17, 30, 31] As such, class III systems are considered as charge-delocalized and no barrier exists for thermal electron transfer.[17, 30, 31] Figure 4.2.5.2.1 provides an illustration of the potential energy surfaces for each class in a symmetrical system. In addition to this classification scheme, additional electron transfer classes are possible such as class II-III systems (i.e. the Creutz-Taube ion). This class will not be discussed here and information can be obtained elsewhere.[17, 30, 31]

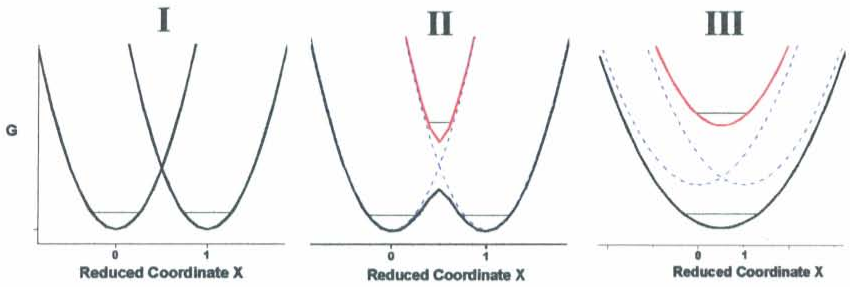

Figure 4.2.5.2.1. Potential energy surfaces for a class I, II, and III electron transfer complex in a symmetrical system.

4.2.6. Excited State Charge-Transfer

In addition to thermal electron transfer discussed in the previous sections, electron transfer between a donor and acceptor can also be activated optically.[31] As opposed to electron transfer being dictated by the transition state structure, through the interaction of a donor-acceptor system with light, electron density is allowed to be globally

redistributed within the boundaries of the complex to form the electronic structure of the electron transfer products prior to nuclear rearrangement. The parameters and terminology presented previously for thermal electron transfer are the same for optical electron transfer. However, the difference between the two lies in the energy source: light versus heat.

4.2.6.1. Radiative electron transfer

A schematic representing radiative electron transfer is given in Scheme 4.2.6.1.1. For radiative electron transfer, a precursor complex is formed through which electron transfer occurs.

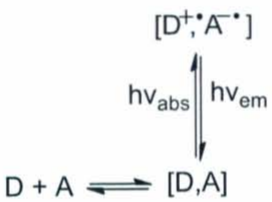

Scheme 4.2.6.1.1. Radiative electron transfer.

As expressed in equation 4.2.6.1.1, single photon absorption is governed by the transition dipole moment ($\vec{M}$) and the intensity of the electric field ($W(\nu)$).[30]

$$w(\nu) = \frac{2\pi}{3h^2\eta^2}\left|\vec{M}\right|^2 W(\nu) \qquad \textit{eqn. 4.2.6.1.1.}$$

The transition dipole moment is given by equation 4.2.5.1.2. The transition dipole $\vec{\mu}$ is given by equation 4.2.6.1.3 where $e\sum\vec{r}$ is the dipole operator and Ψ_{el} is the electronic wavefunction which contains spin.[30]

$$\vec{M} = \vec{\mu} < \Psi^{es}_{vib} | \Psi^{gs}_{vib} > \qquad \textit{eqn. 4.2.6.1.2.}$$

$$\vec{\mu} = < \Psi_{el}^{es} | e \sum \vec{r} | \Psi_{el}^{gs} > \qquad \textit{eqn. 4.2.6.1.3}$$

The integrated band intensity for a radiative transition is given by equation 4.2.6.1.4.[30]

$$\int \epsilon(\nu) d\nu = \frac{4\pi^2 N_A \nu}{3000 c \eta \hbar \ln 10} \left|\vec{M}\right|^2 \qquad \textit{eqn. 4.2.6.1.4.}$$

Likewise, for emission,[30]

$$k_r = 8\pi\hbar c\eta^3 (E_{em}^3) B \qquad \textit{eqn. 4.2.6.1.5.}$$

where the Einstein parameter B is given in equation 4.2.6.1.6.[30]

$$B = \frac{8\pi^3}{3\hbar^2 c} \left|\vec{M}\right|^2 \qquad \textit{eqn. 4.2.6.1.5.}$$

4.2.6.2. Non-radiative decay

In addition to the radiative decay expressed in equation 4.2.6.1.4, an excited state may also decay non-radiatively. For non-radiative decay, the electronic energy of the excited state is funnelled into vibrational and solvent modes in the ground state. This relaxation process is induced by promoting vibrational modes in the excited state which serve to perturb the electron density in the state. This perturbation effectively mixes vibrational wavefunctions associated with excited state promoting modes and ground state accepting modes. The net result is that the excess energy of the excited state is channelled into the solvent and the vibrational structure in the ground state. This excess energy is ultimately dissipated in the form of heat. For this type of decay, the Born-Oppenheimer approximation is no longer valid. Non-radiative decay is illustrated in Figure 4.2.6.2.1.

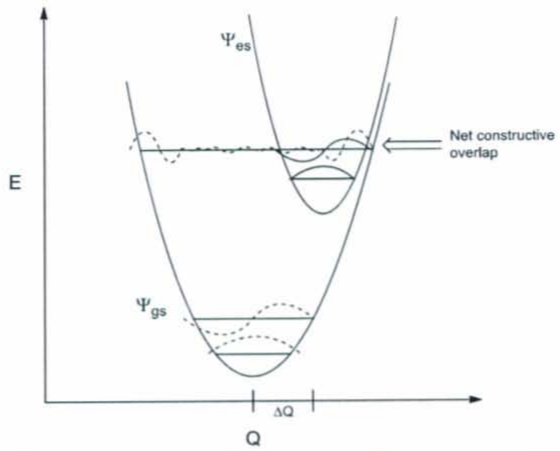

Figure 4.2.6.2.1. Potential energy surfaces illustrating non-radiative decay. Q is the coordinate system which includes both solvent and system coordinates.

Using energy gap law, the rate constant for non-radiative decay is given by equation 4.2.6.2.1 where V_k is the vibrationally-induced electronic coupling matrix element which arises from the effect of mixing the excited and ground state wavefunctions by select vibrations.[32, 33] $\hbar\omega$ is the average quantum spacing in the ground and excited states and S is the Huang-Rhys factor which reflects the degree of distortion (i.e. ΔQ) associated with the ground and excited state potential energy surfaces. γ is given by equation 4.2.6.2.2.

$$k_{nr} = \left(\frac{2\pi}{\hbar^3 E_0}\right)^{\frac{1}{2}} V_k^2 e^{-\left[S+\frac{\gamma E_0}{\hbar\omega}-\left(\frac{\gamma+1}{\hbar\omega}\right)^2 \lambda_0 k_B T\right]} \qquad \textit{eqn. 4.2.6.2.1.}$$

$$\gamma = \ln\left[\frac{E_0}{S\hbar\omega}\right] - 1 \qquad \textit{eqn. 4.2.6.2.2.}$$

4.2.6.3. Classifying excited state electron transfer systems

In general, for class I symmetrical and unsymmetrical systems, the optical energy for charge-transfer is given by the equation below. Optical energies for class I symmetrical and unsymmetrical systems are shown in Figure 4.2.6.3.1.

$$\nu = \lambda_t \text{ (Symmetrical system)} \qquad \textit{eqn. 4.2.6.3.1.}$$

$$\nu = \lambda_t + \Delta G_{00} \text{(Unsymmetrical system)} \qquad \textit{eqn. 4.2.6.3.2.}$$

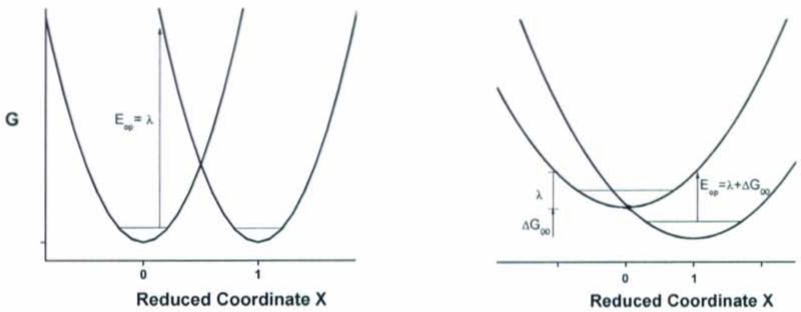

Figure 4.2.6.3.1. Potential energy surfaces and optical energies for a class I symmetrical (left) and unsymmetrical (right) system.

For class II (charge-localized) systems, the expression for the optical energy associated with charge transfer for a symmetric system is equivalent to that for a symmetrical class I system. Although electronic coupling results in a lowering of the energies of the diabatic states, there is no net effect for a symmetrical system as both reactant and product curves are lowered. However, the situation is different for an unsymmetrical system as both surfaces are offset. Therefore reactant and product curves are affected to a different degree by electronic coupling. As such, the optical energy for

charge transfer in a class II unsymmetrical system is given below.[17] Class II potential energy surfaces are illustrated in Figure 4.2.6.3.2.

$$\nu = (\lambda + \Delta G_{00})\left[1 + \frac{2H_{ab}^2 \Delta G_{00}}{(\lambda+\Delta G_{00})^3} + \frac{2H_{ab}^4 \Delta G_{00}(3\lambda-\Delta G_{00})}{(\lambda+\Delta G_{00})^6}\right] \qquad \textit{eqn. 4.2.6.3.3.}$$

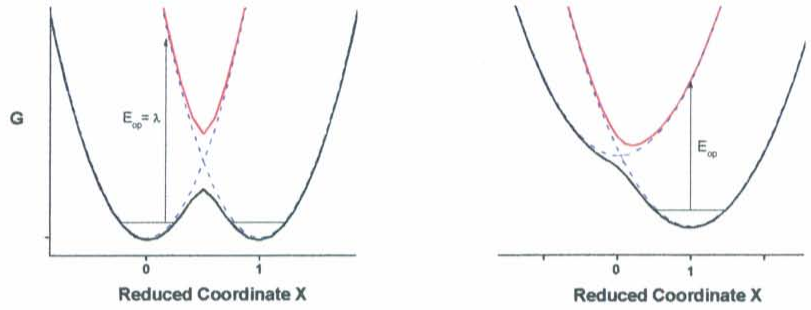

Figure 4.2.6.3.2. Potential energy surfaces and optical energies for symmetrical and unsymmetrical class II systems.

Optical transitions in a class III (delocalized) system, however, are directly related to the electronic coupling as given below for both symmetrical and unsymmetrical systems.[17] The class III systems are illustrated in Figure 4.2.6.3.3.

$$\nu = 2\mathrm{H_{ab}} \text{ (symmetrical)} \qquad \textit{eqn. 4.2.6.3.4.}$$

$$\nu = \Delta G_{00} + 2H_{ab} \text{ (unsymmetrical)} \qquad \textit{eqn. 4.2.6.3.5.}$$

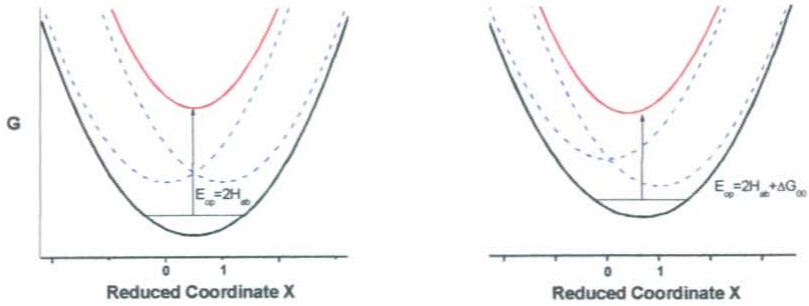

Figure 4.2.6.3.3. Potential energy surfaces and optical energies for symmetrical and unsymmetrical class III systems.

To calculate the electronic coupling element H_{ab} for class II and class III systems, the Mulliken-Hush equation can be applied in which H_{ab} is directly related to the optical charge transfer absorption profile.[17, 30, 31]

$$H_{ab}(cm^{-1}) = \left[\frac{(4.2\times10^{-4})E_{ct}\int\epsilon(\nu)d\nu}{r_{ab}{}^2}\right]^{\frac{1}{2}} \approx \left[\frac{(4.2\times10^{-4})E_{ct}(\epsilon_{max}\Delta\nu_{\frac{1}{2}})}{r_{ab}{}^2}\right]^{\frac{1}{2}} \quad \textit{eqn. 4.2.6.3.6.}$$

Therefore, by analysis of the optical charge-transfer absorption profiles, the electronic coupling element can be estimated and the electron transfer class may then be determined.

4.3. Conclusion

In this chapter, the electron transfer formalisms proposed by Mulliken and Marcus have been presented, along with the mechanisms proposed by Taube. Potential energy surfaces for a two-state electron transfer system were constructed in which the parameters ΔG_{00}, λ_t, and H_{ab} were defined. Using these parameters, optical electron transfer in

symmetrical ($\Delta G_{00} = 0$) and unsymmetrical (($\Delta G_{00} \neq 0$) systems were classified as class I, II, and III depending on the value of H_{ab} relative to that of λ_t; much akin to the nomenclature used in classifying mixed-valence complexes.

4.4. References

[1] V. Balzani, A. Credi and M. Venturi, *ChemSusChem* **2008**, *1*, 26.

[2] R. E. Blankenship, *Molecular Mechanisms of Photosynthesis*, Blackwell Science, Oxford, **2002**.

[3] M. R. Wasielewski, *J. Org. Chem.* **2006**, *71*, 5051.

[4] D. Voet, J. G. Voet and C. W. Pratt, *Fundamentals of Biochemistry*, Rev. ed., Wiley, **2002**.

[5] R. S. Mulliken, *Journal of the American Chemical Society* **1952**, *74*, 811.

[6] N. S. Hush, *Transactions of the Faraday Society* **1961**, *57*, 557.

[7] N. S. Hush, *The Journal of Chemical Physics* **1958**, *28*, 962.

[8] R. A. Marcus, *The Journal of Chemical Physics* **1957**, *26*, 867.

[9] R. A. Marcus, *Angewandte Chemie International Edition in English* **1993**, *32*, 1111.

[10] R. A. Marcus, *The Journal of Chemical Physics* **1956**, *24*, 966.

[11] R. A. Marcus, *The Journal of Chemical Physics* **1957**, *26*, 872.

[12] R. A. Marcus, *Discussions of the Faraday Society* **1960**, *29*, 21.

[13] R. A. Marcus, *The Journal of Physical Chemistry* **1963**, *67*, 853.

[14] R. A. Marcus, *The Journal of Chemical Physics* **1965**, *43*, 679.

[15] H. Taube, H. Myers and R. L. Rich, *Journal of the American Chemical Society* **1953**, *75*, 4118.

[16] S. V. Rosokha and J. K. Kochi, *Accounts of Chemical Research* **2008**, *41*, 641.

[17] B. S. Brunschwig and N. Sutin, *Coordination Chemistry Reviews* **1999**, *187*, 233.

[18] G. L. Closs and J. R. Miller, *Science* **1988**, *240*, 440.

[19] M. B. Robin, P. Day, H. J. Emeléus and A. G. Sharpe, in *Advances in Inorganic Chemistry, Vol. Volume 10*, Academic Press, **1968**, pp. 247.

[20] J. Jortner, *The Journal of Chemical Physics* **1976**, *64*, 4860.

[21] M. Bixon and J. Jortner, *The Journal of Chemical Physics* **1968**, *48*, 715.

[22] H. Taube, *Nobel Lecture* **1983**.

[23] H. A. Benesi and J. H. Hildebrand, *Journal of the American Chemical Society* **1949**, *71*, 2703.

[24] H. A. Benesi and J. H. Hildebrand, *Journal of the American Chemical Society* **1948**, *70*, 2832.

[25] V. Balzani, *Electron Transfer in Chemistry, Vol. 1*, Wiley VCH, **2001**.

[26] J. V. Beitz and J. R. Miller, *The Journal of Chemical Physics* **1979**, *71*, 4579.

[27] J. R. Miller and J. V. Beitz, *The Journal of Chemical Physics* **1981**, *74*, 6746.

[28] J. R. Miller, L. T. Calcaterra and G. L. Closs, *Journal of the American Chemical Society* **1984**, *106*, 3047.

[29] M. R. Wasielewski, *Chem. Rev.* **1992**, 435.

[30] K. D. Demadis, C. M. Hartshorn and T. J. Meyer, *Chemical Reviews* **2001**, *101*, 2655.

[31] B. S. Brunschwig, C. Creutz and N. Sutin, *Chemical Society Reviews* **2002**, *31*, 168.

[32] G. F. Strouse, J. R. Schoonover, R. Duesing, S. Boyde, W. E. Jones, Jr. and T. J. Meyer, *Inorganic Chemistry* **1995**, *34*, 473.

[33] P. Chen and T. J. Meyer, *Chemical Reviews* **1998**, *98*, 1439.

Chapter 5:

"Ground and Excited States in the [3X3] $Zn(II)_9$ Grid-Type Complex"

Abstract: The purpose of this chapter is to develop an understanding of the ligand excited states in [3x3] grid-type complexes. These states will be shown to involve excited state electron transfer. With the electron transfer formalisms presented in the previous chapter, the ligand-based excited states of [3x3] Zn_9^{II} grid-type complexes will be classified. 1D ^{1}H-NMR, 2D correlated NMR, variable-temperature ^{1}H-NMR, and crystal structural data will initially be presented to formalize insights into the grid ground-state structure. Excited state data will then be presented and discussed.

5.1. Introduction

The structure of the [3x3] grid-type complex $[Zn(II)_9(2POAP\text{-}2H)_6]^{6+}$ is given in Figure 5.1.1. This structure may be subdivided into two distinct substructures: the metal core and the ligand framework.

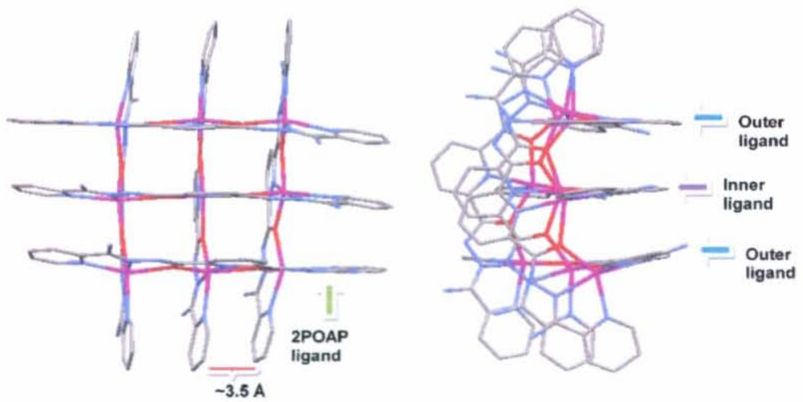

Figure 5.1.1. Structure of the [3x3] grid-type complex $[Zn(II)_9(2POAP\text{-}2H)_6]^{6+}$. The data were obtained from the CIF file attached with references [1, 2].

In $[Zn(II)_9(2POAP\text{-}2H)_6]^{6+}$, the metal core consists of 9 metal centers arranged in a flat grid-like motif; each separated by a distance of ~4 Å (when $M=Zn^{II}$) and connected through an oxide bridge. As a consequence of this structural motif, the core may be considered to contain three types of metal centers: the four corner metal atoms (α), the 4 periphery central metal atoms (β), and the central metal atom at the core (γ). A structural representation of the metal core is given in Figure 5.1.2.

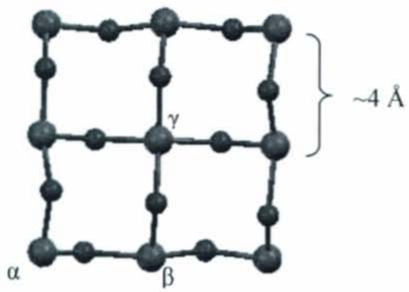

Figure 5.1.2. Structure of the metal core for a [3x3] $[Zn_9^{II}(2POAP\text{-}2H)_6]^{6+}$ grid-type complex. The data were obtained from the CIF file attached with references [1, 2].

For the ligand structure in $[Zn(II)_9(2POAP\text{-}2H)_6]^{6+}$, ligands are arranged in a π-stacked fashion whereby each side of the grid consists of 3 ligands stacked in a face-to-face manner separated by a distance of ~3.5 Å. As 3 ligands constitute each side of the complex, [3x3] grids (and larger) contain chemically inequivalent ligands inherent to their 3D structure such that the ligand framework consists of inner and outer ligands. In addition, in the grid-type complexes of Zn(II), Mn(II), and Mn(II)/Mn(III) studied in this thesis, the coordinated 2POAP ligand exhibits exposed NH_2 groups. As is demonstrated later in this chapter, these exposed groups allow for the presence of unique dynamic and

optical properties. In Chapter 8, these exposed groups are exploited to form higher-order supramolecular adducts.

5.2. Results and Discussion

5.2.1. 1D and 2D NMR

For the [3x3] grid-type complexes studied, the $[Zn(II)_9(2POAP\text{-}2H)_6]^{6+}$ was the only complex that was NMR active as Zn^{II} ions are closed-shell d^{10} systems that are diamagnetic. As such, this complex offers a unique opportunity to explore the properties associated with the ligand framework. NMR data on this complex is presented below. NMR data for this complex has not been previously reported and is therefore thoroughly discussed.

The ^{1}H-NMR spectrum of $[Zn(II)_9(2POAP\text{-}2H)_6]^{6+}$ and its associated ligand in d_3-acetonitrile are given in Figure 5.2.1.1. The absence of an OH resonance at 11.1 ppm on formation of the grid is consistent with the loss of the hydroxyl protons. The chemical shifts associated with the ligand protons on coordination with Zn(II) is in agreement with the expectations for metal coordination. As all proton peaks for $[Zn(II)_9(2POAP\text{-}2H)_6]^{6+}$ were located in the aromatic region, this suggests that the ligands in $[Zn(II)_9(2POAP\text{-}2H)_6]^{6+}$ are composed of aromatic groups. However, of interest is the presence of an approximately two-fold number of proton peaks for the Zn grid relative to that of the uncoordinated ligand. This two-fold number of peaks is assigned to the presence of chemically inequivalent ligands within the grid-like architecture, and is attributed to the presence of exterior and interior ligand environments. This is as expected given the crystal structure presented in the introductory section of this chapter when one considers

the symmetry associated with the arrangement of ligands in the complex. However, this NMR data confirms the presence of chemically inequivalent ligands from both a nuclear and electronic perspective. The notion of chemically inequivalent ligands in inner and outer environments has also been observed with other grid-like arrays.[3] The assignment of peaks as originating from inner and outer ligands was based on peak integration of the NMR signals. This peak integration yields an even number of peaks with integrals which are double that of other peaks (Table 5.2.1.1). These peaks have been attributed to signals resulting from the outer ligand given that there is a 2:1 ratio between outer and inner ligands.

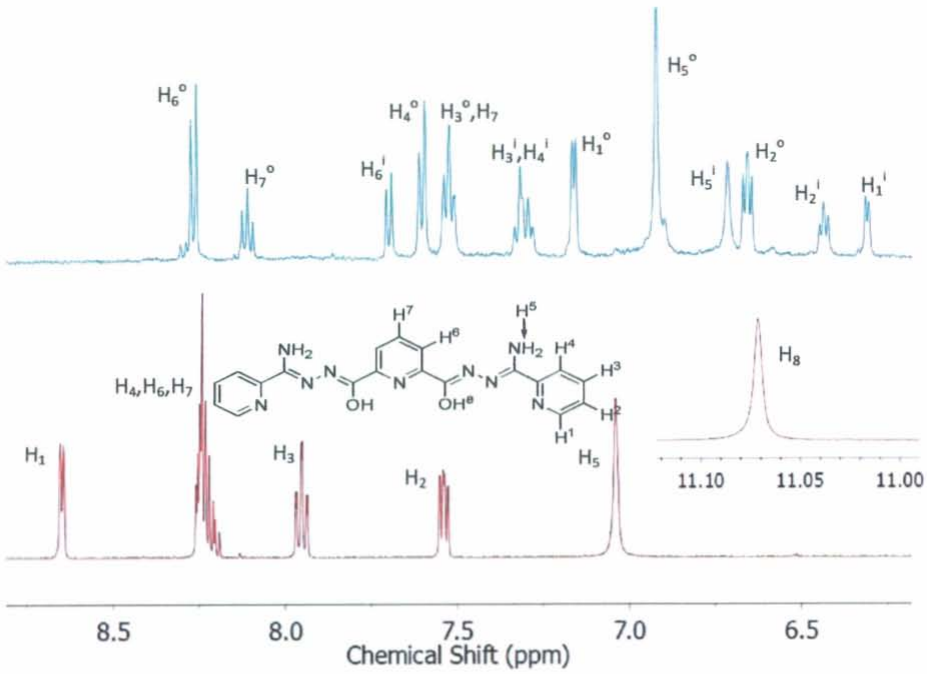

Figure 5.2.1.1. ^{1}H-NMR spectra of $[Zn_9(2POAP\text{-}2H)_6]^{6+}$ (top) with its uncoordinated 2POAP ligand (bottom) in d_3-acetonitrile. The superscripts i and o refer to inner and outer ligands.

In order to correctly assign the proton peaks presented in Figure 5.2.1.1, 2D NMR data were collected and are presented in Figure 5.2.1.2 and Figure 5.2.1.3. The overall method employed for peak identification (as used in Chapter 3 for the uncoordinated ligand) was to first use (^{1}H-^{13}C) COSY data presented in Figure 5.2.1.2 to determine which peaks originate from C-H bonds. After C-H peaks were identified, (^{1}H-^{1}H) COSY data presented in Figure 5.2.1.3 were used to determine which protons were adjacent to one another.

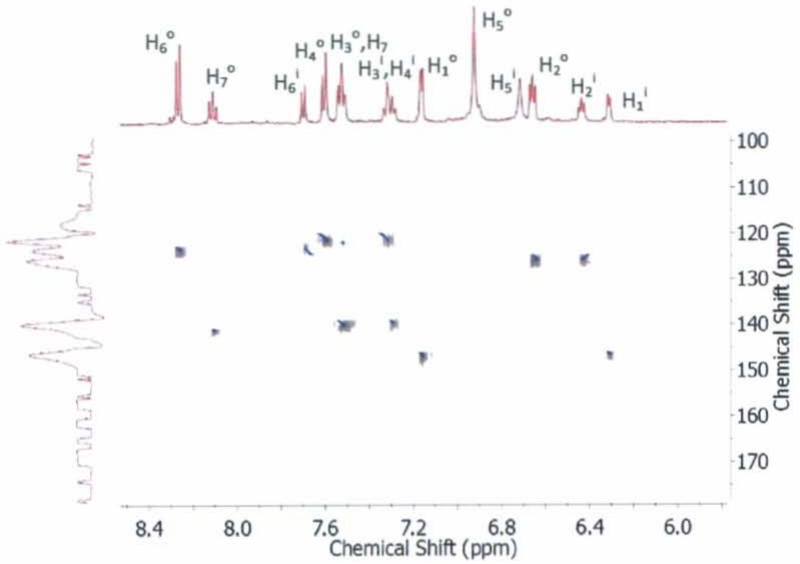

Figure 5.2.1.2. (^{1}H-^{13}C) COSY data for $[Zn_9(2POAP\text{-}2H)_6]^{6+}$ in d_3-acetonitrile.

(^{1}H-^{13}C) COSY data presented in Figure 5.2.1.2 suggests that all peaks are attributable to protons involved in a C-H bonding interaction with the exception of both the H_5^i and H_5° peaks. Therefore, these H_5^i and H_5° peaks may be attributed to NH_2 groups located on the inner and outer ligands, respectively. Since integration of these

peaks results in a value of 8 for H_5^i and 16 for H_5^o, H_5^i is assigned to the NH_2 groups on the inner ligand and H_5^o is assigned to the NH_2 groups on the outer ligand. In addition, the triplet present at 7.53 ppm and multiplet at 7.31 ppm exhibits two (^1H-^{13}C) COSY peaks which is consistent with the presence of two different C-H environments within each of these chemical shifts.

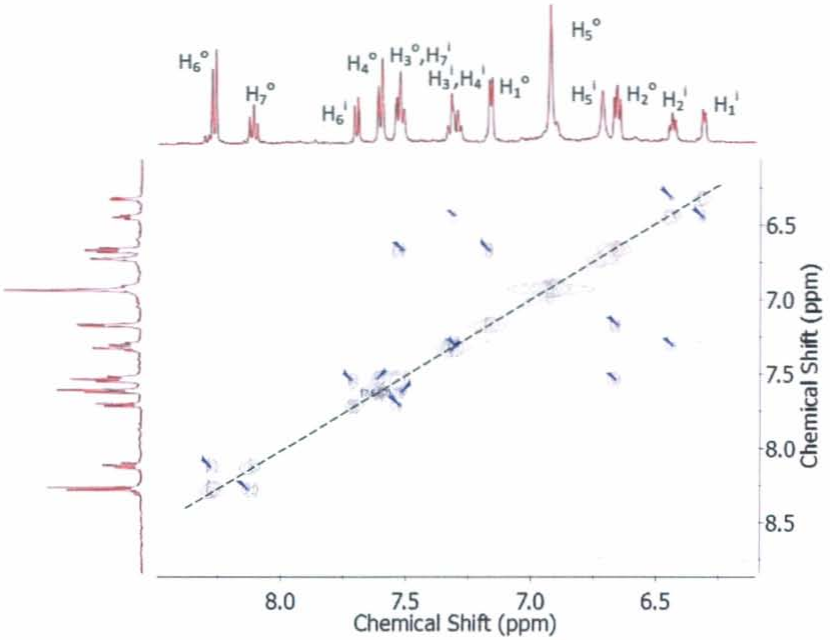

Figure 5.2.1.3. (^1H-^1H) COSY data for $[Zn_9(2POAP\text{-}2H)_6]^{6+}$ in d_3-acetonitrile.

(^1H-^1H) COSY data presented in Figure 5.2.1.3 suggests that both H_5^i and H_5^o protons are not coupled to any of the peaks present. Therefore, these protons are not adjacent to any of the other protons present in the coordinated 2POAP structure. This is consistent with assigning these peaks to NH_2 groups located on the inner and outer ligands. What is apparent from the (^1H-^1H) COSY data and the data listed in Table 5.2.1.1

is that of the peaks which have lower integral values (designated with a superscript i), peak H_1^i is coupled to peak H_2^i, which in turn is coupled to H_3^i. A proton contained in the multiplet assigned as H_4^i is coupled to H_3^i given the (^1H-^{13}C) COSY data discussed above which suggests that this peak is the result of two overlaying C-H signals. In addition to the above coupled peaks, the data also indicates that proton H_6^i is only coupled to H_7^i which in turn is only also coupled to H_6^i. As the coupling constant for H_1^i is about the same as that for H_2^i (Table 5.2.1.1), H_1^i is coupled to H_2^i. Moreover, since the coupling constant for H_6^i is about the same as that for H_7^i, H_6^i is coupled to H_7^i. Therefore, the assignment of the inner peaks in Figure 5.2.1.1 is justified.

The assignment of peaks associated with the outer ligands follows this same approach. The (^1H-^1H) COSY data and the data listed in Table 5.2.1.1 suggest that of the peaks which have upper integral values (designated with a superscript o), peak H_1^o is coupled to peak H_2^o, which in turn is coupled to H_3^o. Moreover, this peak is coupled to H_4^o. In addition to the above coupled peaks, the data also indicates that proton H_6^o is only coupled to H_7^o which in turn is only coupled to H_6^o. Since the coupling constant for H_1^o is about the same as that for H_2^o (Table 5.2.1.1), H_1^o is coupled to H_2^o. Moreover, since the coupling constant for H_6^o is about the same as that for H_7^o, H_6^o is coupled to H_7^o. Likewise comparisons of coupling constants may also be made from the data listed in Table 5.2.1.1. Therefore, the assignment of the outer peaks in Figure 5.2.1.1 is also justified.

Table 5.2.1.1. NMR parameters for $[Zn(II)_9(2POAP\text{-}2H)_6]^{6+}$ in d_3-acetonitrile.

Peak[a]	*Chemical Shift (ppm)*	*Multiplicity*	*J*[d]	*Integral*[a]
H_1^i	6.32	Doublet	5.0	4
H_2^i	6.44	Triplet	5.5	4
H_3^i	7.30	Triplet	6.5	4
H_4^i	7.32	Doublet	7.5	4
H_5^i	6.72	Singlet	-	8
H_6^i	7.69	Doublet	7.5	4
H_7^i	7.53[b]	Triplet	7.5	2[c]
H_1^o	7.17	Doublet	4.5	8
H_2^o	6.66	Triplet	5.5	8
H_3^o	7.53[b]	Triplet	7.5	8[c]
H_4^o	7.60	Doublet	8.0	8
H_5^o	6.93	Singlet	-	16
H_6^o	8.26	Doublet	7.5	8
H_7^o	8.11	Triplet	8.0	4

[a] There are 2 inner ligands (i) and 4 outer ligands (o) in the complex. [b] These peaks have protons in the same environment but are due to different protons, as given by (C, H)-correlated NMR data previously). [c] The actual integral for this peak is 5. The integral values have been separated to reflect the two convoluted NMR signals for this peak. [d] Coupling Constant.

5.2.2. Temperature dependent ^{1}H-NMR

Temperature dependent ^{1}H-NMR data for $[Zn(II)_9(2POAP\text{-}2H)_6]^{6+}$ are given in Figure 5.2.2.2 and Table 5.2.2.1. For this complex, the inner and outer NH_2 groups appear to exhibit exchange broadening. As the temperature is varied, the NH_2 groups appear to become broadened and shift upfield. It is to be expected that both the inner and outer NH_2 protons will exhibit exchange between two chemically inequivalent conformers, with one conformer corresponding to the protons in-plane with the ligand, and the other conformer corresponding to protons out-of-plane with the ligand with protons exposed to the metal pocket. These protons appear to exhibit exchange broadening on lowering the temperature

for both inner and outer NH_2 groups, indicating that these protons are in the fast-exchange regime for the temperatures utilized. Due to symmetry arguments, both protons contained in the in-plane and out-of-plane conformations of the inner NH_2 groups are chemically equivalent (Figure 5.2.2.3). However, for the outer NH_2 protons, the in-plane conformation contains protons in chemically equivalent environments whereas the out-of-plane conformation alleviates the proton chemical equivalencies due to the exposure of one of the protons to the metal pocket (Figure 5.2.2.3). As a result, for the outer NH_2 groups, the out-of-plane conformation exhibits two proton peaks corresponding to a proton pointing away from the metal pocket while the other proton points towards this pocket. The in-plane conformation for this group, however, only exhibits one proton peak corresponding to both protons in-plane with the ligand. Given the electronic structure of the grid complex, the out-of-plane conformers are suggested to be upfield from the in-plane conformers. A plot of peak position versus temperature for the NH_2 groups is given in Figure 5.2.2.1. NMR shifts in other protons with temperature in Table 5.2.2.1 are attributed to the effect of NH_2 rotation on the interactions between the inner and outer ligands.

Table 5.2.2.1. Variable temperature NMR shifts for $[Zn(II)_9(2POAP\text{-}2H)_6]^{6+}$ in d_3-acetonitrile.

Peak[a]	*278 K*	*288 K*	*298 K*	*308 K*	*318 K*
H_1^i	6.300	6.309	6.317	6.326	6.324
H_2^i	6.416	6.427	6.438	6.448	6.458
H_3^i	7.296	7.298	7.299	7.300	7.301
H_4^i	7.311	7.312	7.313	7.317	7.317
H_5^i	6.734	6.722	6.716	6.714	6.709
H_6^i	7.665	7.679	7.692	7.706	7.718
H_7^i	7.525[b]	7.527[b]	7.528[b]	7.530[b]	7.529[b]
H_1^o	7.144	7.162	7.160	7.168	7.176
H_2^o	6.648	6.655	6.659	6.664	6.673
H_3^o	7.525[b]	7.527[b]	7.528[b]	7.530[b]	7.529[b]
H_4^o	7.588	7.593	7.597	7.602	7.608
H_5^o	6.971	6.949	6.928	6.912	6.895
H_6^o	8.244	8.252	8.261	8.270	8.278
H_7^o	8.114	8.113	8.113	8.114	8.114

[a] There are 2 inner ligands (i) and 4 outer ligands (o) in the complex. [b] Peaks are convoluted.

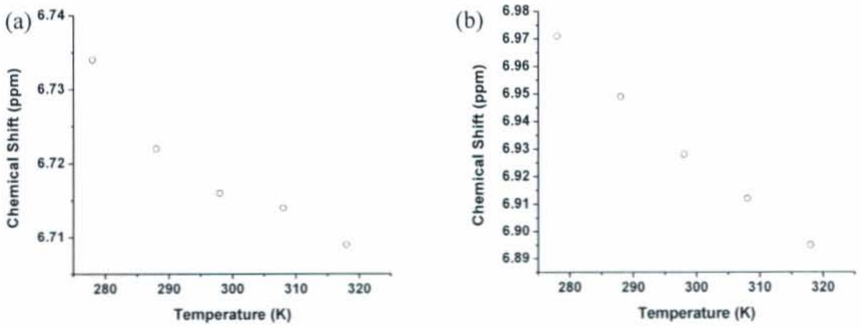

Figure 5.2.2.1. NMR shifts for H_5^i (a) and H_5^o (b) from 278 K to 318 K.

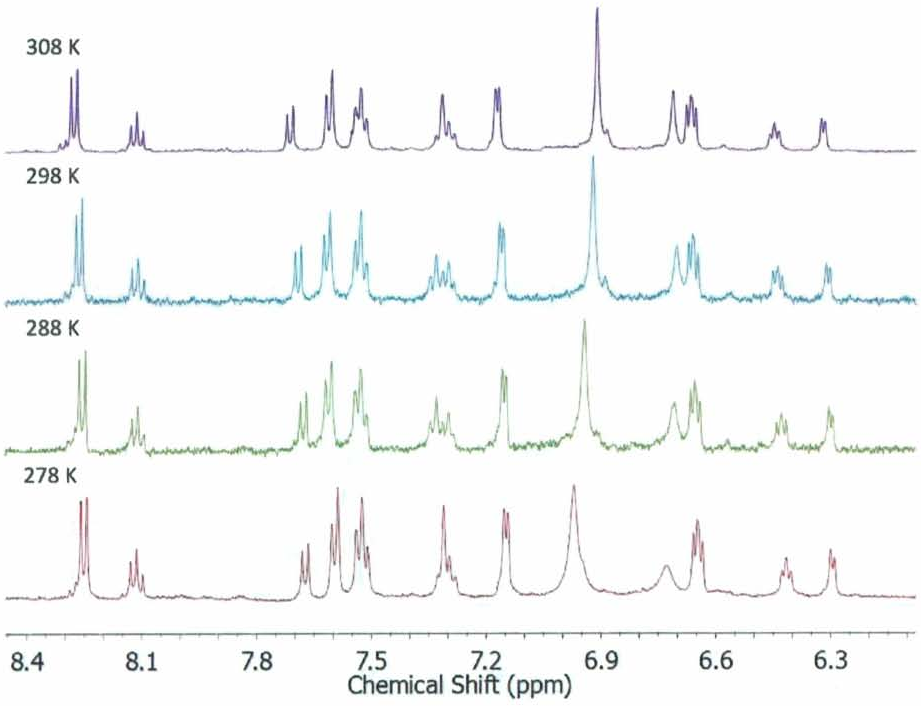

Figure 5.2.2.2. Temperature dependent ^{1}H-NMR on $[Zn_9^{II}(2POAP\text{-}2H)_6]^{6+}$. See Figure 5.2.1.1.1 for peak assignments.

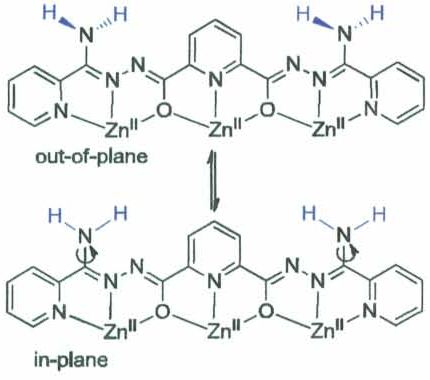

Figure 5.2.2.3. Rotational dynamics associated with inner and outer ligands of a Zn grid.

5.2.3. Excited States of the Ligand Framework

With an understanding of the structure for the $Zn(II)_9$ grid-type complex studied in this chapter, the optical states for this complex is now described.

5.2.3.1. UV-Vis spectral deconvolution

The absorption spectrum for $[Zn(II)_9(2POAP\text{-}2H)_6](NO_3)_6$ and its uncoordinated ligand in acetonitrile are shown in Figure 5.2.3.1.1. The observed red shift of the ligand absorption bands on binding Zn^{II} ions to form the grid-type structure is attributed to structural effects associated with ligand rigidity induced by metal ion coordination. The UV-Vis spectrum for $[Zn(II)_9(2POAP\text{-}2H)_6](NO_3)_6$ was deconvoluted using first and second derivatives and is given in Figure 5.2.3.1.2. The first and second derivative plots with the proposed locations of transitions are given in Figure 5.2.3.1.3. For a discussion on using first and second derivatives for deconvoluting spectra, see appendix D. The deconvoluted spectrum shows transitions located at 20151 cm^{-1} (496 nm, 2013 $M^{-1}cm^{-1}$), 23066 cm^{-1} (433 nm, 18800 $M^{-1}cm^{-1}$), 26289 cm^{-1} (380 nm, 161008 $M^{-1}cm^{-1}$), 30629 cm^{-1} (326 nm, 57588 $M^{-1}cm^{-1}$), 40110 cm^{-1} (249 nm, 67890 $M^{-1}cm^{-1}$), 48226 cm^{-1} (207 nm, 206863 $M^{-1}cm^{-1}$), and 51429 cm^{-1} (194 nm, 340363 $M^{-1}cm^{-1}$). These transitions are designated as G_a, G_b, G_c, G_d, G_e, G_f, and G_g respectively. All proposed transition maxima can be justified with the first derivative as zero and the second derivative as negative except for G_a, G_b, G_d, and G_e. G_a, G_b, and G_e are justified from the second derivative pattern where at the location for these transitions, the second derivative displays a positive-negative-positive pattern suggestive of a maximum. G_d may also be justified using the pattern displayed by the second derivative, yet the second derivative at G_d is not

clear enough to make this determination succinctly. However, not defining a gaussian function at this energy does not result in an adequate fit of the spectrum. Therefore, this suggests that a transition is located at G_d. This transition has been designated with a * in Figure 5.2.3.1.3.

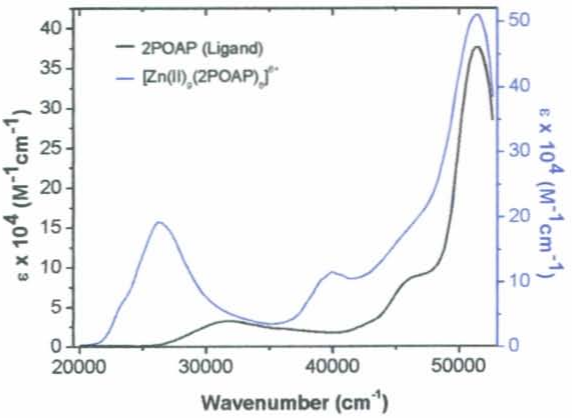

Figure 5.2.3.1.1. Overlay of UV-Vis absorption spectrum for 2POAP and $[Zn(II)_9(2POAP\text{-}2H)_6](NO_3)_6$ in acetonitrile.

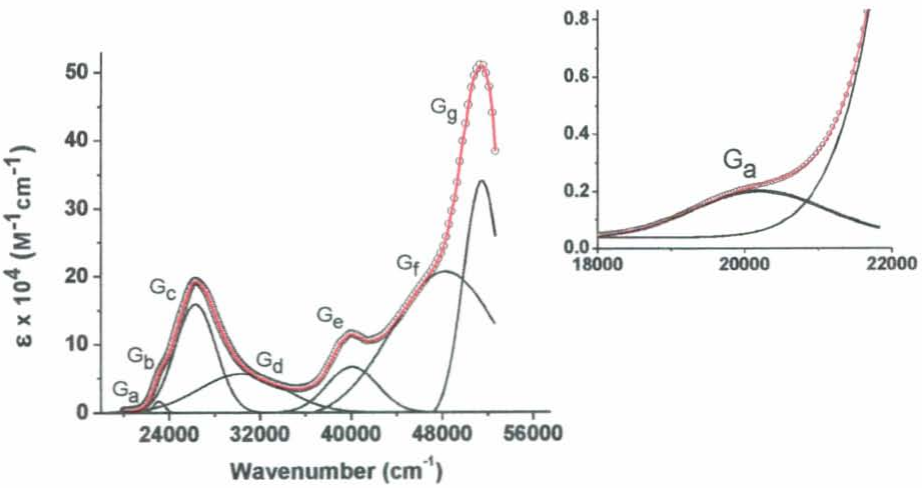

Figure 5.2.3.1.2. Deconvoluted UV-Vis absorption spectrum for $[Zn(II)_9(2POAP\text{-}2H)_6](NO_3)_6$ in acetonitrile. The inset is an expanded spectrum from 18000 – 22000 cm^{-1}.

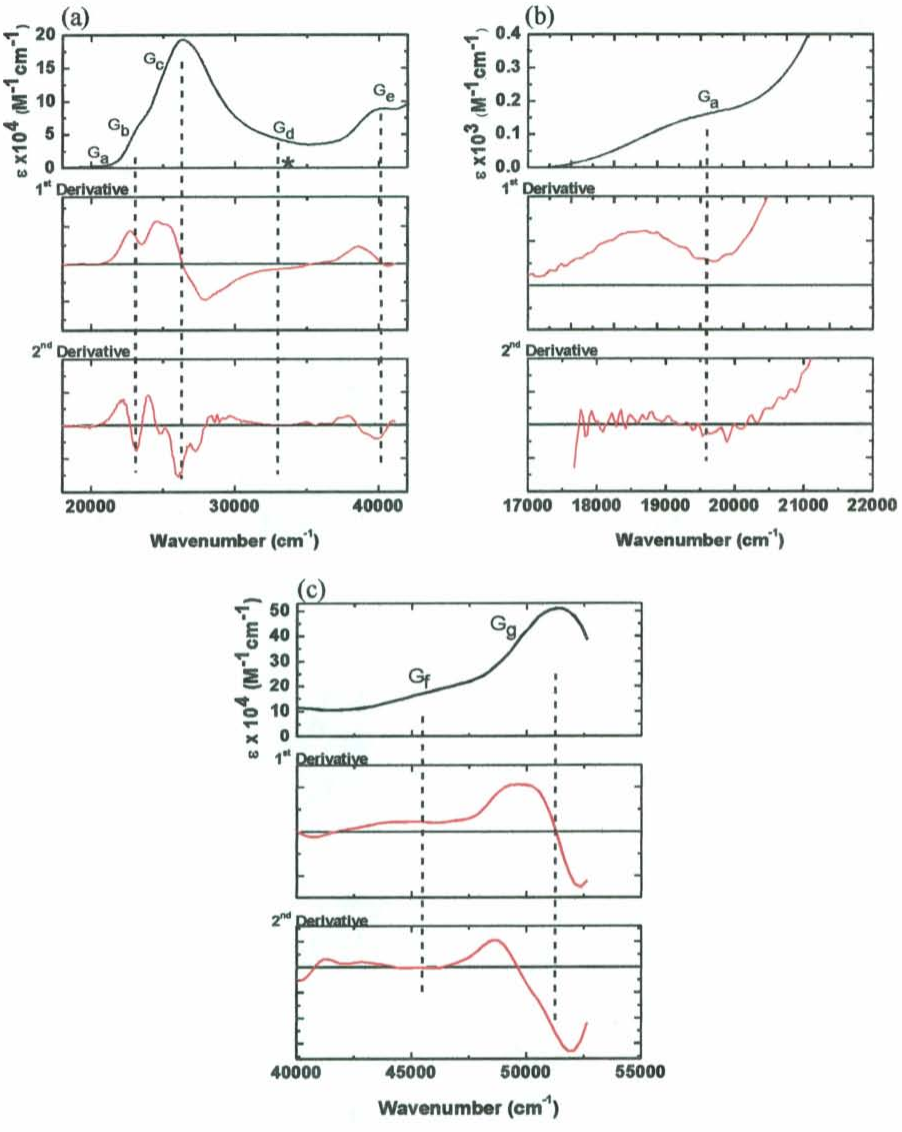

Figure 5.2.3.1.3. Derivative plots for the UV-Vis spectrum of a 4.0 μM $[Zn(II)_9[2POAP\text{-}2H)_6](NO_3)_6$ solution in acetonitrile. (a) is low energy side of the UV-Vis spectrum, (b) is this same spectrum expanded from 17000 cm^{-1} to 22000 cm^{-1}, and (c) is the high energy side of the spectrum. The dashed black lines correspond to the proposed location of a transition.

As the Zn(III/II) potential is too high and the Zn(II/I) potential is too low, the absorption spectrum for $[Zn(II)_9(2POAP\text{-}2H)_6](NO_3)_6$ are not associated with charge transfer involving the metal center and are dominated by the transitions associated with the coordinated ligands and their corresponding interactions with one another. The bandwidth at half-height ($\Delta\bar{\upsilon}_{1/2}$) for each transition is related to the solvent reorganizational energy (λ_o) via equation 5.2.3.1.1. λ_o is defined by equation 5.2.3.1.2 where a is the radius of the solvent cavity assuming a spherical cavity, $\vec{\mu}_{gs}$ and $\vec{\mu}_{gs}$ are the transition dipole moments for the ground and excited states respectively, and D_s and D_{op} are the static and optical dielectric constants of the solvent, respectively.[4]

$$\left(\Delta\bar{\upsilon}_{1/2}\right)^2 = 16k_BT\lambda_o\ln 2 \qquad \textit{eqn. 5.2.3.1.1.}$$

$$\lambda_o = \frac{1}{a^3}\left(\vec{\mu}_{gs} - \vec{\mu}_{es}\right)\left(\frac{D_S-1}{2D_s+1} - \frac{D_{op}-1}{2D_{op}+1}\right) \qquad \textit{eqn. 5.2.3.1.2.}$$

Given that the arrangement of ligands in the grid architecture allows one to partition the ligands in terms of inner and outer, through equation 5.2.3.1.1, outer ligands are expected to exhibit broader transitions (larger $\Delta\bar{\upsilon}_{1/2}$ values) than those same transitions on the inner ligand. This is because they are susceptible to the solvent and will exhibit a solvent reorganization energy that is approximately double that for the inner ligand. This "double approximation" is based on the dimensions of the ligand which is accessible to the solvent, assuming that the contribution of the solvent through each dimension is identical irrespective of the location of the ligand and that there are no specific solvent interactions with the ligand. If each ligand was analyzed separately and the solvent coordinates around each ligand defined in terms of the solvent encompassing the edge and facial dimensions

of the ligand, then the solvent reorganization can be defined in terms of components which interact with the edge and face of the ligand as follows. For each of the outer ligands, the solvent will interact with the ligand through both the ligands' edge and facial dimensions. However, for the inner ligand, the ligands facial dimension is occupied by the outer ligands due to the nature of the π-stacking arrangement in the complex. Therefore, the solvent is only accessible to the ligand along the ligands edge dimension. Since there are 4 outer ligands in the complex, there are a total of 8 solvent reorganization parameters corresponding to reorganization in terms of edge (λ_o^{edge}) and facial (λ_o^{face}) coordinates. Likewise, since there are 2 inner ligands in the complex, there are a total of 2 solvent reorganization parameters corresponding to reorganization in terms of the edge coordinates. This is shown in Scheme 5.2.3.1.1. The solvent reorganization energy for the outer ligand (λ_o^{outer}) and the solvent reorganization energy for the inner ligand (λ_o^{inner}) are given by equations 5.2.3.1.3 and 5.2.3.1.4 where λ_o^{coord} is the solvent reorganization associated with each coordinate system defined by equation 5.2.3.1.5. As given by equation 5.2.3.1.6, the band width for the outer transitions should be double that for the same transition located on the inner ligand.

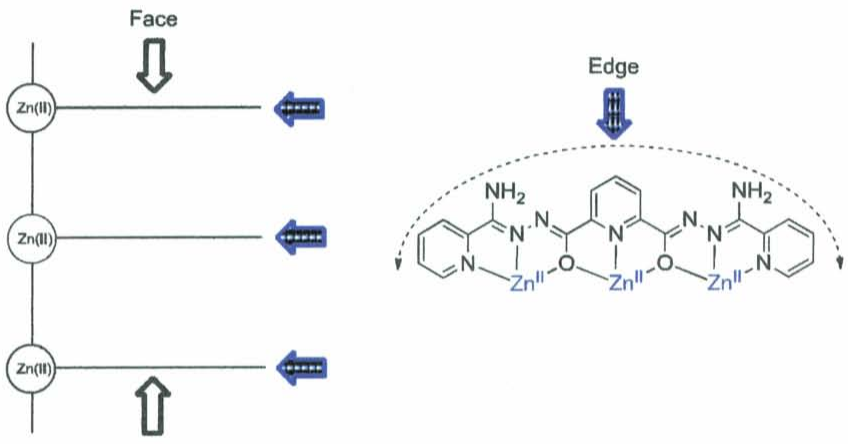

Scheme 5.2.3.1.1. Solvent coordinate system for each ligand in $[Zn(II)_9(2POAP\text{-}2H)_6](NO_3)_6$. One side of the complex is illustrated for clarity.

$$\lambda_o^{outer} = 4\lambda_o^{edge} + 4\lambda_o^{face} = 8\lambda_o^{coord} \qquad \textit{eqn. 5.2.3.1.3.}$$

$$\lambda_o^{inner} = 2\lambda_o^{edge} = 2\lambda_o^{coord} \qquad \textit{eqn. 5.2.3.1.4.}$$

$$\lambda_o^{coord} = \lambda_o^{edge} = \lambda_o^{face} \qquad \textit{eqn. 5.2.3.1.5.}$$

$$\frac{(\Delta\bar{\upsilon}_{1/2})_{outer}}{(\Delta\bar{\upsilon}_{1/2})_{inner}} = \left(\frac{\lambda_o^{outer}}{\lambda_o^{inner}}\right)^{\frac{1}{2}} = \left(\frac{8\lambda_o^{coord}}{2\lambda_o^{coord}}\right)^{\frac{1}{2}} = 2 \qquad \textit{eqn. 5.2.3.1.6.}$$

Based on the solvent accessibility of the ligands, inner and outer ligand transitions have been assigned based on $\Delta\bar{\upsilon}_{1/2}$ values. The oscillator strength (f_{osc}) and transition dipole moment ($\vec{\mu}$) for each transition were calculated via equations 5.2.3.1.7 and 5.2.3.1.8. f_{osc} for G_a, G_b, G_c, G_d, G_e, G_f, and G_g were calculated to be 0.022, 0.10, 2.99, 2.12, 1.52, 9.55, and 5.3 respectively. Likewise, $\vec{\mu}$ for G_a, G_b, G_c, G_d, G_e, G_f, and G_g were calculated to be 0.32 *e*Å, 0.62 *e*Å, 3.25 *e*Å, 2.53 *e*Å, 1.87 *e*Å, 4.28 *e*Å, and 3.10 *e*Å

respectively. Given the large oscillator strengths and transition dipole moments for G_c, G_d, G_e, G_f, and G_g, these transitions have been assigned as (π-π^*). Furthermore, given that $\Delta\bar{\upsilon}_{1/2}$ for G_d (8487 cm^{-1}) is approximately double that for G_c (4290 cm^{-1}), and $\Delta\bar{\upsilon}_{1/2}$ for G_f (10661 cm^{-1}) is approximately double that for G_e (5174 cm^{-1}), G_d and G_f have been assigned to a (π-π^*) transition specific to the outer ligand, and G_c and G_e have been assigned to these same respective (π-π^*) transitions specific to the inner ligand. Of the remaining unassigned transitions, since $\Delta\bar{\upsilon}_{1/2}$ for G_a (2488 cm^{-1}) is approximately double that for G_b (1167 cm^{-1}), G_a is assigned to a transition specific to the outer ligand and G_b is assigned to a transition specific to the inner ligand. These transitions are not assumed to be (π-π^*) in origin due to their relatively small oscillator strengths and transition dipole moments (table 5.2.3.5.1). G_g has been assigned to a (π-π^*) transition specific to the inner ligand due to the relatively small band width and the inner/outer pattern associated with the (π-π^*) transitions.

$$f_{osc} = 4.33 \times 10^{-9} \int \varepsilon(\nu) d\nu \approx 4.33 \times 10^{-9} \left(\varepsilon_{max} \Delta\bar{\nu}_{\frac{1}{2}}\right) \quad \textit{eqn. 5.2.3.1.7.}$$

$$\mu\,(e\text{Å}) = \left[\frac{f_{osc}}{(1.08\times10^{-5}) E_{op}(cm^{-1})}\right]^{\frac{1}{2}} \quad \textit{eqn 5.2.3.1.8.}$$

5.2.3.2. Fluorescence

The corrected fluorescence spectrum for $[Zn(II)_9(2POAP\text{-}2H)_6](NO_3)_6$ in acetonitrile is given in Figure 5.2.3.2.1(a) and is normalized and overlaid with the UV-Vis absorption spectrum in Figure 5.2.3.2.1(b). Spectra were normalized by setting the absorption and emission band maximums to 1 through multiplication of the spectra by $\frac{1}{E_{max}}$ for the transition. The overlaid spectra in Figure 5.2.3.2.1(b) illustrate that both absorption and emission display similar gaussian band shapes. The normalized emission and absorption spectra cross at 19149 cm^{-1}. This suggests that the emitting state is associated with the same electronic state as the G_a transition in the deconvoluted absorption spectrum in Figure 5.2.3.1.2.

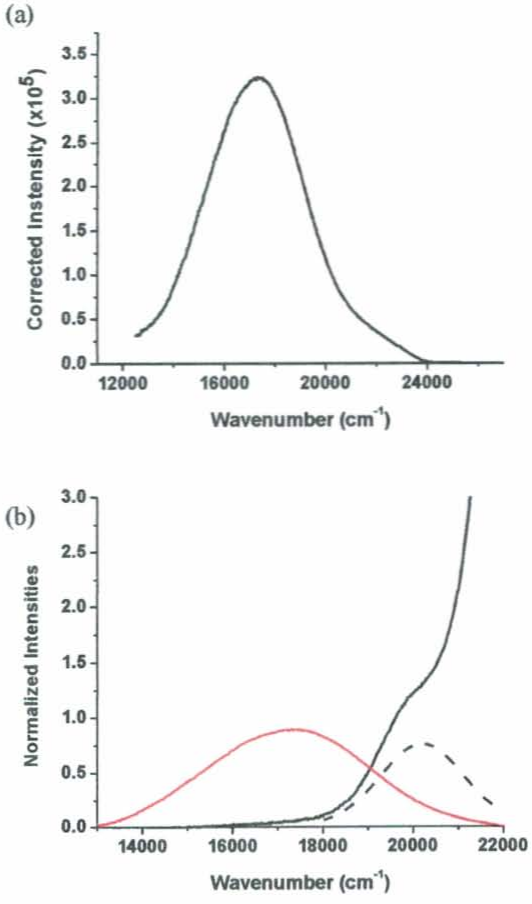

Figure 5.2.3.2.1. (a) Corrected emission spectra and (b) overlay of emission spectra with the UV-Vis spectra for $[Zn(II)_9(2POAP\text{-}2H)_6](NO_3)_6$ in acetonitrile. The dashed band is the deconvoluted G_a transition.

5.2.3.3. Effect of Protonation

The effect of protonation on the ground and excited states of $[Zn(II)_9(2POAP\text{-}2H)_6](NO_3)_6$ are given in Figure 5.2.3.3.1. In this study, 1 M trifluoroacetic acid was

progressively added in μL additions to a solution containing $[Zn(II)_9(2POAP\text{-}2H)_6](NO_3)_6$ in acetonitrile.

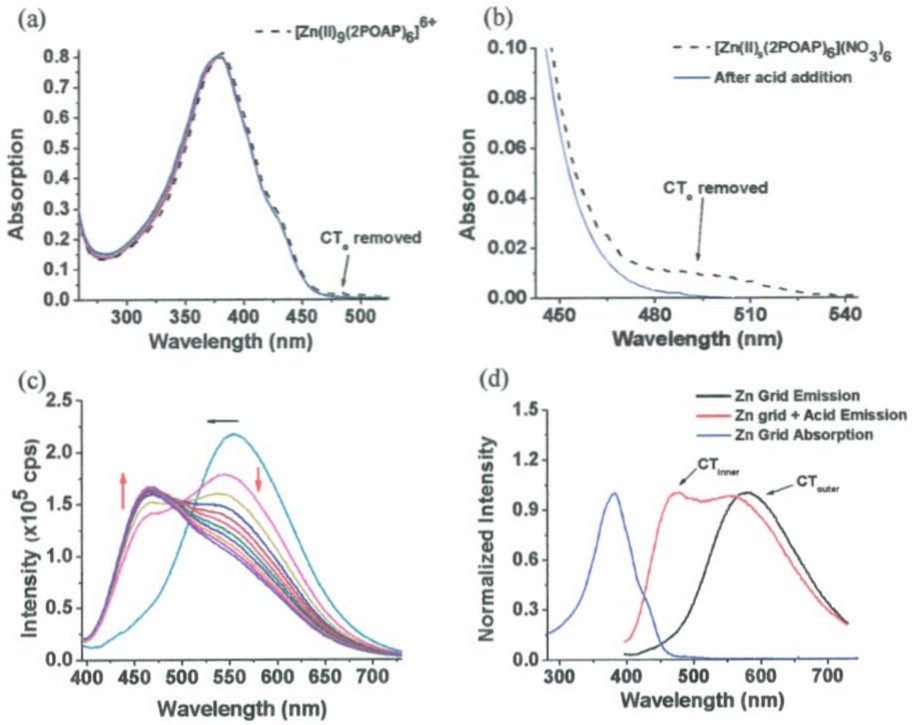

Figure 5.2.3.3.1. Effect of protonation on a 4.1 μM $[Zn(II)_9(2POAP\text{-}2H)_6]^{6+}$ solution in acetonitrile via titration of trifluoroacetic acid. (a) Absorption spectra of $[Zn(II)_9(2POAP\text{-}2H)_6]^{6+}$ at 298 K as a function of [TFA] = 1.0 μM, 2.0 μM, 3.0 μM, 4.0 μM, 5.0 μM, 6.0 μM, 6.9 μM, 7.9 μM, 8.9 μM, and 9.9 μM, respectively. (b) Overlay of absorption spectra before and after acid addition. (c) steady-state emission spectra for $[Zn(II)_9(2POAP\text{-}2H)_6]^{6+}$ at 298 K, 1 atm air, λ_{exc} = 380 nm, and the same [TFA] given in (a). (d) overlay of UV-Vis and steady-state emission spectra.

There does not appear to be an appreciable global effect on the ground state structure of $[Zn(II)_9(2POAP\text{-}2H)_6]^{6+}$ with the exception of the loss of the outer ligand

transition at 496 nm (Figure 5.2.3.3.1(b)). This would indicate that at higher [TFA] values, the outer ligand appears to be more appreciably affected. Not unexpected given that the outer ligand is more exposed to the solvent. The fact that [TFA] effects the G_a transition and not any of the assigned (π-π^*) transitions suggests that this UV-Vis transition is not solely due to (π-π^*) on the 2POAP ligand. The functional group which is most affected by [TFA] would be the NH_2 group. Thus, G_a, the UV-Vis transition at 496 nm, must involve the NH_2 group. Given the donating capacity of NH_2 groups, and that transitions involving this group typically involve intramolecular charge-transfer where this group serves as the charge donor,[5-8] G_a is assumed to be associated with a charge-transfer transition located on the outer ligand. It is assumed that the accepting group is a periphery pyridine given that the 2POAP ligand exhibits no other discernible structural features which would likely serve as an electron acceptor.

Analysis of the protonation effect on the excited states in Figure 5.2.3.3.1(c) indicates a more dramatic effect. As the [TFA] is increased, a loss of the emission transition at 552 nm is observed with growth of an emission band at 465 nm. Given the loss of the UV-Vis absorption transition at 496 nm under the same protonation conditions (Figure 5.2.3.3.1(b)), and that this transition exhibited charge-transfer character involving the NH_2 group on the outer 2POAP ligand, the emission band centered at 552 nm is assumed to involve this same charge-transfer transition. Therefore, the assignment of the emitting state as G_a is justified. Moreover, the loss of the G_a transition coincides with G_b as the new lowest-lying state. As such, the new emitting state at 465 nm is assigned to the G_b transition.

Further evidence to suggest that G_a is associated with charge transfer involving the amino groups is given in Figure 5.2.3.3.2 where the emission data in Figure 5.2.3.3.1 was plotted as a function of the [TFA] added. The data in Figure 5.2.3.3.2(a) suggests that the emission band centered at 552 nm saturates after addition of ~8 μM of TFA. This coincides to an 8:4 (or 2:1) ratio of TFA to grid. This 8:4 ratio is consistent with the number of amino groups in the grid on the outer ligands. What is interesting is that growth of the band at 465 nm saturates after a 4:4 (or 1:1) ratio of TFA to grid. This is probably due to protonation of one of the amino groups on each of the outer ligands.

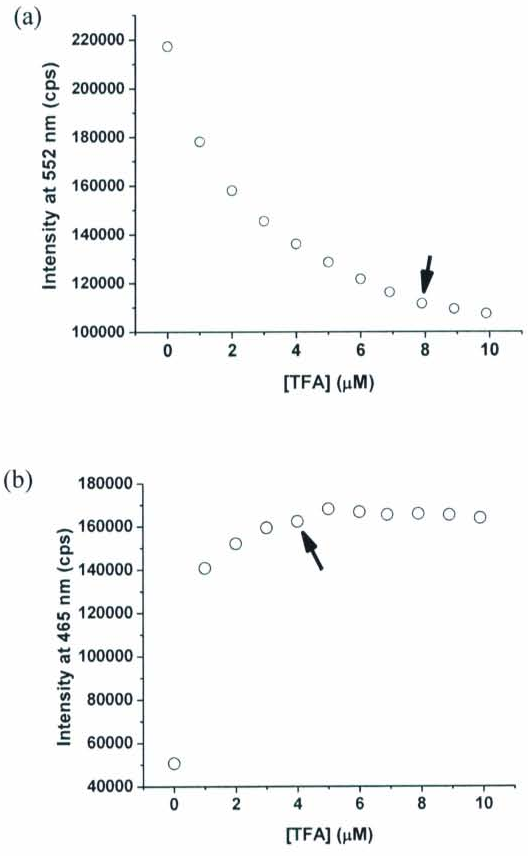

Figure 5.2.3.3.2. Plot of [TFA] with the intensities of the emission bands at (a) 552 nm and (b) 465 nm using the data in Figure 5.2.3.3.1.

5.2.3.4. UV-Vis Band Analysis

Thus far, G_a has been assigned as charge-transfer, and G_c/G_d and G_e/G_f have been assigned as (π-π^*) situated on the inner and outer ligands. However, how is G_b assigned? In order to assign this transition, an extended analysis of the deconvoluted transitions is

required. This analysis is presented below. The spectroscopic paramaters obtained from this analysis are summarized in table 5.2.3.4.1.

The deconvoluted UV-Vis spectrum for $[Zn(II)_9(2POAP\text{-}2H)_6](NO_3)_6$ in acetonitrile was analyzed as follows. E_{00}, the difference in energies between the ground and excited state $\upsilon = 0$ vibrational states, was estimated by drawing a tangent to the deconvoluted band on its low energy side and recording the point at which this tangent intercepted the baseline for the spectrum.[9-12] Using equation 5.2.3.4.1, the total reorganization energy (λ_t) was calculated by taking the difference in the optical transition energy (E_{op}) and E_{00}.

$$E_{op} = \lambda_t + E_{00} \qquad \textit{eqn. 5.2.3.4.1.}$$

$$\lambda_t = \lambda_i + \lambda_o \qquad \textit{eqn. 5.2.3.4.2.}$$

As given by equation 5.2.3.4.2, the total reorganization energy contains inner and outer reorganization components (λ_i and λ_o) which result from vibrational and solvent reorganization, respectively. As such, by directly extracting the band width at half maximum for each of the deconvoluted bands, the solvent reorganization energy was calculated via equation 5.2.3.4.3 and the vibrational reorganization energy was calculated by rearranging equation 5.2.3.4.2.

$$\lambda_o(cm^{-1}) = \frac{\left(\frac{\Delta\bar{\nu}_1}{2}\right)^2}{16k_bT\ln 2} = \frac{\left(\frac{\Delta\bar{\nu}_1}{2}\right)^2}{2296} \qquad \textit{eqn. 5.2.3.4.3.}$$

Using a Franck-Condon analysis, the oscillator strength (f_{osc}) was calculated using equation 5.2.3.4.4 and the transition dipole was calculated by equation 5.2.3.4.5 where

ε_{max} is the maximum extinction coefficient for the transition. The electronic coupling element (H_{DA}) was then calculated via equation 5.2.3.4.6 where r_{DA} is the distance between the donor and acceptor. This distance was estimated to be 3.7 Å from crystal structural data[13] assuming that the NH_2 group serves as the donor and the nearest periphery pyridine group serves as the acceptor. Note that H_{DA} values calculated using these distances are lower limits as these distances are based on the ground state structure and do not include the effect of donor-acceptor orbital mixing associated with the charge transfer excited state.[14]

$$f_{osc} = 4.33 \times 10^{-9} \int \varepsilon(\nu) d\nu \approx 4.33 \times 10^{-9} \left(\varepsilon_{max} \Delta\bar{\nu}_{\frac{1}{2}}\right) \qquad \textit{eqn. 5.2.3.4.4.}$$

$$\mu\ (e\text{Å}) = \left[\frac{f_{osc}}{(1.08\times10^{-5}) E_{op}(cm^{-1})}\right]^{\frac{1}{2}} \qquad \textit{eqn 5.2.3.4.5.}$$

$$H_{DA}(cm^{-1}) = \left[\frac{(4.2\times10^{-4}) E_{op} \int \epsilon(\nu) d\nu}{{r_{DA}}^2}\right]^{\frac{1}{2}} \approx \left[\frac{(4.2\times10^{-4}) E_{op}(cm^{-1})(\epsilon_{max}\Delta\bar{\nu}_{\frac{1}{2}})}{{r_{DA}}^2}\right]^{\frac{1}{2}} \qquad \textit{eqn. 5.2.3.4.6.}$$

Table 5.2.3.4.1. Summary of the spectroscopic parameters for $[Zn(II)_9(2POAP\text{-}2H)_6](NO_3)_6$ in acetonitrile using the absorption analysis described above.

	G_a	G_b	G_c	G_d	G_e	G_f	G_g
λ_{abs}, nm	496	433	380	326	249	207	194
E_{abs}, cm^{-1}	20151	23066	26289	30629	40110	48226	51429
ε, cm^{-1} M^{-1}	2013	18800	161008	57588	67890	206863	340363
$\Delta\nu_{1/2}$, cm^{-1}	2488	1167	4290	8487	5174	10661	3609
f_{osc}	0.022	0.10	2.99	2.12	1.52	9.55	5.30
μ, eÅ	0.32	0.62	3.25	2.53	1.87	4.28	3.10
H_{DA}, cm^{-1}	1768	3961					
E_{00}, cm^{-1}	18280	21790	22515	19217	35519	39212	48476
λ_o, cm^{-1}	1765	593					
λ_i, cm^{-1}	106	683					
λ_t, cm^{-1}	1871	1276					
r_{DA}, (Å)	3.7	3.7					
Assignment	CT_o	CT_i	$(\pi\text{-}\pi^*)_{i1}$	$(\pi\text{-}\pi^*)_{o1}$	$(\pi\text{-}\pi^*)_{i2}$	$(\pi\text{-}\pi^*)_{o2}$	[a] $(\pi\text{-}\pi^*)_{i3}$

[a] assignment assumed given the band width and the (π-π^*) transition pattern.

The difference in the ligand electronic structures appears pronounced when comparing E_{00} values for (π-π^*) transitions on each ligand. The difference between the (π-π^*) transition energies for the inner and outer ligand (3298 cm^{-1} for the G_c/G_d pair and 3693 cm^{-1} for the G_e/G_f pair) is nearly equivalent to the difference in energy between G_a and G_b transition energies (3510 cm^{-1}). Furthermore, the E_{00} value for the $(\pi\text{-}\pi^*)_{o1}$ transition (19217 cm^{-1}) is nearly the same as the E_{00} value for the CT_o transition (18280 cm^{-1}) and the E_{00} value for the $(\pi\text{-}\pi^*)_{i1}$ transition (22515 cm^{-1}) is nearly the same as that for the G_b transition (21790 cm^{-1}). Therefore, based on these energy arguments, and the fact that the inner and outer ligands are structurally identical, G_b is assigned to a charge

transfer transition specific to the inner ligand. This transition is assumed to involve the same donor and acceptors as that for G_a except it is located on the inner ligand. This difference in the ligand environments predisposes a *ligand electronic transition asymmetry* within the [3x3] grid-type complex which is mainly controlled by the accessible nature of the ligand to the solvent. A Jablonski diagram illustrating this model is given in Figure 5.2.3.4.1.

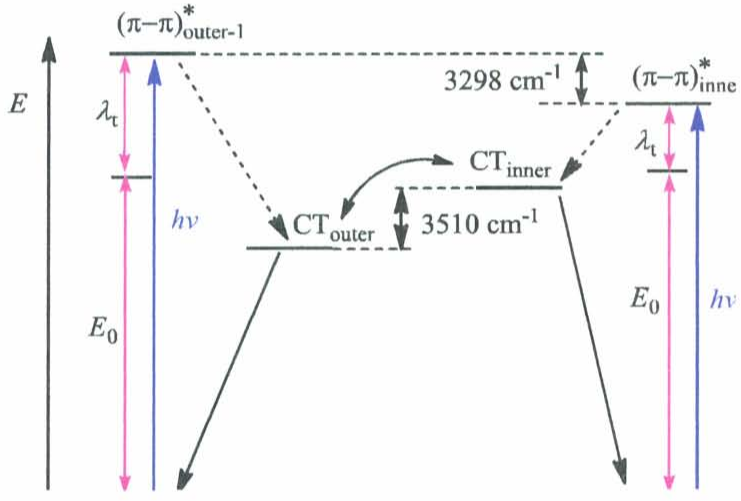

Figure 5.2.3.4.1. Model for ligand electronic transition asymmetry in $[Zn(II)_9(2POAP-2H)_6](NO_3)_6$.

5.2.3.5. Emission spectral fitting

The emission spectral analysis on $[Zn(II)_9(2POAP-2H)_6](NO_3)_6$ is shown in Figure 5.2.3.5.1 and uses a Franck-Condon line-shape analysis in which the emission band is fit with a number of gaussian functions. For a discussion on emission spectral

fitting, see section 2.4 of this thesis. This analysis has been formulated for a two-state system. As discussed in section 5.2.3.3 above, the emitting state for $[Zn(II)_9(2POAP\text{-}2H)_6](NO_3)_6$ is a composition of two charge-transfer transitions (at 465 nm and 550 nm) corresponding to a four-state system. However, the emitting state is dominated by the outer ligand charge-transfer state. Thus, the purpose of this analysis is to show the general similarities to the parameters calculated for this charge-transfer transition through the absorption analysis. The analysis should not be taken rigorously. A summary of the analysis is given in table 5.2.3.5.1 and includes the spectroscopic parameters obtained from the absorption analysis for comparison.

For the fitting emission spectra, units linear in energy are preferred over units linear in wavelength as the vibrational spacing becomes clearer.[11] The fluorescence instrument used detects data in terms of quanta per interval wavelength ($dQ/d\lambda$). As such, the data must be converted from an output of quanta per interval wavelength to an output of quanta per frequency interval ($dQ/d\upsilon$) via equation 5.2.3.5.1 as reported by Parker and Rees.[15]

$$\frac{dQ}{d\nu} = \left(\frac{dQ}{d\lambda}\right)\left(\frac{d\lambda}{d\nu}\right) = -\left(\frac{dQ}{d\lambda}\right)\frac{\lambda^2}{c} \qquad \textit{eqn. 5.2.3.5.1.}$$

where, $\lambda = \frac{c}{\nu}$ and $\frac{d\lambda}{d\nu} = \frac{-c}{\nu^2} = -\frac{\lambda^2}{c}$.

Therefore, the emission data for $[Zn(II)_9(2POAP\text{-}2H)_6](NO_3)_6$ were reduced by multiplying the data by a factor of λ^2 to correct for this interval and then renormalizing to 1000 by multiplying the data by the factor $\frac{1000}{E_{em}^{max}}$.

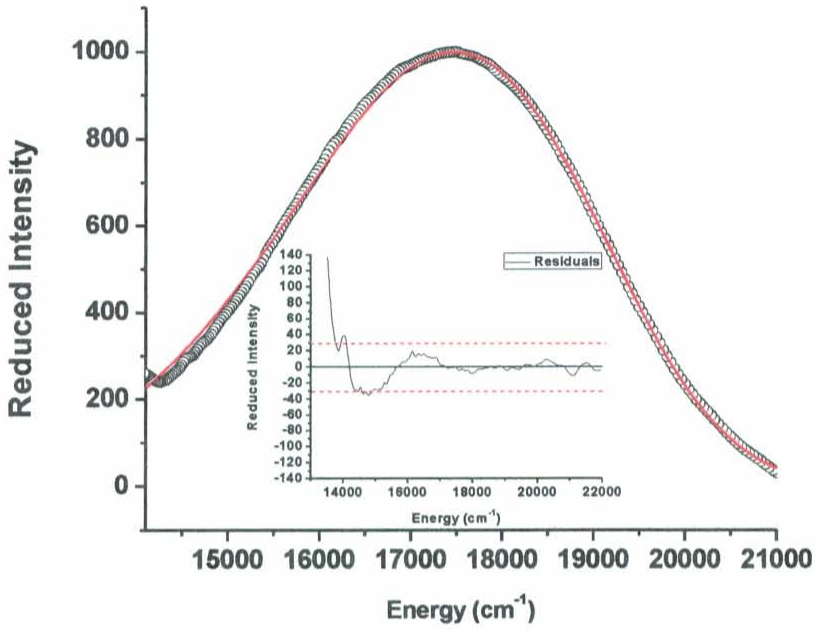

Figure 5.2.3.5.1. Emission spectral fitting for $[Zn(II)_9(2POAP\text{-}2H)_6](NO_3)_6$ in acetonitrile.

For the emission spectral analysis shown in Figure 5.2.3.5.1, a one mode spectral fitting analysis was performed by consistently varying ħω between 1000 cm^{-1} and 1400 cm^{-1} and allowing the fit to converge. The fit which gave the best residuals was with a ħω of 1300 cm^{-1}. The results of this analysis are summarized in Table 5.2.3.5.1. The obtained values of E_{00}, S_m, $\Delta\bar{\nu}_{1/2}$, and ħω were then used to calculate the Franck-Condon vibrational overlap factors (ln F(Calc)) via equation 5.2.3.5.2.

$$\ln[F(calc)] = -\frac{1}{2}\ln\left[\frac{\hbar\omega E_0}{(1000\ cm^{-1})^2}\right] - S_m - \left(\frac{\gamma E_0}{\hbar\omega}\right) + \frac{(\gamma+1)^2\left(\frac{\Delta\bar{\nu}_{1/2}}{\hbar\omega}\right)^2}{16\ln 2} \quad \textit{eqn. 5.2.3.5.2(a).}$$

where,

$$\gamma = \ln\left(\frac{E_o}{S_m \hbar\omega}\right) - 1 \qquad \textit{eqn. 5.2.3.5.2(b).}$$

These vibrational overlap factors are related to the rate constant for non-radiative decay of the excited state and the vibrationally induced electronic coupling matrix element contained in β_o via equation 5.2.3.5.3.

$$\ln k_{nr} = \ln \beta_o + \ln F(calc) \qquad \textit{eqn. 5.2.3.5.3.}$$

To calculate the solvent reorganization energy (λ_o) and the inner-sphere reorganization energy (λ_i), equations 5.2.3.5.4 and equation 5.2.3.5.5 were used. These reorganization energies were then summed to yield the total reorganizational energy via equation 5.2.3.5.6.

$$\lambda_o = \frac{\left(\frac{\Delta\bar{\nu}_1}{2}\right)^2}{16 k_b T \ln 2} \qquad \textit{eqn. 5.2.3.5.4.}$$

$$\lambda_i = S_m \hbar\omega \qquad \textit{eqn. 5.2.3.5.5.}$$

$$\lambda_t = \lambda_i + \lambda_o \qquad \textit{eqn. 5.2.3.5.6.}$$

Radiative and non-radiative rate constants were calculated using equations 5.2.3.5.7 and 5.2.3.5.8. The electronic coupling matrix element H_{DA} was calculated via equation 5.2.3.4.6 in the absorption analysis while H_{DA} in the emission analysis was calculated using equation 5.2.3.5.9. The frequency factor for electron transfer (υ_{et}) was calculated by equation 5.2.3.5.10 in addition to equation 5.2.3.5.3 above where β_o is equivalent to υ_{et}.

$$k_r = \frac{\Phi_{em}}{\tau_F} \qquad \textit{eqn 5.2.3.5.7.}$$

$$k_{nr} = \frac{k_r}{\Phi_{em}} - k_r \qquad \textit{eqn. 5.2.3.5.8.}$$

$$H_{DA} = \frac{E_{abs}\left[(1.39\times10^5)k_r(\nu_{em})^{-3}\right]^{\frac{1}{2}}}{r_{DA}} \qquad \textit{eqn. 5.2.3.5.9.}$$

$$\upsilon_{et} = \frac{2\pi}{\hbar}\left(\frac{1}{2\pi\hbar\omega E_{00}}\right)^{\frac{1}{2}} \qquad \textit{eqn. 5.2.3.5.10.}$$

Table 5.2.3.5.1. Spectroscopic parameters using an absorption analysis and an emission spectral analysis on the emission profile for $[Zn(II)_9(2POAP\text{-}2H)_6](NO_3)_6$ in acetonitrile.

	Absorption					Emission
	CT_o	CT_i	$(\pi\text{-}\pi^*)_{il}$	$(\pi\text{-}\pi^*)_{ol}$		CT_o
λ_{abs}, nm	496	433	380	326	λ_{em}, nm	580
E_{abs}, cm^{-1}	20151	23066	26289	30629	E_{em}, cm^{-1}	17240
ε, cm^{-1} M^{-1}	2013	18800	161008	57588	Φ_{em}	$\sim10^{-3}$
$\Delta\nu_{1/2}$, cm^{-1}	2488	1167	4290	8487	$\Delta\nu_{1/2}$, cm^{-1}	2559
f_{osc}	0.022	0.10	2.99	2.12	τ, ps	250
μ, eÅ	0.32	0.62	3.25	2.53	$\hbar\omega$, cm^{-1}	1300
H_{DA}, cm^{-1}	1768	3961			H_{DA}, cm^{-1}	1794
E_{00}, cm^{-1}	18280	21790	22515	19217	E_{00}, cm^{-1}	18575
λ_o, cm^{-1}	1765	593			λ_o, cm^{-1}	2852
λ_i, cm^{-1}	106	683			λ_i, cm^{-1}	1929
λ_t, cm^{-1}	1871	1276			λ_t, cm^{-1}	4781
r_{DA}, (Å)	3.7	3.7			S_m	1.484
					ln[FC]	-19.3
					ln υ_{et}	32.2
					k_r, s^{-1}	4×10^6
					k_{nr}, s^{-1}	4×10^9

Based on the spectroscopic parameters given in Table 5.2.3.5.1, the E_{00} value obtained through the emission analysis is equivalent to that calculated for the outer-ligand charge-transfer transition (CT_o) from the absorption analysis. In addition, $\Delta\nu_{1/2}$ calculated for the CT_o band is approximately the same as that obtained from the emission spectral fitting analysis. This suggests that the emitting state and the CT_o absorption state involve transitions between the same states. The differences obtained for the inner and outer sphere reorganization energies are assumed to be due to the contribution from the inner-ligand charge-transfer to the emission profile.

Comparison of the electronic coupling matrix element (H_{DA}) with that of the total reorganizational energy (λ_t) would suggest that $2H_{DA} > \lambda_t$ ($2H_{DA}/\lambda_t \approx 2$) for the CT_o band while $2H_{DA} >> \lambda_t$ ($2H_{DA}/\lambda_t \approx 7$) for the CT_i band. This would suggest that the electronic structure constituting that between the donor and acceptor in the ground state is initially delocalized. This analysis should be taken lightly as the transitions have not been corrected for statistical effects.

What is the meaning behind the term "delocalization" presented above? One may argue that coordination of Zn(II) to 2POAP would invoke an inductive effect on the ligand whereby the lone pair on the NH_2 group becomes "delocalized" onto the 2POAP structure and is stabilized by resonance energy (H_{ab}). This statement is certainly true. The real question is: *by how much is resonance energy dictating the structure?* The resonance energy (or electronic coupling) is dictated by the coupling between the resonance structures associated with the molecule relative to the reorganization energy associated with moving from one resonance structure to the other. If we use aniline as an example,

the common chemist would draw the resonance structures of aniline by pushing electrons to give the structures in Scheme 5.2.3.5.1.

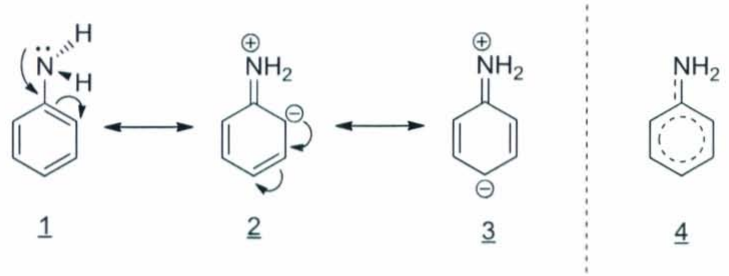

Scheme 5.2.3.5.1. Resonance structures for aniline.

If we allow structure 1 to be described by wavefunction Ψ_1, structure 2 to be described by wavefunction Ψ_2, and structure 3 to be described by wavefunction Ψ_3, then the total wavefunction describing a state (Ψ_{state}) is given by equation 5.2.3.5.11. These designations are justified since each structure really represents a different state as each defined resonance structure exhibit different nuclear and electronic coordinates.

$$\Psi_{state} = a_1\Psi_1 + a_2\Psi_2 + a_3\Psi_3 \qquad \textit{eqn. 5.2.3.5.11.}$$

The contribution of each structure to a given state is determined by the coefficient corresponding to each individual wavefunction. For example, if a_1, a_2, and a_3 were all the same in the ground state, then each structure will contribute the same degree to the structure in the ground state. The result is the commonly drawn structure 4 shown in Scheme 5.2.3.5.1. However, this structure is unlikely since structure 1 is lower in energy than structure 2 and structure 2 is lower in energy than structure 3 due to the "separated"

charges being closer. This is due to the quantum mechanics of the situation. Quantum mechanically, the coupling between wavefunctions corresponding to states which differ in energy is less than the wavefunctions which are similar in energy. This is illustrated by the potential energy surfaces shown in Figure 5.2.3.5.2 for Ψ_{gs} consisting of Ψ_1 and Ψ_2.

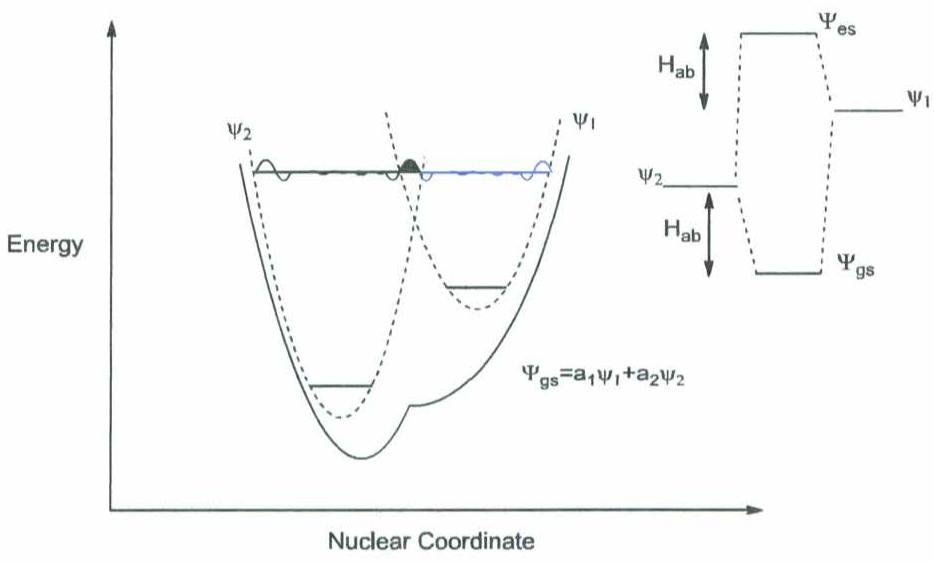

Figure 5.2.3.5.2. Potential energy surface illustrating coupling between structure 1 and structure 2 in Scheme 5.2.3.5.1 for aniline. The potential energy surface for Ψ_{es} has been ignored for clarity.

Therefore, in $[Zn(II)_9(2POAP\text{-}2H)_6](NO_3)_6$, the delocalized nature of the NH_2 group with the periphery pyridine is associated with a ground state structure similar to structure 4 in scheme 5.2.3.5.1 whereby a_1 and a_2/a_3 have values which are on the same order of magnitude. The excited state is likely associated with a structure similar to structure 2 or 3 in scheme 5.2.3.5.1 whereby a_2 and a_3 are on the same order of magnitude

and larger than a_1. A detailed discussion of localization versus delocalization was presented previously in chapter 4.

5.2.3.6. Spatial Confinement

Thus far, the UV-Vis spectrum for $[Zn(II)_9(2POAP\text{-}2H)_6]^{6+}$ has been assigned in terms of the transitions specific to the inner and outer ligands based on band widths. For example, the transition located at 326 nm has been assigned as (π-π^*) on the outer ligand and the transition at 380 nm has been assigned as (π-π^*) on the inner ligand since the band width for the transition at 326 nm is approximately double that of the value at 380 nm. The molar absorptivities for these transitions were 57588 $M^{-1}cm^{-1}$ and 161000 $M^{-1}cm^{-1}$, respectively. Since there is a 2:1 ratio between the outer and inner ligands, one would predict that the transitions associated with the outer ligand should display greater intensities since there are more outer ligands than inner ligands in the complex. However, assignments based on band widths suggests otherwise. How is it true that transitions specific to the inner ligand display greater intensities than those same transitions on the outer ligands even though there are less inner ligands than outer ligands?

The integrated band intensity for a radiative transition is given by equation 5.2.3.6.1 where $\vec{M}$ is the transition dipole moment defined by equation 5.2.3.6.2 with $\vec{\mu}$ as the transition dipole.[14] The integrated band intensity is proportional to the oscillator strength for the transition.[14]

$$f_{osc} \sim \int \epsilon(\nu) d\nu = \frac{4\pi^2 N_A \nu}{3000 c \eta \hbar \ln 10} \left|\vec{M}\right|^2 \qquad \textit{eqn. 5.2.3.6.1.}$$

$$\vec{M} = \vec{\mu} < \Psi_{vib}^{es} | \Psi_{vib}^{gs} > \qquad \textit{eqn. 5.2.3.6.2.}$$

The vibrational overlap term $< \Psi_{vib}^{gs} | \Psi_{vib}^{es} >$ is dictated by the details of the wavefunction. Using the harmonic oscillator approximation and the particle in a box model, the wavefunction in a one dimensional box of length L is defined by equation 5.2.3.6.3.[16]

$$\Psi_n^{1D} = \begin{cases} \sqrt{\frac{2}{L}} \sin k_n x & 0 < x \leq L \\ 0 & x > L \end{cases} \qquad \textit{eqn. 5.2.3.6.3.}$$

where $k_n = \frac{n\pi}{L}$ and $\sqrt{\frac{2}{L}}$ corresponds to the amplitude of the wavefunction. Extending this model into three dimensions yields the following wavefunction:[16]

$$\Psi_n^{3D} = \left(\sqrt{\frac{2}{L_x}} \sin[k_{n_x} x]\right)\left(\sqrt{\frac{2}{L_y}} \sin\left[k_{n_y} y\right]\right)\left(\sqrt{\frac{2}{L_z}} \sin[k_{n_z} z]\right) \quad \textit{eqn. 5.2.3.6.4.}$$

$$k_{n_x} = \frac{n_x \pi}{L_x} \qquad \textit{eqn. 5.2.3.6.5.}$$

$$k_{n_y} = \frac{n_y \pi}{L_y} \qquad \textit{eqn. 5.2.3.6.6.}$$

$$k_{n_z} = \frac{n_z \pi}{L_z} \qquad \textit{eqn. 5.2.3.6.7.}$$

The total amplitude for this wavefunction is defined by equation 5.2.3.6.8.

$$A_{Total} = A_x \times A_y \times A_z = \sqrt{\frac{8}{L_x \cdot L_y \cdot L_z}} \qquad \textit{eqn. 5.2.3.6.8.}$$

As illustrated in Figure 5.2.3.6.1, if we place both inner and outer ligands in separate boxes and set the boundaries of the box such that $0 < x \leq L_x$ and $0 < y \leq L_y$, then both inner and outer ligands display the same x and y coordinate boundaries. However, for the z-coordinate, if we allow the inner ligand to be defined by $0 < z \leq$

L_{inner} and the outer ligand to be defined by $0 < z \leq L_{outer}$, and assume $L_{inner} < L_{outer}$, then the amplitude of the wavefunction which describes the inner ligand is greater than the amplitude which describes the wavefunction for the outer ligand. This assumption is justified if we assume $L_{solvent} > \frac{1}{2}L_{inner}$. Since $A_{inner} > A_{outer}$, then it follows that $< \Psi^{gs}_{inner} | \Psi^{es}_{inner} >$ is greater than $< \Psi^{gs}_{outer} | \Psi^{es}_{outer} >$. Thus, $|\vec{M}|_{inner} > |\vec{M}|_{outer}$ and $|\int \epsilon(\nu) d\nu|_{inner} > |\int \epsilon(\nu) d\nu|_{outer}$. This is the justification behind the observation that f_{osc} for the inner transitions are greater than those observed for the same transitions on the outer ligand. See appendix D and Figure 5.2.3.6.2 for further details.

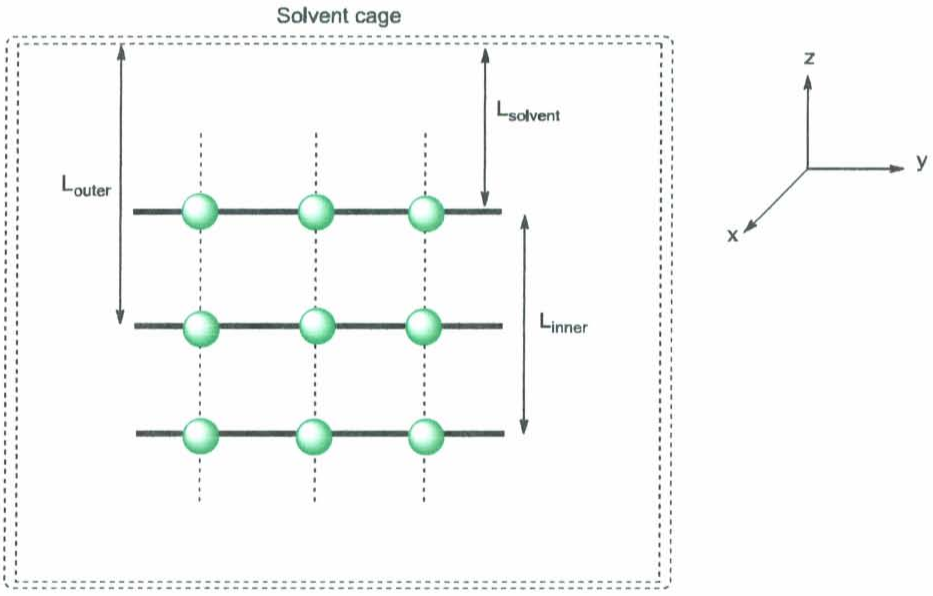

Figure 5.2.3.6.1. Particle in a box model for the ligands in $[Zn(II)_9(2POAP\text{-}2H)_6]^{6+}$.

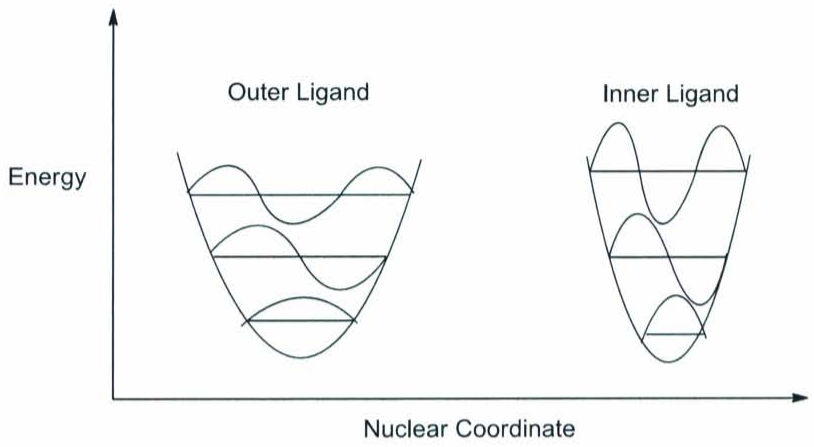

Figure 5.2.3.6.2. Potential energy surfaces for inner and outer ligands in $[Zn(II)_9(2POAP\text{-}2H)_6]^{6+}$.

5.2.3.7. Solvent dependence

Data reflecting the effect of solvent dielectric on the excited states of $[Zn_9^{II}(2POAP\text{-}2H)_6]^{6+}$ is given in Figure 5.2.3.7.1. A deconvoluted spectrum for a 3:1 chloroform:acetonitrile solvent mixture is given in Figure 5.2.3.7.2. The spectrum was deconvoluted using the first and second derivatives given in Figure 5.2.3.7.3. Transitions are proposed at 19648 cm^{-1}, 22890 cm^{-1}, 26090 cm^{-1}, and 29481 cm^{-1} and are labelled G_a, G_b, G_c, and G_d, respectively.

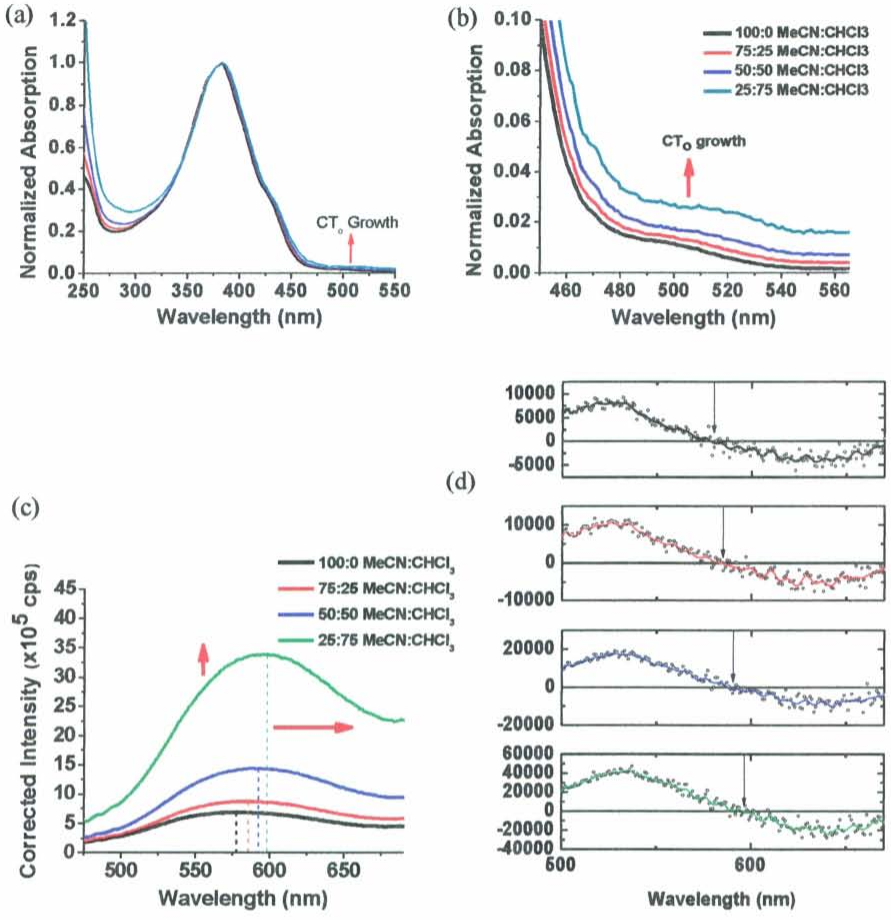

Figure 5.2.3.7.1. Solvent effect on the excited states of $[Zn(II)_9(2POAP\text{-}2H)_6]^{6+}$ in 100:0 MeCN:$CHCl_3$, 75:25 MeCN:$CHCl_3$, 50:50 MeCN:$CHCl_3$, and 25:75 MeCN:$CHCl_3$. (a) normalized UV-Vis spectra; (b) normalized spectra for CT_o band; (c) emission for $[Zn(II)_9(2POAP\text{-}2H)_6]^{6+}$ solutions; and (d) change in emission intensity for each of the solvents. Emission spectra were recorded at 298±3 K at an excitation at 380 nm. The slit width controlling the light level from the excitation source and to the detector was held constant.

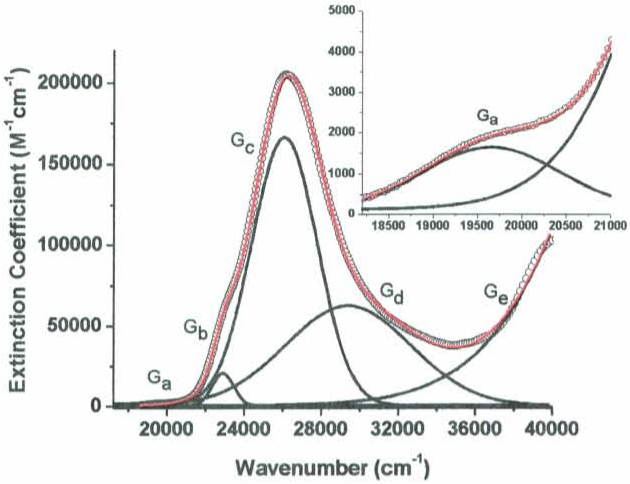

Figure 5.2.3.7.2. Deconvoluted UV-Vis spectrum for $[Zn_9^{II}(2POAP)_6](NO_3)_6$ in a 3:1 chloroform:acetonitrile solvent mixture.

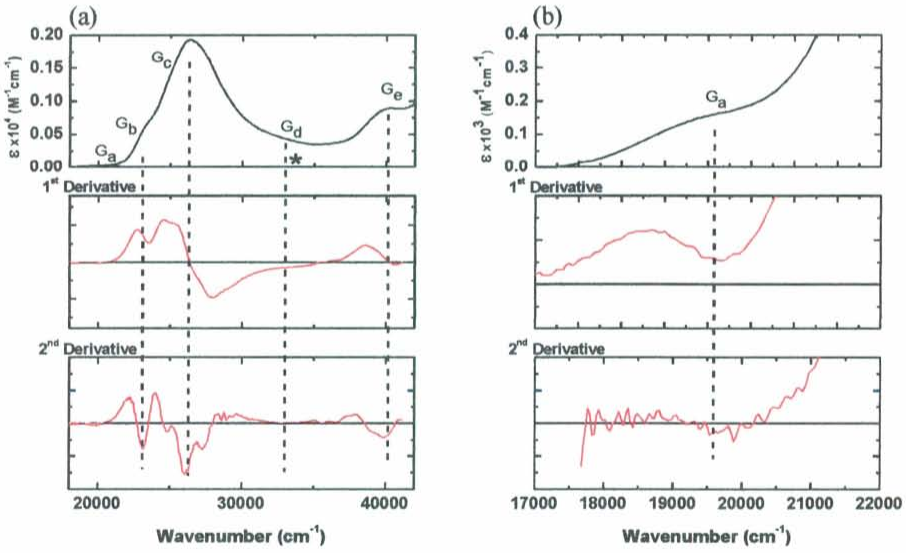

Figure 5.2.3.7.3. Derivative plots for the UV-Vis spectrum of a $[Zn(II)_9[2POAP\text{-}2H)_6](NO_3)_6$ solution in 3:1 chloroform:acetonitrile. (a) is the UV-Vis spectrum with derivative plots and (b) is this same spectrum expanded from 17000 cm^{-1} to 22000 cm^{-1}. The dashed black lines correspond to the proposed location of a transition.

The data indicate that on lowering the dielectric constant of the medium, a shift to lower energy and coincident growth of the outer ligand charge-transfer absorption band at 496 nm is observed (Figure 5.2.3.7.1(b)). In addition, the emission band shifts to lower energy (Figure 5.2.3.7.1(c) and (d)). These observations suggest that lowering the solvent dielectric results in a decrease in the energy gap between the ground and excited states within the grid. More precisely, a lowering of the solvent dielectric appears to result in a decrease in the energy gap between the ground and excited state potential energy surfaces on the outer ligand but not on the inner ligand (as it is not appreciably accessible to the solvent). Intuitively, one would imagine that the energy gap associated with a charge-transfer state would move to *higher energy* (i.e. lower wavelength) in lower dielectric solvents. However, the opposite is apparent in this study. One must remember that this intuition is valid when considering the energy difference between the *diabatic* surfaces corresponding to the electron transfer event. In addition, one must keep in mind that in a 100:0 acetonitrile:chloroform solvent mixture, the ground state potential energy surface is heavily delocalized (as discussed previously) such that we must take into account the contribution of the electronic coupling to the optical transition (equation 4.2.5.5) in an unsymmetrical system.

In this study, when decreasing the solvent dielectric, it is reasonable to conclude that the energy difference between the diabatic surfaces representing the electron transfer reactants and products increases (i.e. $\Delta E_{diabatic}$) increases. However, what is the effect on the electronic coupling for a heavily delocalized system when the solvent dielectric is lowered? Quantum mechanically, one would predict that when two states are more divergent in energy, the mixing between those states is reduced. Since E_{op} and E_{em} are

related to $\Delta E_{diabatic}$ and $2H_{DA}$ in a delocalized system, it would appear that in the $[Zn(II)_9(2POAP\text{-}2H)_6]^{6+}$ system, the effect of lowering the solvent dielectric on E_{em} appears to be reduced by H_{DA} more so than it is increased by $\Delta E_{diabatic}$. This is illustrated in Scheme 5.2.3.7.1 and Figure 5.2.3.7.3.

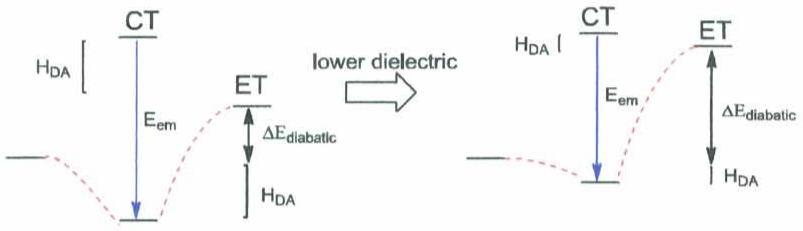

Scheme 5.2.3.7.1. Energy diagram illustrating the effect of decreasing solvent dielectric on the excited states in $[Zn(II)_9(2POAP\text{-}2H)_6]^{6+}$. CT and ET refer to charge-transfer and electron transfer states, respectively.

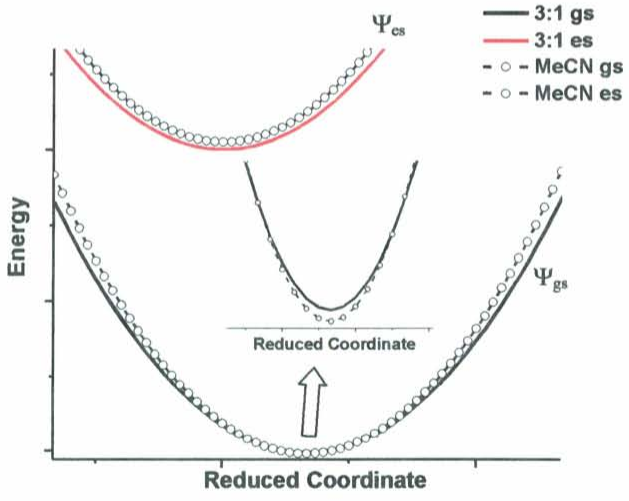

Figure 5.2.3.7.3. Potential energy surfaces for $[Zn(II)_9(2POAP\text{-}2H)_6]^{6+}$ in a 3:1 chloroform:acetonitrile and an acetonitrile solvent mixture. Surfaces were constructed using the data in Table 5.2.3.7.1. gs and es refer to the ground state and excited state, respectively.

The data in Table 5.2.3.7.1 is given for the deconvoluted spectrum of $[Zn(II)_9(2POAP\text{-}2H)_6]^{6+}$ in Figure 5.2.3.7.2 using the same absorption band analysis presented in section 5.2.3.4. The data indicate that on lowering the solvent dielectric from acetonitrile to a 3:1 chloroform:acetonitrile mixture, E_{00}, H_{DA}, and E_{abs} for CT_o decrease. There does not appear to be any appreciable change associated with the remaining transitions. As discussed above, this would suggest that a lowering of the dielectric constant of the solvent serves to shift the electronic coupling associated with the transition to involve less delocalization. This decrease in the electronic coupling provides a means to decreasing E_{abs} since the system is heavily delocalized in the initial solvent. This is illustrated in Table 5.2.3.7.1 by the value of $2H_{DA}/\lambda_t$. As presented in chapter 4, if $2H_{DA}/\lambda_t > 1$, the system is considered to exhibit a substantial degree of delocalization. If $2H_{DA}/\lambda_t < 1$, the system is considered to exhibit localized behaviour. Since $2H_{DA}/\lambda_t$ decreases to 1.6 in a 3:1 chloroform:acetonitrile mixture from that of 1.9 in acetonitrile, this would suggest that the system is exhibiting a reduction in the degree of delocalization. Overall, by controlling the dielectric of the solvent, it would appear that in the $[Zn(II)_9(2POAP\text{-}2H)_6]^{6+}$ system, one can control the electronic coupling between the donor and acceptor and potentially probe the class III (delocalized) to class II-III (partially delocalized/localized) to class II (localized) regime.

Table 5.2.3.7.1. Summary of the spectroscopic parameters obtained by from analysis of the absorption profiles for $[Zn_9^{II}(2POAP\text{-}2H)_6]^{6+}$in 3:1 chloroform:acetonitrile. Acetonitrile data are presented for comparison.

	3:1 chloroform:acetonitrile				acetonitrile			
	G_a	G_b	G_c	G_d	G_a	G_b	G_c	G_d
λ_{abs}, nm	509	437	383	339	496	433	380	326
E_{abs}, cm^{-1}	19648	22890	26090	29481	20151	23066	26289	30629
ε, cm^{-1} M^{-1}	1645	20819	166976	63045	2013	18800	161008	57588
$\Delta\nu_{1/2}$, cm^{-1}	1819	1345	3978	7556	2488	1167	4290	8487
f_{osc}	0.013	0.12	2.88	2.06	0.022	0.10	2.99	2.12
μ, eÅ	0.25	0.70	3.20	2.54	0.32	0.62	3.25	2.53
H_{DA}, cm^{-1}	1350	4457			1768	3961		
E_{00}, cm^{-1}	17972	21671	21671	22187	18280	21790	22515	19217
λ_o, cm^{-1}	1441	788	$(\pi\text{-}\pi^*)_i$		1765	593	$(\pi\text{-}\pi^*)_i$	
λ_i, cm^{-1}	235	431	383		106	683	380	
λ_t, cm^{-1}	1676	1219	26090		1871	1276	26289	
r_{DA}, (Å)	3.7	3.7	166976		3.7	3.7	161008	
$2H_{DA}/\lambda_t$	1.6	7.3	3978		1.9	6.2	4290	
Assignment	CT_o	CT_i	$(\pi\text{-}\pi^*)_{il}$	$(\pi\text{-}\pi^*)_{ol}$	CT_o	CT_i	$(\pi\text{-}\pi^*)_{il}$	$(\pi\text{-}\pi^*)_{ol}$

5.2.3.8. Temperature-dependent fluorescence

Temperature dependent fluorescence data for $[Zn(II)_9(2POAP\text{-}2H)_6](NO_3)_6$ in acetonitrile is given in Figure 5.2.3.8.1. In this experiment, a 4.1 μM solution of $[Zn(II)_9(2POAP\text{-}2H)_6](NO_3)_6$ in acetonitrile was placed in a transparent glass rod and sealed using parafilm. The rod was then placed the sample chamber of an OptistatDN-V liquid nitrogen optical cryostat supplied by Oxford instruments. The temperature dependent fluorescence data were then measured using the PTI Quantamaster 2400-4

spectrofluorometer equipped with this cryostat. This instrument was discussed previously in section 2.3.4.

The data in Figure 5.2.3.8.1 indicate that on lowering the temperature, the intensity of the fluorescence transition increases; consistent with the dependence of concentration on temperature in acetonitrile where the concentration increases due to solvent contraction. However, what is of more importance is the shift of the emission band to higher energy on increasing the temperature. More specifically, there appears to be a dominant shift in the emission band profile once the temperature is raised beyond 278 K. This would suggest that the lowest-lying excited state within $[Zn(II)_9(2POAP\text{-}2H)_6]^{6+}$ is dynamically coupled to some other state. Given that the lowest-lying excited state has been shown to involve charge transfer located on the outer ligand, and that the state closest in energy to this state involves charge transfer located on the inner ligand, this dynamic behaviour would suggest that both the outer and inner ligand charge transfer states are dynamically coupled. In the excited state at 278 K, it would appear that both charge transfer states are separated by ~186 cm^{-1} (i.e. k_BT where T is 298 K). As such, based on energy arguments, the difference in energy between ligand environments (~3300 cm^{-1} discussed previously) must originate through the energy difference between the energies of the highest occupied molecular orbitals for the outer and inner ligands (as shown in Scheme 5.2.3.8.1).

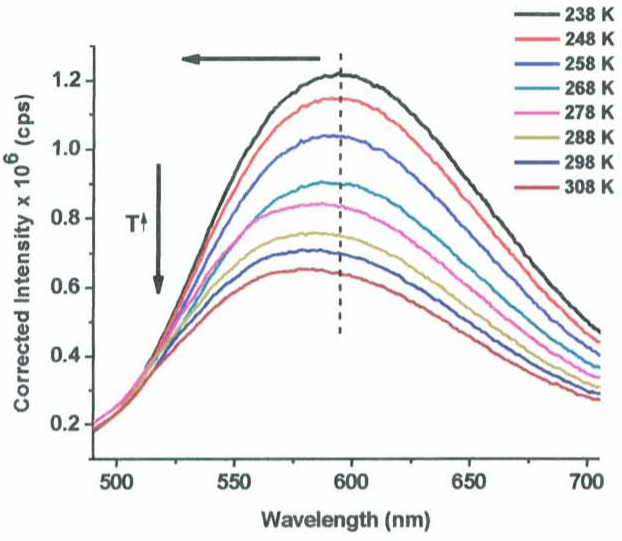

Figure 5.2.3.8.1. Temperature-dependent fluorescence for a 4.1 μM solution of $[Zn_9^{II}(2POAP\text{-}2H)_6]^{6+}$ in acetonitrile.

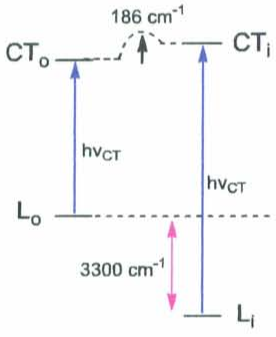

Scheme 5.2.3.8.1. MO diagram illustrating the dynamically coupled nature of the excited states in $[Zn_9^{II}(2POAP\text{-}2H)_6](NO_3)_6$.

5.2.3.9. Near-IR spectral deconvolution and band assignments

As $[Zn(II)_9(2POAP\text{-}2H)_6]^{6+}$ displays π-stacked ligands in a different electronic environment, one may expect there to be an interligand charge transfer transition given

that similar π-stacked organic complexes have displayed such transitions.[17-21] For example, a unique organic π-stacked system which displays charge separation includes the $5PDI_2$ system in which electron transfer between the individual π-stacked 5PDI units occurs in 170 fs due to a symmetry breaking mechanism provided by an appended pyrrolidine ring.[17-20] To enhance and further integrate light harvesting and charge separation within this dimeric unit, organic complexes with extended aromatic and hydrocarbon groups were synthesized in which the charge transfer characteristics of the $5PDI_2$ π-stacked core was maintained.[18, 21] As such, NIR data were collected and the spectrum was deconvoluted using first and second derivatives. This deconvoluted spectrum is given in Figure 5.2.3.9.1 and first and second derivative plots with the proposed locations of transitions are given in Figure 5.2.3.9.2. For a discussion on using first and second derivatives for deconvoluting spectra, see appendix D.

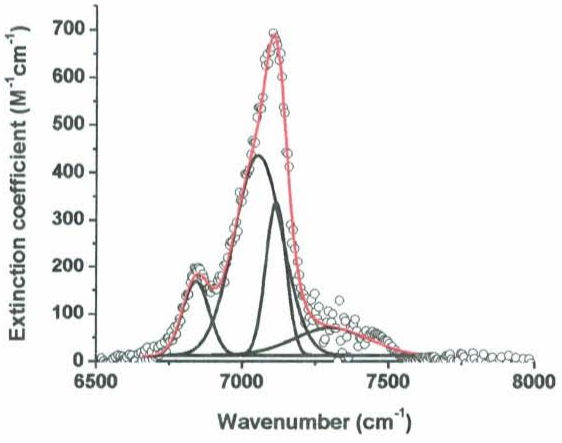

Figure 5.2.3.9.1. NIR spectrum of $[Zn_9^{II}(2POAP\text{-}2H)_6]^{6+}$ in d_3-acetonitrile.

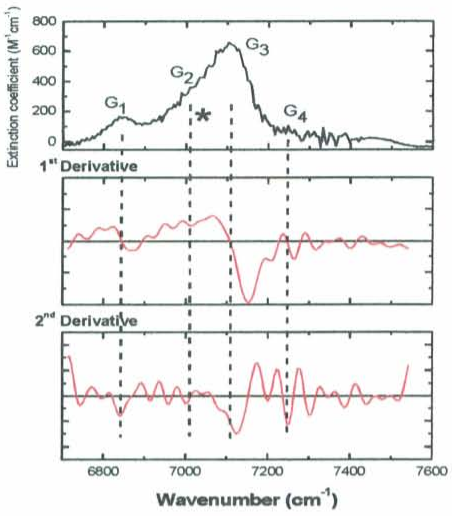

Figure 5.2.3.9.2. Derivative plots for the NIR spectrum of a 4.0 μM $[Zn(II)_9(2POAP\text{-}2H)_6](NO_3)_6$ solution in acetonitrile. The dashed black lines correspond to the proposed location of a transition.

Deconvoluted NIR transitions are proposed at 6841 cm^{-1}, 7053 cm^{-1}, 7115 cm^{-1}, and 7312 cm^{-1} and are labelled G_1, G_2, G_3, and G_4, respectively. All proposed transition maxima can be justified with the first derivative as zero and the second derivative as negative except for the G_2 transitions. G_2 may be justified using the pattern displayed by the second derivative, yet the second derivative at G_2 is not clear enough to make this determination. However, if a gaussian function is not defined at this wavelength, the spectrum does not fit properly. Therefore, G_2 must be present and this proposed transition is justified. This transition has been labelled with a * in Figure 5.2.3.9.2.

A summary of the fitted data are given in Table 5.2.3.9.1 using the same absorption band analysis described in section 5.2.3.4. $\Delta\nu_{1/2}$ for G_1, G_2, G_3, and G_4 were

calculated to be 100 cm^{-1}, 184 cm^{-1}, 78 cm^{-1}, 286 cm^{-1} directly from the gaussian functions of the NIR spectrum. Extinction coefficients for these transitions were determined to be 135 $M^{-1}cm^{-1}$, 392 $M^{-1}cm^{-1}$, 313 $M^{-1}cm^{-1}$, and 37 $M^{-1}cm^{-1}$ respectively. Given the structure of the grid-type complex and the NIR transitions for other comparable π-stacked systems[17-21], these transitions are assumed to originate from ligand-to-ligand charge transfer.

The complex under investigation contains an inner ligand confined to its spatial coordinates. This creates a local "cage effect" inhibiting translational, vibrational, and rotational motion of the ligand. As such, the rigid nature of this ligand allows one to treat the grid-type complex as a ligand surrounded by a rigid matrix.

In the classical limit, the optical energy is given by equation 5.2.3.9.1 where λ_i and λ_o are the inner-sphere and outer-sphere reorganizational energies, respectively.

$$E_{op}^{fl} = E_{00}^{fl} + \lambda_o + \lambda_i \qquad \textit{eqn. 5.2.3.9.1.}$$

Following a treatment by Marcus, λ_o can be partitioned into frozen (λ_o^{fr}), and non-frozen (λ_{oi}) contributions in a rigid matrix, as given by equation 5.2.3.9.2.[14, 22]

$$\lambda_o = \lambda_{oo}^{fr} + \lambda_{oi} \qquad \textit{eqn. 5.2.3.9.2.}$$

The term λ_{oo}^{fr} originates from the collective displacements in the surrounding matrix that are frozen in place. As such, λ_{oo}^{fr} becomes part of E_{00} in a rigid matrix and no longer contributes to the reorganization energy, equation 5.2.3.9.3.[14, 22, 23] In contrast, λ_{oi} originates from displacements that are not frozen.

$$E_{00}^{fr} = E_{00}^{fl} + \lambda_{oo}^{fr} \qquad eqn.\ 5.2.3.9.3.$$

Therefore, the optical energy associated with a complex in a rigid matrix may be reformulated as that given in equation 5.2.3.9.4. A more familiar expression is given in equation 5.2.3.9.5 using the reorganization energy term in a frozen matrix (λ_t^{fr}) in equation 5.2.3.9.6.

$$E_{op}^{fr} = E_{00}^{fr} + \lambda_{oi} + \lambda_i \qquad eqn.\ 5.2.3.9.4.$$

$$E_{op}^{fr} = E_{00}^{fr} + \lambda_t^{fr} \qquad eqn.\ 5.2.3.9.5.$$

$$\lambda_t^{fr} = \lambda_{oi} + \lambda_i \qquad eqn.\ 5.2.3.9.6.$$

The energy difference between the outer and inner ligand environments was estimated to be ~3300 cm^{-1} in section 5.2.3.5. Given that the inner ligand is spatially confined as a result of Zn(II) coordination and π-stacking interactions with the outer ligands, it is assumed to be frozen in a rigid framework. Therefore, to a reasonable approximation, this energy difference is assumed to be equivalent to λ_{oo}^{fr}. Since the energy of the electronic transitions were 6841 cm^{-1}, 7053 cm^{-1}, 7115 cm^{-1}, and 7312 cm^{-1} for G_1, G_2, G_3, and G_4 respectively, this would suggest that the contribution of the energy in fluid solution (E_{00}^{fl}) is 3440 cm^{-1}, 3568 cm^{-1}, 3739 cm^{-1}, and 3690 cm^{-1} for G_1, G_2, G_3, and G_4 respectively through use of equation 5.2.3.9.5.

Calculation of the electron transfer matrix element H_{DA}, the resonance energy resulting from the mixing of wavefunctions between the donor and acceptor, proves problematic without assigning appropriate transitions to each of the gaussian functions

defined in Table 5.2.3.9.1 and Figure 5.2.3.9.1. This is due to the issue associated the interaction of 3 π-stacked systems. As such, the assignment of these transitions is made below and is based on the methodology used previously to assign the transitions in the UV-Vis portion of the spectrum. In addition, as was discussed in section 5.2.3.8, since the HOMO for the inner ligand is higher in energy than the HOMO for the outer ligand, it is assumed that the interligand transitions occur outer-to-inner and involve a π* orbital on the inner ligand.

In the 2POAP ligand, the main π components are the periphery and central pyridine units. Therefore, when coordinated in a grid-type complex, the main π-stacked components are assumed to be these pyridine units. Based on this assumption, four interligand or inter-pyridine transitions are possible: two may originate from interaction of the outer ligand with that of one of the inner ligands (denoted as outer-inner or o,i), while the other two transitions may originate from interaction of both outer ligands (denoted as outer-outer or o,o) bridged by an inner ligand unit. More specifically, of these outer-inner and outer-outer transitions, one of the outer-inner and one of the outer-outer transitions should originate from interaction of the central pyridine units (designated as $ILCT_1$), while the remaining outer-inner and outer-outer transitions should originate from the interaction of the periphery pyridine units (designated as $ILCT_2$). These transitions are illustrated in Figure 5.2.3.9.2 below. Based on solvent arguments, $ILCT_1^{o,o}$ will have a larger band width ($\Delta\upsilon_{1/2}$) than $ILCT_1^{o,i}$ as the outer ligands are more exposed to the solvent. Likewise, $ILCT_2^{o,o}$ will have a larger band width than $ILCT_2^{o,i}$ as the outer ligands are more exposed to the solvent. Moreover, given that the outer-outer transitions span two equivalent ligand-ligand pockets, the band width for the $ILCT^{o,o}$ transitions are

expected to be approximately double that of their $ILCT^{o,i}$ counterparts. In addition, since the periphery pyridines have greater exposure to the solvent than the central pyridine units, $ILCT_2$ bands are expected to have a larger solvent dependence than their $ILCT_1$ counterparts.

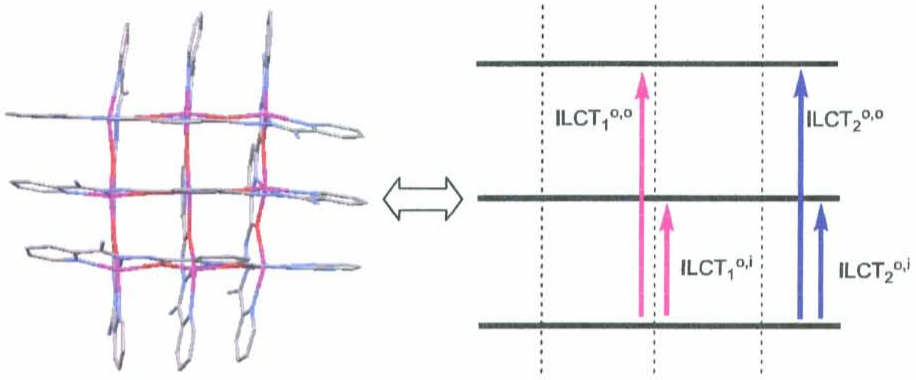

Figure 5.2.3.9.2. Possible ILCT transitions for $[Zn_9^{II}(2POAP\text{-}2H)_6]^{6+}$.

Given the discussion above and the data in Table 5.2.3.9.1, since G_4 has the largest $\Delta\upsilon_{1/2}$, it is assigned as $ILCT_2^{o,o}$. In addition, G_2 has a $\Delta\upsilon_{1/2}$ value approximately half that of G_4 and is therefore assigned to as $ILCT_2^{o,i}$. Likewise, of the remaining gaussian bands, since $\Delta\upsilon_{1/2}$ for G_1 is approximately double that of G_3, G_1 is assigned to $ILCT_1^{o,o}$ whereas G_3 is assigned to $ILCT_1^{o,i}$.

With the NIR transitions assigned, a Mulliken-Hush analysis was used to calculate the electronic coupling matrix element H_{DA} for each interligand transition. These values should be taken as lower limits as the electron transfer distances were estimated using crystal structural data which overestimates this distance as it does not take include donor-acceptor orbital mixing associated with the charge transfer transition.[14] H_{DA} values were

determined to be 28 cm^{-1}, 77 cm^{-1}, 13 cm^{-1}, and 132 cm^{-1} for $ILCT_1^{o,o}$, $ILCT_1^{o,i}$, $ILCT_2^{o,o}$, and $ILCT_2^{o,i}$, respectively. Since the reorganization energy for the frozen matrix was determined to be 101 cm^{-1}, 76 cm^{-1}, 322 cm^{-1}, and 185 cm^{-1}, respectively for each of these transitions, this would propose that $2H_{ab}/\lambda_t$ for $ILCT_1^{o,o}$, $ILCT_2^{o,i}$, $ILCT_1^{o,o}$, and $ILCT_2^{o,i}$ were 0.7, 2.0, 1.4 and 0.2. As such, these interligand transitions may be classified as class II/II-III, II-III/III, III, and II interligand charge transfer systems. See section 4.2.4.2 for a discussion on classifying electron transfer systems. Note that the data have not been corrected for statistical effects. Therefore, the classification of the intervalence transitions has not yet been formally finalized.

Table 5.2.3.9.1. Summary of the spectroscopic parameters obtained using a Rigid Matrix and Mulliken-Hush analysis on the NIR bands.

	G_1	G_2	G_3	G_4
λ_{abs} (nm)	1462	1418	1405	1368
E_{abs} (cm^{-1})	6841	7053	7115	7312
ε ($cm^{-1}M^{-1}$)	135	392	313	37
$\Delta\upsilon_{1/2}$ (cm^{-1})	100	184	78	286
f_{osc}	$5.8x10^{-5}$	$3.1x10^{-4}$	$1.1x10^{-4}$	$4.6x10^{-5}$
μ (eÅ)	0.028	0.049	0.038	0.024
H_{DA} (cm^{-1})	28	132	77	13
r_{DA} (Å)	7.0	3.5	3.5	7.0
[a] $(E_{00})^{fr}$ (cm^{-1})	6740	6868	7039	6990
$(\lambda_t)^{nfr}$ (cm^{-1})	101	185	76	322
λ_{oi} (cm^{-1})	4.4	15	2.6	36
λ_i (cm^{-1})	96	170	73	286
$(\lambda_{oo})^{fr}$ (cm^{-1})	3300	3300	3300	3300
$(E_{00})^{fl}$ (cm^{-1})	3440	3568	3739	3690
[b] Assignment	$ILCT_1^{o,o}$	$ILCT_2^{o,i}$	$ILCT_1^{o,i}$	$ILCT_2^{o,o}$
$2H_{DA}/(\lambda_t)^{nfr}$	0.7	1.4	2.0	0.2
[c] Class	II/II-III	II-III/III	III	II

[a] See section 5.2.3.4 for a discussion on the absorption analysis. [b] See Figure 5.2.3.6.2 for explanation of band assignments. [c] The data has not yet been corrected for statistical effects. Although these classes are stated, they are subject to scrutiny.

5.3. Conclusion

The excited states for the ligands in the [3x3] grid-type complex $[Zn(II)_9(2POAP\text{-}2H)_6]^{6+}$ have been adequately modelled in terms of discrete units which are energetically offset as a result of the location of the ligand in the complex. It has been shown that both inner and outer ligands display their own unique excited states as well as states which result from inter-ligand interactions. For example, in $[Zn(II)_9(2POAP\text{-}2H)_6]^{6+}$, the inner ligand exhibits a (π-π^*) transition at 26289 cm^{-1} and a charge transfer transition at 23066 cm^{-1}, whereas the outer ligand displays these same (π-π^*) and charge transfer transitions at 30629 cm^{-1} and 20151 cm^{-1}, respectively. Moreover, interligand transitions have been proposed at 6841 cm^{-1}, 7053 cm^{-1}, 7115 cm^{-1}, and 7312 cm^{-1}.

As a result of the effect of the solvent medium on the potential energy surface for the outer ligand, a ligand electronic transition asymmetry model has been proposed to describe the excited states in the [3x3] grid-type complex $[Zn(II)_9(2POAP\text{-}2H)_6]^{6+}$. As such, the difference in the E_{00} values for the (π-π^*) and CT transitions located on the inner and outer ligands (~3500 cm^{-1} in the $[Zn^{II}_9(2POAP)_6]^{6+}$ complex) has been attributed to the effect of the solvent on the more exposed outer ligand.

In describing the ligand excited states in the [3x3] grid-type complex $[Zn(II)_9(2POAP\text{-}2H)_6]^{6+}$, charge transfer behaviour has been observed on each ligand and between ligands. The electron donor for intraligand charge transfer has been suggested to be the NH_2 group given the protonation effect on the excited state. The acceptor for this transition has been tentatively assigned to the periphery pyridine group as the 2POAP ligand does not appear to exhibit any other logical electron accepting group. Likewise, the

electron donor and acceptor associated with the interligand transitions are assumed to involve the pyridine units of the ligand. Based on the band widths and energies of the charge transfer bands, it has been suggested that the intramolecular charge transfer states may be considered as class III delocalized whereas the interligand charge transfer states may be considered to range from class II to class III depending on the transition. However, these classifications are tentative as the transitions have not been corrected for statistical effects.

5.4. References

[1] L. Zhao, Z. Xu, H. Grove, V. A. Milway, L. N. Dawe, T. S. M. Abedin, L. K. Thompson, T. L. Kelly, R. G. Harvey, D. O. Miller, L. Weeks, J. G. Shapter and K. J. Pope, *Inorganic Chemistry* **2004**, *43*, 3812.

[2] L. Zhao, C. Matthews, L. K. Thompson and S. L. Heath, *Royal Society of Chemistry, Chem. Commun.* **2000**, 265.

[3] E. Breuning, G. S. Hanan, F. J. Romero-Salguero, A. M. Garcia, P. N. W. Baxter, J.-M. Lehn, E. Wegelius, K. Rissanen, H. Nierengarten and A. v. Dorsselaer, *Chemistry - A European Journal* **2002**, *8*, 3458.

[4] P. Chen and T. J. Meyer, *Chemical Reviews* **1998**, *98*, 1439.

[5] L.-q. Song, J. Feng, X.-s. Wang, J.-h. Yu, Y.-j. Hou, P.-h. Xie, B.-w. Zhang, J.-f. Xiang, X.-c. Ai and J.-p. Zhang, *Inorganic Chemistry* **2003**, *42*, 3393.

[6] J. A. Mondal, M. Sarkar, A. Samanta, H. N. Ghosh and D. K. Palit, *The Journal of Physical Chemistry A* **2007**, *111*, 6122.

[7] D. B. Oâ€™Connor, G. W. Scott, K. Tran, D. R. Coulter, V. M. Miskowski, A. E. Stiegman and G. E. Wnek, in *Journal of Chemical Physics, Vol. 97*, American Institute of Physics, **1992**, p. 4018.

[8] Z. R. Grabowski, K. Rotkiewicz and W. Rettig, *Chemical Reviews* **2003**, *103*, 3899.

[9] N. J. Turro, V. Ramamurthy and J. C. Scaiano, *Principles in Molecular Photochemistry: An introduction*, University Science Books, **2009**.

[10] J. R. Lakowicz, *Principles of Fluorescence Spectroscopy*, Third ed., Springer, **2006**.

[11] G. H. Allen, R. P. White, D. P. Rillema and T. J. Meyer, *Journal of the American Chemical Society* **1984**, *106*, 2613.

[12] J. V. Caspar and T. J. Meyer, *Journal of the American Chemical Society* **1983**, *105*, 5583.

[13] L. K. Thompson, L. Zhao, Z. Xu, D. O. Miller and W. M. Reiff, *Inorganic Chemistry* **2002**, *42*, 128.

[14] K. D. Demadis, C. M. Hartshorn and T. J. Meyer, *Chemical Reviews* **2001**, *101*, 2655.

[15] C. A. Parker and W. T. Rees, *Analyst* **1960**, *85*, 587.

[16] C. Cramer, *Essentials of Computational Chemistry: Theories and Models*, 2 ed., Wiley, **2002**.

[17] J. M. Giaimo, A. V. Gusev and M. R. Wasielewski, *Journal of the American Chemical Society* **2002**, *124*, 8530.

[18] M. R. Wasielewski, *Accounts of Chemical Research* **2009**, *42*, 1910.

[19] A. S. Lukas, P. J. Bushard and M. R. Wasielewski, *The Journal of Physical Chemistry A* **2001**, *106*, 2074.

[20] A. S. Lukas, Y. Zhao, S. E. Miller and M. R. Wasielewski, *The Journal of Physical Chemistry B* **2002**, *106*, 1299.

[21] B. Rybtchinski, L. E. Sinks and M. R. Wasielewski, *Journal of the American Chemical Society* **2004**, *126*, 12268.

[22] R. A. Marcus, *The Journal of Physical Chemistry* **1989**, *93*, 3078.

[23] R. J. Watts and D. Missimer, *Journal of the American Chemical Society* **1978**, *100*, 5350.

Chapter 6:

"EXCITED STATES IN [3X3] $Mn(II)_9$ AND $Mn(III)_4Mn(II)_5$ GRID-TYPE COMPLEXES"

Abstract: The purpose of this chapter is to develop an understanding of the excited states in the metal cores of the [3x3] grid-type complexes $[Mn(II)_9(2POAP\text{-}2H)_6]^{6+}$ and $[Mn(III)_4Mn(II)_5(2POAP\text{-}2H)_6]^{10+}$. These states will be shown to involve excited state electron transfer. With the electron transfer formalisms presented in chapter 4 and the ligand excited states presented in chapter 5, the metal core excited states of [3x3] $Mn_9(II)$ and $Mn(III)_4Mn(II)_5$ 2POAP grids will be classified.

6.1. Introduction

With the effects associated with the ligand framework in a *closed-shell* metal system described in Chapter 5, the effects of an *open-shell* metal core on the excited states in 2POAP [3x3] grid-type complexes are now discussed.

6.2. Results and Discussion

6.2.1. $[Mn(II)_9(2POAP\text{-}2H)_6](ClO_4)_6$

6.2.1.1. UV-Vis spectral deconvolution and band assignments

The UV-Vis absorption spectrum for $[Mn(II)_9(2POAP\text{-}2H)_6](ClO_4)_6$ is given in Figure 6.2.1.1.1. This spectrum was deconvoluted using first and second derivatives. The first and second derivative plots with the proposed locations of transitions are given in Figure 6.2.1.1.2. For a discussion on using first and second derivatives for deconvoluting spectra, see appendix D and section 5.2.3.1. The deconvoluted spectrum shows transitions located at 23362 cm^{-1} (428 nm, 10282 $M^{-1}cm^{-1}$), 26601 cm^{-1} (376 nm, 108182 $M^{-1}cm^{-1}$),

30733 cm^{-1} (325 nm, 47371 $M^{-1}cm^{-1}$), 399991 cm^{-1} (250 nm, 59115 $M^{-1}cm^{-1}$), 46258 cm^{-1} (216 nm, 53764 $M^{-1}cm^{-1}$), and 48839 cm^{-1} (205 nm, 128350 $M^{-1}cm^{-1}$). These transitions are designated as G_b, G_c, G_d, G_e, G_f, and G_g respectively. All proposed transition maxima can be justified with the first derivative as zero and the second derivative as negative except for G_b, G_d, and G_f. G_b is justified from the pattern displayed by the second derivative. G_d and G_f may also be justified using the pattern displayed by the second derivative, yet the second derivatives at G_d and G_f are not clear enough to make this determination succinctly. However, by not defining a gaussian function at these energies results in an inadequate fit to the spectrum. Therefore, this suggests the presence of transitions at G_d and G_f. These transitions have been designated with a * in Figure 6.2.1.1.2.

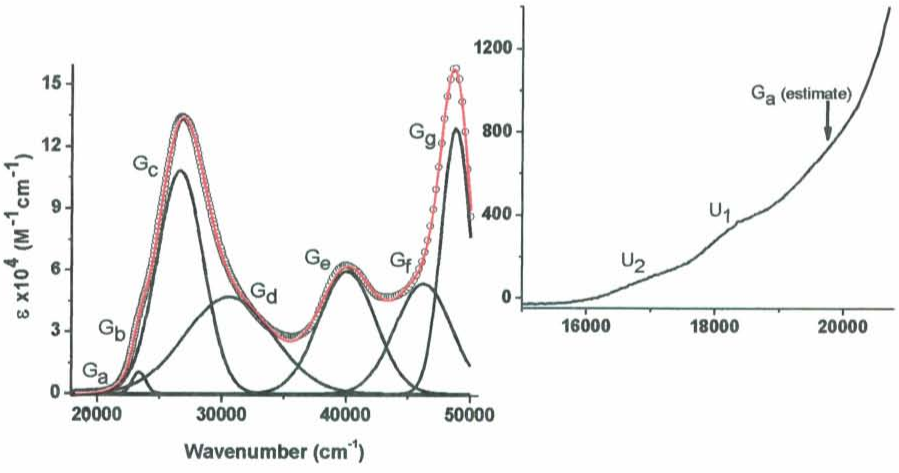

Figure 6.2.1.1.1. Deconvoluted UV-Vis absorption spectrum of $[Mn(II)_9(2POAP\text{-}2H)_6](ClO_4)_6$ in acetonitrile at 298±3 K. The inset is the low energy portion of the spectrum from 15000-21000 cm^{-1}.

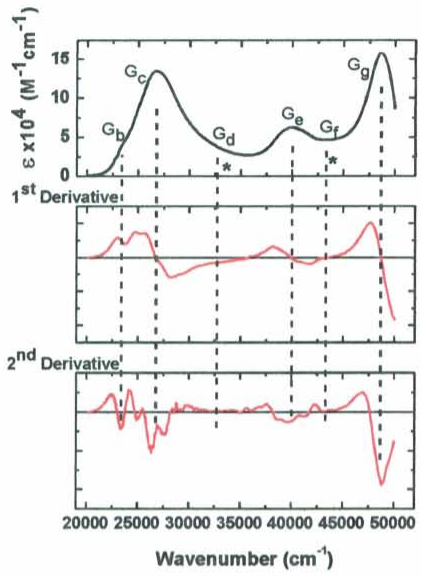

Figure 6.2.1.1.2. Derivative plots for the UV-Vis spectrum of a $[Mn(II)_9[2POAP\text{-}2H)_6](ClO_4)_6$ solution in acetonitrile.

The deconvoluted absorption transitions G_b, G_c, G_d, G_e, G_f, and G_g in Figure 6.2.1.1.1 have been assigned as CT_i, $(\pi\text{-}\pi^*)_{i1}$, $(\pi\text{-}\pi^*)_{o1}$, $(\pi\text{-}\pi^*)_{i2}$, $(\pi\text{-}\pi^*)_{o2}$, and $(\pi\text{-}\pi^*)_{i3}$ based on the assignments made for $[Zn(II)_9(2POAP\text{-}2H)_6](NO_3)_6$ in chapter 5. The UV-Vis spectrum in Figure 6.2.1.1.1 also shows low-energy transitions located at 16943 cm^{-1} (590 nm, 100 $M^{-1}cm^{-1}$), 18314 cm^{-1} (546 nm, 372 $M^{-1}cm^{-1}$), and 19768 cm^{-1} (506 nm, 730 $M^{-1}cm^{-1}$) which have been designated as U_1, U_2, and G_a, respectively. Deconvolution of this low-energy side of the UV-Vis absorption spectrum has proven problematic. However, given that the energy difference between ligand environments can be estimated as the difference in E_{00} values between the inner and outer $(\pi\text{-}\pi^*)$ transitions, the difference in energy between the ligand environments is 2260 cm^{-1}. Therefore, E_{00} for the outer ligand charge transfer band (CT_o) is expected to be at ~19935 cm^{-1} by subtracting

the ligand environmental energy difference (2260 cm^{-1}) from E_{00} for the inner ligand charge transfer band. This transition is thus expected to be in the midst of the spectral congestion shown in the inset of Figure 6.2.1.1.1. As such, G_a has been assigned to this CT_o transition. A summary of the photophysical parameters obtained on the deconvoluted UV-Vis spectrum for $[Mn(II)_9(2POAP\text{-}2H)_6](ClO_4)_6$ is given in Table 6.2.1.1.1.

Table 6.2.1.1.1. Summary of the spectroscopic parameters for $[Mn(II)_9(2POAP\text{-}2H)_6](ClO_4)_6$ in acetonitrile using absorption analysis described in section 5.2.3.4.

	G_a	G_b	G_c	G_d	G_e	G_f	G_g
λ_{abs}, nm		428	376	325	250	216	205
E_{abs}, cm^{-1}		23362	26601	30733	39991	46258	48839
ε, cm^{-1} M^{-1}		10282	108182	47371	59115	53764	128350
$\Delta\nu_{1/2}$, cm^{-1}		1280	4355	7476	5376	5514	2796
f_{osc}		0.057	2.04	1.53			
μ, eÅ		0.47	2.66	2.15			
H_{DA}, cm^{-1}		3087					
E_{00}, cm^{-1}	~19935	22195	22703	20443	35567	41420	46388
λ_o, cm^{-1}		709					
λ_i, cm^{-1}		450					
λ_t, cm^{-1}		1167					
r_{DA}, (Å)		3.7					
Assignment	CT_o	CT_i	$(\pi\text{-}\pi^*)_{i1}$	$(\pi\text{-}\pi^*)_{o1}$	$(\pi\text{-}\pi^*)_{i2}$	$(\pi\text{-}\pi^*)_{o2}$	[a] $(\pi\text{-}\pi^*)_{i3}$

[a] assignment assumed given the band width and the (π-π^*) transition pattern.

6.2.1.2. NIR spectral deconvolution and band assignments

Given the existence of an interligand transitions at 1407 nm in the $[Zn(II)_9(2POAP\text{-}2H)_6]^{6+}$ complex, and since the energies of the ligand transitions in

$[Mn(II)_9(2POAP\text{-}2H)_6]^{6+}$ appear to be similar, then it is expected that $[Mn(II)_9(2POAP\text{-}2H)_6]^{6+}$ should also exhibit similar transitions. As such, the NIR spectrum was recorded and is given in Figure 6.2.1.2.1. First and second derivatives for this spectrum are given in Figure 6.2.1.2.2.

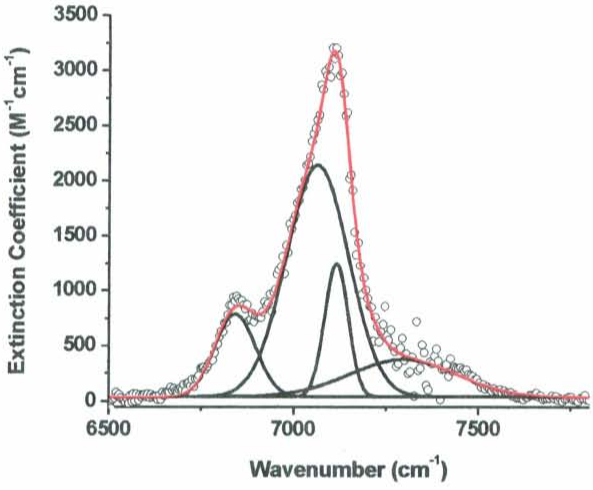

Figure 6.2.1.2.1. NIR spectrum of $[Mn(II)_9(2POAP\text{-}2H)_6](ClO_4)_6$ in d_3-acetonitrile at room temperature.

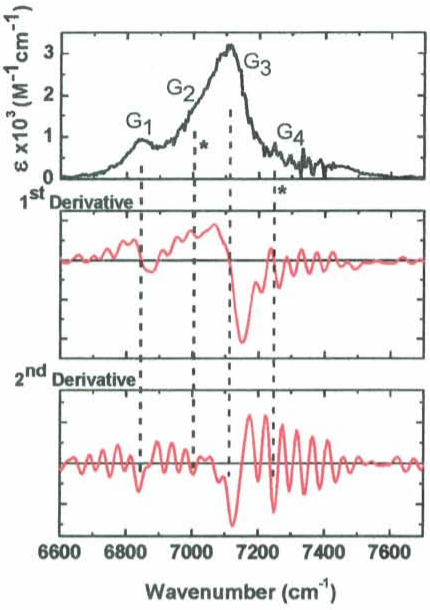

Figure 6.2.1.2.2. Derivative plots for the NIR spectrum of $[Mn(II)_9[2POAP\text{-}2H)_6](ClO_4)_6$ in acetonitrile at room temperature.

Deconvoluted NIR transitions are proposed at 6839 cm^{-1}, 7062 cm^{-1}, 7117 cm^{-1}, and 7327 cm^{-1} and are labelled G_1, G_2, G_3, and G_4, respectively. All proposed transition maxima can be justified with the first derivative as zero and the second derivative as negative except for the G_2 and G_4 transitions. G_2 and G_4 may be justified using the pattern displayed by the second derivative, yet the second derivative at these energies is not clear enough to make this determination. However, if a gaussian function is not defined at these energies, the spectrum does not fit properly. Therefore, this suggests the presence of transitions at G_2 and G_4. These transitions have been labelled with a * in Figure 6.2.1.2.2.

A summary of the fitted data are given in Table 6.2.1.2.1 using the same absorption band analysis described in section 5.2.3.4. $\Delta\nu_{1/2}$ for G_1, G_2, G_3, and G_4 were calculated to be 130 cm^{-1}, 187 cm^{-1}, 73 cm^{-1}, and 329 cm^{-1} respectively directly from the gaussian functions of the NIR spectrum. Extinction coefficients for these transitions were determined to be 789 $M^{-1}cm^{-1}$, 2147 $M^{-1}cm^{-1}$, 1262 $M^{-1}cm^{-1}$, and 387 $M^{-1}cm^{-1}$ respectively. Given the structure of this grid-type complex with the NIR transitions for $[Zn(II)_9(2POAP\text{-}2H)_6]^{6+}$ discussed in chapter 5 and other comparable π-stacked systems[1-5], these transitions are assumed to originate as a result of ligand-to-ligand charge transfer.

Much like $[Zn(II)_9(2POAP\text{-}2H)_6]^{6+}$, $[Mn(II)_9(2POAP\text{-}2H)_6]^{6+}$ also contains an inner ligand confined to its spatial coordinates. This creates a local "cage effect" inhibiting translational, vibrational, and rotational motion of the ligand. As such, the rigid nature of this ligand allows one to treat this grid-type complex as a ligand surrounded by a rigid matrix. A discussion on this rigid matrix effect is given in section 5.2.3.9.

The energy difference between the outer and inner ligand environments was previously estimated to be 2260 cm^{-1} (~2300 cm^{-1}) from the difference in E_{00} between G_c and G_d. Given that the inner ligand is spatially confined as a result of Mn(II) coordination and π-stacking interactions with the outer ligands, it is assumed to be frozen in a rigid framework. Therefore, to a reasonable approximation, this energy difference is assumed to be equivalent to λ_{oo}^{fr}. Since the energy of the electronic transitions were 6839 cm^{-1}, 7062 cm^{-1}, 7117 cm^{-1}, and 7327 cm^{-1} for G_1, G_2, G_3, and G_4 respectively, this would suggest that the contribution of the free energy in fluid solution (E_{00}^{fl}) is 4420 cm^{-1}, 4582 cm^{-1}, 4752 cm^{-1}, and 4668 cm^{-1} for G_1, G_2, G_3, and G_4 respectively.

The assignment of the NIR bands for $[Mn(II)_9(2POAP\text{-}2H)_6]^{6+}$ is made below and is based on the methodology used previously to assign the transitions in $[Zn(II)_9(2POAP\text{-}2H)_6]^{6+}$. As with $[Zn(II)_9(2POAP\text{-}2H)_6]^{6+}$, since the HOMO for the inner ligand is higher in energy than the HOMO for the outer ligand, it is assumed that the interligand transitions for $[Mn(II)_9(2POAP\text{-}2H)_6]^{6+}$ occur outer-to-inner and not inner-to-outer. They are also assumed to involve π orbitals on the ligands.

As discussed in chapter 5, four interligand or inter-pyridine transitions are possible through a π-stacked 2POAP ligand framework: two assigned as $ILCT_1$ which involve interaction of the central pyridine units, and two assigned as $ILCT_2$ which involve interaction of periphery pyridine units. These ILCT transitions may further be subdivided into the outer-outer and outer-inner components $ILCT_1^{o,o}$, $ILCT_1^{o,i}$, $ILCT_2^{o,o}$, and $ILCT_2^{o,i}$. These transitions have been illustrated in Figure 5.2.3.8.2. Based on solvent arguments, $ILCT_1^{o,o}$ will have a larger band width than $ILCT_1^{o,i}$ as the outer ligands are more exposed to the solvent. Likewise, $ILCT_2^{o,o}$ will have a larger band width than $ILCT_2^{o,i}$ as the outer ligands are more exposed to the solvent. Moreover, given that the outer-outer transitions span two equivalent ligand-ligand pockets, the band widths for the $ILCT^{o,o}$ transitions are expected to be approximately double those of their $ILCT^{o,i}$ counterparts. In addition, since the periphery pyridines have greater exposure to the solvent than the central pyridine units, $ILCT_2$ bands are expected to have a larger solvent dependence than their $ILCT_1$ counterparts.

Given the discussion above and the data in Table 6.2.1.2.1, since G_4 has the largest $\Delta\upsilon_{1/2}$, it is assigned as $ILCT_2^{o,o}$. In addition, G_2 has a $\Delta\upsilon_{1/2}$ value approximately half that of G_4 and is therefore assigned to as $ILCT_2^{o,i}$. Likewise, for the remaining

gaussian bands, since $\Delta\upsilon_{1/2}$ for G_1 is approximately double that of G_3, G_1 is assigned to $ILCT_1^{o,o}$ whereas G_3 is assigned to $ILCT_1^{o,i}$.

With the NIR transitions assigned, a Mulliken-Hush analysis was used to calculate the electronic coupling matrix element H_{DA} for each interligand transition. These values should be taken as lower limits as they are estimated using distances from crystal structural data on the ground state.[6] H_{DA} values were determined to be 78 cm^{-1}, 151 cm^{-1}, 90 cm^{-1}, and 313 cm^{-1} for $ILCT_1^{o,o}$, $ILCT_1^{o,i}$, $ILCT_2^{o,o}$, and $ILCT_2^{o,i}$, respectively. Since the reorganization energy for the frozen matrix was determined to be 119 cm^{-1}, 65 cm^{-1}, 359 cm^{-1}, and 180 cm^{-1}, respectively for each of these transitions, this would indicate that $2H_{ab}/\lambda_t$ for $ILCT_1^{o,o}$, $ILCT_2^{o,i}$, $ILCT_1^{o,o}$, and $ILCT_2^{o,i}$ were 1.3, 4.6, 3.5 and 0.5. As such, these interligand transitions may be classified as class III-II, III, III, and II interligand charge transfer systems. See section 4.2.5.2 for a discussion on classifying electron transfer systems. Note that the data has not yet been corrected for statistical effects. Therefore, the classification of the intervalence transitions has not yet been formally finalized.

Table 6.2.1.2.1. Photophysical constants for $[Mn(II)_9(2POAP\text{-}2H)_6]^{6+}$ using a Rigid Matrix and an absorption analysis on the NIR bands. The data for $[Zn(II)_9(2POAP\text{-}2H)_6]^{6+}$ is given in brackets.

	G_1	G_2	G_3	G_4
λ_{abs} (nm)	1462 (1462)	1416 (1418)	1405 (1405)	1365 (1368)
E_{abs} (cm^{-1})	6839 (6841)	7062 (7053)	7117 (7115)	7327 (7312)
ε ($cm^{-1}M^{-1}$)	789 (135)	2147 (392)	1262 (313)	387 (37)
$\Delta\upsilon_{1/2}$ (cm^{-1})	130 (100)	187 (184)	73 (78)	329 (286)
f_{osc}	$4.4x10^{-4}$ ($5.8x10^{-5}$)	$1.7x10^{-3}$ ($3.1x10^{-4}$)	$4.0x10^{-4}$ ($1.1x10^{-4}$)	$5.5x10^{-4}$ ($4.6x10^{-5}$)
μ (eÅ)	0.077 (0.028)	0.15 (0.049)	0.072 (0.038)	0.083 (0.024)
H_{DA} (cm^{-1})	78 (28)	313 (132)	151 (77)	90 (13)
r_{DA} (Å)	7.0	3.5	3.5	7.0
$(E_{00})^{fr}$ (cm^{-1})	6720 (6740)	6882 (6868)	7052 (7039)	6968 (6990)
$(\lambda_t)^{nfr}$ (cm^{-1})	119 (101)	180 (185)	65 (76)	359 (322)
λ_{oi} (cm^{-1})	7.4 (4.4)	15 (15)	2.3 (2.6)	47 (36)
λ_i (cm^{-1})	112 (96)	165 (170)	63 (73)	312 (286)
$(\lambda_{oo})^{fr}$ (cm^{-1})	2300 (3300)	2300 (3300)	2300 (3300)	2300 (3300)
$(E_{00})^{fl}$ (cm^{-1})	4420 (3440)	4582 (3568)	4752 (3739)	4668 (3690)
[a]Assignment	$ILCT_1^{o,o}$	$ILCT_2^{o,i}$	$ILCT_1^{o,i}$	$ILCT_2^{o,o}$
$2H_{DA}/(\lambda_t)^{nfr}$	1.3 (0.7)	3.5 (1.4)	4.6 (2.0)	0.5 (0.2)
[b]Class	III-II (II-III)	III (III-II)	III (III)	II (II)

[a] See Figure 5.2.3.9.2 for explanation of band assignments. [b] The data has not yet been corrected for statistical effects. Although these classes are stated, they are not finalized.

6.2.1.3. Metal core effects

A summary of the photophysical parameters obtained on the deconvoluted spectrum for $[Mn(II)_9(2POAP\text{-}2H)_6](ClO_4)_6$ using the band analysis described in section 5.2.3.4 are given in Table 6.2.1.1.1. Parameters obtained for selected transitions for $[Mn(II)_9(2POAP\text{-}2H)_6](ClO_4)_6$ are compared to those for $[Zn(II)_9(2POAP\text{-}2H)_6](NO_3)_6$ in Table 6.2.1.3.1.

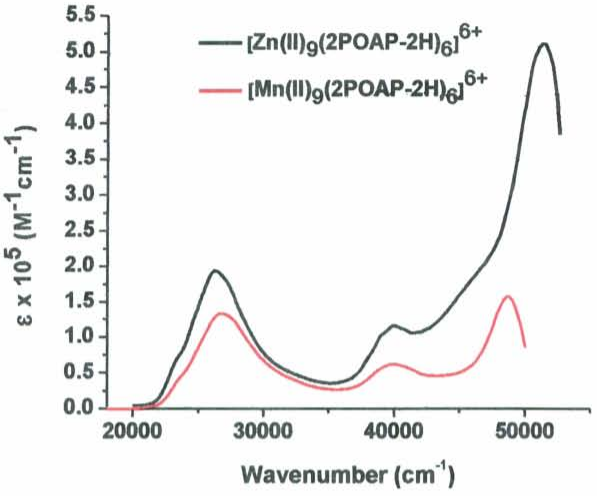

Figure 6.2.1.3.1. Overlaid UV-Vis spectra of $[Mn_9^{II}(2POAP\text{-}2H)_6](ClO_4)_6$ with $[Zn_9^{II}(2POAP\text{-}2H)_6](NO_3)_6$ in acetonitrile at 298±3 K.

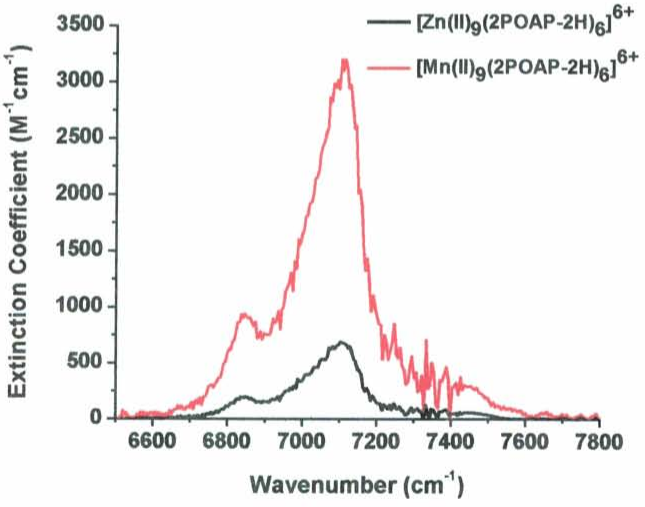

Figure 6.2.1.3.2. Overlaid NIR spectra of $[Mn_9^{II}(2POAP\text{-}2H)_6](ClO_4)_6$ with $[Zn_9^{II}(2POAP\text{-}2H)_6](NO_3)_6$ in acetonitrile at 298±3 K.

Table 6.2.1.3.1. Photophysical constants from analysis of the absorption profiles for $[Mn(II)_9(2POAP\text{-}2H)_6](ClO_4)_6$ and $[Zn(II)_9(2POAP\text{-}2H)_6](NO_3)_6$ in acetonitrile.

	$[Mn(II)_9(2POAP\text{-}2H)_6]^{6+}$				$[Zn(II)_9(2POAP\text{-}2H)_6]^{6+}$			
	G_a	G_b	G_c	G_d	G_a	G_b	G_c	G_d
λ_{abs}, nm		428	376	325	496	433	380	326
E_{abs}, cm^{-1}		23362	26601	30733	20151	23066	26289	30629
ε, cm^{-1} M^{-1}		10282	108182	47371	2013	18800	161008	57588
$\Delta\nu_{1/2}$, cm^{-1}		1280	4355	7476	2488	1167	4290	8487
f_{osc}		0.057	2.04	1.53	0.022	0.10	2.99	2.12
μ, eÅ		0.47	2.66	2.15	0.32	0.62	3.25	2.53
H_{DA}, cm^{-1}		3087			1768	3961		
E_{00}, cm^{-1}	~19935	22195	22703	20443	18280	21790	22515	19217
λ_o, cm^{-1}		709			1765	593		
λ_i, cm^{-1}		450			106	683		
λ_t, cm^{-1}		1167			1871	1276		
r_{DA}, (Å)		3.7			3.7	3.7		
Assignment	CT_o	CT_i	$(\pi\text{-}\pi^*)_{il}$	$(\pi\text{-}\pi^*)_{ol}$	CT_o	CT_i	$(\pi\text{-}\pi^*)_{il}$	$(\pi\text{-}\pi^*)_{ol}$

In Figure 6.2.1.3.1, the absorption spectrum for this complex is overlaid with the absorption spectrum for $[Zn(II)_9(2POAP\text{-}2H)_6](NO_3)_6$. The data in Figure 6.2.1.3.1 and Table 6.2.1.3.1 indicate that there is not much change in the ligand transition energies in going from $[Zn(II)_9(2POAP\text{-}2H)_6]^{6+}$ to $[Mn(II)_9(2POAP\text{-}2H)_6]^{6+}$ as the transition energies are similar. Moreover, the intensities of the transitions corresponding to the inner ligand are still larger than those corresponding to the outer ligand. However, the UV-Vis intensities of the absorption transitions in $[Mn(II)_9(2POAP\text{-}2H)_6]^{6+}$ are less that those observed in $[Zn(II)_9(2POAP\text{-}2H)_6]^{6+}$. NIR data given in Figure 6.2.1.3.2 illustrate the opposite effect where the intensities of the transitions for $[Mn(II)_9(2POAP\text{-}2H)_6]^{6+}$ are

greater than those in $[Zn(II)_9(2POAP\text{-}2H)_6]^{6+}$. As the metal-metal contacts in $[Zn(II)_9(2POAP\text{-}2H)_6]^{6+}$ and $[Mn(II)_9(2POAP\text{-}2H)_6]^{6+}$ range from 3.908 – 4.116 Å and 3.909 – 3.956 Å, respectively, the overall size of the metal core in $[Zn(II)_9(2POAP\text{-}2H)_6]^{6+}$ is larger than that in $[Mn(II)_9(2POAP\text{-}2H)_6]^{6+}$.[7, 8] Therefore, the ligand-ligand separation in $[Mn(II)_9(2POAP\text{-}2H)_6]^{6+}$ should be shorter than in $[Zn(II)_9(2POAP\text{-}2H)_6]^{6+}$. Since the NIR transitions have been assigned as interligand transitions, these transitions are expected to become more intense in $[Mn(II)_9(2POAP\text{-}2H)_6]^{6+}$ than in $[Zn(II)_9(2POAP\text{-}2H)_6]^{6+}$ as the separation between the ligands decreases allowing for greater electronic coupling between the ligand donor and acceptor orbitals involved in the transition (equations 6.2.1.3.1, 6.2.1.3.2, and 6.2.1.3.3).

$$H_{DA} = \frac{\mu \nu_{max}}{ed} \qquad \textit{eqn. 6.2.1.3.1.}$$

$$\mu^2 = \frac{f_{osc}}{(1.08x10^{-5})\nu_{max}} \qquad \textit{eqn. 6.2.1.3.2.}$$

$$\mu^2 = \left[\int \Psi_{gs}(\sum_{i=1}^{n} er_i)\,\Psi_{es}\right]^2 = \vec{M}^2 < \Psi_{gs}|\Psi_{es} >^2 \qquad \textit{eqn. 6.2.1.3.3.}$$

Moreover, since the ligand-ligand separation decreases in going from $[Zn(II)_9(2POAP\text{-}2H)_6]^{6+}$ to $[Mn(II)_9(2POAP\text{-}2H)_6]^{6+}$, and as discussed in section 5.2.3.6 for $[Zn(II)_9(2POAP\text{-}2H)_6]^{6+}$, the effect of ligand confinement in $[Mn(II)_9(2POAP\text{-}2H)_6]^{6+}$ should be more drastic and the intensities of the ligand transitions should increase for $[Mn(II)_9(2POAP\text{-}2H)_6]^{6+}$. However, the UV-Vis data indicate that the intensities of the ligand transitions are reduced when Mn(II) replaces Zn(II) in the grid complex.

In order to explain this phenomenon, the effect of spatial confinement should be revisited. In section 5.2.3.6, it was shown that by spatially confining a molecule, the amplitude of the wavefunction defining the molecule increases. As such, the overlap between ground and excited states for this molecule increases, and therefore, the intensities associated with the transition between these states increases. The potential energy surface defining the confined molecule is expected to be narrower than the same molecule in a less confined state. In terms of the ligands in the grid-type complexes studied here, the potential energy surface defining the inner ligand is narrower than the potential energy surface defining the outer ligand. As such, the force constants defining the inner ligand are greater than those defining the outer ligand. *The observation that the intensities of the ligand transitions are reduced when Mn(II) replaces Zn(II) in the grid complex is presumably associated with the effect of Zn(II) and Mn(II) on the force constants for the ligand.* In order for the ligand transitions to become less intense, the force constants associated with the ligand must decrease. This will only occur when ligand antibonding orbitals are involved in the binding event. In terms of the force constants for the ligands in $[Zn(II)_9(2POAP\text{-}2H)_6]^{6+}$ and $[Mn(II)_9(2POAP\text{-}2H)_6]^{6+}$, the decrease in the intensities when Mn(II) replaces Zn(II) is assumed to be due an enhanced interaction of the metal with the π^* orbitals on the ligand. Moreover, the difference in the rigid matrix energies for $[Zn(II)_9(2POAP\text{-}2H)_6]^{6+}$ and $[Mn(II)_9(2POAP\text{-}2H)_6]^{6+}$ appears to be reduction of this energy by ~1000 cm^{-1}. This difference is also assumed to be due to the decrease in the force constants in $[Mn(II)_9(2POAP\text{-}2H)_6]^{6+}$ through enhanced interaction of the metal with the π^* orbitals on the ligand.

As the Mn(II) ions in $[Mn(II)_9(2POAP\text{-}2H)_6]^{6+}$ are all high spin[8-10], d-d transitions involving high-spin d^5 complexes are spin forbidden and are expected to exhibit very weak extinction coefficients. For example, for $[Mn(H_2O)_6]^{2+}$, the d-d transition exhibits an extinction coefficient of ~ 10^{-2} $M^{-1}cm^{-1}$ at 18300 cm^{-1}.[11] The interaction of the metal with the π^* orbitals on the 2POAP ligand predisposes metal-to-ligand charge transfer (MLCT) to be a prominent factor in $[Mn(II)_9(2POAP\text{-}2H)_6]^{6+}$. As such, the unassigned transitions U_1 (16943 cm^{-1}) and U_2 (18314 cm^{-1}) are assigned to $d^5(\pi^*)^0 \rightarrow d^4(\pi^*)^1$ MLCT transitions. The fact that these transitions are not observed in $[Zn(II)_9(2POAP\text{-}2H)_6]^{6+}$ suggests that these transitions are not solely ligand based and must originate from Mn(II)-ligand interactions.

In order to assign the MLCT transitions to a specific metal center, the coordination spheres for Mn(II) in $[Mn(II)_9(2POAP\text{-}2H)_6]^{6+}$ must be analyzed. The coordination sphere associated with the Mn(II) ions in $[Mn(II)_9(2POAP\text{-}2H)_6]^{6+}$ may be divided into three specific coordination sites: *cis*-MnN_4O_2 (corner metal ions labelled α), *trans*-MnN_2O_4 (the central metal ion labelled γ), and *mer*-MnN_3O_3 (side center metal ions labelled β). This is shown in Figure 6.2.1.3.2. The specific coordination spheres containing their respective coordinating atoms are shown in Figure 6.2.1.3.3.

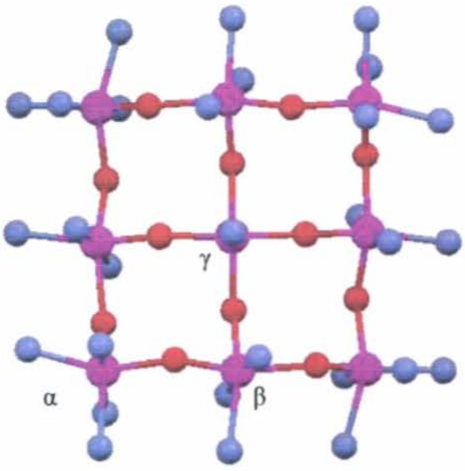

Figure 6.2.1.3.2. Coordination spheres for Mn(II) in $[Mn(II)_9(2POAP\text{-}2H)_6](ClO_4)_6$. The data were obtained from the CIF file attached with references [8, 9].

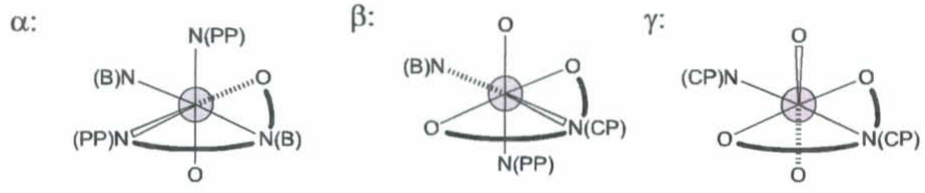

Figure 6.2.1.3.3. Coordination sites for Mn(II) in $[Mn(II)_9(2POAP\text{-}2H)_6](ClO_4)_6$.

Since the intraligand and interligand charge transfer transitions have been assumed to involve pyridine groups, it is likely that the MLCT transitions also involve these groups. Moreover, since the intraligand charge transfer transitions (CT_o and CT_i) are attributed to periphery pyridine groups acting as electron acceptors, it is suggested that the MLCT transitions also involve the periphery pyridine groups as electron acceptors. Therefore, $Mn^{II}(\alpha)$ and $Mn^{II}(\beta)$ centers are likely to be associated with the transitions at U_1 and U_2.

Furthermore, given the effect of spatial confinement on the intensities of the inner ligand, and that U_2 is more intense than U_1, U_2 is assigned to an MLCT transition involving $Mn^{II}(\beta)$ and an inner ligand. Likewise, U_1 is assigned to an MLCT involving $Mn^{II}(\alpha)$ and an outer ligand.

6.2.1.4. Emission

Coordination of Zn(II) is very similar to coordination of Mn(II) in that there is no crystal field stabilization energy (CFSE) associated with the coordination event. As such, all d-orbitals are occupied equally and there is no basis for Jahn-Teller distortions. When comparing emission spectra between $[Zn(II)_9(2POAP\text{-}2H)_6]^{6+}$ and $[Mn(II)_9(2POAP\text{-}2H)_6]^{6+}$, the Zn(II) complex is emissive whereas the Mn(II) complex is not. The overlaid emission spectra for the $Zn(II)_9$ grid and the $Mn(II)_9$ grid in acetonitrile is given in Figure 6.2.1.4.1. The data for $Mn(II)_9$ is attributed to light scattering in the instrument.

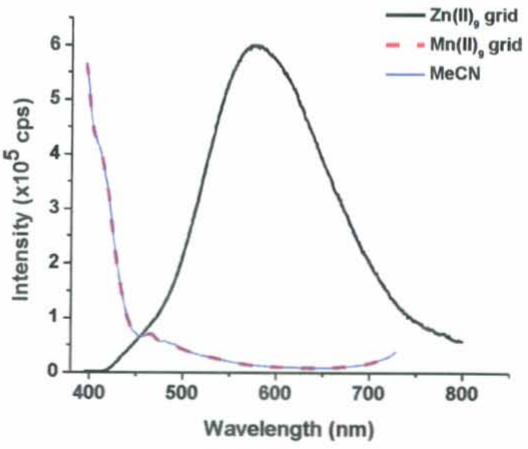

Figure 6.2.1.4.1. Overlay of emission spectra for $[Mn(II)_9(2POAP\text{-}2H)_6]^{6+}$ and $[Zn(II)_9(2POAP\text{-}2H)_6]^{6+}$ in acetonitrile at an excitation wavelength of 380 nm.

The main spectral differences in the excited states for $[Mn(II)_9(2POAP\text{-}2H)_6]^{6+}$ are the proposed MLCT transitions. Given that these transitions are the lowest-lying states, then the non-emissive nature of $[Mn(II)_9(2POAP\text{-}2H)_6]^{6+}$ may be attributed to these states. The MLCT transitions have been proposed to involve a $d^5(\pi^*)^0 \rightarrow d^4(\pi^*)^1$ transition. As the d-orbitals are not equally occupied in the $d^4(\pi^*)^1$, Jahn-Teller distortions play a major role in the structure of this state. The result is that the MLCT state will be highly distorted and exhibit enhanced non-radiative decay due to vibrational relaxation of the excited state. A Jablonski diagram is given in Figure 6.2.1.4.2.

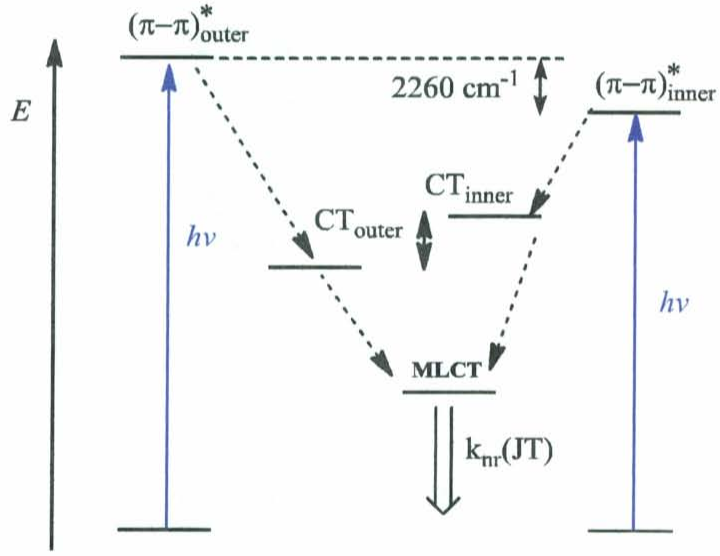

Figure 6.2.1.4.2. Electronic transition asymmetry in $[Mn_9^{II}(2POAP\text{-}2H)_6](ClO_6)_4$.

6.2.2. $[Mn_4^{III}Mn_5^{II}(2POAP\text{-}2H)_6](ClO_4)_{10}$

The first report on the optical states in 2POAP grid-type complexes was that presented for $[Mn_4^{III}Mn_5^{II}(2POAP\text{-}2H)_6](ClO_4)_{10}$.[10] Tentative assignments were

originally reported for selected transitions. Therefore, in this section, with the information presented in the previous sections of this chapter, conclusions are drawn with respect to these tentative assignments.

6.2.2.1. UV-Vis spectral deconvolution and band assignments

The UV-Vis absorption spectrum for $[Mn_4^{III}Mn_5^{II}(2POAP\text{-}2H)_6](ClO_4)_{10}$ is given in Figure 6.2.2.1.1. This spectrum was deconvoluted using first and second derivatives. The first and second derivative plots with the proposed locations of transitions are given in Figure 6.2.2.1.2. For a discussion on using first and second derivatives for deconvoluting spectra, see appendix D and section 5.2.3.1. The deconvoluted spectrum shows transitions located at 23132 cm^{-1} (432 nm, 4821 $M^{-1}cm^{-1}$), 26749 cm^{-1} (374 nm, 81159 $M^{-1}cm^{-1}$), 29750 cm^{-1} (336 nm, 61448 $M^{-1}cm^{-1}$), 38903 cm^{-1} (257 nm, 43014 $M^{-1}cm^{-1}$), 47735 cm^{-1} (209 nm, 147635 $M^{-1}cm^{-1}$), and ~52632 cm^{-1} (190 nm, 132073 $M^{-1}cm^{-1}$). These transitions are designated as G_b, G_c, G_d, G_e, G_f, and G_g respectively. All proposed transition maxima can be justified with the first derivative as zero and the second derivative as negative except for G_b, G_c, G_e, and G_f. These transitions are, however, justified from the pattern displayed by the second derivative.

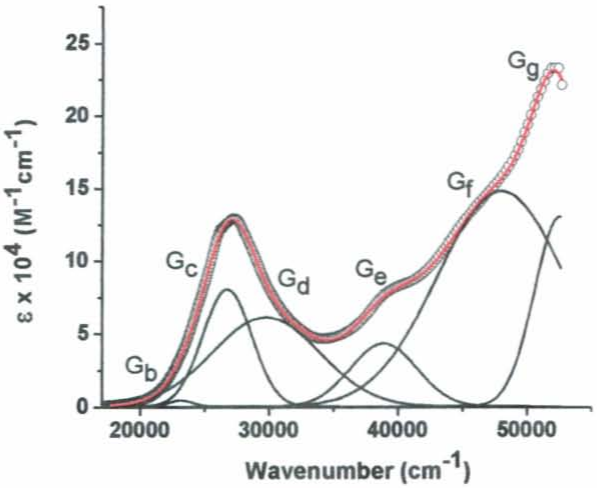

Figure 6.2.2.1.1. Deconvoluted UV-Vis absorption spectrum of $[Mn(III)_4Mn(II)_5(2POAP\text{-}2H)_6](ClO_4)_{10}$ in acetonitrile at 298±3 K.

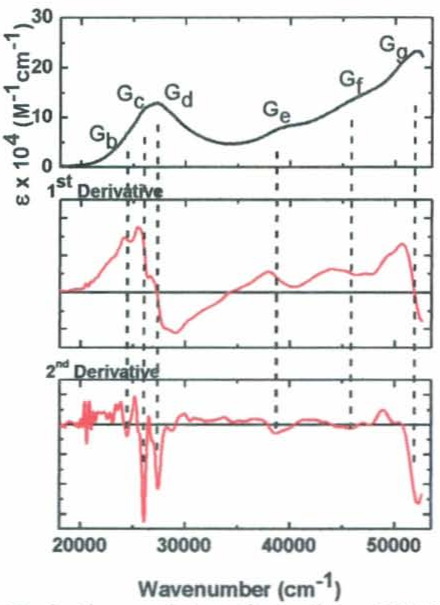

Figure 6.2.2.1.2. Derivative plots for the UV-Vis spectrum of a $[Mn(III)_4Mn(II)_5(2POAP\text{-}2H)_6](ClO_4)_{10}$ solution in acetonitrile.

A summary of the photophysical parameters obtained on the deconvoluted UV-Vis spectrum for $[Mn(III)_4Mn(II)_5(2POAP\text{-}2H)_6](ClO_4)_{10}$ is given in Table 6.2.2.1.1. The deconvoluted absorption transitions G_b, G_c, G_d, G_e, G_f, and G_g in Figure 6.2.2.1.1 have been assigned as CT_i, $(\pi\text{-}\pi^*)_{i1}$, $(\pi\text{-}\pi^*)_{o1}$, $(\pi\text{-}\pi^*)_{i2}$, $(\pi\text{-}\pi^*)_{o2}$, and $(\pi\text{-}\pi^*)_{i3}$ based on the assignments made for $[Mn(II)_9(2POAP\text{-}2H)_6](NO_3)_6$ previously. The previously deconvoluted UV-Vis spectrum from 7200 cm^{-1} to 20000 cm^{-1} is given in Figure 6.2.2.1.3 and shows low-energy transitions designated as band I, band II, band III, and band IV, respectively.[10]

Table 6.2.2.1.1. Summary of the spectroscopic parameters for $[Mn(III)_4Mn(II)_5(2POAP\text{-}2H)_6](ClO_4)_{10}$ in acetonitrile using absorption analysis described in section 5.2.3.4.

	G_b	G_c	G_d	G_e	G_f	G_g
λ_{abs}, nm	432	374	336	257	209	[a]190
E_{abs}, cm^{-1}	23132	26749	29750	38903	47735	[a]52632
ε, cm^{-1} M^{-1}	4821	81159	61448	43014	147635	[a]132073
$\Delta\nu_{1/2}$, cm^{-1}	2479	4425	9776	6392	11120	
f_{osc}	0.052	1.56	2.60	1.19	7.11	
μ, eÅ	0.46	2.32	2.84	1.68	3.71	
H_{DA}, cm^{-1}	2927					
E_{00}, cm^{-1}	21126	22895	21259	33867	38284	[a]48784
r_{DA}, (Å)	3.7					
Assignment	CT_i	$(\pi\text{-}\pi^*)_{i1}$	$(\pi\text{-}\pi^*)_{o1}$	$(\pi\text{-}\pi^*)_{i2}$	$(\pi\text{-}\pi^*)_{o2}$	$(\pi\text{-}\pi^*)_{i3}$

[a] estimated as transition is not fully resolved.

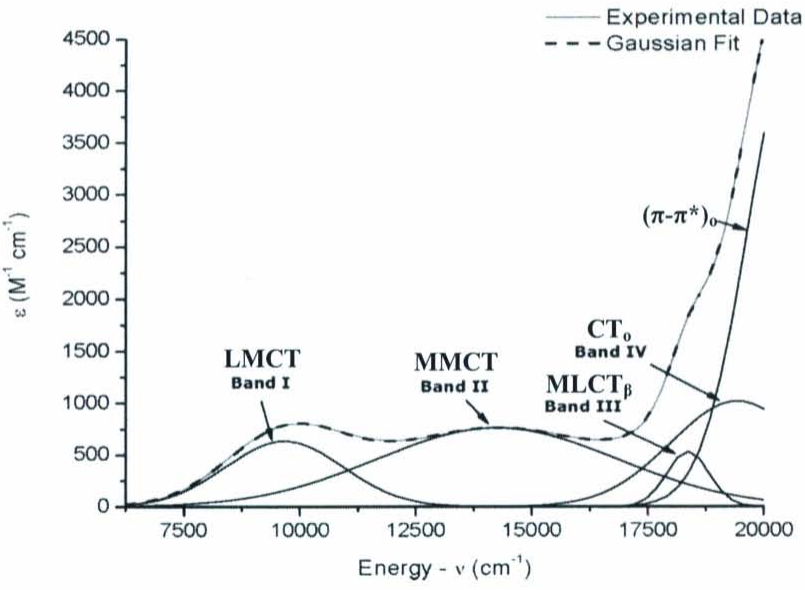

Figure 6.2.2.1.3. Reassignment of the excited states in the $[Mn_4^{III}Mn_5^{II}(2POAP\text{-}2H)_6]^{10+}$ complex. Reprinted with permission from reference [10]. Copyright 2006 Royal Society of Chemistry.

Bands I and II have been assigned as ligand-to-metal charge transfer (LMCT) and metal-metal charge transfer (MMCT) based on the $\Delta\nu_{1/2}$ values for these bands and λ_t. Given the degree of Jahn-Teller distortions associated with a Mn(II)→Mn(III) transition, and given that one would expect a greater reorganization associated with a MMCT transition, band II is assigned as MMCT since it demonstrates the greatest reorganization energy. Moreover, band I is assigned as LMCT given the solvent dependent data associated with this transition.[10] In addition, bands I and II are likely associated with the metal core since transitions involving the ligand are not observed in this area of the spectrum for $[Mn(II)_9(2POAP\text{-}2H)_6]^{6+}$ and $[Zn(II)_9(2POAP\text{-}2H)_6]^{6+}$.

For the $[Mn(III)_4Mn(II)_5(2POAP\text{-}2H)_6]^{10+}$ system, bands III and IV were not previously assigned. The high-energy transition was previously assigned to a metal-to-ligand charge transfer. However, given the data presented in Figure 6.2.2.1.1, this high-energy transition is reassigned as a (π-π^*) transition located on the outer ligand.

As was a constant theme when analyzing spectra of $[Zn(II)_9(2POAP\text{-}2H)_6]^{6+}$ and $[Mn(II)_9(2POAP\text{-}2H)_6]^{6+}$, the effect of the solvent on the ligand electronic structure appears more pronounced when comparing E_{00} values for (π-π^*) and charge-transfer transitions on each ligand. The E_{00} values for the $(\pi\text{-}\pi^*)_i$ and $(\pi\text{-}\pi^*)_o$ transitions were estimated to be 22895 cm^{-1} and 21259 cm^{-1}, respectively. Therefore, the difference between the (π-π^*) transition energies is 1636 cm^{-1}. Since the electronic excitation energies for the previously classified grid-type complexes were offset as a result of the specific location of the ligand within the complex, then we can assume that the energy difference between the inner and outer (π-π^*) transitions is equivalent to the difference in energy between the E_{00} values for the intraligand charge-transfer transitions on the inner and outer ligand. Therefore, the value of E_{00} for the CT_o transition is expected to be at 19490 cm^{-1}. This energy is located near band IV. Thus, band IV is assigned to the CT_o transition which was designated G_a in the previous complexes.

To assign band III, the excited states for $[Mn(II)_9(2POAP\text{-}2H)_6]^{6+}$ must be revisited. In the $Mn(II)_9$ system, the lowest lying excited states were attributed the MLCT transitions due to π back bonding associated with the metal. There were two MLCT states which involved the corner $Mn^{II}(\alpha)$ and side $Mn^{II}(\beta)$ ions. In forming $[Mn(III)_4Mn(II)_5(2POAP\text{-}2H)_6]^{10+}$, the four corner $Mn^{II}(\alpha)$ ions were oxidized to Mn(III).[10] Therefore, it is anticipated that the MLCT transitions associated with the side

$Mn^{II}(\beta)$ ions should still be present. This transition was located at 18314 cm^{-1} in $[Mn(II)_9(2POAP\text{-}2H)_6]^{6+}$. In the spectrum for $[Mn(III)_4Mn(II)_5(2POAP\text{-}2H)_6]^{10+}$ in Figure 6.2.2.1.3, 18314 cm^{-1} is directly located at the position of band III. Therefore, band III is assigned to the MLCT transition involving the $Mn^{II}(\beta)$ ion. This is labelled as $MLCT_\beta$ in Figure 6.2.2.1.3.

6.2.2.2. NIR spectrum

NIR absorption data on $[Mn(III)_4Mn(II)_5(2POAP\text{-}2H)_6]^{10+}$ is given in Figure 6.2.2.2.1. A band centered at 1406 nm is observed; this is not surprising given that $[Mn(II)_9(2POAP\text{-}2H)_6]^{6+}$ and $[Mn(II)_9(2POAP\text{-}2H)_6]^{6+}$ display this same transition. However, what is apparent is that the intensity of this transition is low. This low intensity is most likely due to the fact that the ligand structure in $[Mn(III)_4Mn(II)_5(2POAP\text{-}2H)_6]^{10+}$ is much more distorted than in $[Mn(II)_9(2POAP\text{-}2H)_6]^{6+}$ due to a distribution of Jahn-Teller distortions along the corners of the metal core. As such, this will lead to a significant increase in the ligand-ligand distances within the structure. This results in a reduction in the orbital overlap between the orbitals involved in the transition and a decrease in electronic coupling.

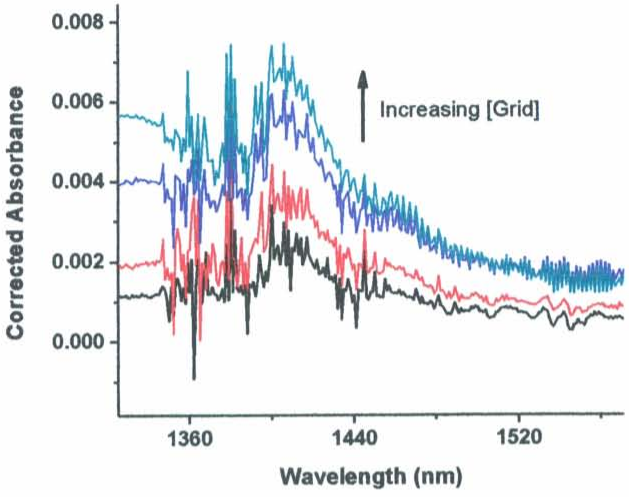

Figure 6.2.2.2.1. Vis-NIR absorption spectra of $[Mn(III)_4Mn)II)_5(2POAP\text{-}2H)_6]^{10+}$ in d_3-acetonitrile.

6.2.2.3. Emission

Excited state analysis on $[Mn(III)_4Mn(II)_5(2POAP\text{-}2H)_6]^{10+}$ has yet to detect any type of emission. However, as the lowest-lying state in the $[Mn(III)_4Mn(II)_5(2POAP\text{-}2H)_6]^{10+}$ system is attributed to a LMCT near ~700 nm, and the instrument used in detecting emission is only effective to ~900 nm, the existence of an emissive state may be observed if one detects below 900 nm. Until such an analysis, the $[Mn(III)_4Mn(II)_5(2POAP\text{-}2H)_6]^{10+}$ complex is assumed to be non-emissive. This assumption is plausible when considering the effect of Jahn-Teller distortions on the LMCT state. The LMCT state is composed of a $d^4(\pi)^2 \rightarrow d^5(\pi)^1$ transition. The initially distorted Mn(III) (i.e. d^4) center becomes Mn(II) (i.e. d^5) upon excitation. The net effect is

a Jahn-Teller distortion of the coordination sphere associated with Mn(II). The result is that the LMCT state will be highly distorted and exhibit enhanced non-radiative decay due to vibrational relaxation of the LMCT state. A Jablonski diagram illustrating electronic transition asymmetry is given in Figure 6.2.2.3.1.

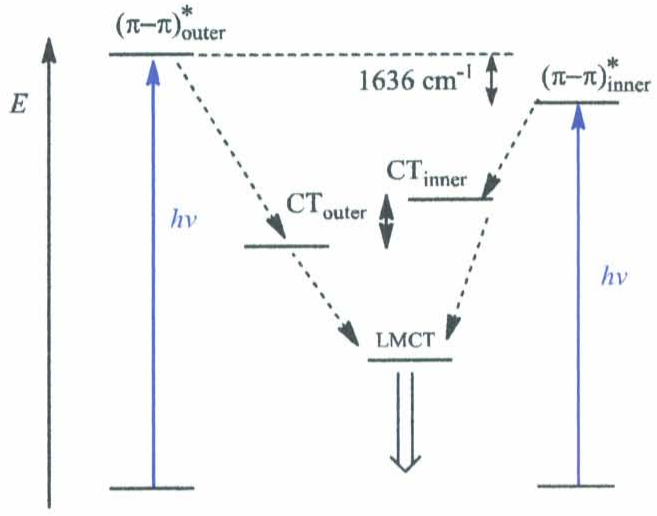

Figure 6.2.2.3.1. Electronic transition asymmetry in $[Mn(III)_4Mn(II)_5(2POAP\text{-}2H)_6]^{6+}$.

6.3. Conclusion

In this chapter, the effect of the metal core on $[Mn(II)_9(2POAP\text{-}2H)_6]^{6+}$ and $[Mn(III)_4Mn(II)_5(2POAP\text{-}2H)_6]^{10+}$ excited states has been discussed. Overall, in going from a closed-shell metal system in $[Zn(II)_9(2POAP\text{-}2H)_6]^{6+}$ to an open-shell metal system in $[Mn(II)_9(2POAP\text{-}2H)_6]^{6+}$, the energies of the ligand states were not appreciably affected. The main effect appears to be the intensity of the ligand transitions, which were lowered in the UV-Vis region in going from a $[Zn(II)_9(2POAP\text{-}2H)_6]^{6+}$ system to a

$[Mn(II)_9(2POAP\text{-}2H)_6]^{6+}$ system. Moreover, the intensity of the interligand transitions were increased in the NIR region in going from $[Zn(II)_9(2POAP\text{-}2H)_6]^{6+}$ to $[Mn(II)_9(2POAP\text{-}2H)_6]^{6+}$. Given that Jahn-Teller distortions have a greater influence on the coordination spheres in Mn(III) metal centers than in Mn(II) and Zn(II), the effect of the metal core on the ligand excited states has been shown to provide a means to modulate the Franck-Condon factors and the electronic coupling between intraligand *and* interligand states.

6.4. References

[1] J. M. Giaimo, A. V. Gusev and M. R. Wasielewski, *Journal of the American Chemical Society* **2002**, *124*, 8530.

[2] M. R. Wasielewski, *Accounts of Chemical Research* **2009**, *42*, 1910.

[3] A. S. Lukas, P. J. Bushard and M. R. Wasielewski, *The Journal of Physical Chemistry A* **2001**, *106*, 2074.

[4] A. S. Lukas, Y. Zhao, S. E. Miller and M. R. Wasielewski, *The Journal of Physical Chemistry B* **2002**, *106*, 1299.

[5] B. Rybtchinski, L. E. Sinks and M. R. Wasielewski, *Journal of the American Chemical Society* **2004**, *126*, 12268.

[6] K. D. Demadis, C. M. Hartshorn and T. J. Meyer, *Chemical Reviews* **2001**, *101*, 2655.

[7] L. K. Thompson, L. Zhao, Z. Xu, D. O. Miller and W. M. Reiff, *Inorganic Chemistry* **2002**, *42*, 128.

[8] L. Zhao, C. Matthews, L. K. Thompson and S. L. Heath, *Royal Society of Chemistry, Chem. Commun.* **2000**, 265.

[9] L. Zhao, Z. Xu, H. Grove, V. A. Milway, L. N. Dawe, T. S. M. Abedin, L. K. Thompson, T. L. Kelly, R. G. Harvey, D. O. Miller, L. Weeks, J. G. Shapter and K. J. Pope, *Inorganic Chemistry* **2004**, *43*, 3812.

[10] V. A. Milway, S. M. T. Abedin, V. Niel, T. L. Kelly, L. N. Dawe, S. K. Dey, D. W. Thompson, D. O. Miller, M. S. Alam, P. Muller and L. K. Thompson, *Dalton Transactions* **2006**, 2835.

[11] G. Miessler and D. Tarr, *Inorganic Chemistry*, 3 ed., Pearson Prentice Hall, New Jersey, **2004**.

Chapter 7:

"ELECTRONIC EXCITATION ENERGY TRANSFER"

Abstract: The purpose of this chapter is to introduce electronic excitation energy transfer theory which will be utilized in the next chapter involving the $Zn(II)_9$ grid-type complex. In this chapter, electronic excitation energy transfer will be presented in terms of the formalisms proposed by Förster and Dexter. Excitation energy transfer will then be discussed in terms of an excitonic model which is typically used for compact nanoscale systems.

7.1. Introduction

The hierarchy of life is ultimately driven by the photosynthetic organism through which higher-order organisms obtain their energy needs. Moreover, it is through solar energy that the photosynthetic organism meets its energy requirements. Solar energy is a clean and abundant energy source; however, it is intermittent and dispersed over a large area. In order for the photosynthetic organism to make use of solar energy, solar energy must be concentrated and stored in the form of a readily consumable molecule (i.e. a fuel) within the organism. For billions of years, nature has implemented a light harvesting process by which it concentrates solar energy to drive the formation of new chemical bonds. This light harvesting process transports light energy absorbed by antenna pigments from their initial location to a reaction center (via electronic excitation energy transfer) where this energy storage process occurs. [1] Electronic excitation energy transfer typically occurs over relatively large distances on the order of hundreds of Angstroms. This process is very fast as it must out-compete other excited state deactivation processes such as internal conversion and intersystem crossing which occur on the nanosecond timescale. The photosynthetic apparatus in purple bacteria is illustrated in Figure 7.1.1.

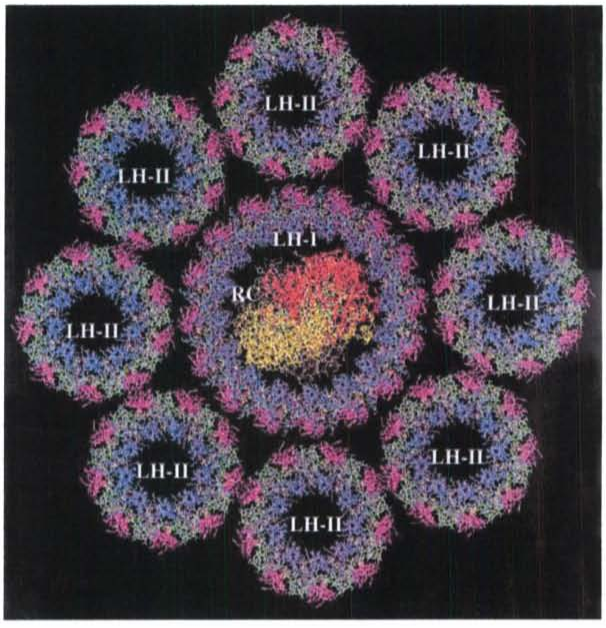

Figure 7.1.1. The photosynthetic apparatus in purple bacteria. LH-I and LH-II refer to the light harvesting complexes I and II respectively. RC refers to the photosynthetic reaction center. Reprinted with permission from reference [2]. Copyright 2002 Cambridge University Press.

The light-harvesting system in purple bacteria is expanded in Figure 7.1.2. The overall energy transfer process is illustrated in Figure 7.1.3. In the photosynthetic apparatus of this bacterium, photons are initially captured by a system of light-harvesting antenna which funnels electronic excitation energy to a special pair of porphyrin molecules P_A and P_B. These antennae are composed of many chlorophyll and carotenoid molecules, all of which are confined within the membrane environment.

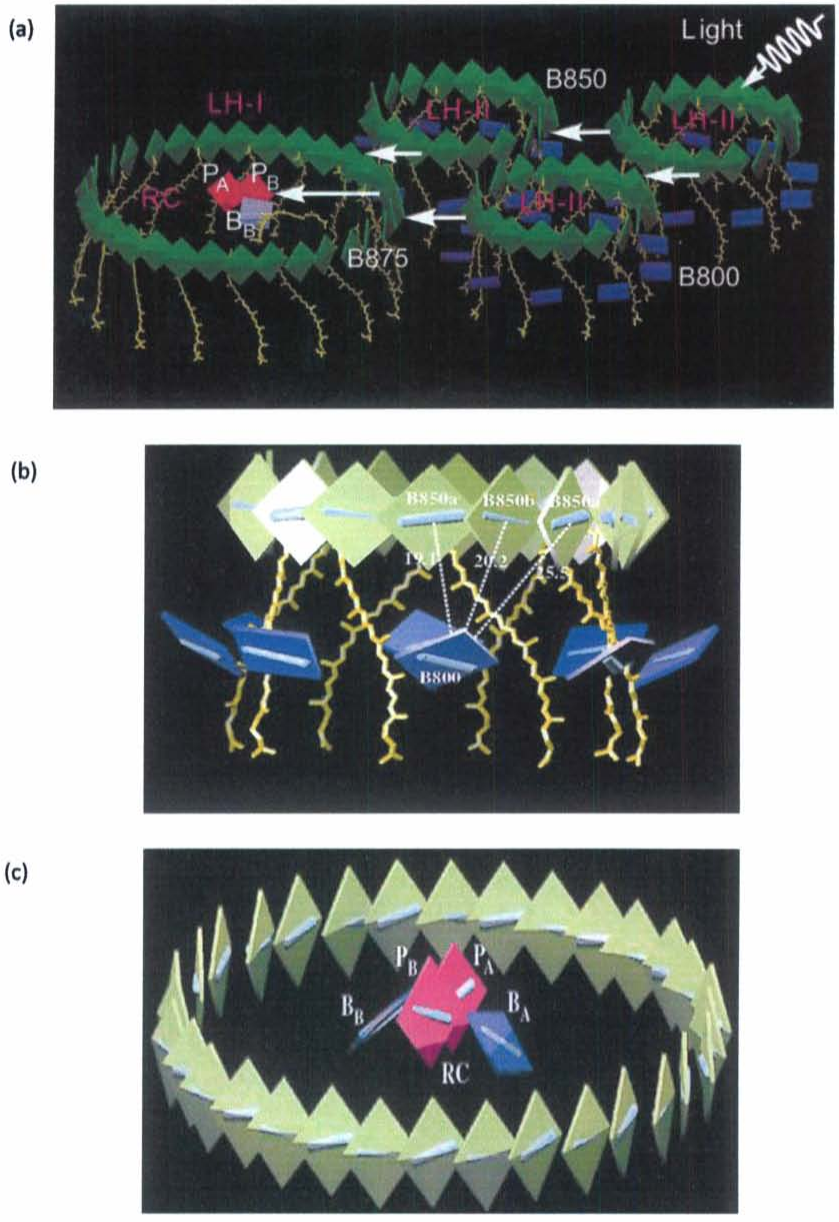

Figure 7.1.2. Solar antennae system in bacterial photosynthetic apparatus. (a) the energy transfer scheme; (b) structure of LH-II; and (c) the structure of LH-I. Reproduced with permission from reference [3]. Copyright 1998 National Academy of Sciences.

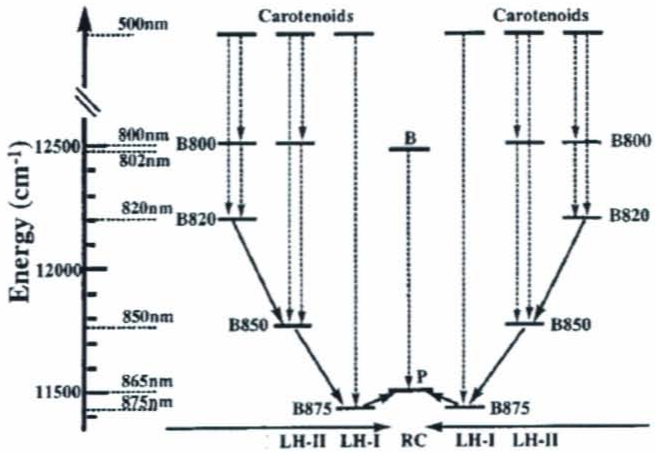

Figure 7.1.3. The energetics of energy transfer in photosynthesis. Solid lines imply intermolecular transitions whereas dashed lines imply intramolecular transitions. Reproduced with permission from reference [3]. Copyright 1998 National Academy of Sciences.

Within LH-II, bacteriochlorophyll molecules (B800) and carotenoids absorb light between 500-800 nm and transfer this electronic excitation energy to a cluster of B850 molecules within 700 fs.[2-4] This energy is then transferred to the B875 molecules of LH-I which surrounds the reaction center within 4 ps.[2-4] Finally, this collected energy is transferred to the reaction center where charge separation occurs within 35 ps.[2-4] The confinement of B800 and B875 molecules allows for strong exciton coupling, giving rise to quantum effects such as exciton migration.[5, 6]

Overall, photosynthesis is a process that utilizes a unique molecular construct in which solar energy is absorbed by specifically placed chromophores. This energy is then concentrated via funnelling excitation energy to a reaction center where it is converted to redox equivalents. The photosynthetic apparatus illustrates an important aspect of nature

and its ability to carry out the intricate processes involved in life: useful functions performed by biological systems result from chemical constructs which exhibit a high-degree of organization in terms of space, time, and energy. Therefore, studying energy transfer and its conversion in highly-organized molecular constructs, such as the grid-type complex, inevitably allows one to study energy, and its subsequent transfer and conversion, as a function of the spatial arrangement of atoms and molecules within the construct. In the following sections of this chapter, the theoretical models which describe excitation energy transfer will be presented.

7.2. Electronic excitation energy transfer

The constructive overlap of molecular orbitals (or wavefunctions) can result in a stabilizing electronic exchange interaction between the electrons in these orbitals if the orbitals are not completely filled. For example, the interaction of a half-filled HOMO in *D with that of the filled HOMO in A, and the half-filled LUMO in *D with the LUMO in A is stabilizing. The degree of this stabilization depends on the energy difference between the interacting orbitals and the net constructive overlap between their wavefunctions. The net effect can result in either the formal transfer of an electron or transfer of the electronic excitation energy. These net effects are dictated by the degree of orbital overlap and electronic exchange. Therefore, interactions of excited state molecules with other molecules may result in the transfer of excitation energy to form a new excited state (equation 7.2.1).

$$D + A \xrightarrow{h\nu} {}^{*}D + A \xrightarrow{k_{ent}} D + {}^{*}A \qquad \textit{eqn. 7.2.1.}$$

In describing electron transfer in Chapter 4, electron transfer was shown to involve orbital overlap. However, excitation energy transfer does not necessarily involve orbital overlap; it may occur by electron exchange involving orbital overlap or by a dipole-dipole interaction which occurs through an oscillating electric field in space. The key difference between these mechanisms is that the electron exchange mechanism involves orbital overlap whereas the dipole-dipole mechanism does not and can occur over longer distances.

There are three mechanisms by which excitation energy can be transferred from one molecule to another. The first, trivial mechanism, occurs when a photon emitted by D* is subsequently absorbed by A. The second, the Förster mechanism, requires dipole-dipole coupling between the molecules involved. Lastly, in the third, the Dexter mechanism, exchange coupling between molecules is heavily implicated.

7.2.1. Trivial excitation energy transfer

Excitation energy transfer may occur in the absence of any electronic interaction (i.e. electron exchange or dipole-dipole) between the molecules involved in the energy transfer event. In this mechanism, one of the molecules involved is promoted to its excited state via electronic excitation and this excitation energy is transferred radiatively from this molecule to an energy acceptor. This occurs through emission of a photon from the excited molecule and absorption of this photon by the energy acceptor. This may be easily visualized as a photon hopping mechanism and classified as radiative emission-absorption excitation energy transfer.[7] This occurs when there is substantial overlap of the emission and absorption spectrum between the uncoupled emitting and absorbing

molecules (eqn. 7.2.1.1 and 7.2.1.2).[7] This mechanism is similar to the Förster mechanism discussed below except that the energy donor and acceptor are not coupled to one another.

$$*D \longrightarrow D + h\upsilon \qquad \textit{eqn. 7.2.1.1.}$$

$$h\upsilon + A \longrightarrow *A \qquad \textit{eqn. 7.2.1.2.}$$

7.2.2. Förster excitation energy transfer

In the Förster mechanism for electronic energy transfer, a dipole-dipole resonance interaction is involved which operates through an oscillating electric field produced by a molecule in its excited state (i.e. *D).[7-9] This mechanism may be viewed much like the interaction of light and matter where the electrons of a molecule oscillate along the nuclear framework. In the ground state, electrons oscillate at some resting frequency. However, in the excited state, electrons oscillate at a frequency which is governed by the force constants of the bonds expressed by the excited state potential energy surface. As a result of such oscillations, an oscillating electric dipole is created.

Consider a system consisting of an energy transfer donor D and acceptor A. Excitation of D produces *D. Since *D is oscillating at an increased frequency along the nuclear framework of D, the magnitude of this oscillating electric dipole is much greater than the oscillating electric dipole exhibited by a species in its ground state. Therefore, the oscillating electric dipole in *D can be assumed to possess a dominating oscillating electric dipole over A and can be viewed to oscillate about the nuclear framework of D. The net effect of *D on A can be visualized as A being driven into resonance by the

oscillating electric field generated by *D assuming that the frequency of this oscillation matches the frequency for oscillation in A, and that D and A are sufficiently close to allow for resonance to take place.[7-9] This, then, results in the flow of excitation from *D to A to form *A. As such, in the Förster mechanism, the transitions *D→D and A→*A occur as resonance where the oscillating electric field of *D leads to a coupled oscillating electric field on A to form *A. This mechanism is illustrated in Figure 7.2.2.1.

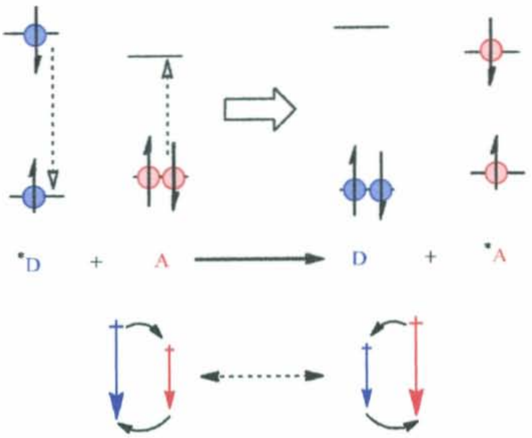

Figure 7.2.2.1. Förster excitation energy transfer mechanism. The double-headed arrows correspond to oscillating dipoles.

Quantum mechanically, the Förster mechanism (and energy transfer in general!) may be described as follows. Consider the energy transfer process given below.

$$*D + A \longrightarrow D + *A \qquad \textit{eqn. 7.2.2.1.}$$

The initial state and final state may be described in terms of the following wavefunctions where Ψ_i and Ψ_f are the total wavefunctions describing the initial and final state for the system.

$$\Psi_i = \Psi(^*D)\Psi(A) \qquad \textit{eqn. 7.2.2.2.}$$

$$\Psi_f = \Psi(D)\Psi(^*A) \qquad \textit{eqn. 7.2.2.3.}$$

The operator which provides the dipole-dipole interaction and mixes the initial and final states may be defined by H_{dd}. Thus, according to the time-independent Schrödinger equation:

$$\langle\Psi_i|H_{dd}|\Psi_f\rangle = E_{dd}\langle\Psi_i|\Psi_f\rangle \approx E_{dd}\langle\psi_i|\psi_f\rangle\langle S_i|S_f\rangle\langle\chi_i|\chi_f\rangle \qquad \textit{eqn. 7.2.2.4.}$$

This expression suggests that energy transfer via the Förster mechanism must be orbitally allowed (in that the orbitals involved cannot be orthogonal), spin allowed, and vibrationally allowed. Therefore, singlet-triplet excitation energy transfer is highly unlikely as spin must be conserved throughout the process.

To reduce equation 7.2.2.4, one may note that the energy associated with the electrostatic interaction of two dipoles is related to the magnitude of these interacting dipoles and the distance between them as given below[7-9].

$$E_{dd} = \alpha\frac{\mu_D\mu_A}{R_{DA}^3} \qquad \textit{eqn.7.2.2.5.}$$

Thus, equation 7.2.2.4 may be expressed as,

$$\langle\Psi_i|H_{dd}|\Psi_f\rangle = \alpha \frac{\mu_D \mu_A}{R_{DA}^3} \langle\psi_i|\psi_f\rangle\langle S_i|S_f\rangle\langle\chi_i|\chi_f\rangle \quad eqn.\ 7.2.2.6.$$

In equations 7.2.2.5 and 7.2.2.6, α is a proportionality constant, μ_D is the transition dipole of the donor, μ_A is the transition dipole of the acceptor, and R is the distance between the donor and the acceptor. In addition, ψ, S, and χ are the electronic, spin, and vibrational wavefunctions, respectively.

From equation 7.2.2.6, one can conclude that excitation energy transfer via the Förster mechanism is primarily associated with singlet-singlet energy transfer since triplet transition dipoles are relatively weak, and therefore, highly improbable through application of the Fermi Golden rule to energy transfer given in equation 7.2.2.7 which reduces to equation 7.2.2.8.[7, 9]

$$k_{ET} = \left(\frac{2\pi}{\hbar}\right) \langle\Psi_{D^*}|H_{dd}|\Psi_A\rangle^2 = \left(\frac{2\pi}{\hbar}\right) [\langle\psi_{D^*}|\psi_A\rangle\langle S_{D^*}|S_A\rangle\langle\chi_{D^*}|\chi_A\rangle]^2 \quad eqn.\ 7.2.2.7.$$

$$k_{ET} = \left(\frac{2\pi}{\hbar}\right) V_{en}^2 \langle\chi_{D^*}|\chi_A\rangle^2 = \left(\frac{2\pi}{\hbar}\right) V_{en}^2 F(calc) \quad eqn.\ 7.2.2.8$$

Based on the equations 7.2.2.7 and 7.2.2.8, the electronic wavefunctions cannot be orthogonal and therefore the coupling of the transition dipole moments is angle dependent. In addition, spin must be conserved as $\langle S_i|S_f\rangle \neq 0$. More specifically, the rate constant for Förster energy transfer is given by equation 7.2.2.9[7, 10] where Φ_D is the emission quantum yield of the donor, η is the refractive index of the medium, τ_D is the donor lifetime, N_A is the Avogadro constant, R_{DA} is the distance between the energy transfer donor and acceptor, and κ^2 is the orientation factor which is defined by the total angle (ϕ_T) between the transition dipoles of the donor and the acceptor given in equation

7.2.2.10.[7, 9, 10] Φ_D and Φ_A are the angles linking the dipole moments of the donor and acceptor with the distance vector between the two.

$$k_{E_nT}^{Forster} = \frac{9000(\ln 10)\kappa^2 J_{DA}\phi_D}{128\pi^5 N_A \tau_D \eta R_{DA}^6} = \frac{1}{\hbar^2 c}|V_{DA}|^2 J_{DA} \qquad \textit{eqn. 7.2.2.9.}$$

$$\kappa^2 = (\cos\phi_T - 3\cos\phi_D \cos\phi_A) \qquad \textit{eqn. 7.2.2.10.}$$

This equation specifically reflects a resonance energy requirement: the energy emitted by the donor must match that absorbed by the acceptor. Thus, it is required that the emission spectrum of the donor overlaps the absorption spectrum of the acceptor. This is reflected by J_{DA} which is the spectral overlap integral between the emission spectrum of the donor and the absorption spectrum of the acceptor defined by equation 7.2.2.11 where F_D is the normalized emission spectrum of the donor, and $\varepsilon_A(\upsilon)$ is the absorption profile for the acceptor in units of molar absorptivity.[7, 9, 10]

$$J_{DA} = \int \frac{F_D(\upsilon)\varepsilon_A(\upsilon)}{\upsilon^4} \qquad \textit{eqn. 7.2.2.11.}$$

7.2.3. Dexter excitation energy transfer

A similar quantum mechanical formulation as in equations 7.2.2.4 and 7.2.2.7 may be developed for energy transfer via the Dexter (or exchange) mechanism by replacing H_{dd} with $H_{exchange}$ and E_{dd} with $E_{exchange}$.[7, 8, 11] It may be viewed as a simultaneous two electron transfer process. As such, the formalisms associated with the theory of energy transfer via the Dexter mechanism follows closely to those associated with Marcus theory for single electron transfer. In the Dexter mechanism, energy transfer

is induced by the electron exchange interactions of the donor and the acceptor resulting from direct orbital interaction of the donor and acceptor (Figure 7.2.3.1).[7, 8, 11]

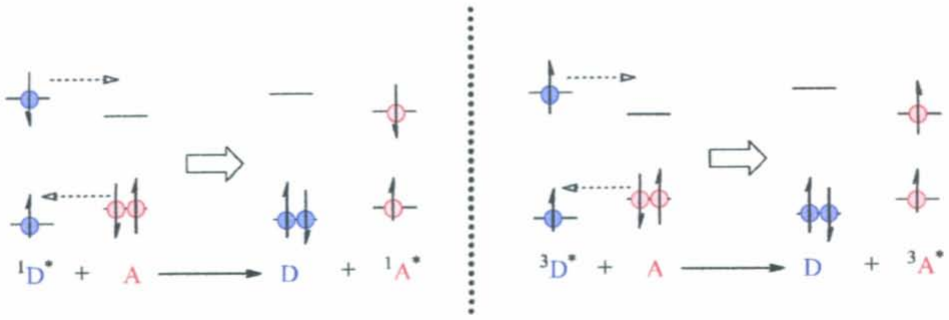

Figure 7.2.3.1. Dexter mechanism for excitation energy transfer.

Consideration of these interactions yields the rate constant for energy transfer via the Dexter mechanism (equation 7.2.3.1)[7, 8, 11, 12]:

$$k_{ET}^{Dexter} = KJ' \exp\left(\frac{-2R_{DA}}{R^o}\right) \quad eqn.\ 7.2.3.1.$$

where J' is the overlap integral defined by equation 7.2.2.10 and reflects the extent to which the donor and acceptor absorption spectrums overlap; K is an experimental constant which relates the magnitude of the orbital interaction for electron exchange; R_{DA} is the distance between the donor and acceptor; and R^o is the sum of the Van Der Waals radii of the donor and acceptor. The efficiency of energy transfer via the exchange mechanism decreases exponentially with donor-acceptor distance.

7.2.4. Driving force correlations in excitation energy transfer

In the Dexter mechanism, electron transfer was summarized as a two-electron transfer process. As such, it is expected that driving force (ΔG) dependence should be similar. The rate constant for energy transfer is related to the square of the electronic coupling matrix element (V^2) and the Franck-Condon vibrational overlap (F(Calc)) as is given by equation 7.2.4.1 where F(calc) is defined in equation 7.2.4.2.[13, 14]

$$k_{ET} = \left(\frac{2\pi}{\hbar}\right) V_{en}^2 \langle \chi_{D^*} | \chi_A \rangle^2 = \left(\frac{2\pi}{\hbar}\right) V_{en}^2 F(calc) \qquad \textit{eqn. 7.2.4.1}$$

$$F(calc) = \frac{1}{(4\pi\lambda_o k_B T)^{\frac{1}{2}}} \left[\sum_{n^*=0}^{\infty} \sum_{m=0}^{\infty} e^{-S_D} e^{-S_A} \left(\frac{S_D^{n^*}}{n^*!}\right) \left(\frac{S_A^m}{m!}\right)\right] e^{-\left[\frac{(\Delta G + \lambda_o + m\hbar\omega_D + n^*\hbar\omega_A)^2}{4\lambda_o k_B T}\right]}$$

eqn. 7.2.4.2.

In equation 7.2.4.2, S_D and S_A are the electron-vibrational coupling constants, $\hbar\omega_D$ and $\hbar\omega_A$ are the donor and acceptor quantum spacing, k_B is the Boltzmann constant, m and n* are the vibrational quantum numbers for the donor and acceptor, and λ_o is the solvent reorganization energy term given as the sum of the solvent reorganization terms associated with the donor ($\lambda_{o,D}$) and the acceptor ($\lambda_{o,A}$) in equation 7.2.4.3.[14]

$$\lambda_o = \lambda_{o,D} + \lambda_{o,A} \qquad \textit{eqn. 7.2.4.3.}$$

As F(calc) ~ exp[-$(\Delta G)^2$] and k_{ET} ~ F(calc), then it is expected that the rate constant for energy transfer (k_{ET}) will exhibit similar Marcus behaviour and a Marcus inverted region. This is illustrated in Figure 7.2.4.1.

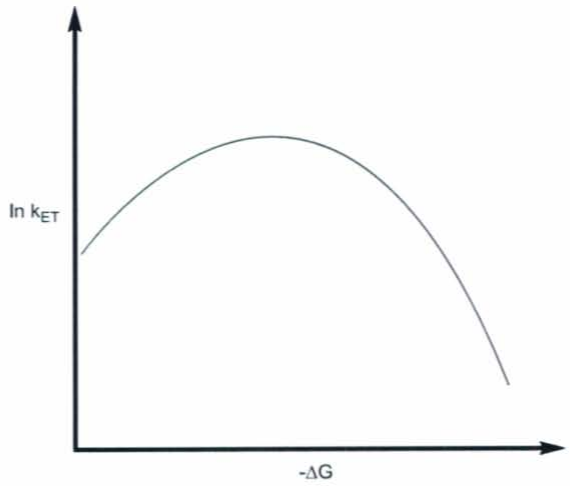

Figure 7.2.4.1. Driving force dependence on the rate constant for excitation energy transfer.

7.2.5. Comparison between electronic excitation energy transfer mechanisms

The Dexter mechanism requires direct orbital overlap of the donor and the acceptor for an electron exchange interaction to occur. However, the Förster mechanism is primarily associated with energy transfer through a dipole-dipole mechanism and does not require direct orbital overlap of the donor and acceptor. In reality, both of these mechanisms occur to some extent. Thus, the observed rate constant for excitation energy transfer is actually a combination of both mechanisms and is given by equation 7.2.5.1 where k_{Dexter} is the rate constant for Dexter energy transfer, $k_{Förster}$ is the rate constant for Förster energy transfer, and α and β are proportionality constants.[7, 8]

$$k_{ET}^{Total} = k_{Dexter} + k_{Forster} = [\alpha\langle\Psi_i|H_{exchange}|\Psi_f\rangle]^2 + [\beta\langle\Psi_i|H_{dd}|\Psi_f\rangle]^2 \quad eqn.\ 7.2.5.1.$$

Since $k_{Dexter} \sim \exp(-2R_{DA})$ and $k_{Förster} \sim 1/R_{DA}^{6}$, the relationship between these mechanisms is illustrated by Figure 7.2.5.1 which shows that at short distances, the Dexter mechanism is dominant whereas the Förster mechanism is the dominant energy transfer mechanism at longer distances.

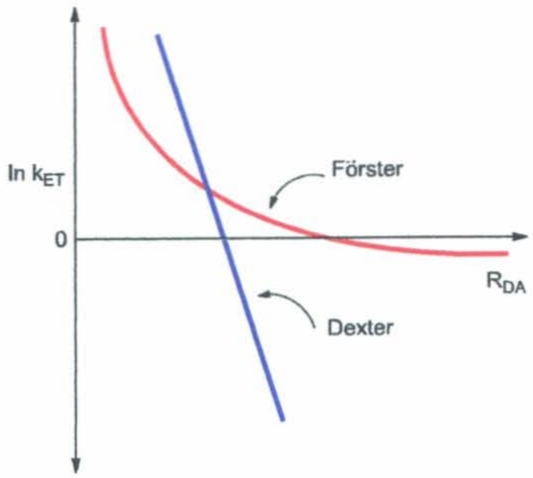

Figure 7.2.5.1. Comparison of Forster and Dexter excitation energy transfer rate constants as a function of donor-acceptor distance.

7.2.6. Electron transfer versus excitation energy transfer: The exciton

Up to now, excitation energy transfer and electron transfer have been shown to exhibit many conceptual similarities in that both processes may involve orbital overlap and electron exchange. In excitation energy transfer, the excited species is always the energy donor. However, for electron transfer, this excited species may act as an electron transfer donor or acceptor due to the specific electron distribution in the excited molecule. In this regard, because of the half-filled nature of the orbitals involved in forming an

excited state, an excited molecule is both a stronger oxidant and reductant than its ground state counterpart. This is easily explained using the exciton model for an excited state where the half-filled HOMO contains an "electron hole" (or region of electron deficiency) and the half-filled LUMO contains the excited electron. Through this exciton model (or electron-hole pair model), it is conceptually easy to rationalize why the dipole in an excited state is generally greater than the dipole in the ground state: there is a greater region of positive charge (or electron deficiency) and negative charge (or a surplus in electron density). In using such a model to represent an excited state, electron transfer may be visualized in terms of the transfer of the excited electron or the transfer of the electron hole (hole transfer). This is illustrated in the figure below.

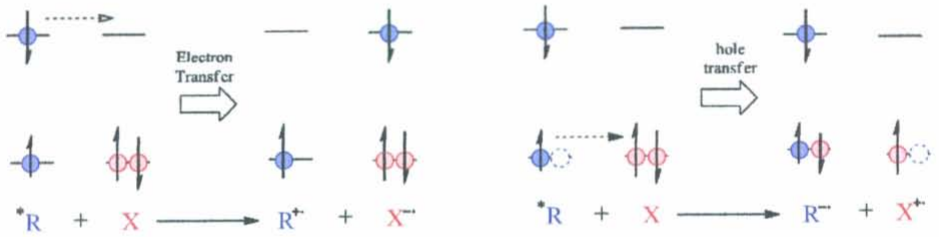

Figure 7.2.6.1. Charge transfer in terms of the exciton model.

Therefore, in keeping with this exciton model, excitation energy transfer may be visualized in terms of the transfer of the exciton from the energy donor to the acceptor.

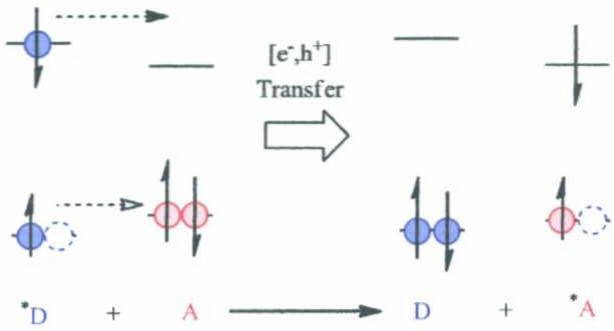

Figure 7.2.6.2. Excitation energy transfer in terms of the exciton model.

7.3. Conclusion

In this chapter, electronic excitation energy transfer theory has been discussed in terms of the Förster and Dexter formalisms. In the Förster mechanism, excitation energy is transferred via a dipole-dipole interaction. In the Dexter mechanism, an electron exchange interaction results in the transfer of excitation energy. In reality, both of these mechanisms occur to an appreciable extent with Förster energy transfer dominating over longer distances and Dexter energy transfer dominating at shorter distances.

In comparing excited state electron transfer with that of excitation energy transfer, the exciton model provides a simple link between the two processes. In excited state electron transfer, an electron or electron hole may be transferred. However, in excitation energy transfer, this electron-electron hole pair remains intact and is transferred from the donor to the acceptor.

7.4. References

[1] R. E. Blankenship, *Molecular Mechanisms of Photosynthesis*, Blackwell Science, Oxford, **2002**.

[2] X. Hu, T. Ritz, A. Damjanovic, F. Autenrieth and K. Schulten, *Quarterly Reviews of Biophysics* **2002**, *35*, 1.

[3] X. Hu, A. Damjanovia, T. Ritz and K. Schulten, *Proceedings of the National Academy of Sciences of the United States of America* **1998**, *95*, 5935.

[4] T. n. Pullerits and V. Sundstram, *Accounts of Chemical Research* **1996**, *29*, 381.

[5] G. R. Fleming and G. D. Scholes, *Nature* **2004**, *431*, 256.

[6] G. S. Engel, T. R. Calhoun, E. L. Read, T.-K. Ahn, T. Mancal, Y.-C. Cheng, R. E. Blankenship and G. R. Fleming, *Nature* **2007**, *446*, 782.

[7] N. J. Turro, V. Ramamurthy and J. C. Scaiano, *Principles in Molecular Photochemistry: An introduction*, University Science Books, **2009**.

[8] C.-P. Hsu, *Accounts of Chemical Research* **2009**, *42*, 509.

[9] T. Forster, *Discussions of the Faraday Society* **1959**, *27*, 7.

[10] J. R. Lakowicz, *Principles of Fluorescence Spectroscopy*, Third ed., Springer, **2006**.

[11] D. L. Dexter, *A Theory of Sensitized Luminescence in Solids, Vol. 21*, AIP, **1953**.

[12] E. V. Anslyn and D. A. Dougherty, *Modern Physical Organic Chemistry*, University Science Books, **2006**.

[13] D. B. MacQueen, J. R. Eyler and K. S. Schanze, *Journal of the American Chemical Society* **1992**, *114*, 1897.

[14] Z. Murtaza, D. K. Graff, A. P. Zipp, L. A. Worl, W. E. Jones, Jr., W. D. Bates and T. J. Meyer, *The Journal of Physical Chemistry* **1994**, *98*, 10504.

Chapter 8:

"SUPRAMOLECULAR ADDUCTS INVOLVING THE [3X3] $Zn(II)_9$ GRID-TYPE COMPLEX"

Abstract: In chapters 5 and 6, the excited states for the [3x3] grid-type complexes $[Zn(II)_9(2POAP\text{-}2H)_6]^{6+}$, $[Mn(II)_9(2POAP\text{-}2H)_6]^{6+}$, and $[Mn(III)_4Mn(II)_5(2POAP\text{-}2H)_6]^{10+}$ have been described in terms of the ligand framework and the metal core. Such states were shown to exhibit charge transfer whereby the excited states for the ligands in these complexes were associated with charge transfer specific to each of the discrete ligands that compose the molecule. With these excited states in mind, this chapter serves to demonstrate excitation energy transfer using the excitation energy transfer formalisms described in chapter 7 to enhance the formation of a charge transfer state within the $Zn(II)_9$ grid. As such, excitation energy transfer experiments are presented involving $[Zn(II)_9(2POAP)_6]^{6+}$ and anthracene-9-carboxylic acid. The interaction of these molecules is shown to result from the formation of a hydrogen bonded supramolecular adduct.

8.1. Introduction

The funnelling of excitation energy to charge transfer states in reaction centers is a fundamental process in the photosynthetic organism which allows for its survival. In the previous chapters, the grid-type complexes studied have been shown to possess accessible charge transfer states via light excitation. In this chapter, the formation of a charge-transfer state within $[Zn(II)_9(2POAP\text{-}2H)_6]^{6+}$ is shown to be enhanced through excitation energy transfer. In the following sections, the excitation energy transfer theory discussed in chapter 7 will be applied to the [3x3] $Zn(II)_9$ grid-type complex which displays excitation energy transfer from anthracene-9-carboxylic acid through the formation of a supramolecular hydrogen-bonded adduct. Initially, NMR data will be presented to characterize the interaction in the ground state. Following this characterization,

fluorescence quenching data are presented involving $[Zn(II)_9(2POAP\text{-}2H)_6]^{6+}$ and anthracene-9-carboxylic acid.

8.2. Results and Discussion

8.2.1. ^{1}H-NMR titration

^{1}H-NMR titration of anthracene-9-carboxylic acid ($AnCO_2(H)$) with $[Zn(II)_9(2POAP\text{-}2H)_6]^{6+}$ is shown in Figure 8.2.1.1. For a discussion on the NMR assignments in the $Zn(II)_9$ grid, see section 5.2.1. In this experiment, the amount of $[Zn(II)_9(2POAP\text{-}2H)_6]^{6+}$ remained constant and equivalent portions of $AnCO_2(H)$ were varied. A plot of the relative splitting between H_3^i and H_4^o grid peaks is given in Figure 8.2.1.2, which suggests that the interaction saturates after 4 equivalents of $AnCO_2(H)$ added. Given that the NH_2 peaks are broadened and shift, this may suggest hydrogen bonding between $AnCO_2(H)$ and the ligands in this grid. More specifically, since the inner NH_2 groups are most broadened, and that there are four of these groups, this suggests that hydrogen bonding between $AnCO_2(H)$ and the inner ligands of $[Zn(II)_9(2POAP\text{-}2H)_6]^{6+}$ is the dominant interaction in the 4:1 mixture. Further analysis is presented below to support this hypothesis.

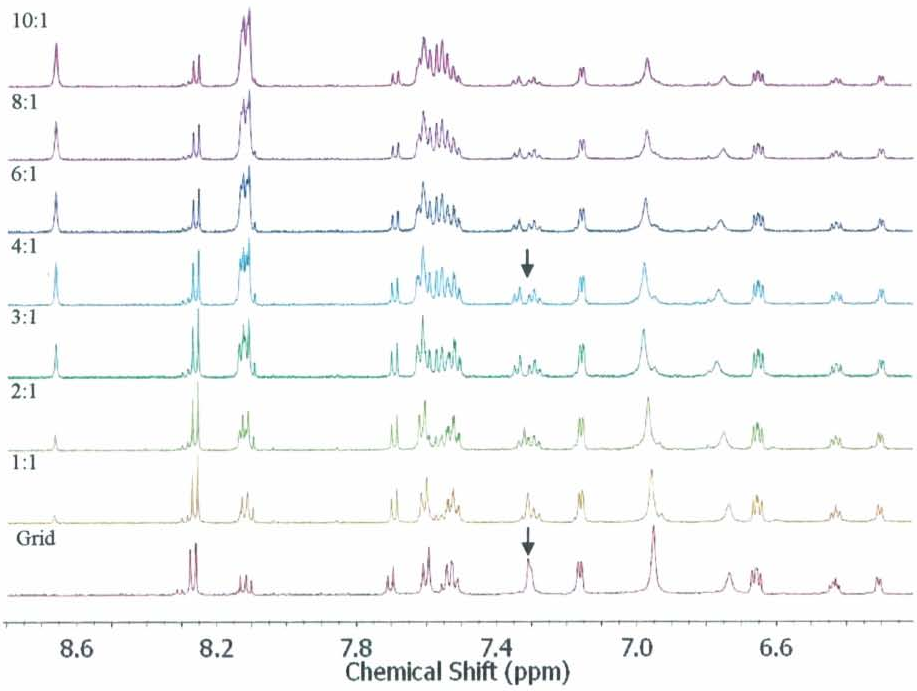

Figure 8.2.1.1. ^{1}H-NMR titration of $AnCO_2(H)$ with $[Zn(II)_9(2POAP\text{-}2H)_6](NO_3)_6$ in d_3-acetonitrile.

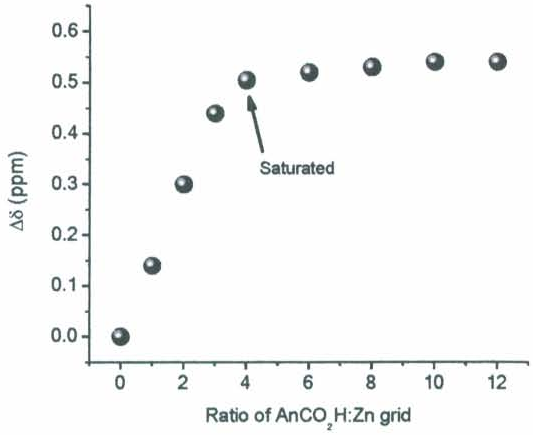

Figure 8.2.1.2. Change of splitting between H_3^i and H_4^i for $[Zn(II)_9(2POAP\text{-}2H)_6]^{6+}$ relative to $AnCO_2(H)$ equivalents added.

The interaction of $[Zn(II)_9(2POAP\text{-}2H)_6]^{6+}$ with $AnCO_2(H)$ is summarized in Figure 8.2.1.3. In the weak coupling limit between the grid and $AnCO_2(H)$, where no interaction between the grid and $AnCO_2(H)$ exists, a calculated ^{1}H-NMR spectrum of the interaction may be given as the sum of each of the individual free induction decay patterns. However, on interaction of $[Zn(II)_9(2POAP\text{-}2H)_6]^{6+}$ with $AnCO_2(H)$, the observed ^{1}H-NMR spectrum does not match the calculated spectrum, indicating that both molecules are coupled to one another. The observed ^{1}H-NMR spectrum for this interaction exhibits three important features:

(i) Chemical environments of H_2^A and H_5^A are no longer equivalent while H_1^A remains unaffected. This indicates that the interaction takes place on the carboxylate side of the anthracene derivative whereby the interaction shields H_5^A causing an upfield shift.

(ii) $H_3^{i,o}$ and $H_4^{i,o}$ of the grid are shifted on interaction with the anthracene derivative. This may suggest an opening of the grid along the periphery of the ligand structure.

(iii) NH_2 protons (H_5^i, H_5^o) are shifted downfield and are broadened.

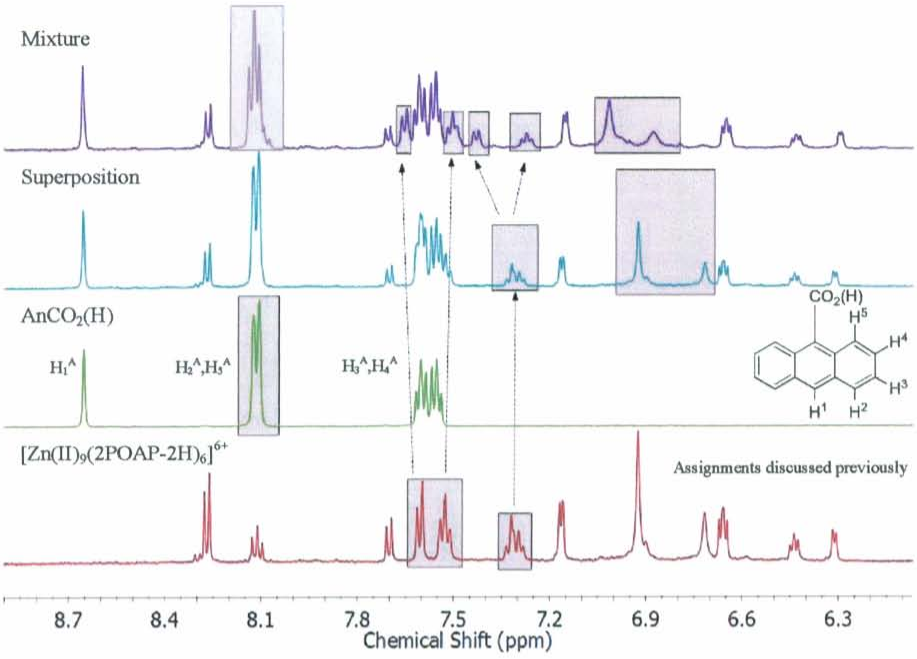

Figure 8.2.1.3. Summary of the interaction of $AnCO_2(H)$ with $[Zn(II)_9(2POAP\text{-}2H)_6]^{6+}$ in d_3-acetonitrile.

The temperature dependent ^{1}H-NMR data for $[Zn(II)_9(2POAP\text{-}2H)_6]^{6+}$ interacting with $AnCO_2(H)$ is given in Figure 8.2.1.4(a). The data indicate a shift in ligand peaks associated with $H_3^{i,o}$ and $H_4^{i,o}$ on lowering the temperature towards those exhibited solely by the $Zn_9(II)$ grid (discussed in Chapter 5). NH_2 peaks associated with inner and outer ligands appear to broaden and shift downfield on lowering the temperature, with a single broad peak present at 278 K. The H_5^A peak appears to shift on changing the temperature as exhibited by the anthracene derivative in the absence of $[Zn(II)_9(2POAP\text{-}2H)_6]^{6+}$ (Figure 8.2.1.4(b)). However, the chemical environment of this proton on interaction with $[Zn(II)_9(2POAP\text{-}2H)_6]^{6+}$ does not match that exhibited by this molecule when present

solely in solution. If one considers a hydrogen bonding interaction between the anthracene derivative and the NH_2 groups of the grid, then it is expected that proton peaks should show a greater shift with respect to each other on lowering the temperature. This was not observed, with proton peaks showing a greater shift at increasing temperatures. Given the shifting pattern of the $H_3^{i,o}$ and $H_4^{i,o}$ peaks of the Zn_9(II) grid, and the shifting pattern of H_5 of the anthracene derivative, it is proposed that the ligand-stacked structure of the grid preferentially opens at higher temperatures and preferentially closes at lower temperatures on interaction with $AnCO_2$(H). Furthermore, given the shifting pattern associated with H_5 of the anthracene derivative within this interaction, it may be suggested that these molecules form a penetrating close-contact ion pair[1] with the $AnCO_2$(H) inserting within the vacant pockets between ligands of the grid in an edge-on T-shaped fashion, causing these ligands to open in order to accommodate the inserting molecule. However, a hydrogen bonding interaction is also plausible if one takes into account the reorganization of the ligand-ligand framework associated with the interaction of the grid with $AnCO_2$(H). As the ligand-ligand distance is ~3.5-3.8 Å, and the total distance between the H_5 protons of the anthracene derivative is ~5 Å, formation of a penetrating ion pair is not feasible. Furthermore, given the removal of the inner NH_2 peak in lowering the temperature within this interaction, exchange of this proton through a hydrogen bonding interaction with the inner ligand of the grid is highly plausible and is therefore proposed (Scheme 8.2.1.1).

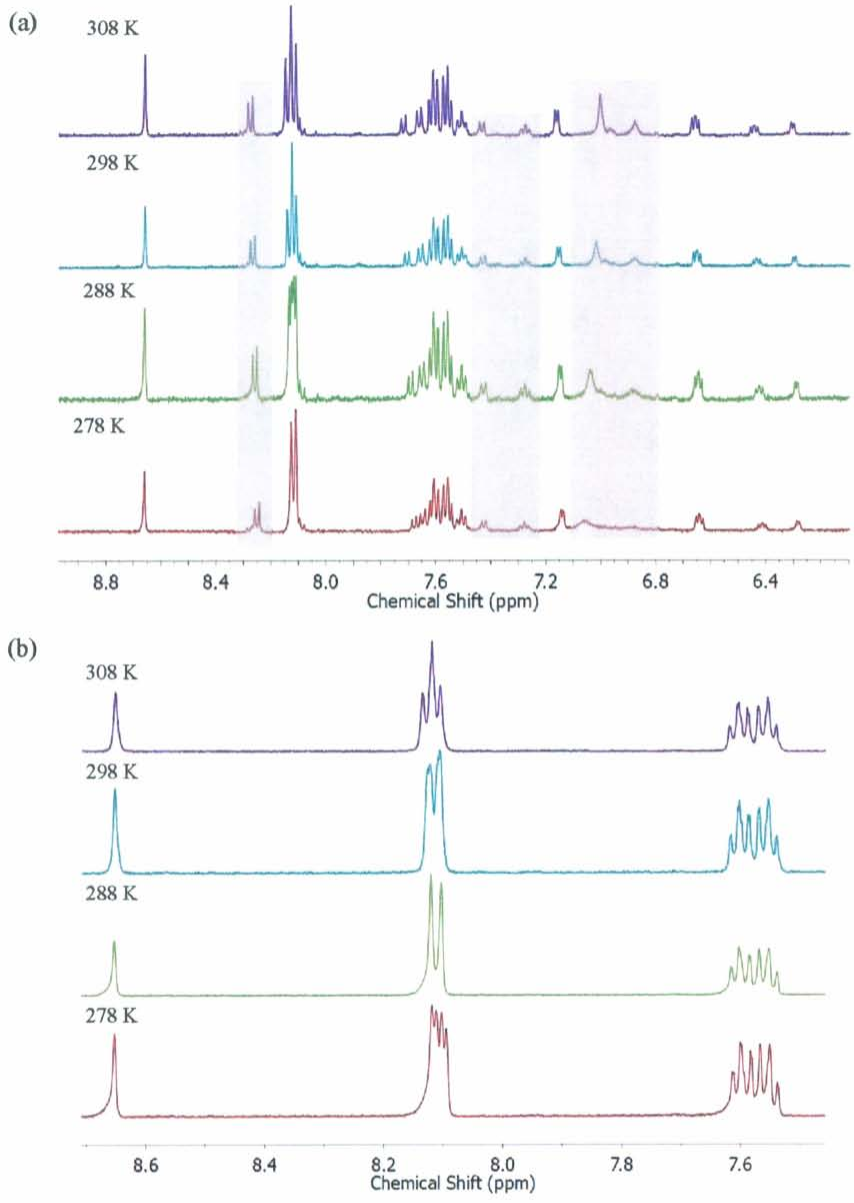

Figure 8.2.1.4. Temperature-dependent ^{1}H-NMR data for (a) the interaction of $AnCO_2(H)$ with $[Zn(II)_9(2POAP\text{-}2H)_6]^{6+}$ and (b) $AnCO_2(H)$ in d_3-acetonitrile.

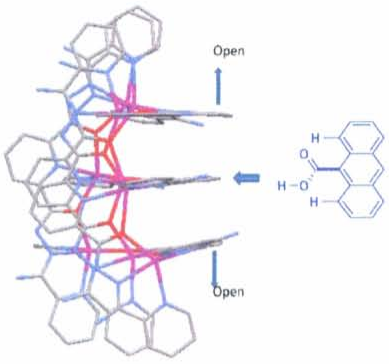

Scheme 8.2.1.1. Proposed inner-ligand hydrogen bonding interaction. Structural data were obtained from the CIF file attached with references [2, 3].

8.2.2. Spectrophotometric Titration

In order to further assess the interaction between the Zn_9(II) grid and the anthracene derivative presented in the previous section, the interaction was monitored through a spectrophotometric titration (Figure 8.2.2.1). On addition of $[Zn(II)_9(2POAP\text{-}2H)_6]^{6+}$ to a solution of $AnCO_2(H)$ in acetonitrile, growth of absorption bands corresponding to $[Zn(II)_9(2POAP\text{-}2H)_6]^{6+}$ are observed (Figure 8.2.2.1(a)). Emission from the $AnCO_2(H)$ appears to be quenched on addition of $[Zn(II)_9(2POAP\text{-}2H)_6]^{6+}$ (Figure 8.2.2.1(b)), with no observed emission from $[Zn(II)_9(2POAP\text{-}2H)_6]^{6+}$ even at higher grid concentrations. This may suggest that the formation of the emissive charge-transfer state within the grid has been prevented on interaction with $AnCO_2(H)$; however, the lowest lying excited state between these two molecules is still the outer ligand charge transfer state in the grid. Therefore, this quenching may be considered as a consequence of excitation energy transfer as discussed below.

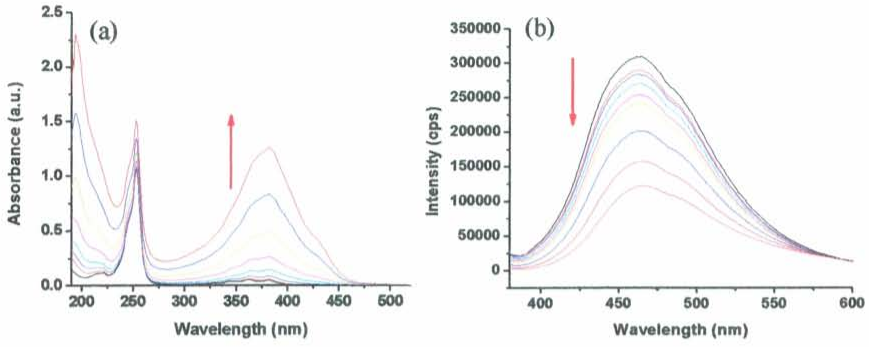

Figure 8.2.2.1. Spectrophotometric titration of $AnCO_2(H)$ with $[Zn(II)_9(2POAP\text{-}2H)_6]^{6+}$ in acetonitrile. (a) UV-Vis absorption data and (b) fluorescence data. 5, 10, 20, 30, 40, 80, 140, and 220 μL additions of a 72 μM solution were made to 2.0 mL of an 8.9 μM solution of $AnCO_2H$ in acetonitrile.

8.2.2.1. Stern-Volmer Analysis

A Stern-Volmer plot (Figure 8.2.2.1.1) of the spectrophotometric data using equation 8.2.2.1[4, 5] produces an upward curve suggesting the presence of both static and dynamic quenching. The presence of static quenching is expected given the previous ^{1}H-NMR data suggesting ground state complexation. The data was fit to equation 8.2.2.1.1 to yield a static quenching constant (K_S) of $1.6x10^5$ M^{-1} and a dynamic quenching constant (K_d) of $1.9x10^4$ M^{-1}. In equation 8.2.2.1.1, I_o is the initial emission intensity in the absence of the quencher, I_t is the emission intensity in the presence of the quencher, and $[Q]_{Total}$ is the total quencher concentration.[4, 5]

$$\frac{I_o}{I_t} = (1 + K_S[Q]_{Total})(1 + K_d[Q]_{Total}) \qquad \textit{eqn. 8.2.2.1.1.}$$

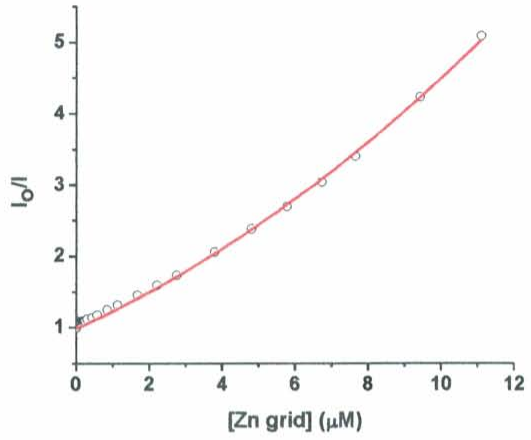

Figure 8.2.2.1.1. Stern-Volmer analysis of the interaction of $AnCO_2(H)$ with the $Zn_9(II)$ grid in acetonitrile. R^2 for the fit was 0.998.

8.2.2.2. Energy Transfer Mechanism and quenching sphere

Given the degree of UV-Vis spectral overlap between $AnCO_2(H)$ and $[Zn(II)_9(2POAP\text{-}2H)_6]^{6+}$, and the degree of overlap associated with $AnCO_2(H)$ emission and UV-Vis absorption of the $Zn(II)_9$ grid (Figure 8.2.2.2.1(a)), it is expected that energy transfer from $AnCO_2(H)$ to the $Zn(II)_9$ grid via the Förster mechanism will be a dominate process. Additionally, trivial energy transfer to the grid charge-transfer state whereby the emitted light from the $AnCO_2(H)$ is absorbed by the grid (Figure 8.2.2.2.1.) may also occur through uncoupled $Zn(II)_9$ grid and $AnCO_2H$ molecules in solution. Since $\phi_{em}^{An} >> \phi_{em}^{grid}$, grid emission may be overshadowed by $AnCO_2(H)$ emission. A proposed energy transfer pathway is given in Figure 8.2.2.2.1(b).

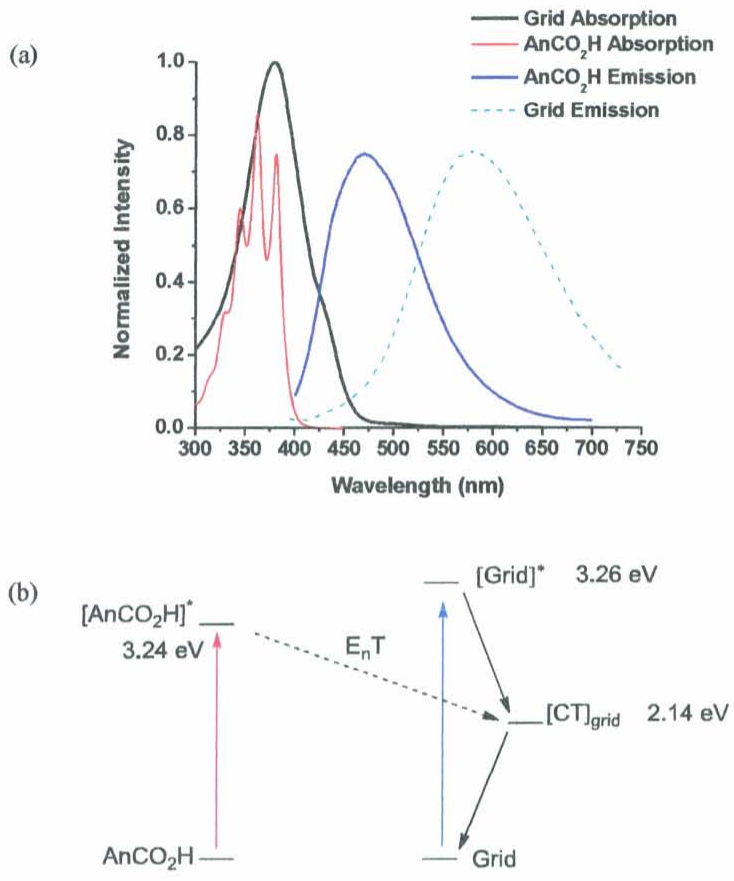

Figure 8.2.2.2.1. Illustration of spectral overlap and energy transfer between the Zn_9(II) grid and $AnCO_2$(H) in acetonitrile. (a) Normalized absorption and emission spectra and (b) a proposed energy transfer pathway.

The Stern-Volmer expression in equation 8.2.2.1.1 may also be expressed as that given in equation 8.2.2.2.1 where V_Q is the volume of the quenching sphere assuming a spherical model for the quenching.[4, 5]

$$\frac{I_0}{I_t} = (1 + K_S[Q]_{Total})e^{N_A V_Q [Q]_{Total}} \qquad \textit{eqn. 8.2.2.2.1.}$$

Using equations 8.2.2.1.1 and 8.2.2.2.1, V_Q is expressed as that given in equation 8.2.2.2.2.

$$V_Q = \frac{\ln(1+K_S[Q]_{Total})}{N_A[Q]_{Total}} \qquad \textit{eqn. 8.2.2.2.2.}$$

Since the volume of a sphere is related to the radius of the sphere (equation 8.2.2.2.3), the radius of the quenching sphere (R_Q) as a function of total quencher concentration is given by equation 8.2.2.2.4.

$$V_Q = \frac{4}{3}\pi(R_Q)^3 \qquad \textit{eqn. 8.2.2.2.3.}$$

$$R_Q(\text{Å}) = \left[\frac{3\ln(1+K_S[Q]_{Total})}{4\pi N_A[Q]_{Total}}\right]^{\frac{1}{3}} x10^9 \qquad \textit{eqn. 8.2.2.2.4.}$$

As such, R_Q was calculated using equation 8.2.2.2.4 using the static quenching value of 1.6 x 10^5 M^{-1} determined previously. A plot of R_Q as a function of the concentration of $Zn(II)_9$ grid added for the above Stern-Volmer analysis is given in Figure 8.2.2.2.2.

(a)

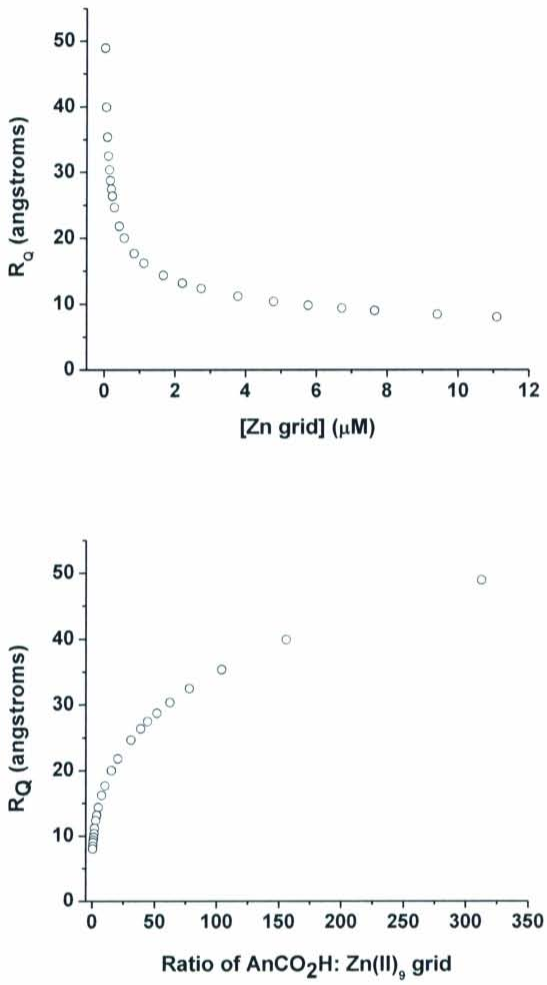

Figure 8.2.2.2.2. Quenching sphere radius for the $AnCO_2H/Zn(II)_9$ grid interaction (a) as a function of $Zn(II)_9$ grid concentration in solution, and (b) as a function of the ratio of $AnCO_2H$ to $Zn(II)_9$ grid in solution. [$AnCO_2H$] was constant at 8.9 μM.

The data in Figure 8.2.2.2.2 indicate that at relatively high $Zn(II)_9$ grid concentrations and at low ratios $AnCO_2H$:$Zn(II)_9$ grid, the radius of the quenching sphere

is constant at ~8 Å. However, as the ratio of $AnCO_2H$:$Zn(II)_9$ grid increases, the quenching sphere radius drastically increases up to ~50 Å. This value is well beyond the dimensions of each molecule and suggests an extended quenching sphere of $AnCO_2H$ encompassing the $Zn(II)_9$ grid. As excitation energy transfer involves some degree of coupling, this long-range excitation energy transfer is thought to occur via dipole-dipole coupling through a Förster excitation transfer mechanism. Moreover, coupling between the $AnCO_2H$ and the $Zn(II)_9$ grid over this long distance may also occur via a framework of appropriately aligned dipoles of $AnCO_2H$ molecules. This may occur by alignment of dipoles through interaction of a number of anthracene π systems.

8.3. Conclusion

In this chapter, the funnelling of excitation energy from an anthracene derivative to an intraligand charge-transfer state in a $Zn(II)_9$ grid has been illustrated. The interaction of the anthracene derivative with the $Zn(II)_9$ grid has been shown to occur via a hydrogen-bonded interaction with on the inner ligands of the grid complex. The funnelling of excitation energy to a charge-transfer state in a grid-type complex opens new areas for the chemistry associated with polymetallic grids which may be heavily linked to solar energy storage. Moreover, the formation of a hydrogen bonding interaction involving these complexes suggests a methodology for further self-assembly of grid-type complexes onto appropriately derivatised molecular constructs. This ultimately provides a means to the construction of higher-order supramolecular grid-type architectures.

8.4. References

[1] A. Macchioni, *Chemical Reviews* **2005**, *105*, 2039.

[2] L. Zhao, Z. Xu, H. Grove, V. A. Milway, L. N. Dawe, T. S. M. Abedin, L. K. Thompson, T. L. Kelly, R. G. Harvey, D. O. Miller, L. Weeks, J. G. Shapter and K. J. Pope, *Inorganic Chemistry* **2004**, *43*, 3812.

[3] L. Zhao, C. Matthews, L. K. Thompson and S. L. Heath, *Royal Society of Chemistry, Chem. Commun.* **2000**, 265.

[4] J. R. Lakowicz, *Principles of Fluorescence Spectroscopy*, Third ed., Springer, **2006**.

[5] N. J. Turro, V. Ramamurthy and J. C. Scaiano, *Principles in Molecular Photochemistry: An introduction*, University Science Books, **2009**.

Chapter 9:

"GENERAL CONCLUSIONS"

9.1. Conclusions

The work presented in this thesis encompasses the photophysical aspects of three highly-organized multi-metallic grid-type nanoscale systems with respect to the arrangement of metal ions and ligands. These three [3x3] grid-type complexes exhibit a rich tapestry of unique excited state properties. Of these unique properties, excited state electron transfer appears to be the most dominant. Given the appearance of interligand charge transfer, the ligands in [3x3] grid-type complexes act not only as discrete units, but also as coupled units! As such, the ligand motif in this type of architecture has been shown to exhibit properties similar to the photosynthetic special pair. As such, these complexes may serve as model systems to explore excited state properties similar to those of the photosynthetic special pair.

The first part of this thesis (Chapters 1-2) was a review of photophysical theory and grid synthesis. In chapter 1, the synthetic methodology, the structures available, and the unique properties known for [nxn] polytopic grid-type complexes were presented. In chapter 2, an overview of the photophysical theory and experimental techniques relevant to this thesis were presented.

The second part of this thesis (Chapter 3) discussed the photophysical properties of the ligand in the [3x3] grid-type complexes studied. Studies were presented on the uncoordinated ligand which demonstrated that the ligand was dominated by (π-π^*) transitions in the UV-Vis region. In addition, this ligand was shown to be non-emissive.

Coordination studies were also presented via computational and experimental data which suggest that metal ion coordination greatly affect the photophysical properties of this ligand.

The third part of this thesis (Chapters 4-6) classified the excited states for three [3x3] grid-type complexes. These excited states were shown to exhibit charge transfer phenomena. As such, electron transfer theory was described in Chapter 4 which included the formalisms proposed by Mulliken, Marcus, and Taube. In chapter 5, the excited states for $[Zn(II)_9(2POAP\text{-}2H)_6](NO_3)_6$ were classified through pH, solvent, and temperature studies. As Zn(II) is a d^{10} ion, properties of Zn(II) complexes are associated with the ligands encompassing the complex. Therefore, the ligand excited states for the [3x3] 2POAP grid-type complexes studied were defined in $[Zn(II)_9(2POAP\text{-}2H)_6](NO_3)_6$. With these ligand states classified, the excited states associated with the metal core of $[Mn(II)_9(2POAP\text{-}2H)_6](ClO_4)_6$, and $[Mn(III)_4Mn(II)_5(2POAP\text{-}2H)_6](ClO_4)_{10}$ were presented in Chapter 6. The excited states for these open-shell metal complexes displayed not only charge transfer phenomena attributable to the ligand framework, but also charge transfer phenomena attributed to the metal core.

The final chapters of this thesis (Chapters 7-8) focused on enhancing the light-harvesting properties of a [3x3] grid-type complex. Following a discussion of excitation energy transfer in Chapter 7, titration data were presented in Chapter 8 on the interaction of the $Zn(II)_9$ grid with anthracene-9-carboxylic acid. This interaction was shown to occur through a hydrogen-bonded adduct involving the inner ligands of the grid. It was demonstrated that Förster excitation energy transfer from the anthracene derivative to the

outer ligands of the $Zn(II)_9$ grid was a dominant feature associated with the excited state relaxation within the supramolecular assembly.

Overall, this thesis represents a first step in the technology development sector involving grid-type complexes. Discovery and innovation succinctly reflects the development of new technologies. It is through the discovery of the physical properties of new molecules and the optimization of these properties that leads to new technological milestones and new technologies. The discovery that [3x3] grid-type complexes exhibit intramolecular and intermolecular charge transfer within the ligands and metals of the complex bodes well for implementing grid-type complexes into new solar cell technologies. However, before such technologies can be envisioned, the charge transfer phenomena displayed by these molecules must be optimized.

Appendices

Appendix A: Molecular Orbitals for [Zn(II)$_3$(2POAP-2H)]

Drawings of the main orbitals involved in excited states 1-5 for [Zn(II)$_3$(2POAP-2H)] based on TD-DFT calculations. See table 3.3.4.2 for further details.

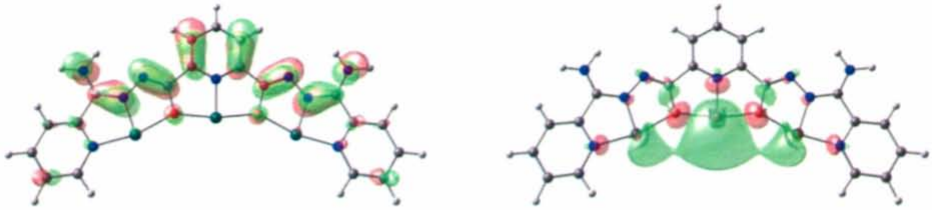

147ϕ ⟶ 148ϕ

Excited State 1

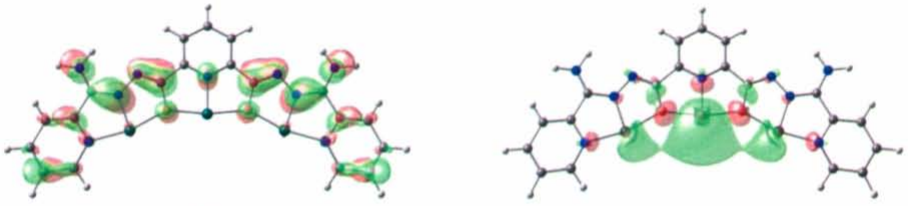

146ϕ ⟶ 148ϕ

Excited State 2

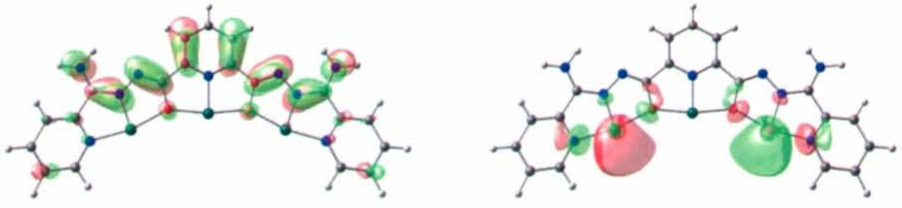

147ϕ ⟶ 149ϕ

Excited State 3

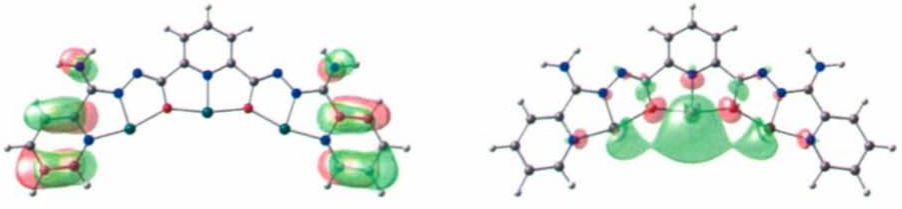

145ϕ ⟶ 148ϕ

Excited State 4

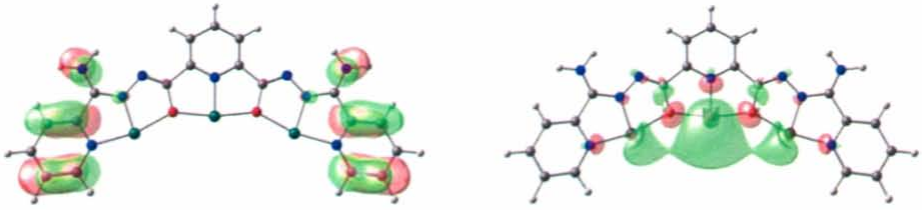

144ϕ ⟶ 148ϕ

Excited State 5

Appendix B: Derivation of Marcus Theory

If we let the parabolic function Ψ_1 be centered at the origin, then the mathematical expression for this function is given by:

$$\Psi_1: \quad y = x^2 \qquad \textit{eqn. A-1.}$$

Since Ψ_1 is set at the origin, then the expression for a second parabolic function Ψ_2 relative to the origin is defined as follows:

$$\Psi_2: \quad (y-b) = (x-a)^2 = x^2 - 2ax + a^2 \rightarrow y = x^2-2ax+a^2+b \qquad \textit{eqn. A-2.}$$

To determine the activation free energy for the transition from $\Psi_1 \rightarrow \Psi_2$, the following is used to determine the coordinates for the intersection point between the parabolas.

$$\Delta G^{\ddagger} = y_{int} = x_{int}^2 \qquad \textit{eqn. A-3.}$$

At $\Delta G^{\ddagger}$,

$$y_{int}(\Psi_1) = y_{int}(\Psi_2)$$
$$x_{int}^2 = x_{int}^2 - 2ax_{int} + a^2 + b$$
$$0 = -2ax_{int} + a^2 + b \Longrightarrow x_{int} = \frac{b+a^2}{2a} \qquad \textit{eqn. A-4.}$$

Therefore,

$$\Delta G^{\ddagger} = x_{int}^2 = \frac{(b+a^2)^2}{4a^2} \qquad \textit{eqn. A-5.}$$

In this expression, the parameter b represents the difference in energy between the zero-point energies on each of the potential energy surfaces. Thus, $b = \Delta G^{\circ}$. In contrast, the parameter *a* represents the distortion of Ψ_2 relative to Ψ_1. Therefore, the energy associated with distorting Ψ_1 to Ψ_2 is given by:

$$y(a) = a^2 \text{ (for } \Psi_1 \text{ at the reaction coordinate } a) \qquad \textit{eqn. A-6.}$$

This distortion energy is referred to as the reorganizational energy λ_t which represents the energy associated with reorganizing (or distorting) the electronic and nuclear coordinates of the system and the electronic and nuclear coordinates of the solvent from that of Ψ_1 to Ψ_2. With this parameter defined, the more famous Marcus expression for $\Delta G^{\ddagger}$ and k_{et} are shown below.

$$\Delta G^{\ddagger} = \frac{(\Delta G^o + \lambda_t)^2}{4\lambda_t} \qquad \textit{eqn. A-7.}$$

$$k_{et} = \nu_N e^{-\frac{(\Delta G^o + \lambda_t)^2}{4\lambda_t RT}} \qquad \textit{eqn. A-8.}$$

Appendix C: Derivation of Potential Energy Surfaces for Electron Transfer

The interaction of two diabatic states (non-interacting wavefunctions) attributable to the electron transfer reactants and products gives rise to two adiabatic states (interacting wavefunctions) which are associated with the wavefunctions for the ground state (Ψ_1 – a lower adiabatic state) and the excited state (Ψ_2 – a higher adiabatic state).

$$\Psi_1 = c_a\psi_a + c_b\psi_b \qquad \textit{eqn. B-1}$$
$$\Psi_2 = c_a\psi_a - c_b\psi_b \qquad \textit{eqn. B-2}$$

Mixing coefficients are given by c_a and c_b with the functions normalized ($c_a^2 + c_b^2 = 1$). ψ_a is the wavefunction for the [D,A] encounter complex and ψ_b is the wavefunction for the $[D^{+\cdot},A^{-\cdot}]$ complex.

Application of the variational theorem[1] to the equations given above results in a two-state secular determinant which when solved results in the energies of the two adiabatic states (i.e. the ground and excited state) given below.[2, 3]

$$G_{g.s.} = \frac{1}{2}\left\{(G_{bb} + G_{aa}) - [(G_{bb} - G_{aa})^2 + 4H_{ab}^2]^{\frac{1}{2}}\right\} \qquad \textit{eqn. B-3}$$
$$G_{e.s.} = \frac{1}{2}\left\{(G_{bb} + G_{aa}) + [(G_{bb} - G_{aa})^2 + 4H_{ab}^2]^{\frac{1}{2}}\right\} \qquad \textit{eqn. B-4}$$

where G_{bb} is the free energy associated with the electron transfer products and G_{aa} is the free energy associated with the encounter complex. H_{ab} is the electron transfer coupling matrix element which arises from mixing reactant and product diabatic states.

As molecules readily oscillate, both G_{aa} and G_{bb} vary with the nuclear coordinate. By defining x as the displacement from the energy minimum and assuming nuclear

motion is governed by a harmonic oscillation, the corresponding energies of the diabatic states are given below where G_{aa}^{o} and G_{bb}^{o} are the free energies at the minima for each diabatic state and d is the difference in displacement between the minima of the diabatic states for electron transfer.

$$G_{bb} = G_{bb}^{o} + \frac{1}{2} f x^2 \qquad \textit{eqn. B-5}$$

$$G_{aa} = G_{aa}^{o} + \frac{1}{2} f (x - d)^2 \qquad \textit{eqn. B-6}$$

With these expressions given above and assuming G_{aa}^{o} to be the zero of energy, the free energy surfaces for the ground and excited states are equated below where $\lambda = \frac{1}{2} f d^2$ and the reduced coordinate $X = \frac{x}{d}$.[2, 3]

$$\begin{aligned}(G_{bb} - G_{aa}) &= (G_{bb}^{o} - G_{aa}^{o}) + \frac{1}{2} f [x^2 - (x - a)^2] \\ &= \Delta G_{00} + \frac{1}{2} f [x^2 - (x^2 - 2ax + a^2)] \\ &= \Delta G_{00} + \frac{1}{2} f [x^2 - x^2 + 2ax - a^2] \\ &= \Delta G_{00} + \frac{1}{2} f a^2 [2 \frac{x}{a} - 1] \\ &= \Delta G_{00} + \lambda [2X - 1] \qquad \textit{eqn. B-7}\end{aligned}$$

$$\begin{aligned}(G_{bb} + G_{aa}) &= (G_{bb}^{o} + G_{aa}^{o}) + \frac{1}{2} f [x^2 + (x - a)^2] \\ &= \Delta G_{00} + \frac{1}{2} f [x^2 + (x^2 - 2ax + a^2)] \\ &= \Delta G_{00} + \frac{1}{2} f a^2 [2 \left(\frac{x}{a}\right)^2 - 2 \left(\frac{x}{a}\right) + 1] \\ &= \Delta G_{00} + \lambda [2X^2 - 2X + 1] \qquad \textit{eqn. B-8}\end{aligned}$$

$$\therefore \quad G_{g.s} = \frac{1}{2} (G_{bb} + G_{aa}) - \frac{1}{2} \left\{ [(G_{bb} - G_{aa})^2 + 4H_{ab}^2]^{\frac{1}{2}} \right\}$$

$$= \frac{1}{2} (\Delta G_{00} + \lambda [2X^2 - 2X + 1]) - \frac{1}{2} \left\{ [(\Delta G_{00} + \lambda [2X - 1])^2 + 4H_{ab}^2]^{\frac{1}{2}} \right\} \qquad \textit{eqn. B-9}$$

and,

$$G_{e.s} = \frac{1}{2}(G_{bb} + G_{aa}) + \frac{1}{2}\left\{[(G_{bb} - G_{aa})^2 + 4H_{ab}^2]^{\frac{1}{2}}\right\}$$
$$= \frac{1}{2}(\Delta G_{00} + \lambda[2X^2 - 2X + 1]) + \frac{1}{2}\left\{[(\Delta G_{00} + \lambda[2X - 1])^2 + 4H_{ab}^2]^{\frac{1}{2}}\right\} \quad \textit{eqn. B-10}$$

The equations derived above for the free energies for a two-state system consisting of a ground and excited state can be applied to both unsymmetrical ($\Delta G_{00} \neq 0$) and symmetrical ($\Delta G_{00}=0$) systems. For a symmetrical system, the free energy surfaces are given below for the ground and excited state by substituting $\Delta G_{00}=0$ into the above equations.

$$G_{g.s} = \frac{1}{2}(\lambda[2X^2 - 2X + 1]) - \frac{1}{2}\left\{[(\lambda[2X - 1])^2 + 4H_{ab}^2]^{\frac{1}{2}}\right\} \qquad \textit{eqn. B-11}$$
$$G_{e.s} = \frac{1}{2}(\lambda[2X^2 - 2X + 1]) + \frac{1}{2}\left\{[(\lambda[2X - 1])^2 + 4H_{ab}^2]^{\frac{1}{2}}\right\} \qquad \textit{eqn. B-12}$$

In the energy coordinate curve for the ground state defined above, the minima occur at x=0 and x=d which correspond to a reduced coordinate X=0 and X=1 if $H_{ab}=0$. However, if $H_{ab} \neq 0$, the minima are shifted and occur at $X_{min}=\frac{1\pm[1-4\left(\frac{H_{ab}}{\lambda}\right)^2]^{\frac{1}{2}}}{2}$ and have a free energy $G_{gs}=-\frac{H_{ab}^2}{\lambda}$.[2-4]

For a symmetrical system, the point of intersection for each of the diabatic curves occur at X=1/2 (x=a/2). At this reduced coordinate,

$$G_{g.s}(X = \tfrac{1}{2}) = \frac{\lambda}{4} - H_{ab} \qquad \textit{eqn. B-13}$$
$$G_{e.s}\left(X = \tfrac{1}{2}\right) = \frac{\lambda}{4} + H_{ab} \qquad \textit{eqn. B-14}$$

As a result of electronic coupling between diabatic states, the splitting at the intersection between curves is $2H_{ab}$. As discussed in the section on Marcus theory, the energy at the point of intersection is the activation energy. This energy is derived below for a symmetrical system with the incorporation of electronic coupling between states. In deriving this equation, the energy minima are corrected for electronic coupling. The rate constant for electron transfer is also given for a symmetrical system when coupling is accounted for.

$$\begin{aligned}\Delta G^{*} &= G_{g.s}\left(X=\frac{1}{2}\right) - G_{H_{ab}}^{corr} \\ &= \frac{\lambda}{4} - H_{ab} - \left(-\frac{H_{ab}^2}{\lambda}\right) \\ &= \frac{\lambda}{4} - H_{ab} + \frac{H_{ab}^2}{\lambda} \\ &= \frac{\lambda - 4H_{ab} + 4\left(\frac{H_{ab}^2}{\lambda}\right)}{4} \\ &= \frac{\lambda^2 - 4\lambda H_{ab} + 4H_{ab}^2}{4\lambda} \\ &= \frac{(\lambda - 2H_{ab})^2}{4\lambda} \qquad \textit{eqn. B-15}\end{aligned}$$

$$k_{et} = Ae^{\frac{-\Delta G^{*}}{RT}}$$

$$k_{et} = Ae^{\frac{-(\lambda-2H_{ab})^2}{4\lambda RT}}$$

$$k_{et} = \frac{2\pi}{\hbar} H_{ab}^2 \left(\frac{1}{4\pi\lambda RT}\right)^{\frac{1}{2}} e^{\frac{-(\lambda-2H_{ab})^2}{4\lambda RT}} \qquad \textit{eqn. B-16}$$

References

[1] C. Cramer, *Essentials of Computational Chemistry: Theories and Models*, 2 ed., Wiley, **2002**.

[2] K. D. Demadis, C. M. HartshornandT. J. Meyer, *Chemical Reviews* **2001**, *101*, 2655.

[3] B. S. Brunschwig, C. CreutzandN. Sutin, *Chemical Society Reviews* **2002**, *31*, 168.

[4] B. S. BrunschwigandN. Sutin, *Coordination Chemistry Reviews* **1999**, *187*, 233.

Appendix D: Deconvoluting spectra using 1st and 2nd derivatives

Experimentally, a UV-Vis-NIR spectrum consists of a convolution of gaussian-type bands which correspond to specific electronic transitions. As such, using first and second derivatives, spectra can be deconvoluted using the following procedure.

Mathematically, the first derivative for a curve represents the slope for that curve. Coordinates where the slope is 0 corresponds to both maxima and minima. In contrast, the second derivative represents the curvature for the curve. Values where this derivative is 0 corresponds to points where the curvature for the curve is changing whereas values where it is negative/positive correspond to points at which the curve is curving inward/outward (i.e. it is concave/convex). As such, to deconvolute a convoluted spectrum, one needs to locate the coordinates at which there are maxima. These coordinates correspond to where both first and second derivatives are 0 and negative, respectively. Likewise, maxima can also be determined solely from the second derivative where a positive-negative-positive pattern corresponds to a maximum.